High Voltage Power Converter for Large Wind Turbine

Sztykiel, Michal

Publication date:
2014

Document Version
Publisher's PDF, also known as Version of record

Link to publication from Aalborg University

Citation for published version (APA):
Sztykiel, M. (2014). High Voltage Power Converter for Large Wind Turbine. Department of Energy Technology, Aalborg University.

High Voltage Power Converter for Large Wind Turbine

by

Michal Sztykiel

Dissertation submitted to Faculty of Engineering, Science, and Medicine
at Aalborg University in partial fulfilment of the requirements
for the degree of Doctor of Philosophy in Electrical Engineering

Aalborg University
Department of Energy Technology
Aalborg, Denmark
June 2014

Aalborg University
Department of Energy Technology
Pontoppidanstræde 101
9220 Aalborg East
Denmark
Phone: +45 9940 9240
Fax: +45 9815 1411
Web: http://www.et.aau.dk

Abstract

The increasing penetration of the wind energy has resulted in newly planned installations of offshore wind turbines. In order to minimize installation, material and transportation costs of the offshore wind power plants, large multi-MW wind turbine systems are being preferably employed and developed, which allow high power generation of each single unit. Nevertheless, further increase in the power ratings of the newly emerging turbines becomes a major concern related to the operating voltage level.

In order to accommodate larger powers, presently employed low voltage (690 V) systems already require multi-parallel converter and filter modules, which increase the overall complexity.

In this thesis, a concept for the medium voltage wind turbine is examined and evaluated, where voltage increase is dictated by the removal of the step-up transformer. As a result, an entire wind turbine electrical system operates at 20 kV level - identical as for the collector distribution network. Medium voltage operation allows the converter unit along with the filter to be installed on the base platform inside the tower. In this manner, more space in the nacelle can be flexibly accommodated by the mechanical parts.

Due to limited voltage level of the generator insulation system (15 kV) along with the increasing grid integration requirements, special care has been made over the search for optimal full-scale power converter circuitry, which additionally has to compensate voltage differences between the generator-side and a grid-side. Three converter topologies with different conversion philosophies have been introduced (A, B and C), their performance examined and eventually compared with the conventional low voltage system. System A is a back-to-back MMC converter, which is commonly used in HVDC application. System B consists of the generator-side 2-level converter, DC/DC boost unit and a grid-side NPC-3L converter. System C is made of a series-connected full-bridge cells on the generator-side, and a grid-side NPC-5L converter.

The performance of the proposed topologies is analyzed both under the normal and fault operation. In normal operation, medium and low voltage converter topologies are compared with regard to the efficiency and the required amount of silicon material in the semiconductor switches. In fault operation, maximum temporary ratings of the collector feeder components are compared also for different grounding schemes, which impact is the result of the removed step-up transformer.

Finally, the ground fault detection scheme for feeder cable system is proposed - with the usage of current differential relay. Due to lack of the galvanic separation between the wind turbines and the feeder cable sections, careful investigation for the relay selective operation has been made, which distinguishes ground faults located at the wind turbine terminals from faults within the protected cables.

The obtained results from the computer simulations in EMTDC/PSCAD software show, that the best performance has been achieved by the transformer-less turbine with a back-to-back modular multilevel converter (MMC) topology, which is single grounded only through its DC link common-mode point. It has also occurred that the results derived from losses and short circuit analyses have become advantageous over the equivalent conventional system consisting of low voltage wind turbines equipped with the step up transformer.

Acknowledgements

I would like to acknowledge my supervisors; Remus Teodorescu, Stig Munk-Nielsen from Aalborg University, Pedro Rodriguez (from 1st February 2011 to 31st Sepember 2012) from Technical University of Catalonia, and to Vestas Reference Group members; Lars Helle, Philip Carne Kjaer from Vestas Wind Systems A/S for their guidance, support, encouragement, and valuable contributions throughout my PhD study period.

I would also like to acknowledge all my friends from the Department of Energy Technology (AAU) and members of the Vestas Power Programme for their co-operation, guidance and careful assistance during my PhD period, especially during the experimental work.

I would like also to acknowledge staff of the Department of Energy Technology and the Doctoral School for their help throughout my doctorate study

Finally, I acknowledge that this doctorate study was supported by the Aalborg University - Vestas Wind Systems partnership under the Vestas Power Programme.

Table of Contents

List of Abbreviations

2L	- Two-level
3L	- Three-level
5L	- Five-level
AC	- Alternating Current
AC/AC	- Alternating Current-to-Alternating Current
AC/DC	- Alternating Current-to-Direct Current
ANPC	- Active Neutral Point Clamped
B2B	- Back-to-Back
C filter	- Capacitor filter
CM	- Common-mode
CTL	- Cascaded Two Level
DC	- Direct Current
DC/DC	- Direct Current-to-Direct Current
EMTDC	- Electromagnetic Transients with DC Analysis
PSCAD	- Power Systems Computer Aided Design
FC	- Flying Capacitor
FFT	- Fast Fourier Transform
H-Cascaded	- Cascaded H-Bridge
HVDC	- High Voltage Direct Current
IEC	- International Electrotechnical Commission
IEEE	- Institute of Electrical and Electronics Engineers
IEGT	- Injection-Enhanced Gate Transistor
IGBT	- Isolated Gate Bipolar Transistor
IGCT	- Integrated Gate Commutated Thyristor

L filter	- Inductor filter
LV	- Low voltage
MATLAB	- Matrix laboratory
MMC	- Modular Multilevel Converter
NESC	- National Electrical Safety Code
NPC	- Neutral Point Clamped
P	- Proportional
PCC	- Point of Common Coupling
PLL	- Phase Lock Loop
PI	- Proportional and Integrated
PMSG	- Permanent Magnet Synchronous Generator
PQ	- Active power and reactive power
PS	- Phase Shifted
PWM	- Pulse Width Modulation
REF	- Reference
RMS	- Root Mean Squared
RWSG	- Rotor Wound Synchronous Generator
SC	- Short circuit
TSO	- Transmission System Operator
XLPE	- Cross-linked Polyethylene
ZCS	- Zero Current Switched

Chapter 1

Introduction

1.1 Background

This chapter considers an option to revise presently available electrical designs for offshore wind turbines. This is primarily dictated by growing commercial pressure, which forces turbine manufacturers to go bigger in terms of size and weight of each single turbine. An improved design relies on the turbine transformer-less operation, where all the electrical components operate at the increased voltage level.

According to Global Wind 2012 Report [1], a continuous trend is observed in the annual growth of the installed worldwide wind capacity. By the end of 2012, total installed capacity reached 282.5 GW, which satisfies more than 3% of the global electricity demand. Emerging new potential markets in Latin America, Eastern Europe, Africa and Asia continue to keep highest growth rates, gradually leading to geographical diversification of the wind industry. Nevertheless, short term perspectives for the wind market development are rather uncertain, as they still highly depend on few major markets, i.e. China, Western Europe and the United States.

Figure 1.1 presents an annual market forecast by region in 2012-2017 [1]. It is seen that Europe may experience drop by 2.7 GW mainly due to policy uncertainty in the European Union caused by the economical crisis. North America is likely to experience drop in 2013 by the late extension of the Production Tax Credit, which has discouraged potential investors from planning wind farm installations at that year. Asia is expected to remain world largest market, with the highest overall growth potential in China.

Although overall wind market tends to cool down in the coming years, among many available wind resources offshore wind keeps being recognized as an attractive and confident source of energy. Offshore wind turbines have important advantages, such as less environmental constraints, higher wind speeds and less turbulence [1]. As a result, offshore wind sector has already shared about 2% generation in 2012 with 33% increase from 2011, and keeps dynamically evolving mainly within the northern Europe (90% of the total offshore wind capacity). However, offshore systems are becoming an increased source of interest also in other regions: China, India, Taiwan, Japan and South Korea have already drafted road maps for offshore wind power development in their countries [2].

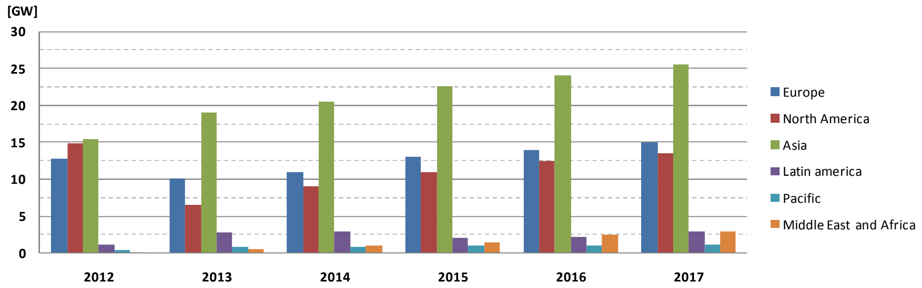

Fig. 1.1. Predicted annual market forecast for wind turbines [1].

Even though offshore wind turbines are getting more attention, there are some clear challenges ahead in the future development of these units. European Union ambitious target set in the National Renewable Energy Action Plan to obtain 5.8 GW offshore capacity by the end of 2012 is lagging by 14%, which is the result of increased costs made by installing turbines located further from the shore with higher waves and deeper ground level conditions [1].

Similar technological problems will have to be faced by South Korea and Japan, where deep water and harsh climate conditions are a problem at even shorter distances from the shore. As a consequence, increased technological efforts are currently made to bring down the costs of the future offshore wind turbines, which might be located further from the shoreline.

1.2 Evolution of Offshore Wind Turbine Concepts - Today and Tomorrow

Improvements within the offshore wind turbine concepts are driven mainly by the economics and availability of the wind energy. Existing solutions for systems with presently available devices are becoming too expensive for the required increase of the wind penetration particularly on distant offshore regions.

As a result, alternative concepts are required, which would substantially cut down material, installation and foundation costs while at the same time extracting more energy by operating at higher altitudes.

As shown in Figure 1.2, a technological trend has been observed to increase power capacity and reduce costs by constructing large wind turbines. Increase of height may allow high wind penetration in regions, which are not practically or economically suited for the smaller turbines. Reduction in material costs, installation costs, foundation costs and space is also likely to be achieved when one compares total number of small turbines required to generate the same amount of electrical power. It is therefore expected that the trend will continue and wind turbines will keep growing in terms of power ratings, which in near future will reach 10 MW or even higher values [3].

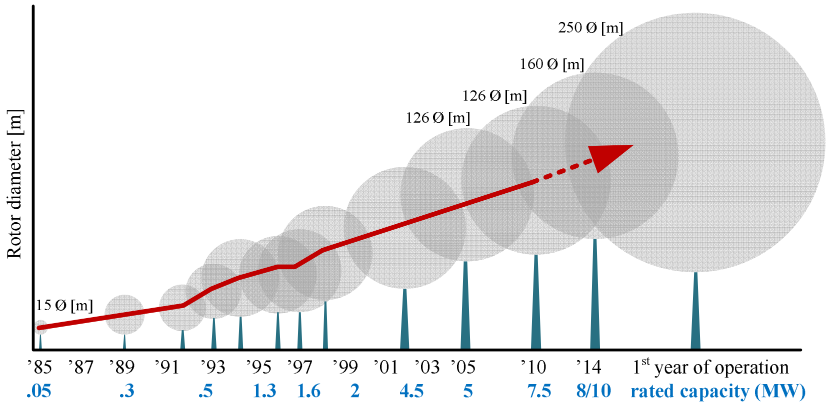

Fig. 1.2. Single wind turbine growth in rated power capacity [4].

Among many technical aspects that introduce new potential challenges for the development of these large offshore wind turbine units, two particular ones are of the major importance with regard to the overall design of the turbine electrical system. These are: grid integration and power density.

1.2.1 Grid Integration

Increasing share of the electricity production from wind has already become a major issue for wind turbine manufactures. Major markets, e.g. United States and China are planning to increase their share accordingly to 20% and 17% in 2030. In some small countries e.g. Denmark, the wind energy penetration has already hit 30% of the overall demand at the end of 2012. Governmental plans are to increase its share up to 50% by the end of 2030, and even up to 100% by the end of 2050 [5].

Increasing wind energy share results in growing impact of wind turbines on the stability of the whole transmission systems. As a result, many countries have already issued grid codes, specific requirements for interconnecting large wind power plants to the grid. As transmission system operators want to minimize costs by adapting the existing network solutions, a growing contribution to stabilize the grid is passed over to the wind turbine manufacturers, and the turbine manufacturers are expected to deliver off-the-shelf products that comply with specific standards.

It is therefore expected that most attractive wind turbine future candidate will be universal, which means that it will provide highest flexibility and controllability in generating wind power at any desired operating condition. Among the existing and available solutions within wind turbine electrical design, the highest controllability is provided by its variable speed generator equipped with full-scale power converter [6].

The variable speed generator allows operating at a certain speed range, which increases wind turbine capability to extract a desired amount of wind energy. Full-scale power converter decouples generator operation from the grid operation via common

DC link. In this manner, generator and grid can be controlled independently by each converter unit, thus greatly simplifying and improving the overall control architecture. Finally, independent full control capability of the reactive power is provided on the grid-side, which is a major asset used for supporting weak grids and during grid faults [7].

As shown in Figure 1.3, two types of variable speed generator systems are currently available on the market: The Permanent Magnet Synchronous Generator (PMSG) [8] and The Rotor Wound Synchronous Generator (RWSG) [8]. RWSG requires additional excitation power for the rotor windings, while in PMSG rotor flux is generated directly by means of the permanent magnets. In both cases the step-up transformer is normally used to increase turbine voltage to the feeder voltage level.

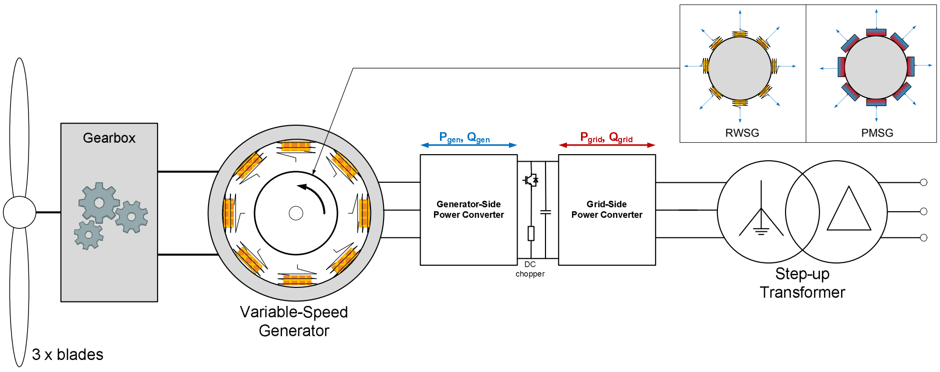

Fig. 1.3. Wind turbine equipped with full-scale power converter - schematic diagram.

1.2.2 Power Density

In order to fit all necessary components inside large offshore turbines with the minimum effort, special considerations should be made for possible space savings and optimal component stacking arrangements. In practice, material, transportation and installation costs should be further reduced to a minimum, resulting in the lowest price for the turbine on the market. From the perspective of the turbine internal electrical system, this aspect primarily corresponds to the operating voltage level.

At present, offshore wind turbines operate at relatively low voltage: 0.69 kV, which value has originated from onshore small turbines with fewer safety regulations [9]. Nevertheless, as wind power increases its share and turbines become larger, maintaining operation at 0.69 kV becomes highly uncertain due to necessity in handling very large currents. Such currents are expected to cause significant thermal-related issues, affecting especially reliability, cooling system design and the required amount of copper [10].

In order to keep a flexible stacking arrangements, reasonable size and complexity of cooling system along with less amount of necessary copper, a shift is likely to take place towards higher voltage level, where currents will be reduced while maintaining high power capacity of the single turbine. As a result, some power converter manufacturers have already developed systems originated from medium voltage drive applications specifically for wind turbines, and consequently keep pressing wind turbine industry to obtain space savings by increasing the turbine operating voltage level up to 4.16 kV [11].

Apart from the existing products available from the medium voltage drive industry, a promising alternative concept for wind turbine manufacturers slowly arises, which may ultimately eliminate issues related with an excessive current flow and what is more, reduce the necessary volume of the required electrical equipment per single turbine.

1.3 Transformer-less Wind Turbine - Future Candidate

The level of optimal operating voltage for future large wind turbines remains uncertain. It is likely that the voltage needs to be increased as the power increases, yet it is still unknown to what degree. Higher voltage means less problems with the excessive currents. Therefore, a justified increase can be either to the level often seen in medium drive industry (4.16 kV), or directly to the collector grid level (12-66 kV).

The first option constrained by the presently available medium voltage drive technology is a “safer” choice for the wind turbine design. In other words, it allows many existing solutions for the presently developed wind turbines to be kept and adapted according to the increased voltage level. Voltage increase on the generator side should not affect wind turbine operation and design substantially, as most new phenomena and issues for the wind turbine can be predicted from previous experiences and observation of commonly used similar size medium voltage variable-speed motors. In this case however, problems related with the excessive currents are not considered solved, but only reduced to a certain degree.

Second option with voltage constrained solely by the collector grid not only adds original and unknown phenomena to the wind turbine operation, but also affects internal design of all turbine electrical components. As a result, more advanced insulation and fault management systems need to be implemented along with strict safety measures for the maintenance work. On the other hand, power density concerns are of the less concern, especially related to the excessive thickness and number of the required bus-bars and cables. This is due to the resulting currents, which for operation at 20 kV level will become 20 times lower than in the equivalent 0.69 kV systems, thus reducing the conduction losses significantly. Furthermore, turbine voltage with collector feeder voltage allows removal of the bulky step-up transformer, which is a critical component in the existing systems and accounts for approximately 2-3 t and 3-4 m^3 respectively per MVA [12].

Even though immature, transformer-less concept is becoming increasingly popular also within high power drive technologies. Increasing interest has been particularly caused in 2012 with the recent development of the modular medium-voltage converter by Siemens AG, which an integral part constitutes well known in Europe modular multilevel converter concept invented by R. Marquardt [13].

In 2013 together with the Technical University of Dresden and the University of the Federal Armed Forces in Munich, Siemens AG carried out a pioneer research project entitled "Medium-voltage converters based on a new type of circuit technology (M2C) for feeding electrical energy into power grids", where a medium-voltage converter based on a modular structure is designed specifically for offshore wind turbines and put into practice that manages for the first time without additional line filters or transformers [14].

1.4 Thesis Motivation and Objectives

Transformer-less wind turbine concept provides some promising opportunities for the optimal arrangement of the electrical part in large offshore wind turbines. Lack of transformer, low cooling system requirements and elimination of the multi-parallel cabling are the main assets that will likely maximize available space, thus reducing overall cost of the turbine. Nevertheless, little scientific research has yet been done in this area, which implies that the proposed philosophy is novel and uncertain in terms of the reliable operation and the overall cost savings.

This project aims at demonstrating opportunities and challenges of the future medium voltage transformer-less wind turbines by answering following questions:

- ***How the removal of the step-up transformer affects wind turbine operation and components design?***
- ***What are the existing solutions that can be adapted for the transformer-less wind turbine?***
- ***Is the transformer-less concept a promising opportunity for future offshore wind power plants?***

The assessment is conducted with chosen aspects related to feasibility and economical issues with special regard to full-scale power converter design.

Feasibility studies include defining technical prospects and challenges for medium voltage transformer-less wind turbines (e.g. surge protection, grounding methods) along with the search and assessment of the optimal components available on the market and in the literature, which are required for the turbine electrical system. In the last part, overview is made of the existing grid codes and standards related to the wind turbine grounding and fault operation. In this manner, existing restrictions for wind turbine transformer-less operation are highlighted and discussed.

Economical assessment includes comparison of three different transformer-less wind turbine concepts with the conventional low voltage wind turbine equipped with a step-up transformer. A comparative assessment is performed by means of the steady state losses analysis. Required momentary ratings for the medium voltage equipment are compared with regard to the applied grounding method by means of the short circuit analysis. Obtained results from both study cases are meant to highlight the in-service performance of the proposed wind turbine candidates.

1.5 Thesis Outline, Delimitations and General Remarks

Following project is organized in accordance to the outline presented below. Scope of delimitations is described starting from the system description. General remarks include usage of simulation tools and modelling techniques.

1.5.1 Thesis Outline

Chapter 2: "State-of-the-Art Review"

Chapter compiles existing knowledge directly related with feasibility for the medium voltage transformer-less wind turbine implementation and design. First part includes a list and description of possible new phenomena and challenges that appear when shift is made towards medium voltage level.

Second part lists and describes design differences of the main components used for conventional low voltage turbines with the ones required for their medium voltage equivalent. Final part concludes findings by proposing 3 wind turbine circuitry candidates, varying with regard to the applied power conversion philosophies.

Chapter 3: "System Description"

Chapter describes and specifies modelled collector feeder network and wind turbine topologies for further evaluation. Models consist of: wind turbines, AC cable sections, substation transformer and grid. The wind turbine model includes generator, three medium voltage full-scale power converter circuitries (A, B and C) and LC filters on both sides.

Chapter 4: "Losses Analysis"

Chapter presents input data and methods used for the losses analysis, along with the obtained results for each wind turbine model. Input data is wind turbine power mission profile at low wind site, while the final results are compiled into weighted efficiency for each converter candidate.

Chapter 5: "Short Circuit Analysis"

Chapter presents results of the maximum short circuit currents measured for each system under different grounding modes. Line-to-ground faults are stimulated across AC cable terminals. Experimentally validated line differential relay model is used for fault detection. Converter block operation is enabled via IGBT over-current protection.

Chapter ends with a comparison of the required component momentary ratings for each system.

Chapter 6: “Conclusions, Future Work”

Chapter summarizes the current potential and future prospects of the transformer-less wind turbines with regard to the performed study cases and lists alternative areas for possible research.

1.5.2 Project Modelling Limitations

- **Wind power plant aggregated modelling** - analyzed complete system includes 5 parallel feeders - each interconnecting 10 wind turbines in a chain mode. For the losses analysis, only a single wind turbine is examined, assuming that the generated power losses in all remaining turbines are identical. For the short-circuit analysis, an equivalent detailed wind turbine model is used only to create an aggregated short circuit model made by the symmetrical sequence current sources. In a similar manner, the single feeder modelled in detail consists of 10 wind turbine aggregated models interconnected via cable PI sections, whereas the short circuit contribution of the remaining 4 feeders is represented by a symmetrical sequence current source.
- **Power electronics devices** - in the losses analysis, power losses are calculated only for the semiconductor switches. Press-pack 4500 V / 340 A devices [59] are employed for all analyzed grid-side medium voltage power converter topologies. Derived switching loss formulas have been validated experimentally at 1000 V. In case of the generator-side topologies which require different device current ratings, power loss estimator scales input collector currents to the number of chips in accordance to the examined 340 A press-pack model, which normally consists of 6 IGBT and 3 diode dies.
- **Equipment temporary ratings** - in the short-circuit analysis, only grounding conductor wire and circuit breakers are rated against fault conditions. In the case of ground wires, temporary ratings are based solely on the rated short-time withstand current (1 s). In the case of circuit breakers, temporary ratings are based solely on the rated maximum short circuit breaking current.
- **No frequency control** - the *theta* reference for the ABC/dq transformation is generated manually with the saw-tooth signal generator coupled with the pre-set nominal frequency value for the generator and grid respectively - each represented by a Thevenin voltage source. In this manner, the need for a PLL controller is avoided in the converter control scheme.
- **Generator and grid represented as a 3-phase Thevenin voltage source** - in order to include zero-sequence component variations across the generator windings, generator steady-state operation is modelled with a star-connected 3-phase voltage sources and zero-sequence impedance.

- **Ideal transformers and sensors** - the saturation effect of the substation transformer is neglected for any case derived from the short circuit analysis. Current and voltage sensors used to determine the instantaneous signal values for the control and fault detection schemes are ideal in a sense that they provide non-distorted and non-delayed input signals.
- **Ideal semiconductor valves** - the IGBT and anti-parallel diode valves consisting of series-connected devices allow equal voltage sharing, thus act as ideal switches.
- **Carrier based PS-PWM modulation for each multilevel topology** - all topologies have been investigated and compared with the PS-PWM modulation technique.
- **No cost-benefit analysis** - only some technical aspects related to cost have been compared of the wind power plant designs with the transformer-less wind turbines, i.e. efficiency, required amount of silicon, required amount of copper for grounding wire and circuit breaker ratings. However, no single merit has been developed, which combines all examined aspects, and compares them by means of the resulting cost.

1.5.3 General Remarks

- All simulation cases in time domain have been performed with the EMTDC/PSCAD software. This includes power converter hardware circuitries, controller blocks and relay models.
- MMC hardware components in system A have been sized according to the generic HVDC sizing tool in an Excel spreadsheet with the additional usage of the Visual Basic toolbox (Appendix D).
- The power losses estimator for the semiconductor devices has been created in an Excel spreadsheet with the additional usage of the Visual Basic toolbox and validated experimentally (Appendix E).
- The EMTDC/PSCAD relay model has been validated experimentally (Appendix G).
- Mathematical formulas for the curve fitting have been obtained from the *cftool* module available in the MATLAB software.
- The PI controller tuning is made in the *sisotool* module available in MATLAB.

Chapter 2

State-of-the-Art Review

2.1 Wind Turbine Design Challenges for Transformer-Less Operation

2.1.1 Dynamic Voltage Sharing in Series-Connected IGBTs

Nowadays, employed 2-level 690 V power converters require 1700 V IGBTs to be connected in parallel, rather than in series [10]. However, due to the limited voltage ratings of the available IGBTs (up to 6.5 kV [15]), series-connected valves have to be formed in order to properly operate at higher DC link voltage. Each valve requires the overall DC link voltage to be divided equally among the series-connected IGBTs. If a rapid over-voltage resulting from voltage unbalance appears on a single device, an insulation breakdown may lead to its destruction and increased voltage share among the rest of IGBTs [16].

Figure 2.1 presents an example of the typical valve incorporating 4 series connected IGBTs, where eventual failure of 3 IGBTs results in full DC voltage imposed on the last remaining device. In order to maintain continuous operation, failed IGBTs must be either shorted externally, or provide short-circuit failure mode.

As power converters operate at unpredictable variable loading conditions dictated by wind energy fluctuations, it becomes a complex issue to design a reliable and efficient voltage equalization scheme for the dynamic states, which would consist of snubber and gate driver circuits. Existing solutions that might be adapted for wind turbines include Active Gate Control [17] from medium voltage drive applications, redundant press-pack IGBTs [18] from HVDC applications, or multilevel converter topologies from the literature.

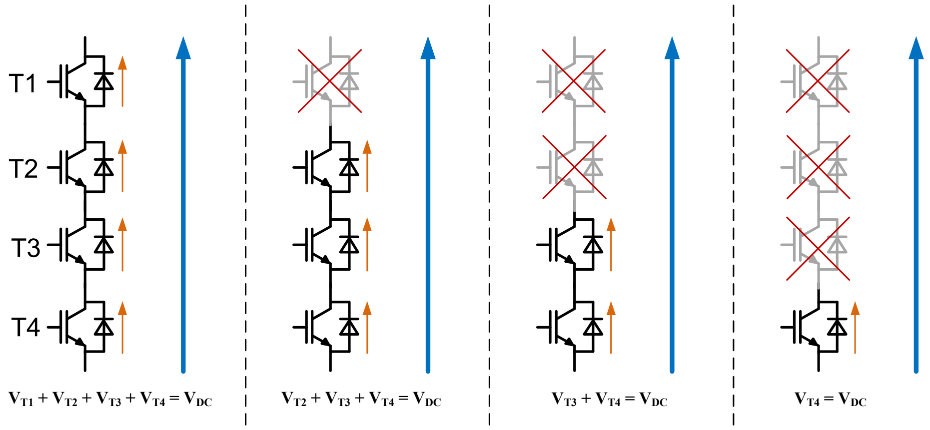

Fig. 2.1. Increased voltage sharing of the series-connected IGBTs in a single valve.

2.1.2 Voltage Rate of Change dv/dt

Switching operation of power converters results in high dv/dt voltage pulses imposed on the generator, series reactor and cable insulation systems. In the low voltage area up to 1 kV, the dv/dt pulses are safe below 16,000 V/µs level provided in NEMA MG-1 standard. In medium voltage area, the dv/dt pulses exceeding this level are expected as well as insulation materials with higher permittivity. Higher permittivity means in general larger stray capacitances, which will be subjected to the increased dv/dt pulses. As shown in Figure 2.2, stray currents are likely to flow through insulation materials, causing its accelerated aging due to thermal stress [20].

Degradation of insulation material may also originate from breaking chemical bonds due to partial discharge effect caused by ion migration. Existing air gaps and voids within insulation systems will create numerous voltage sparks due limited electric strength of the air E_{air}. It is already known from medium voltage drive systems, that the bombardment of electrons from sparks degrade the insulation material properties [20].

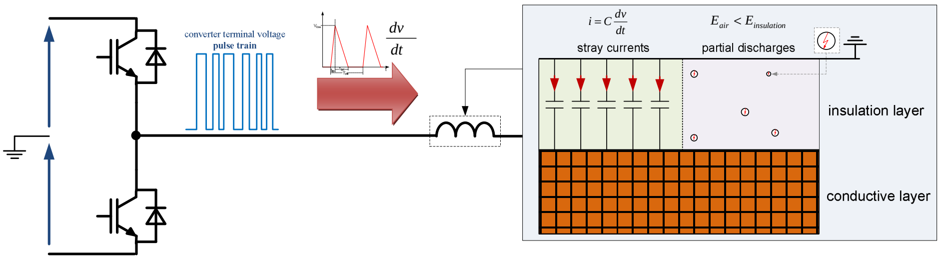

Fig. 2.2. Accelerated aging of the insulation material due to dv/dt pulses

In order to assure reliable operation of the electrical machines, IEC 60034-18-41 standard [21] defines form-wound coil machine stress categories with regard to the imposed dv/dt rate. dv/dt impact is defined by three features of the voltage impulse: frequency, overshoot and rise time. Table 2.1 lists the defined parameter ranges according to stress category.

Table 2.1. Classification of stress categories for form-wound coil windings [21].

Stress Category	**Impulse Voltage Repetition Rate [kHz]**	**Voltage Overshoot (V_{peak}/V_{phase})**	**Impulse Rise Time, t_r [µs]**	
			With Stress Grading	**Without Stress Grading**
Benign	≤ 1	≤ 1.2	> 10	≥ 1
Moderate	≤ 4	≤ 1.5	$10 \geq t_r \geq 1$	$t_r \geq 0.3$
Severe	> 4	> 1.5	Machines are not available to this qualification	

Benign stress category for the medium voltage form-wound machines can be achieved by means of the multilevel converter topologies, which allow operation at the decreased voltage overshoot and impulse rise times.

2.1.3 Common-Mode Voltages and Leakage Currents

In this work, common-mode voltages and leakage currents are considered as steady state zero sequence components, which are generated due to switching operation of the power converter, as shown in Figure 2.3a. In conventional low voltage wind turbines equipped with a step-up transformer, the low-voltage side of the transformer is normally grounded for ground fault detection, safety and in order to provide reference for the control system [22].

In transformer-less wind turbines, removal of the step-up transformer eliminates the ground source along with the zero sequence decoupling between the wind turbine and collector feeder network. As a result, common-mode voltages change not only due to the increased voltage level, but also depend on the applied grounding system over the entire collector feeder network.

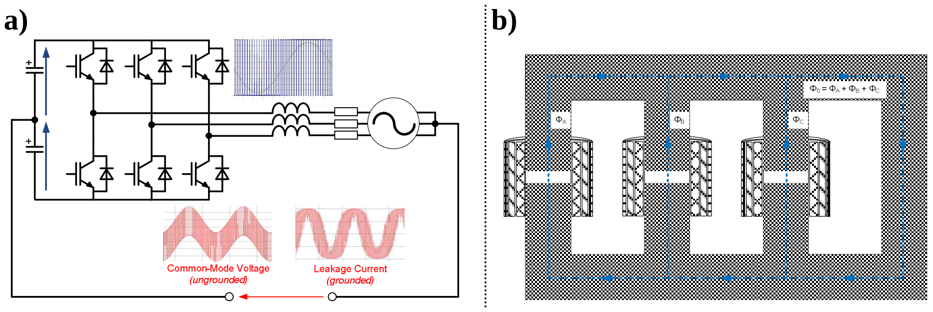

Fig. 2.3. CM voltage between neutral points (left); 4-limb reactor core design (right).

In practice, problems associated with common-mode voltage relate to increased ground insulation requirements of the main circuit components, while problems associated with leakage currents relate to increased ground temperature, limited sensitivity for ground fault detection and specifically: DC link capacitor voltage unbalance when zero-sequence current path is formed through the converter common-mode points [23].

Zero sequence components in collector feeder can be minimized by:

- grounding of characteristic points through derived specific impedance values,
- 0-sequence filtering with 4-limb reactors (tripled 0-seq. magnetic flux - Fig. 2.3b) [24],
- algorithms applied through converter control and modulation schemes [25],
- implementing converter topologies with very high number of levels.

2.1.4 Additional Inductance and Triplen Harmonic Injection

Step-up transformer provides additional series inductance for the required current filtering at the grid terminals. In transformer-less turbines with a similar power converter switching performance, this may result in need for larger series reactor in order to provide an equivalent filtering effect.

Apart from providing the additional inductance, wind turbine transformers with a Y-Δ winding arrangement shown in Figure 2.4 prevent triplen harmonic distortions from entering into the collector feeder system. This is achieved by natural 30^0 phase shift between voltages induced in Wye-windings and Delta-windings [26].

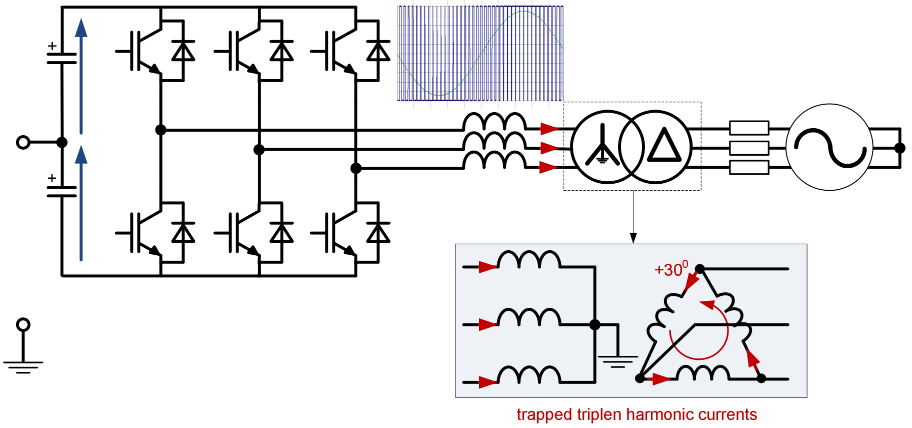

Fig. 2.4. Transformer circulating triplen current harmonics in delta windings.

Delta-winding blocks triplen harmonic components, which normally circulate in Delta-winding, with all its consequences (i.e. increased eddy current losses).

Due to the lack of transformer, it is expected that triplen harmonic currents and voltages will enter into the collector feeder in a form of parasitic zero sequence components (common-mode voltages and leakage currents).

2.1.5 Saturation Effect, Overvoltage Protection and Insulation Coordination

Under normal operation, saturation effect is considered harmful due to substantial decrease of the inductance, which generates heavily distorted waveforms that create additional losses and worsen power quality. Although for the same reason, under abnormal conditions saturation often protects electrical components on low voltage side of the wind turbine against transient voltage spikes coming from the grid, for example caused by lightning strike or switching operation at the substation terminal [22].

Figure 2.5 shows conventional wind turbines with two iron-core components that are located at the grid-side: series reactor and step-up transformer. Series reactor cores are designed with air gaps in order to store certain amount of energy within the gap, which reduces the rate of rise of the magnetizing flux and prevents from saturation [27]. On the other hand, transformer cores are designed without air gaps for energy transfer purpose, which results in narrow hysteresis curve and rapid saturation under induced transient voltage spikes. In this manner, coordinated insulation is provided as only collector cables and transformer medium voltage windings will be subjected to the switching transients.

The lack of the transformer will result in voltage spikes coming from the grid to be distributed directly across insulation systems of the wind turbine components. Insulation coordination studies are therefore required in search for the reliable and cost-efficient insulation systems provided with minimum cost effort.

This includes mainly search for minimum required wind turbine equipment voltage withstand levels, surge arrester sizing and positioning.

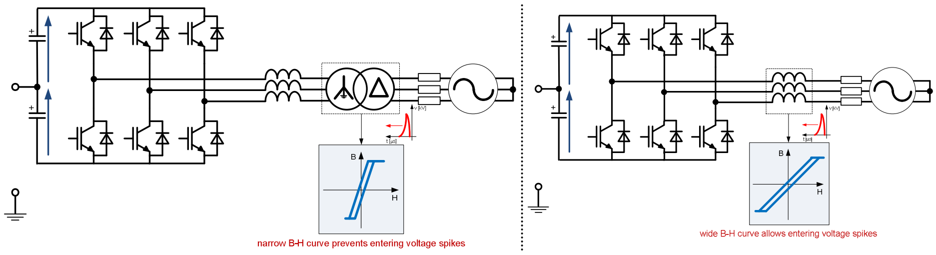

Fig. 2.5. B-H curves for step-up transformer (left) and line reactor (right).

2.1.6 Short-Circuit Protection

Medium voltage wind turbine components need special consideration for fast and reliable protection against excessive momentary short circuit currents, which unprotected will lead to rapid overheat and destruction of the equipment. The critical components of concern for the internal faults are: generator, DC link capacitors, series reactors and AC cables. Critical fault locations for the simplified system with contributions coming from a single wind turbine and a grid are shown in Figure 2.6.

It appears that medium voltage operation and lack of zero-sequence decoupling originally provided by the transformer may require new search for an optimal fault management within the entire collector feeder layout. This includes: fault detection methods, coordinated control methods for mitigating faults, grounding methods and sizing of the wind turbine components in order to withstand fault conditions.

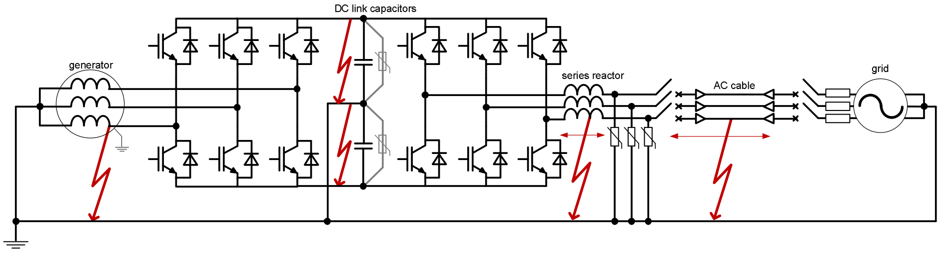

Fig. 2.6. Possible fault locations in the transformer-less wind turbine.

2.1.7 Other Concerns

Apart from the discussed, specific issues that should be investigated are:

a. Safety

Wind turbine transformer-less operation and ground coupling requires special safety equipment and procedures, so that transformer-less wind turbines working on the same feeder string will not generate any dangerous ground potential to the personnel on the particular turbine [29].

b. Humidity

Wind turbine components located distant from the shore are likely to experience insulation accelerated aging due to moisture effect. Absorbed moisture by insulation material can result in degrading the insulation material characteristics, such as tensile strength, dielectric strength or thermal conductivity. This is typically caused by induced sparks across insulation material creepage path [30].

c. Compliance with National Grid Codes and IEEE/NESC Standards

Removal of the step-up transformer affects not only components design, but also the entire grounding system of the collector feeder network. Grounding of the collector network is a concern both for transmission system operators TSOs and presently available NESC safety codes.

Some TSOs in their grid codes require ground source at the PCC in order to maintain non-disturbed ground fault detection schemes for the grid. It means that the substation transformer must have isolated 0-sequence circuit and provide grounded neutral at its high voltage terminals [31].

On the other hand, IEEE/NESC safety rules apply to underground cable neutrals grounding. Normally, "four-grounds each mile" rule (rule 096C) is required for cable grounding, including solid grounding at both sides. This rule assumes that the cable shield is connected from one side to the low-voltage neutral of the wind turbine step-up transformer [32].

Lack of the transformer forces to make a new interpretation on the interconnection between wind turbine and cable neutral. Different combinations of such connection are possible, as there are 2 natural grounding points available: generator neutral point and power converter common-mode point.

2.2 Available Components for the Future Transformer-Less Wind Turbines

The general circuit diagram for the proposed transformer-less wind turbine hardware design is shown in Figure 2.7. It presents the required main circuit elements: variable-speed synchronous generator, generator-side LC filter, full-scale power converter, grid-side LC filter and medium voltage circuit breaker.

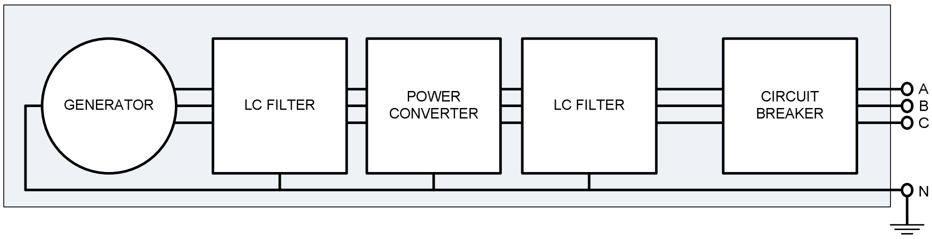

Fig. 2.7. Transformer-less wind turbine electrical hardware design.

2.2.1 Variable-Speed Generator

There are 4 stator winding design concepts, which differ according to the required voltage and power rate of the specific application. Figure 2.8 presents generator winding designs for specific voltage and power levels available in industry. Commonly utilized generator stator winding designs are:

- **Random-wound coils**, integrated design is preferred for low voltage/power machines [19].
- **Form-wound coils**, modular design is preferred for medium voltage/power machines [19].
- **XLPE cables,** recently developed for high voltage/power machines [33].
- **Roebel bars**, commonly used for very high power machines [19].

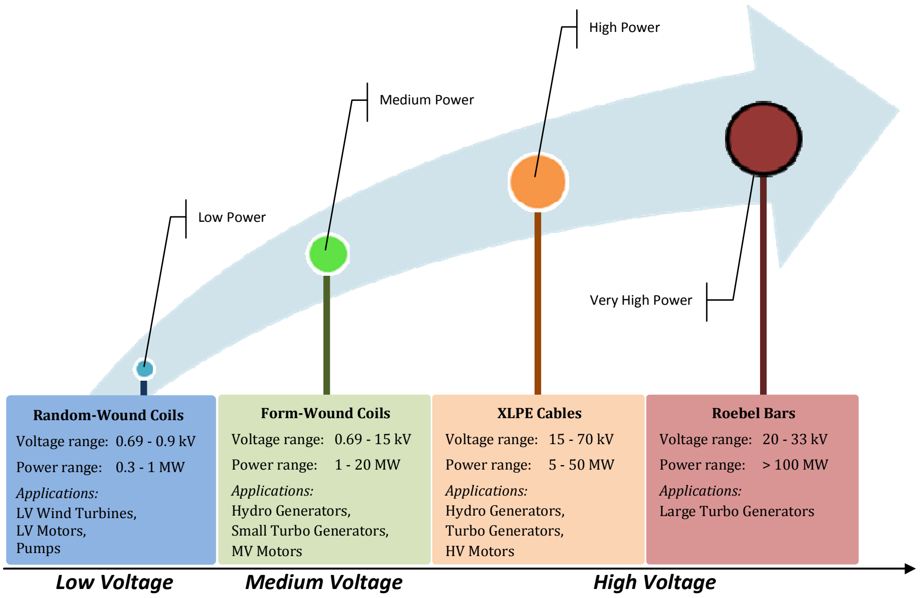

Fig. 2.8. Generator insulation systems for different voltage / power ratings.

2.2.2 Power Converter

In this section, different voltage source power converter systems are examined, in which generator-side control is decoupled from the grid-side control. Search for new power converter designs is dictated by means of the limited voltage capability of the presently available semiconductor switches, along with the voltage sharing issues described in 2.1.1.

a. Semiconductor Switches

Table 2.2 lists and compares presently available semiconductor active switches, suitable for voltage-source power converters.

At present, 4 types of self-commutated switching devices can be used:

- **IGBT (Insulated Gate Bipolar Transistor)**, a hybrid device with high input impedance and wide SOA. Voltage gate drive performance provides high switching frequency with low losses.
- **IEGT (Injected Enhanced Gate Transistor)**, improved through manufacturing IGBTs with low saturation voltage, characteristic of the GTO thyristors.
- **IGCT (Integrated Gate Commutated Thyristor)**, small positive gate signal turns on positive current, and integrated gate wrapped around device turns off the positive current.

Table 2.2. Comparison of the semiconductor devices: IGBT vs. IGCT vs. IEGT [34].

Comparison Area	IGBT	IEGT	IGCT
Efficiency	High	High	Medium / High
Gate Current	< 1 A	< 1.5 A	4000 A
Gate Control Signal	Voltage	Voltage	Current
Gate Control Component Count	Low	Low	High
Voltage Rating	6500 V	4500 V	6500 V
Current Rating	3600 A	4000 A	4000 A
Switching Speed	High / Medium	High / Medium	Medium
Mounting	Press Pack / Module	Press Pack / Module	Press Pack
Manufacturers	ABB, Westcode, Infineon, Dynex	Toshiba	ABB

b. DC Link Capacitor

In low voltage wind turbines, aluminium electrolytic capacitors are often used with DC link due to their low cost and relatively high energy density in comparison to other types of capacitors. This type of capacitors is rated up to 600 V DC.

In the transformer-less future concepts with pole-to-pole DC voltages starting from 12 kV, a capacitor voltage rating should to be of much higher value in order to minimize cost, size and losses. In other words, it is desirable that less number of capacitors will need to be connected in series in order to maintain desired DC voltage level.

An interesting alternative to the electrolytic design provides film capacitor, which shows much better performance in terms of handling transient over-voltages.

At present, two film designs are available on the market for medium voltage operation:

- **Impregnated film capacitors** - conventional design with metal foil electrodes separated by the insulating film [35].
- **Dry metalized film capacitors** - recently developed design with electrodes made of metalized polypropylene film, directly evaporated onto insulation film [36].

Figure 2.9 shows main difference between dry and impregnated design, which results in different method for internal short-circuit protection and capacitor lifetime.

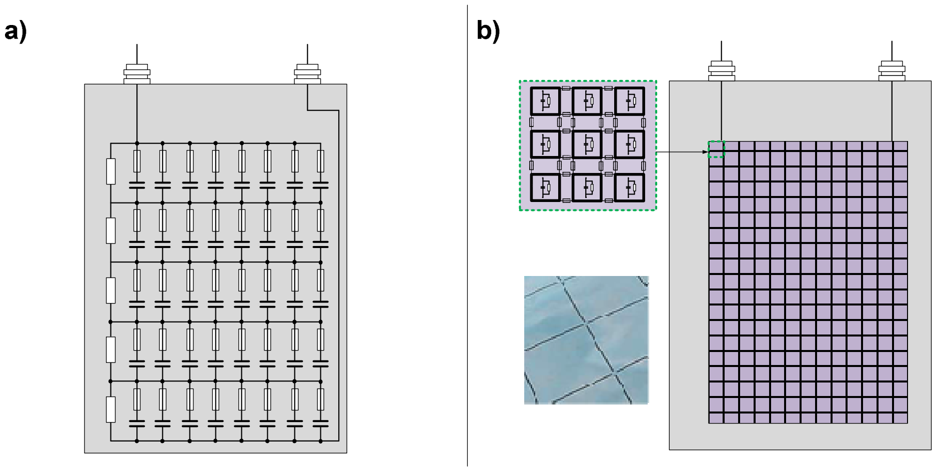

Fig. 2.9. Short circuit protection: a) conventional impregnated capacitor; b) dry capacitor.

Conventional impregnated capacitors consist of multiple small capacitor units divided into sections, which are often connected in H-arrangement. In this manner, sections are balanced with respect to the initial capacitance. If a single capacitor unit fails somewhere in the assembly, this will lead to the measurable imbalance in currents and voltages. All units are protected by individual fuses and interconnected to discharge resistor units for each section [36].

Dry capacitors on the other hand have structurally integrated both discharge resistors and fuse gates. Capacitor units are micro-integrated in form of rectangular blocks, which are chemically doped with special resistive material that acts as a discharge resistor in case of a single unit failure. Instead of the conventional fuses, fuse gates are introduced, which are simply made by interconnecting capacitor units in the edges. In case of a voltage breakdown, edge connection melts down and only micro-capacitor unit remains isolated and discharged. This mechanism is known as self-healing effect [37].

Due to the self-healing effect, metalized film capacitors practically eliminate series-connected capacitor voltage sharing issues while maintaining the maximum amount of the capacitance from the healthy parts. In this manner, power converter can operate in the long term with the maximum allowable DC voltage ripple.

2.2.3 LC Filter

LC filters provide reactive power compensation coming from the inductive series-connected components and harmonic filtering operation with relatively high efficiency, as they take advantage of the resonance phenomenon. In the analyzed system, it is assumed that the LC filters are installed on both generator- and grid-side terminals.

a. Series Reactor L_F Design

Due to the absence of the step-up transformer in wind turbine topology, series reactor is subjected to dangerous transients, occurring especially from the collection site. It is therefore important to properly examine and search for the optimal winding system design, so that risk of a failure can be reduced to the satisfactory level. Similarly to the generator stator core, reactor iron core is expected to be solid grounded for safety reasons and in order to minimize eddy current and hysteresis losses.

In common practice for iron-core reactors, two different coil designs are being applied for high power filter inductors:

- **Layer-wound coils (low voltage)** - coils are wound on an insulating cylinder with aluminium or copper foil conductor, commonly utilized up to 0.69 kV [38].
- **Disc-wound coils (medium voltage)** - coils are made of conductive and rectangular copper turn-wires in form of discs, utilized from 12 kV to 44 kV [39].

In industry, disc-wound coils are commonly used for applications up to 44 kV level. In order to avoid saturation effect, reactors used for higher voltages need more space and are made of air-core, instead of iron-core and consist of copper winding wound around and supported by steel (e.g. aluminium) structure. The support structure is typically floated at line potential with post insulators to minimize insulation requirements and cost [40].

b. Shunt Capacitor C_F Design

Suggested shunt capacitor design is similar to the DC link film capacitor design, so that over-voltage transients can be handled as well as possible. Due to AC filtering rather than DC energy storage requirement, substantially less capacitance is needed. On the other hand, AC current will normally flow through the capacitors, so that provided RMS current rating is essential for the shunt capacitor selection. Finally, higher voltage rating requires higher creepage distance between capacitor terminals and grounded steel case.

2.2.4 Medium Voltage Circuit Breaker

Low voltage wind turbines are in general equipped with circuit breakers on the low-voltage side of the step-up transformer. Due to low voltage recovery requirements, short-circuit currents are interrupted with a minimum required energy provided sufficiently by the air-insulated breakers. Low voltage operation also allows entire over-current fault detection scheme to be enclosed within the breaker case. Along with grounding source available from the transformer, low voltage breaker provides relatively simple short-circuit protection of the turbine [41].

When moving to the medium voltage level with no grounding source available, short circuit protection scheme becomes more sophisticated. Available circuit breakers for nominal voltages up to 66 kV are more expensive and complex. Detailed protection scheme with the external current and voltage sensors is required for voltages above 18 kV, which can detect fault at the specified grounding of the entire feeder network.

From the mid 1960s [42], two most promising candidates have gained wide acceptance on the market for medium and high voltage applications due their superior performances. These are:

- **Vacuum circuit breaker**, where vacuum space is used as an extinguishing medium [43].
- **SF_6 (sulphur hexafluoride) circuit breaker**, in which pressurized SF_6 gas is used as an extinguishing medium [44].

Necessary features for circuit breakers include: fast operation, fast recovery, simplicity, compact design, reliability and low cost. A general comparison with regard to mentioned merits for the described two breaker types is presented in Table 2.3 below.

Table 2.3. Comparison of medium voltage indoor circuit breakers [45]

Comparison Area	SF6 Breaker	Vacuum Breaker
Voltage Ratings	12 kV / 40.5 kV	
Current Ratings	400 A / 3600 A	
Size	Better	Worse
Cost	Better	Worse
Environmental Impact	Worse*	Better
Safety	Worse	Better
Simplicity	Worse	Better
Reliability	Worse	Better
Life Cycle	Worse	Better
Resistance recovery	Worse	Better

*SF_6 is one of the most serious greenhouse gases.

2.3 Medium Voltage Power Converter Topologies

2.3.1 Grid-Side Conversion

According to Figure 2.10, a search for optimal grid-side power converter circuitry in the transformer-less wind turbines has been done by the analysis of the existing solutions in two characteristic areas in terms of power and voltage ratings: **Medium Voltage/Power Area** and **High Voltage/Power Area**.

In both areas, multilevel conversion concepts are favoured due to lower distortions and less filtering requirements.

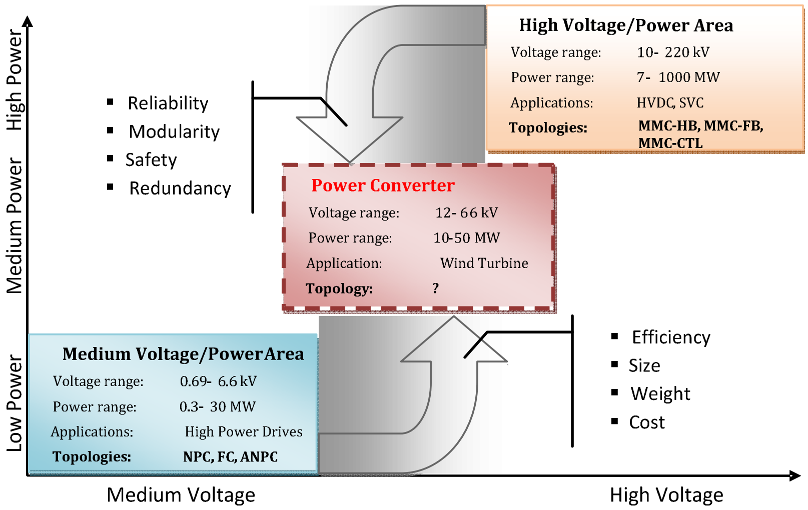

Fig. 2.10. Power converter topologies for different voltage / power ratings.

a. Medium Voltage Area

It consists of topologies available for high power motor drives with voltage conversion up to 5 levels. Primarily optimized merits include: cost, size, losses, and number of components. The main difference between discussed topologies is the utilized voltage clamping/sharing device. These are:

- **for NPC** - series-connected diodes.
- **for FC** - series-connected capacitors.
- **for ANPC** - series connected IGBTs.

From the medium voltage area, NPC [46] topology has been chosen among the FC [47] and ANPC [46]. Using diodes as clamping devices instead of capacitors and IGBTs is seen as more compact, reliable and cheaper solution.

Dynamic and static voltage sharing issues with series-connected IGBTs have been already highlighted in section 2.2.1.

b. High Voltage Area

It consists of topologies available and utilized mainly for the HVDC systems with voltage conversion of the desired number of levels. Primarily optimized merits include: modularity, reliability and safety. The main difference between the discussed topologies is the structure of a single modular cell. These are:

• **for MMC-HB**	- low voltage half-bridges with 2 IGBTs and a single capacitor.
• **for MMC-FB**	- low voltage full-bridges with 4 IGBTs and a single capacitor.
• **for MMC-CTL**	- medium voltage half bridges with 2 valves of series-connected IGBTs and series-connected capacitors.

From high voltage area, an MMC-HB [48] topology has been chosen among MMC-FB [49] and MMC-CTL [50]. Using low voltage cells allows eliminating issues related to the dynamic and static voltage sharing of series-connected components in each cell, as well as obtaining higher number of levels.

Half-bridge structure is preferred over the full-bridge due to lower cost made by reduced by half number of the required semiconductor switches in each cell.

2.3.2 Generator-Side Conversion

A search for the feasible generator-side power converter is made with special regard to the generator insulation system. According to section 2.3.1, it is assumed that currently optimized and already available form-wound coil design will remain the most reliable solution for the next generation of wind turbine generators.

The utilized form-wound coils have a limited capability for keeping voltage at the generator terminals up to 15 kV [51]. In the transformer-less turbines, it is expected that collector feeder voltages will be ranging from 12 to 66 kV [52]. In order to maintain generator reliable operation and avoid rewinding, novel topology concepts are required that allow generator to operate at the lower voltage level.

Furthermore, it is expected that the devised topologies will generate as low dv/dt voltage pulses as possible, so that aging of the generator insulation materials can be maximally extended. In this work, 3 different concepts have been proposed in terms of conversion philosophies:

- *AC/DC conversion by means of MMC [13, 82]*
  Decoupled AC circuit with generator can be controlled independently to provide required AC current at the generator terminals and at the same time not exceeding its insulation limits. Simultaneously, DC circuit can be controlled to provide the required DC current for the grid-side converter.
- *DC/DC boost conversion [53, 54]*
  Generator can operate at a lower voltage, while the grid-side voltage will be boosted to the desired level by means of DC/DC boost converter. The DC/DC converter is located between the generator-side rectifier and grid-side inverter.
- *AC/AC boost conversion*
  Generator can operate at lower voltage, while the common DC link voltage will be boosted to the desired level by means of an AC/AC boost converter. The AC/AC converter is located between the generator terminals and generator-side rectifier.

2.4 Summary

This chapter covered major design aspects that need to be faced when removing the transformer from the wind turbine. Description of the components adaptable for new system is made with regard to their voltage ratings and reliable operation.

Defined technical challenges for the reliable operation of the future transformer-less wind turbines can be summarized as follows:

- **Limited Generator Voltage Level**
  Available range of the operating voltage in generators designed for the wind turbines.
- **Variable Loading Impact on LC Filter Insulation System**
  Unknown thermal cycling impact on the available insulation materials used for the equivalent LC filters in the distribution systems, which is the result of the wind turbine variable loading conditions.
- **Overvoltage Protection**
  Protection against the common-mode voltage and the dv/dt effect under normal operation, as well as the protection against lighting and switching surges under abnormal conditions.
- **Short Circuit Protection**
  Conventional over-current feeder protection may not distinguish a ground fault located at the wind turbine terminals with the ground fault across the feeder cable. As a result, entire feeder can be disconnected instead of a single turbine.
- **Grounding System**
  New grounding options introduce a search for optimal grounding method, which provides desired compromise between safety requirements and equipment ratings.
- **Power Converter Circuitry**
  Existing medium voltage power converter circuitries introduce a search for optimal topology with regard to the efficient and reliable operation provided with the minimum cost and size.

Finally, topology concepts for full-scale power converter are proposed in accordance with the existing solutions and components ratings.

Described findings are concluded by introducing 3 complete transformer-less wind turbine design concepts, which differ with regard to the selected power converter topologies:

1) **System A: *Back-to-Back MMC***
   Solution A is proposed for the generator-side system, which includes MMC topology operating at lower than nominal terminal voltage in order to maintain

generator insulation limits. On the grid-side, MMC topology is proposed, which operates independently at grid nominal ratings.

2) **System B:** ***DC/DC Boost Converter with Grid-Side NPC-3L***
   Solution B is proposed for the generator-side system, which includes DC/DC boost conversion. On the grid-side, 3-level NPC topology is proposed, which operates independently at grid nominal ratings.

3) **System C:** ***AC/AC Boost Converter with Grid-Side NPC-5L***
   Solution C is proposed for the generator-side system, which includes AC/AC boost conversion. On the grid-side, 5-level NPC topology is proposed, which operates independently at grid nominal ratings.

Next chapter will focus on the detailed implementation and modelling of each of the proposed systems. In this manner, the selected circuit candidates can be further examined under normal and fault conditions in terms of the efficiency and the required component ratings.

Chapter 3

System Description

3.1 Introduction

3.1.1 General System Layout

The general system layout for wind turbines A, B and C - is presented in the form of a single line diagram in Figure 3.1. The entire AC collector feeder consists of 10 identical turbines connected via a string with feeder AC cables.

The wind turbine step-up transformer is included only for a single benchmark model of a conventional wind turbine (see section 3.5), which is used for comparison assessment with the transformer-less turbines.

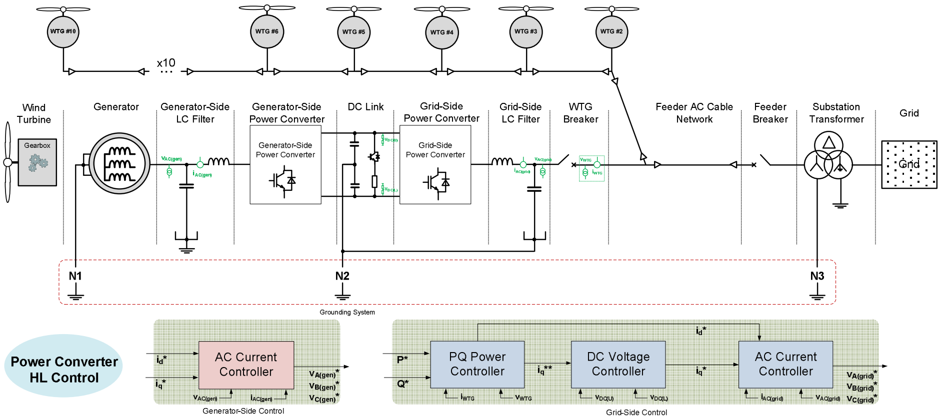

Fig. 3.1. System description of the analyzed system with the implemented control scheme for a full-scale power converter.

In order to maintain a fair comparison, the wind turbine ratings listed in Table 3.1 are common for each system. As a result, 10 MW transformer-less wind turbines are analyzed, which operate at the 20 kV level.

Table. 3.1. Selected turbine electrical characteristics for the evaluation assessment.

Parameter	Value
WTG Power [MVA]	10
WTG Grid Voltage (L-L, RMS) [kV]	20
WTG Frequency [Hz]	50
DC link Voltage (pole-to-pole) [kV]	36

3.1.2 System A: Back-to-Back MMC

MMC feature is not only a high number of levels that minimize dv/dt effect on insulation systems, but also a decoupled AC circuit control from the DC circuit control. As a result, the AC circuit with the generator can be controlled independently to provide the required alternating current at the generator terminals and at the same time not exceeding its insulation limits, while the DC circuit can be controlled to provide required direct current for the grid-side converter. In other words, it means operating at lower than nominal modulation index m_s.

The operating principle is shown in Figure 3.2. A higher direct voltage can be obtained by adding more cells in each arm.

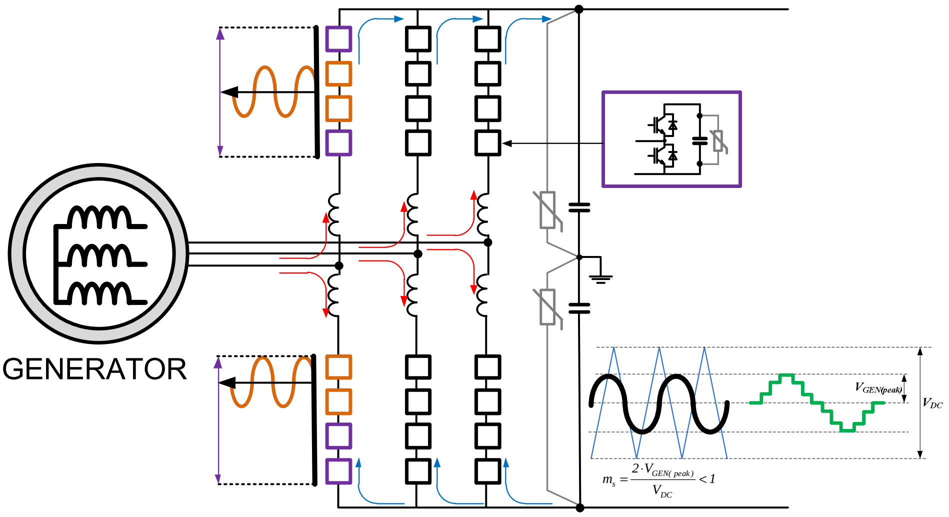

Fig. 3.2. Generator-side MMC operation with decreased modulation index.

A main disadvantage is that operation at the reduced terminal voltage will force the flow of higher alternating currents through the IGBTs in all series-connected cells, which will be dictated according to the generator operating voltage. Thus, all cells will need to be overrated according to the generator nominal currents.

3.1.3 System B: DC/DC Boost Converter with Grid-Side NPC-3L

DC/DC boost converter topologies are widely presented in the literature [53, 83], yet they are rarely seen in the high power industry. As a result, search has been made for optimal topology within the DC/DC step up circuitries, which maintains following merits: modularity, simplicity, low losses, low number of IGBTs and easy voltage scaling.

Among many existing solutions, a recently developed zero current switched (ZCS) converter has been selected, which detailed mathematical formulas governing the power conversion are available in [54] (and in Appendix B). It occurred that the ZCS shows stable performance with a 2-level front end rectifier (no concerns related to DC link balancing), that separately controls the generator. Figure 3.3 presents schematic diagram of the generator-side converter.

The ZCS includes a pair of valves with series-connected IGBTs *T1* and *T2* on the generator DC-side along with the cascaded passive modular cells, each containing: storage capacitor, resonant capacitor, resonant inductor and a pair of free-wheeling diodes.

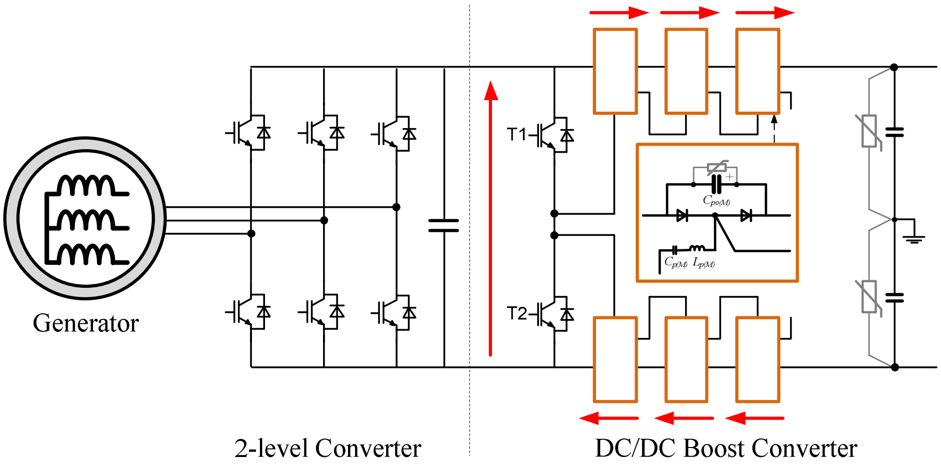

Fig. 3.3. Generator-Side converter with DC/DC boost unit.

The required number of DC/DC boost cells is proportional to the desired output voltage. In this manner, flexible voltage scaling is provided for any system rating, simply by adding more DC/DC boost cells in series.

The resonant components are used to form a resonant path, so that charging and discharging currents can be passed through series resonance in order to achieve soft-switched operation. As a result, valves *T1* and *T2* are controlled complementary with 50% duty cycle and switched at the resonant frequency equal to the generator-side rectifier switching frequency: $f_{res} = f_{sw(gen)}$.

3.1.4 System C: AC/AC Boost Converter with Grid-Side NPC-5L

Figure 3.4 presents an original method proposed in this thesis for stepping-up the voltage, which includes an AC/AC boost converter in front of the generator terminals and a passive diode bridge rectifier for clamping the direct voltage of the grid-side converter.

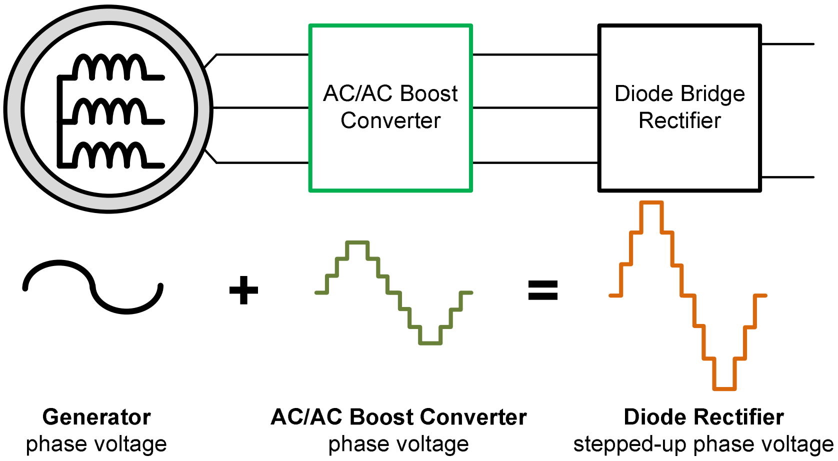

Fig. 3.4. AC/AC Boost philosophy at the generator-side terminals.

The required AC/AC boost operation is achieved by imposing (synchronized in phase) converter phase voltage waveforms with voltages at the generator terminals, so that each phase is controlled and stepped-up separately. In this manner, the desired voltage is reached at the diode rectifier terminals while maintaining operation at the generator voltage limits. Detailed information on converter operating principles is available in Appendix C.

Among the existing candidates for high power AC-AC boost conversion, a chain-link concept [55] is proposed which includes a series-connected full-bridge cells equipped with a DC capacitors. The advantages of the proposed concept include: modular design, flexible voltage scaling, low dv/dt pulses and low number of components.

The main drawback is the necessity to re-charge the DC capacitors through an external circuitry in order to achieve net power flow, as unidirectional currents will be flowing from the generator through the DC sources to supply the grid-side converter.

In order to simplify DC capacitor charging control, a generator split-winding concept is proposed in Figure 3.5, where the first set of windings is in series with the chain-link converter and discharges the chain link capacitors, whereas the second set of windings is used to charge the chain link converter capacitors by means of integrated 3-phase 2-level converter modules.

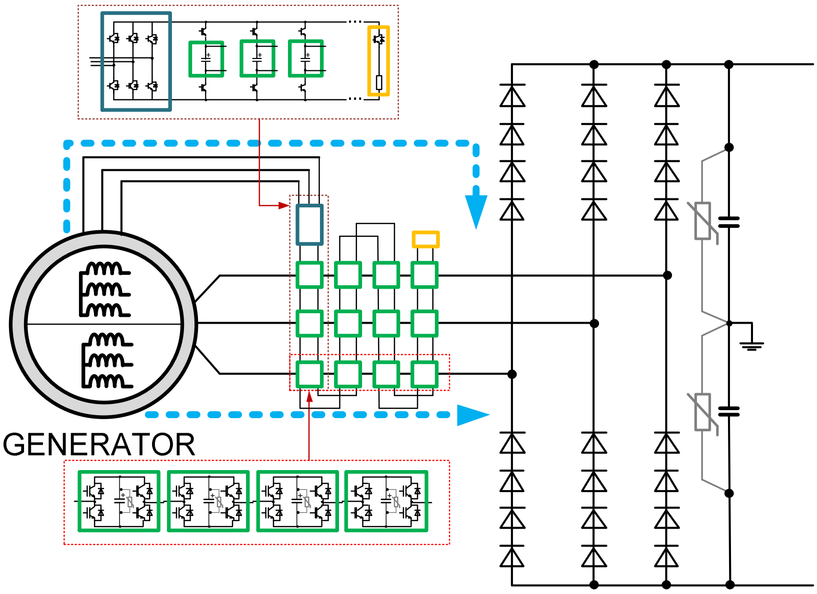

Fig. 3.5. Split-winding concept for recharging AC/AC boost converter cells.

In such an arrangement, the first set of the generator windings maintains operation within ground insulation limits, whereas the second set of the generator windings is imposed to the increased ground insulation stress equal to the resulting voltage of the generator with series-connected chain link converter (even though operating line-to-line RMS voltage is less than a single chain link capacitor voltage).

3.1.5 Solution Methodology for Estimation of Redundant IGBTs / Modules in Systems A, B and C

System A and the generator-side circuit candidates for systems B and C allow adding redundant modules to increase lifetime of a power converter and consequently reduce the downtime period along with the associated costs. In a similar manner, lifetime of the grid-side converter units for systems B and C can be prolonged by adding more series-connected IGBTs/diodes in each valve. If a single IGBT/diode fails, the resulting voltage surplus is clamped by the remaining devices below their nominal threshold and the converter remains operational.

Nevertheless, increasing number of redundancies generates extra costs related to the installation of additional devices. Therefore, an optimal number of redundancies is determined according to Figure 3.6, where the resulting total cost made by the energy loss during downtime period L_{energy} and the redundant IGBTs/diodes L_{device} is compared for different number of redundancies Y - ranging from 0 to 5. An exponential survival function is defined in order to determine the device mean time to failure $t_{failure}$. Results are provided in Tables 3.2/.4/.6 correspondingly for systems A, B and C.

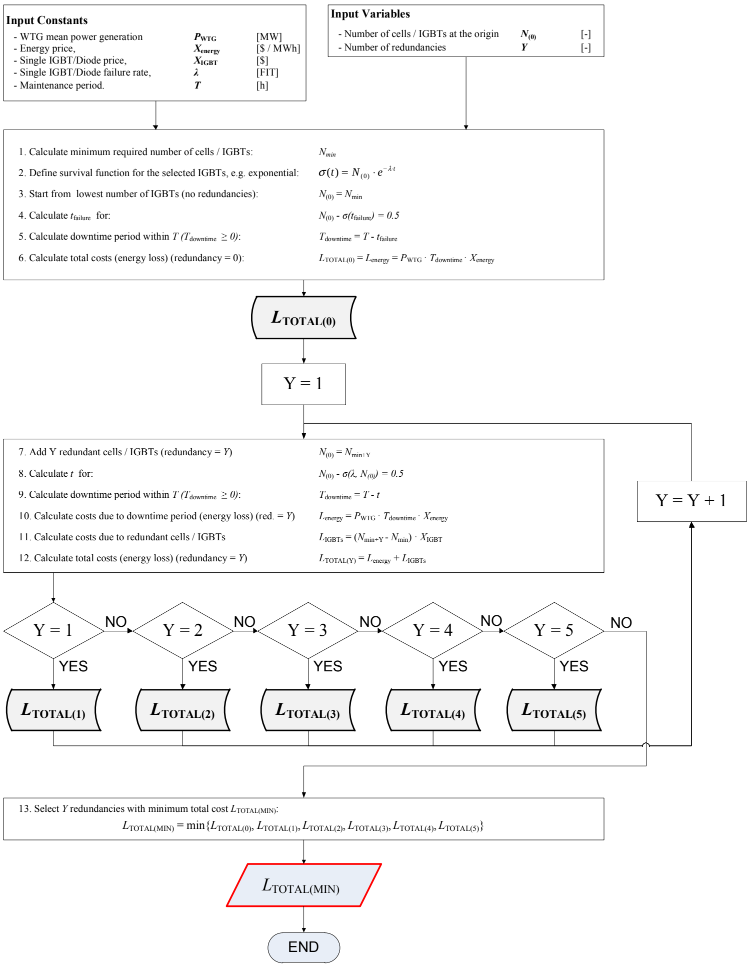

Fig. 3.6. Solution methodology for estimation of the optimal redundant devices Y.

3.2 System A: Back-to-Back MMC

3.2.1 Topology

The back-to-back MMC includes a single redundant cell in each arm (Y = 1), so that when a single cell failure occurs, the MMC can still operate and provide non-distorted power to the grid. As a result, the MMCs on each side require N = 13 cells per arm, which gives individually controlled 156 cell capacitors and 312 IGBTs.

In order to simplify the overall system layout and to reduce the number of required electrical nodes for losses and short circuit studies, a generic model of the MMC shown in Figure 3.7 is used for the generator-side unit, in which cell capacitors are replaced with arm controllable voltage sources. This modification results in an ideal internal cell voltage balancing, as all cells in each arm have identical cell voltage references. As a consequence, a cell voltage balancing controller is no more necessary, and each arm acts as an independently controlled voltage source, consisting only of 2 electrical nodes.

The grid-side MMC is modelled in a sophisticated manner, with each individual cell consisting of 2 IGBTs and a capacitor. Further modification to this approach - required specifically for losses analysis, is described in section 4.2.6.

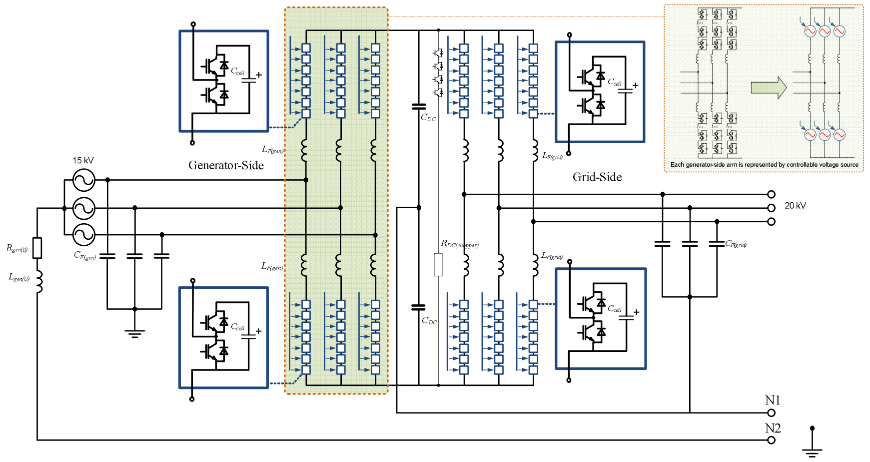

Fig. 3.7. System A: schematic representation of the wind turbine circuit.

More information on the MMC modelling approach and control algorithms can be found in the Appendix A.

3.2.2 Component Sizing

Table 3.2 provides specification and ratings for components in system A. LC filters are sized with regard to the maximum current ratings of the semiconductor switches, (section 4.2.2) whereas cell and DC capacitors are dimensioned against the corresponding maximum voltage ratings from the device datasheets. Switching frequency f_{sw} is the IGBT maximum allowable frequency for the snubber-less operation divided by the number of levels. Generator electrical parameters (power, voltage, impedance, frequency) have been provided by Vestas Wind Systems A/S.

Table. 3.2. System A: component ratings - specification.

Parameter	**Value**	**Component**
Nominal power S_{gen} [MVA]	10	Generator
Nominal frequency f_{gen} [Hz]	50 (± 2 Hz)	
Terminal RMS voltage V_{gen} [kV]	15	
Stator resistance* $R_{gen(0)}$ [mΩ]	3.93	
Stator inductance* $L_{gen(0)}$ [mH]	0.71	

L arm inductance $L_{F(gen)}$ [mH / %]	5.73 / 8	Generator-Side LC Filter
C filter capacitance $C_{F(gen)}$ [µF]	15	
DC link capacitance C_{DC} [µF]	20	DC Link
Total energy stored in cell capacitors [kJ]	GEN: 550 / GRID: 550	
DC chopper resistance R_{DC} [Ω]	129	
L arm inductance $L_{F(grid)}$ [mH / %]	10.19 / 8	Grid-Side LC Filter
C filter capacitance $C_{F(grid)}$ [µF]	8	
Number of cells per arm N	13	B2B Power Converter
Switching frequency (per IGBT) f_{sw} [Hz]	250	
PWM Modulation	phase-shifted carriers	

*Source: Vestas Wind Systems A/S

3.2.3 Sizing Considerations

A rough size and weight estimation based on the components datasheets available for the step-up transformer [77], 2L-VSC electrolytic DC capacitors [78] and MMC cell capacitors [78] with rated values have shown, that the transformer volume in the conventional system is 6 times larger than the resulting volume of the installed cell capacitors in the transformer-less MMC system, whereas the total weight of the step-up transformer is 3 times larger than the resulting weight coming from the corresponding capacitors.

Not only less space is occupied by the transformer-less wind turbine circuitry, but also stacking arrangements are much more flexible, since the total volume is distributed equally among single capacitors. As shown in Figure 3.8, cell capacitors can be single- or multi-stacked horizontally and vertically in order to conveniently fill all the available space limits. On the contrary, step up transformer is formed as a solid cube for the optimized magnetic core design, which prevents its flexible stacking arrangements.

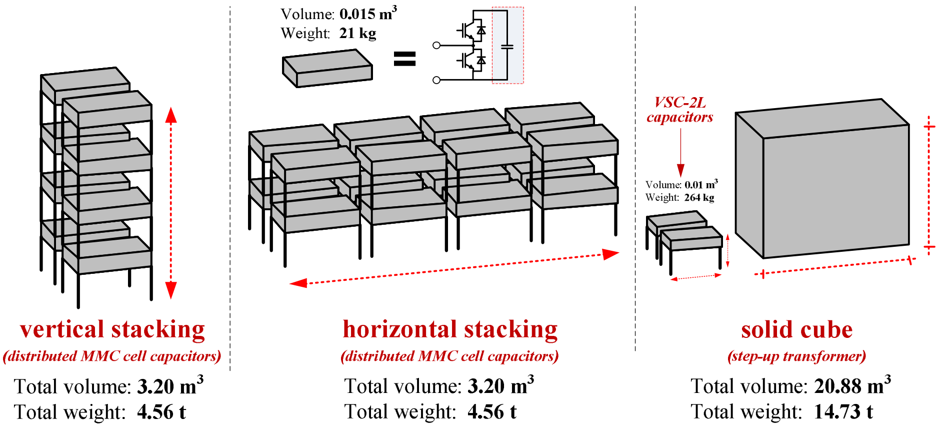

Fig. 3.8. Sizing considerations of the MMC cell capacitors and the conventional step-up transformer with 2L-VSC DC link capacitors (10 MVA).

3.2.4 Control Architecture

a. Generator-Side Unit

General control architecture for the generator-side is shown in Figure 3.9. It consists of an AC Current Controller**,** used for AC-side control. Arm Energy Compensating Controller is responsible for the DC-side control and provides circulating current references for arm cell voltages. PWM modulator with phase-shifted carriers stimulates switching operation effect by modulating voltage references.

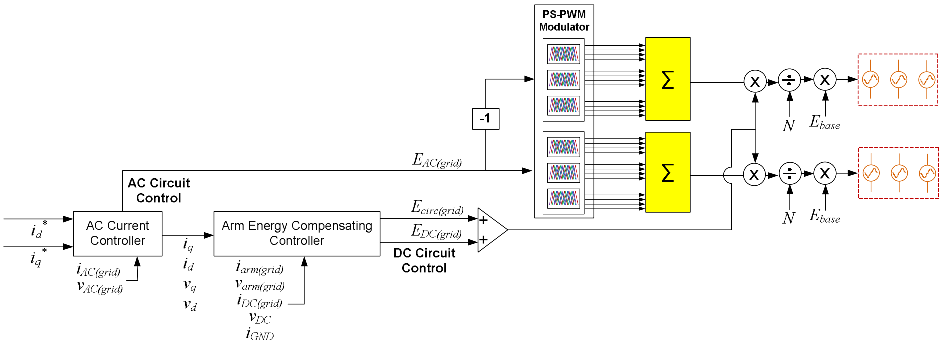

Fig. 3.9. Generator-side MMC control scheme - schematic block representation.

Detailed description and implementation method for each controller is provided in the Appendix A.

b. Grid-Side Unit

A Similar design as shown in Figure 3.10 is proposed for the grid-side unit. AC Current Controller, Arm Energy Compensating Controller and PWM modulator design remain identical. PQ power control is added for flexible active and reactive power regulation at the wind turbine terminals. A direct voltage controller is used for keeping constant direct voltage as an operating principle. A cell voltage balancing controller [82] is necessary to balance individual cell voltages internally within each arm.

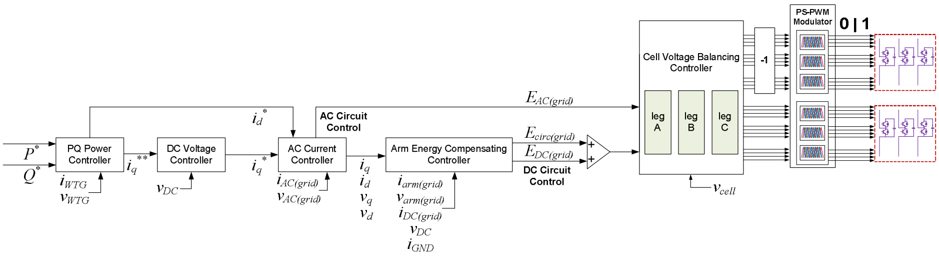

Fig. 3.10. Grid-side MMC control scheme - schematic block representation.

Detailed description and implementation method for each controller is provided in the Appendix A.

3.2.5 Control Tuning

Table 3.3 provides gain values for PI and P controllers used in the control scheme for system A. AC circuit controllers are tuned numerically in *sisotool* (MATLAB) for the overshoot below 10% and rise times below 20 ms [47]. Closed loop s-functions are provided in the Appendix G. DC circuit controllers are tuned by trial error in EMTDC/PSCAD simulations through step response measurements. Implementation of the controllers with the specified parameter values can be found in the Appendix A.

Table. 3.3. System A: converter PI / P controllers - specification.

Parameter	**Generator-Side**	**Grid-Side**	**Control Block**
Signal sampling frequency $f_{s(HL)}$ [kHz]	20	20	***High-Level Control***
Proportional gain $K_{p(PQ)}$ [-]	-	$2.00\cdot10^{-1}$	PQ Power Controller
Integral time constant $T_{i(PQ)}$ [s]	-	$1.00\cdot10^{-1}$	
Proportional gain $K_{p(DC)}$ [s]	-	$6.24\cdot10^{-2}$	DC Voltage Controller
Integral time constant $T_{i(DC)}$ [s]	-	$8.00\cdot10^{-2}$	
Proportional gain $K_{p(AC)}$ [s]	$1.14\cdot10^{0}$	$1.14\cdot10^{0}$	AC Current Controller
Integral time constant $T_{i(AC)}$ [s]	$1.75\cdot10^{-1}$	$1.75\cdot10^{-1}$	
Proportional gain $K_{p(AC)}$ [s]	$6.24\cdot10^{-1}$	$6.24\cdot10^{-1}$	0-Sequence Controller
Integral time constant $T_{i(AC)}$ [s]	$8.00\cdot10^{-1}$	$8.00\cdot10^{-1}$	
Sampling frequency $f_{s(LL)}$ [kHz]	20	20	***Low-Level Control***
Proportional gain $K_{p(circ)}$	$5.05\cdot10^{0}$	$5.05\cdot10^{0}$	Arm Energy Compensating Controller
Proportional gain $K_{p(HB)}$	$5.00\cdot10^{-3}$	$5.00\cdot10^{-3}$	
Integral time constant $T_{i(HB)}$	$8.00\cdot10^{-2}$	$8.00\cdot10^{-2}$	
Proportional gain $K_{p(VB)}$	$2.02\cdot10^{-1}$	$2.02\cdot10^{-1}$	
Low pass filter base frequency [Hz]	10	10	
Proportional gain $K_{p(cell)}$	$5.00\cdot10^{-2}$	$1.00\cdot10^{-2}$	Cell Voltage Balancing Controller

3.3 System B: DC/DC Boost Converter + Grid-Side NPC-3L

3.3.1 Topology

According to Figure 3.11, DC/DC ZCS converter [54] consists of 6 identical DC/DC boost cells; so that the direct voltage available for the generator-side converter is 7 times lower than the direct voltage for the grid-side converter. As a result, the generator now operates at 3.3 kV instead of 15 kV in system A.

Lower voltage operation provides less problems related to the generator insulation system, which allows usage of the conventional 2-level converter at the generator-side terminals. The 2-level converter has been chosen among the other candidates due to its stable performance combined with the DC/DC boost operation. In order to provide operation at 3.3 kV, each converter branch includes 2 series-connected IGBTs.

On the grid-side, a 3-level NPC topology is selected, where each semiconductor valve is modelled as a single semiconductor component. It requires ideal voltage sharing and balancing between the series-connected devices. It is assumed that a single redundant switch in each valve is included to increase power converter non-disturbed operating period, as has been done for the redundant cell in system A (Y = 1). As a result, each valve of the NPC-3L consists of 7 series-connected IGBTs.

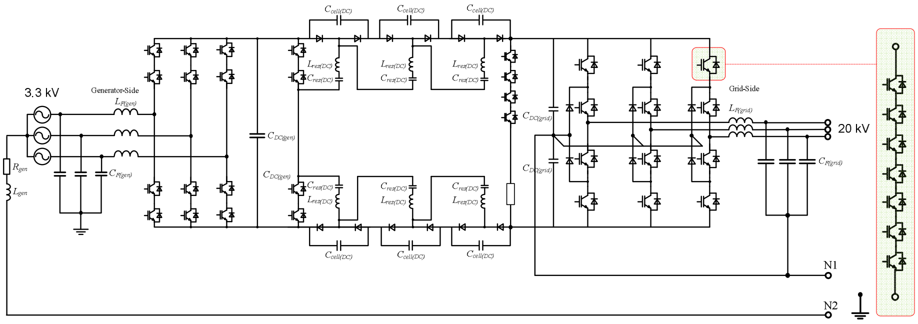

Fig. 3.11. System B: schematic representation of the wind turbine circuit.

Detailed description of the proposed DC/DC boost converter is provided in the Appendix B.

3.3.2 Component Sizing

Table 3.4 provides specification and ratings for components in system B. In similar manner to system A, LC filters are sized with regard to the maximum current ratings of the semiconductor switches, whereas DC and cell capacitors are dimensioned against maximum voltage ratings obtained from the device datasheets.

Table. 3.4. System B: component ratings - specification.

Parameter	Value	Component
Nominal power S_{gen} [MVA]	10	Generator
Nominal frequency f_{gen} [Hz]	50	
Terminal voltage V_{gen} [kV]	3.3	
Stator resistance* R_{gen} [mΩ]	0.19	
Stator inductance* L_{gen} [mH]	0.34	
L filter inductance $L_{F(gen)}$ [mH / %]	0.173 / 20	Generator-Side LC Filter
C filter capacitance $C_{F(gen)}$ [mF]	1.1	
DC link capacitance $C_{DC(grid)}$ [μF]	1000	DC Link
Total energy stored in DC cell capacitors [kJ]	GEN: 192 / GRID: 324	
DC chopper resistance R_{DC} [Ω]	129	
L filter inductance $L_{F(grid)}$ [mH / %]	6.37 / 5	Grid-Side LC Filter
C filter capacitance $C_{F(grid)}$ [μF]	30	
Number of levels N_{gen}	2	Generator-Side Power Converter
Switching frequency (per IGBT) $f_{sw(gen)}$ [Hz]	2100	
PWM Modulation	carrier-based	
Number of levels $N_{DC/DC}$	7	DC/DC Boost Power Converter
Switching frequency (per IGBT) $f_{sw(DC)}$ [Hz]	2100	

Number of levels N_{grid}	3	Grid-Side Power Converter
Switching frequency (per IGBT) $f_{sw(grid)}$ [Hz]	1050	
PWM Modulation	phase-shifted carriers	

*Source: Vestas Wind Systems A/S

3.3.3 Sizing Considerations

In a similar manner to system A (section 3.2.3), the resulting volume and weight of a power converter for system B is compared to the conventional system equipped with a step-up transformer. Results are shown in Figure 3.12.

When selecting components from the equivalent datasheets, it occurred that system B is approximately 3 times smaller and lighter than system A, since the DC cell capacitors transfer the energy at much higher frequency $f_{sw(DC)}$. Due to the modular design of the DC/DC boost cells, vertical and horizontal stacking arrangements remain feasible.

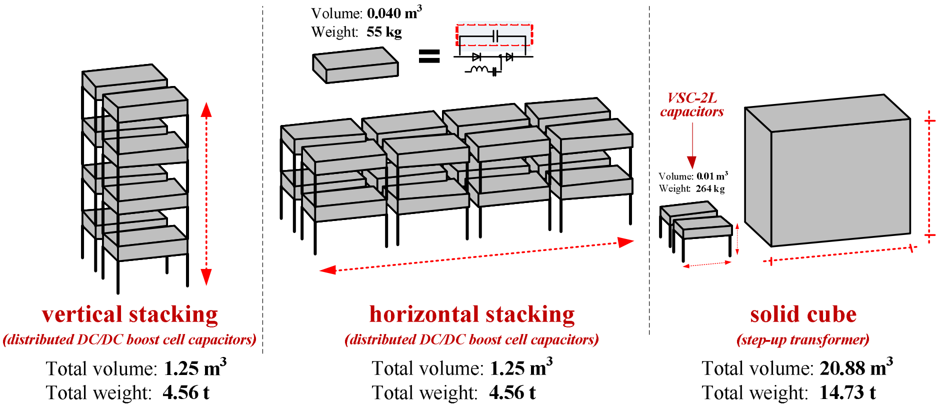

Fig. 3.12. Sizing considerations of the DC/DC boost cell capacitors and the conventional step-up transformer with 2L-VSC DC link capacitors (10 MVA).

3.3.4 Control Architecture

a. Generator-Side Unit + DC/DC Boost Unit

General control architecture for the generator-side 2-level converter is shown in Figure 3.13. It is divided into 2 functional units: AC current control and PWM modulator. AC current control scheme is similar to the one applied for MMC topologies in system A. Measured input voltage and current signals are sampled with sampling frequency $f_{s(gen)}$ and further transformed into the rotating dq frame.

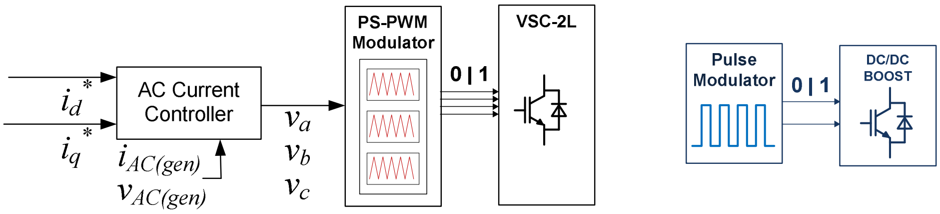

Fig. 3.13. Generator-side 2-level (left) and DC/DC boost (right) control scheme - schematic block representation.

Current dq references $i_{q(ref)}^*$ and $i_{d(ref)}^*$ are set according to the desired amount of generated power. Transformation angle θ is equal to rotor flux angle θ_f. Delays between measured and applied signals are neglected.

DC/DC boost converter control does not require any measured input signal. Only Pulse Generator with 50% duty cycle is used, which switches upper and lower IGBTs in a complementary fashion. Pulse generator switching duty cycle is: $f_{sw(DC)} = f_{sw(gen)}$.

Detailed description and implementation method of each controller is provided in the Appendix B.

b. Grid-Side Unit

Grid-side control is similar to AC circuit control for the grid-side MMC in system A. Its schematic representation is shown in Figure 3.14. It consists of PQ power controller, direct voltage controller and AC current controller. On the contrary to 2-level converter control, AC current control includes 0-sequence control loop, which eliminates DC offset from the AC output waveforms caused by the leakage current.

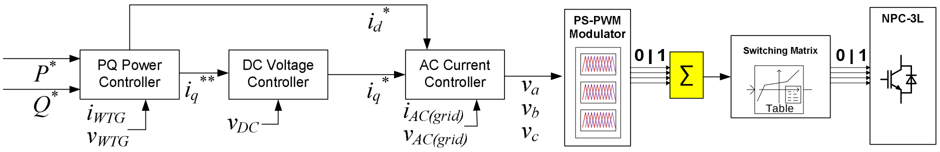

Fig. 3.14. Grid-side NPC-3L control scheme - schematic block representation.

Detailed description and implementation method of each controller is provided in the Appendix B.

3.3.5 Control Tuning

Table 3.5 provides gain values for PI and P controllers used in the control scheme for system B. Tuning procedure is identical as for system A. Implementation of the controllers with specified parameter values can be found in the Appendix B.

Table. 3.5. System B: converter PI / P controllers - specification.

Parameter	Generator-Side	Grid-Side	Control Block
Sampling frequency $f_{s(HL)}$ [kHz]	4.2	6.3	
Proportional gain $K_{p(PQ)}$	-	$2.00 \cdot 10^{-1}$	PQ Power Controller
Integral time constant $T_{i(PQ)}$	-	$1.00 \cdot 10^{-2}$	
Proportional gain $K_{p(DC)}$	-	$6.24 \cdot 10^{-2}$	DC Voltage Controller
Integral time constant $T_{i(DC)}$	-	$8.00 \cdot 10^{-2}$	
Proportional gain $K_{p(AC)}$	-	$6.24 \cdot 10^{-1}$	0-Sequence Controller
Integral time constant $T_{i(AC)}$	-	$8.00 \cdot 10^{-1}$	
Proportional gain $K_{p(AC)}$	$1.14 \cdot 10^{0}$	$1.14 \cdot 10^{0}$	AC Current Controller
Integral time constant $T_{i(AC)}$	$1.75 \cdot 10^{-1}$	$1.75 \cdot 10^{-1}$	

3.4 System C: AC/AC Boost Converter + Grid-Side NPC-5L

3.4.1 Topology

According to Figure 3.15, two separate functional converter circuitries are derived for the generator-side unit: conventional 2-level converter and chain link converter.

The conventional 2-level converter unit is used to re-charge the chain link cell capacitors, which are modelled as direct voltage sources. In this manner, need for the chain link cell direct voltage balancing controller is eliminated. Re-charging is done by controlling the direct current mean value equal to the resulting direct current mean value from the chain link circuit. As all cell voltages are identical, resulting direct current is the sum of the direct currents flowing through each cell capacitor.

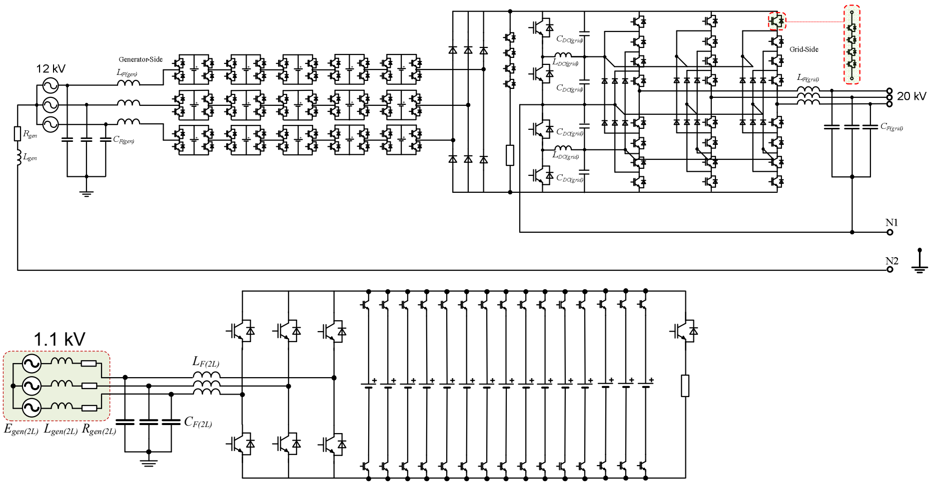

Fig. 3.15. System C: schematic representation of the wind turbine circuit.

The chain link converter consists of 5 series-connected full-bridge cells for each phase, which includes a single redundant cell for each phase in case of IGBT or capacitor failure (Y = 1). On the grid-side, 5-level NPC is modeled in a similar manner as NPC-3L for system B.

The clamping bridge [57] is added in order to balance adjacent DC link capacitors. It consists of active semiconductor switches and inductors, which interconnected through IGBTs discharge selected capacitors in the common DC link.

Detailed description of the proposed AC/AC boost converter and clamping bridge is provided in the Appendix C.

3.4.2 Component Sizing

Table 3.6 provides specification and ratings for components in system C. In similar manner to system A, LC filters are sized with regard to the maximum current ratings of the semiconductor switches (section 4.2.2), whereas DC capacitors are dimensioned against corresponding maximum voltage ratings obtained from the device datasheets.

Table. 3.6. System C: component ratings - specification.

Parameter	Value	Component
Nominal power S_{gen} [MVA]	7.2	Generator (Chain-Link Converter)
Nominal frequency f_{gen} [Hz]	50	
Terminal voltage V_{gen} [kV]	12	
Stator resistance* R_{gen} [mΩ]	2.51	
Stator inductance* L_{gen} [mH]	0.45	
Nominal power S_{2L} [MVA]	2.8	Generator (2-level Converter)
Nominal frequency f_{2L} [Hz]	50	
Terminal voltage V_{2L} [kV]	1.1	
L filter inductance $L_{F(gen)}$ [mH / %]	6.87 / 10	Generator-Side LC Filter (Chain-Link Converter)
C filter capacitance $C_{F(gen)}$ [μF]	21	
L filter inductance $L_{F(2L)}$ [mH / %]	0.308 / 22	Generator-Side LC Filter (2-level Converter)
C filter capacitance $C_{F(2L)}$ [μF]	600	
Total energy stored in DC capacitors [kJ]	GRID: 162	DC Link
DC link inductance $L_{DC(grid)}$ [μH]	5000	
DC chopper resistance R_{DC} [Ω]	129	
DC source cell voltage V_{CL} [V]	2200	
L filter inductance $L_{F(grid)}$ [mH / %]	10.19 / 8	Grid-Side LC Filter
C filter capacitance $C_{F(grid)}$ [μF]	20	
Number of chain link cells (per phase) N_{gen}	5	Generator-Side Chain-Link Converter
Switching frequency (per IGBT) $f_{sw(gen)}$ [Hz]	250	
PWM Modulation	phase-shifted carriers	
Number of levels N_{2L}	2	Generator-Side 2-level Converter
Switching frequency (per IGBT) $f_{sw(2L)}$ [Hz]	2100	
PWM Modulation	carrier-based	
Number of levels N_{grid}	5	Grid-Side NPC-5L Converter
Switching frequency (per IGBT) $f_{sw(grid)}$ [Hz]	550	
PWM Modulation	phase-shifted carriers	

3.4.3 Sizing Considerations

In a similar manner to systems A and B (sections 3.2.3/3.3), the resulting volume and weight of a power converter for system C is compared to the conventional system equipped with a step-up transformer. Results are shown in Figure 3.16.

When selecting components from equivalent datasheets, it occurred that system C is approximately 4 times smaller and lighter than system A, since the number of cells per phase is 5 times lower. Due to the modular design of the AC/AC chain link cells, vertical and horizontal stacking arrangements remain feasible.

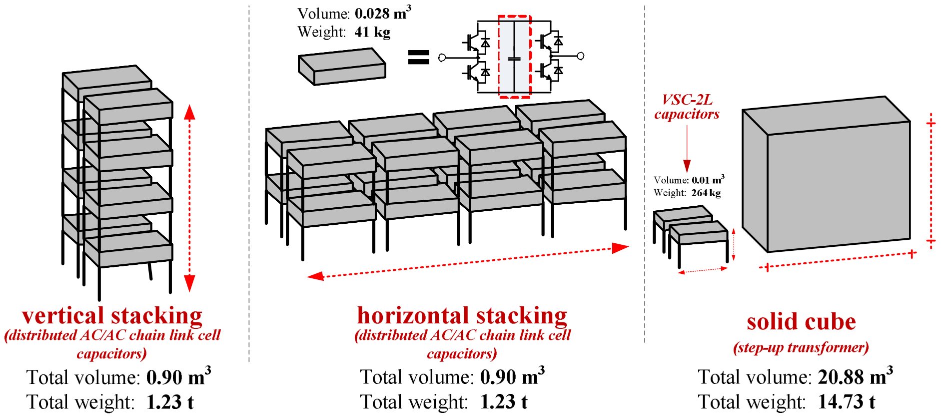

Fig. 3.16. Sizing considerations of the AC/AC chain link cell capacitors and the conventional step-up transformer with 2L-VSC DC link capacitors (10 MVA).

3.4.4 Control Architecture

a. Generator-Side Unit

The general control architecture for the chain link converter is shown in Figure 3.17. Alternating current control of the conventional 2-level converter is identical to the generator-side unit in system B. Additional direct current controller is used to charge DC capacitors with the desired current values.

The *Chain Link AC Voltage Control (Magnitude)* block is used to calculate chain link voltage AC reference magnitudes $V_{CL(AC)}^{*}$ from input power reference P^{*}. Calculations are performed on the basis of measured active power $P_{AC(diode)}$ at the diode rectifier terminals. The *Chain Link AC Voltage Control (Phase)* synchronizes chain link phase voltage references with the generator terminal voltages.

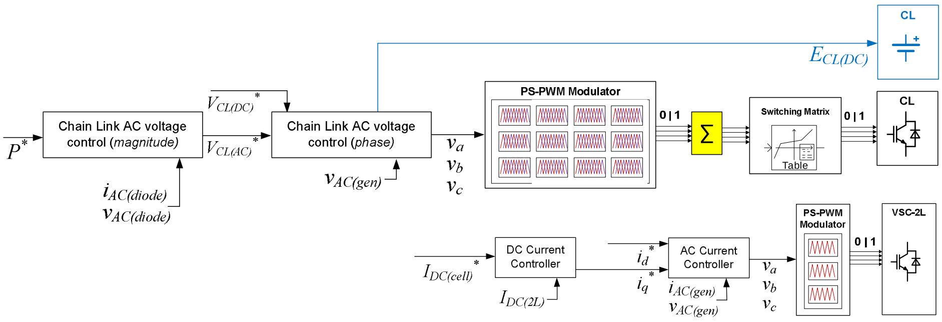

Fig. 3.17. Generator-side 2-level (bottom) and AC/AC boost (top) control scheme - schematic block representation.

Detailed description and implementation method of each controller is provided in the Appendix C.

b. Grid-Side Unit

The grid-side NPC-5L control is identical to the NPC-3L control used for system B. The DC link balancing controller used for the clamping bridge operates by calculating the measured voltage difference between the upper pair of capacitors and between the lower pair of capacitors.

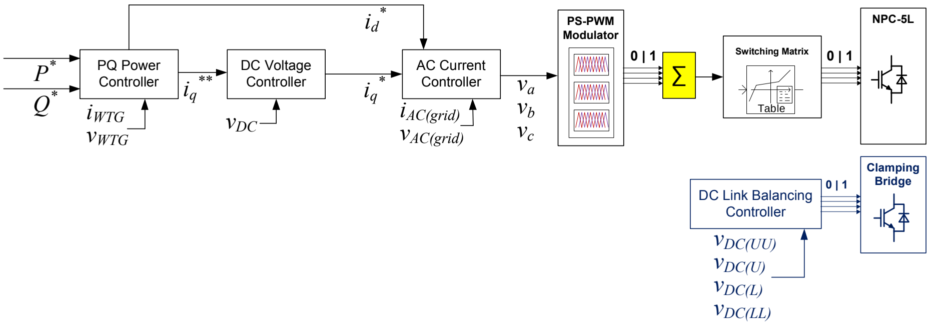

Fig. 3.18. Grid-side NPC-5L (top) and clamping bridge (bottom) control scheme - schematic block representation.

Detailed description and implementation method of each controller is provided in the Appendix C.

3.4.5 Control Tuning

Table 3.7 provides gain values for PI and P controllers used in the control scheme for system C. The tuning procedure is identical as for system A. The implementation of the controllers with specified parameter values can be found in the Appendix C.

Table. 3.7. System C: converter PI / P controllers - specification.

Parameter	Generator-Side	Grid-Side	Control Block
Sampling frequency $f_{s(HL)}$ [kHz]	20 (CL) / 4.2 (2L)	20 (CB) / 8.8 (NPC)	
Proportional gain $K_{p(PQ)}$	$5.00 \cdot 10^{0}$	$2.00 \cdot 10^{-1}$	PQ Power Controller
Integral time constant $T_{i(PQ)}$ [s]	$1.00 \cdot 10^{-2}$	$1.00 \cdot 10^{-3}$	
Proportional gain $K_{p(DC)}$	-	$6.24 \cdot 10^{-2}$	DC Voltage Controller
Integral time constant $T_{i(DC)}$ [s]	-	$8.00 \cdot 10^{-2}$	
Proportional gain $K_{p(AC)}$	-	$6.24 \cdot 10^{-1}$	AC Current Controller
Integral time constant $T_{i(AC)}$ [s]	-	$8.00 \cdot 10^{-1}$	
Proportional gain $K_{p(AC)}$	-	$1.14 \cdot 10^{0}$	0-Sequence Controller
Integral time constant $T_{i(AC)}$ [s]	-	$1.75 \cdot 10^{-1}$	
Non-sensitivity margin [kV / %]	-	±3 / ±8	Clamping Bridge (CB)

3.5 System REF: Back-to-Back 2-Level Power Converter

A conventional 10 MW wind turbine system in Figure 3.19 with a step-up transformer is modelled in order to establish a benchmark platform for comparison (assessment). It includes a conventional back-to-back 2-level converter operating at 0.69 kV alternating voltage level. Added transformer steps-up voltage to the 20 kV level.

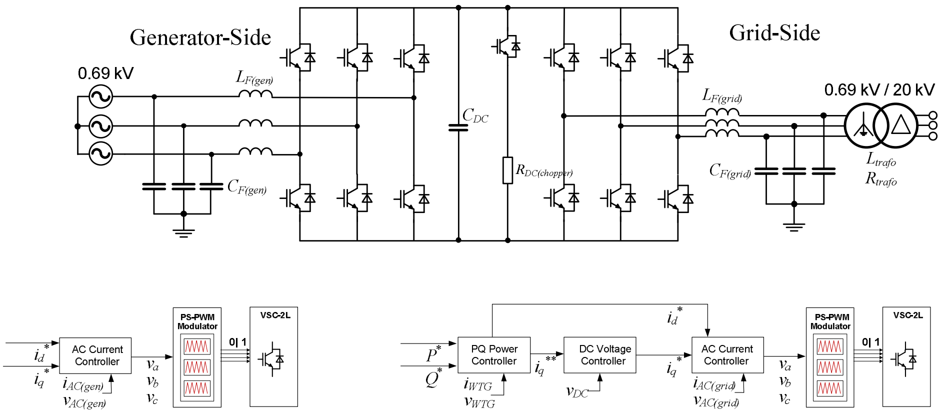

Fig. 3.19. System REF: schematic representation of the wind turbine circuit.

The control architecture is equivalent to the one described in systems A, B and C. The generator-side unit consists of an alternating current controller, while the grid-side unit includes a PQ power controller and direct voltage controller.

Table 3.8 provides specifications and ratings for components in the REF system, while Table 3.9 provides gain values for PI and P controllers used in the control scheme.

Table. 3.8. System REF: component ratings - specification.

Parameter	Value	Component
Nominal power S_{gen} [MVA]	20 x 0.5	Generator
Nominal frequency f_{gen} [Hz]	50	
Terminal voltage V_{gen} [kV]	0.69	
Stator resistance* R_{gen} [mΩ]	0.05	
Stator inductance* L_{gen} [mH]	0.09	
L filter inductance $L_{F(gen)}$ [mH / %]	0.091 / 3	Generator-Side LC Filter
C filter capacitance $C_{F(gen)}$ [μF]	500	
Total energy stored in DC capacitors [kJ]	3	DC Link
DC chopper resistance R_{DC} [Ω]	2.4	
L filter inductance $L_{F(grid)}$ [mH]	4	Grid-Side LC Filter
C filter capacitance $C_{F(grid)}$ [μF]	400	
Transformer winding inductance L_{TR} [mH / %]	0.44 / 10	Step-Up Transformer
Transformer winding resistance R_{TR} [mΩ / %]	9.52 / 1	
Number of levels	2	Generator-Side 2-level Converter
Switching frequency (per IGBT) $f_{sw(REF)}$	4000	
PWM Modulation	carrier-based	

*Source: Vestas Wind Systems A/S

Table. 3.9. System REF: converter PI / P controllers - specification.

Parameter	Generator-Side	Grid-Side	Control Block
Sampling frequency $f_{s(HL)}$ [kHz]	8.4	8.4	
Proportional gain $K_{p(PQ)}$	-	$2.00\cdot10^{-1}$	PQ Power Controller
Integral time constant $T_{i(PQ)}$ [s]	-	$1.00\cdot10^{-2}$	
Proportional gain $K_{p(DC)}$	-	$6.24\cdot10^{-2}$	DC Voltage Controller
Integral time constant $T_{i(DC)}$ [s]	-	$8.00\cdot10^{-3}$	
Proportional gain $K_{p(AC)}$	$6.14\cdot10^{0}$	$6.14\cdot10^{0}$	AC Current Controller
Integral time constant $T_{i(AC)}$ [s]	$1.75\cdot10^{-1}$	$1.75\cdot10^{-1}$	

3.6 Collector Feeder System

3.6.1 AC Cables

All described wind turbine topologies are interconnected to the substation transformer by means of 3-core XLPE cables, each modelled as a Π section. Parameter values for the selected cable are presented in Table 3.10 according to the datasheet given in [58].

Table. 3.10. Single PI cable section in the collector feeder system - specification.

Parameter	Value	Parameter	Value
Rated voltage [kV]	24	Core (Cu) cross-section [mm^2]	95
Current rating [A]	400	Screen (Cu) cross-section [mm^2]	16
Length [km]	1	Weight [kg / m]	30
Parasitic series inductance L_{cable} [µH]	95.2	Nominal temperature [^{0}C]	50
Parasitic series resistance R_{cable} [mΩ]	0.048	Number of sections with regard to number of turbines N_{WTG}	$\sum(N_{WTG})$
Parasitic shunt capacitance C_{cable} [µF]	0.272		

3.6.2 Substation Transformer

AC cables are interconnected to the grid through offshore 3-winding substation transformer shown in Figure 3.20. Additional Δ-winding decouples to a certain degree 0-sequence circuit between the collector feeder and transmission system, which is often required to avoid false tripping made by the utility ground protection relays [31].

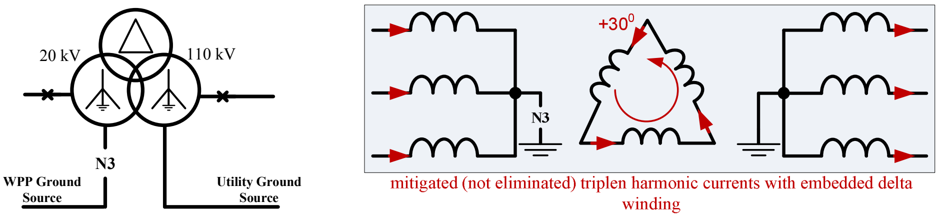

mitigated (not eliminated) triplen harmonic currents with embedded delta winding

Fig. 3.20. 3-winding substation transformer with ground sources to MV and HV sides.

Table 3.11 provides parameter values for the substation transformer model. In order to simplify modelling implementation, it is assumed that the transformer does not saturate at any examined operating point. In this manner, core dimensioning procedure is excluded from this work.

Table. 3.11. Substation transformer for the collector feeder system - specification.

Parameter	Value	Parameter	Value
Winding arrangement [-/-/-]	wye-g / delta / wye-g	Leakage inductance [pu]	0.1
Rated power [MVA]	500	Mutual inductance [pu]	0.05
Voltage ratio [kV/kV/kV]	20 / 20 / 110	Winding resistance [pu]	0.01

3.6.3 Transmission System

Transmission system is modelled with an alternating voltage source and Thevenin short-circuit impedance. Parameter values used for the grid modelling are presented in Table 3.12.

Table. 3.12. Utility transmission system after PCC point - specification

Parameter	Value	Parameter	Value
Grid voltage V_{grid} [RMS, L-L, kV]	110	Short circuit power S_{SC} [MVA]	200
Frequency f_{grid} [Hz]	50	Short circuit ratio X/R [-]	10

Chapter 4

Losses Analysis

4.1 Introduction

Wind turbines may operate in different power generation modes, according to the varying wind conditions and specific loading requirements. In order to provide accurate and universal power generation representation for each wind turbine circuitry, power losses dissipated in the semiconductor devices of each system have been calculated in a single turbine for the power levels shown in Table 4.1 - ranging from 20% to 100%. Schematic system representation shown in Figure 4.1 includes single wind turbine connected to the substation transformer with an AC cable.

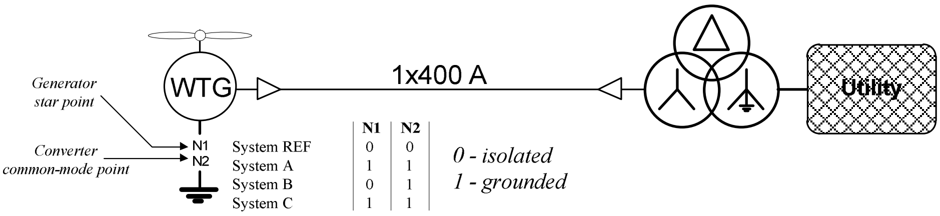

Fig. 4.1. System schematic representation for losses analysis.

In order to minimize risk of insulation breakdown on the generator windings, EMTDC/PSCAD simulations from Figure 4.2 show, that systems A and C should operate with solid grounded generator neutral and converter common-mode points (N1 and N2). In this manner, no common-mode voltage is induced between the generator and the generator-side converter. System B operates with much lower voltage on the generator-side (3.3 kV), so that losses can be safely reduced by isolating the generator neutral N1, thus preventing zero sequence leakage current flow through the IGBTs in the generator-side unit.

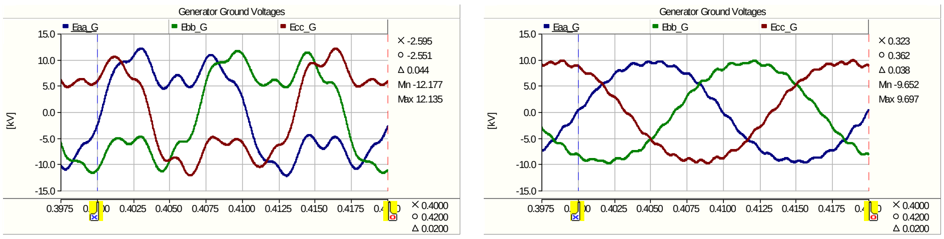

Fig. 4.2. Generator ground voltages induced in system C with N1 point isolated (left) and with N1 point grounded (right).

In medium voltage transformer-less systems (A, B, C), 4500 V press-pack devices [59] are used for loss estimation due to their good thermal properties (double side cooling, low thermal impedance) and short circuit failure mode - necessary for series connections in NPC topologies. MV press-pack devices are confronted with commonly available and optimized 1700 V power modules [60], which allow operation at 0.69 kV of the 2-level system REF. Power losses dissipated in the passive components (i.e. generator, LC filter and step-up transformer) are excluded from the analysis.

Table. 4.1. Calculated power losses for different loading conditions.

WTG Power [MVA]	Power [%]	Load [pu]
10	100	k = 1.0 pu
8	80	k = 0.8 pu
6	60	k = 0.6 pu
4	40	k = 0.4 pu
2	20	k = 0.2 pu

4.2 Solution Methodology

4.2.1 Workflow Diagram

In order to obtain accurate results of power losses generated with converter circuitries operating at various ranges of voltage, current and switching frequency - a common loss estimation platform is created which calculates losses and junction temperatures for each device under the pre-defined steady state conditions according to the device datasheet. Input parameters for the loss estimation platform are established according to the selected device maximum ratings and curves obtained from datasheets (Tables 4.2, D.1), along with instantaneous parameter values measured directly from the performed EMTDC/PSCAD time-domain simulations. General workflow diagram is shown in Figure 4.3, in accordance to which losses in each single IGBT and diode are calculated individually based on the extracted sampling data.

Under nominal loading conditions (k = 1 pu), calculated RMS value from the measured current sampling data is used to estimate required maximum cooling water temperature T_{CW} for the cooling system, which is assumed constant for any examined loading. Approximate junction temperature values T_j for partial loading are obtained according to the applied thermal models for specific devices.

In order to minimize error occurring for systems with high switching frequencies, a very high resolution channel 1 μs / 2 μs is used over the full 20 ms cycle period, meaning that 10,000 data samples are used of each signal for further processing. Table E.1 in Appendix E summarizes input constant values and functions used as an input data to evaluate each system. Derived switching curves have been validated experimentally by calculating switching energies through single pulse switching tests at 1000 V [61].

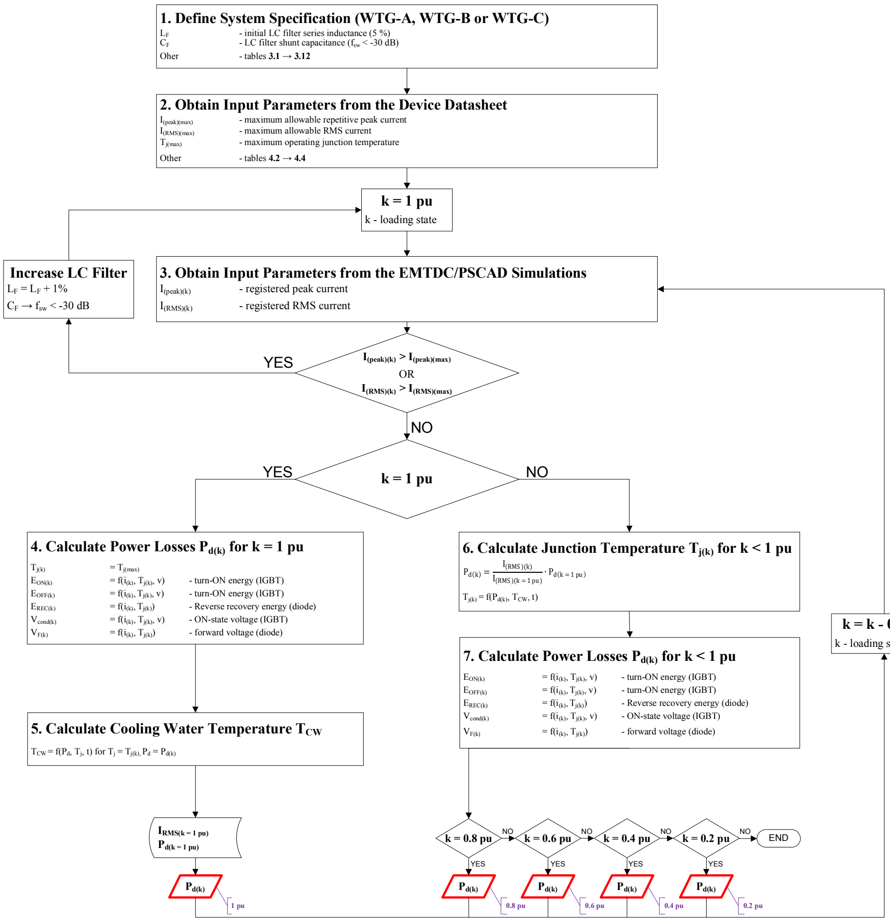

Fig. 4.3. Solution methodology to power loss estimation for different loading conditions

Transient thermal impedances of the press-pack devices are linearly dependant to the number of parallel chips N_p per device, where base formulas (Appendix E) refer to a 340 A press-pack with $N_{p(IGBT)}$ = 6 IGBT dies and $N_{p(D)}$ = 3 diode dies.

4.2.2 System Specification

System specification for each analyzed system is defined according to data listed in Tables from 3.1 to 3.12. LC filter inductance L_F is set for current ripple attenuation below the maximum RMS and peak ratings available from component datasheets. C filter capacitor is used to minimize voltage ripple on the grid-side and dv/dt effect on the generator-side. LC filter transfer function is:

$$H(s) = \frac{1}{1 + s \cdot L_F + s^2 \cdot L_F \cdot C_F} \tag{4.1}$$

Capacitance C_F is selected to form an LC series resonant path for equivalent switching frequency harmonic current, so that it is damped below -30 dB level, as shown on Bode plot from Figure 4.4. Tables 3.2/.6/.4/.8 provide calculated LC filter values for systems A, B, C and REF.

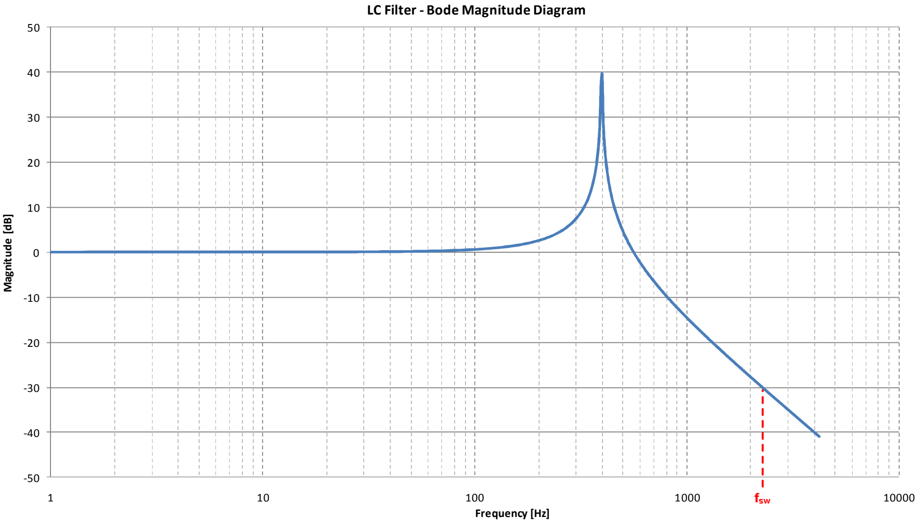

Fig. 4.4. LC filter transfer function magnitude (in dB) in the frequency domain.

4.2.3 Input Parameters from Datasheets

Maximum ratings required for the LC filter dimensioning and power loss calculations are obtained from [59, 60]. Table 4.2 lists electrical and thermal characteristics of the proposed devices used in the conventional low voltage (0.69 kV) and medium voltage (20 kV) power converter circuitries. For the conventional systems with back-to-back 2-level modules, Infineon devices with open-circuit failure mode are utilized, which allow switching at 4 kHz without snubber circuits.

Table. 4.2. Maximum ratings of the applied semiconductor devices [59, 60].

IGBT/Diode Rating	**IGBT/Diode LV Module (per device)**	**IGBT/Diode MV Press-Pack (per die)**
Permanent direct voltage for 100 FIT failure rate, v [V]	900	2800
Direct collector current, IGBT, $I_{RMS(MAX)(T)}$ [A]	450	55
Repetitive peak collector current, t_p = 1 ms, IGBT, $I_{peak(MAX)(T)}$ [A]	900	110
Continuous direct forward current, Diode, $I_{RMS(MAX)(D)}$ [A]	450	110
Repetitive peak forward current, t_p = 1 ms, Diode, $I_{peak(MAX)(D)}$ [A]	900	220
Operating junction temperature, $T_{j(max)}$ [°C]	125	

Devices for medium voltage topologies are Westcode press-packs. Press-pack devices consist of parallel-connected dies, which fail in short-circuit mode, thus they allow a series connection of single IGBTs. Algebraic formulas for energies and ON-state voltages are derived from curve fitting with *cftool* in MATLAB. Formulas for transient thermal impedances of the devices are represented through Foster network equation (4.2).

$$Z_{th(S-J)}(t) = a \cdot \left(1 - e^{-\frac{t}{\alpha}}\right) + b \cdot \left(1 - e^{-\frac{t}{\beta}}\right) + c \cdot \left(1 - e^{-\frac{t}{\gamma}}\right) + d \cdot \left(1 - e^{-\frac{t}{\delta}}\right) \tag{4.2}$$

where weight factors are provided from datasheets in Table 4.3.

Table. 4.3. Derived weight factors for transient thermal impedance Foster formula.

IGBT press-pack (per die)	**a**	$1.35\cdot10^{-1}$	**b**	$6.90\cdot10^{-2}$	**c**	$3.03\cdot10^{-2}$	**d**	$7.47\cdot10^{-3}$
	α	$5.07\cdot10^{-1}$	**β**	$4.58\cdot10^{-2}$	**γ**	$5.40\cdot10^{-3}$	**δ**	$7.00\cdot10^{-4}$
Diode press-pack (per die)	**a**	$8.93\cdot10^{-2}$	**b**	$2.40\cdot10^{-2}$	**c**	$2.21\cdot10^{-2}$	**d**	$8.52\cdot10^{-3}$
	α	$4.70\cdot10^{-1}$	**β**	$9.10\cdot10^{-2}$	**γ**	$1.10\cdot10^{-2}$	**δ**	$4.70\cdot10^{-3}$
IGBT power module	**a**	$1.80\cdot10^{-3}$	**b**	$8.30\cdot10^{-3}$	**c**	$38.30\cdot10^{-3}$	**d**	$5.70\cdot10^{-3}$
	α	$0.8\cdot10^{-3}$	**β**	$1.30\cdot10^{-2}$	**γ**	$5.00\cdot10^{-2}$	**δ**	$6.00\cdot10^{-1}$
Diode power module	**a**	$6.30\cdot10^{-3}$	**b**	$23.80\cdot10^{-3}$	**c**	$62.90\cdot10^{-3}$	**d**	$7.00\cdot10^{-3}$
	α	$0.8\cdot10^{-3}$	**β**	$1.30\cdot10^{-2}$	**γ**	$5.00\cdot10^{-2}$	**δ**	$6.00\cdot10^{-1}$

4.2.4 Input Parameters from the EMTDC/PSCAD Simulations

Instantaneous logic gate signal $S_{gate[n]}$, IGBT collector current $i_{C[n]}$ and diode forward current $i_{F[n]}$ in each device are registered each t_{sample} = 2 µs over T_S = 0.02 s. According to the registered signals, measured peak and RMS current values are obtained from:

$$I_{(peak)} = \max\left(i_{C[1]} \quad : \quad i_{C[10000]}\right) \tag{4.3}$$

$$I_{(RMS)} = \sqrt{\frac{1}{T_S} \cdot \int_0^{T_S} [i(t)]^2 \, dt} \approx \sqrt{\frac{1}{T_S} \cdot \sum_{i=1}^{10000} i_{C[n]}^2 \cdot t_{sample}} \tag{4.4}$$

Calculated values are then compared to the ones in Table 4.2 for LC filter dimensioning.

4.2.5 Power Loss and Temperature Estimation

Extracted input data from EMTDC/PSCAD simulations are transferred into Excel Spreadsheet for further processing. Input measured signals are injected directly as a column of samples, associated with each time step. A single switching sequence with regard to the time frame of the calculated switching energy and ON-state voltage pulses is shown in Figure 4.5.

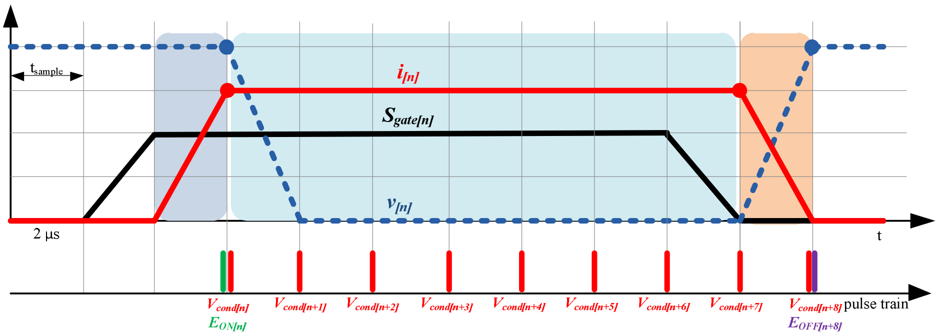

Fig. 4.5. Power loss calculation in IGBT device based on sampled input data.

In order to obtain a 1st order power curve approximation in form of the repetitive pulse response, first step is to obtain information over the number of switching transitions between ON/OFF and OFF/ON states. This is realized by comparing former and latter gate logic signal $S_{gate[n]}$ in each sampling period t_{sample}.

$$N_{SW(ON)[n]} = \begin{cases} 1 & \Leftrightarrow \quad \left(S_{gate[n]} = 0\right) \wedge \left(S_{gate[n+1]} = 1\right) \\ 0 & \Leftrightarrow \quad \left(S_{gate[n]} \neq 0\right) \vee \left(S_{gate[n+1]} \neq 1\right) \end{cases} \tag{4.5}$$

$$N_{SW(OFF)[n]} = \begin{cases} 1 & \Leftrightarrow \quad \left(S_{gate[n]} = 1\right) \wedge \left(S_{gate[n+1]} = 0\right) \\ 0 & \Leftrightarrow \quad \left(S_{gate[n]} \neq 1\right) \vee \left(S_{gate[n+1]} \neq 0\right) \end{cases} \tag{4.6}$$

$N_{SW(ON)}$ logic signal provides logic “1” only when ON transition occurs, while $N_{SW(OFF)}$ provides logic “0” when OFF transition occurs. Hence, total number of switching transitions is obtained by:

$$N_{SW(ON)} = \sum_{n=1}^{n=10000} N_{SW(ON)[n]} \tag{4.7}$$

$$N_{SW(OFF)} = \sum_{n=1}^{n=10000} N_{SW(OFF)[n]} \tag{4.8}$$

The next step is to calculate switching energy losses based on derived logic signals N_{SW} for each sample period:

$$E_{ON(IGBT)[n]} = f\left(v, i_{C[n]}, T_j\right) \cdot N_{SW(ON)[n]} \tag{4.9}$$

$$E_{OFF(IGBT)[n]} = f\left(v, i_{C[n]}, T_j\right) \cdot N_{SW(OFF)[n]} \tag{4.10}$$

$$E_{OFF(D)[n]} = f\left(v, i_{F[n]}, T_j\right) \cdot N_{SW(OFF)[n]} \tag{4.11}$$

The total switching power losses are then obtained from:

$$P_{ON(IGBT)} = \frac{1}{T_S} \cdot \sum_{n=1}^{n=10000} E_{ON(IGBT)[n]} \tag{4.12}$$

$$P_{OFF(IGBT)} = \frac{1}{T_S} \cdot \sum_{n=1}^{n=10000} E_{OFF(IGBT)[n]} \tag{4.13}$$

$$P_{REC(D)} = \frac{1}{T_S} \cdot \sum_{n=1}^{n=10000} E_{OFF(D)[n]} \tag{4.14}$$

Conduction power losses P_{cond} are calculated at each sample instant by multiplying the instantaneous current with the corresponding collector-emitter saturation voltage (IGBT) $V_{cond(IGBT)}$ or forward voltage (diode) $V_{cond(D)}$. The multiplied values are then intergrated over the entire cycle period T_S:

$$P_{cond(IGBT)} = \sum_{n=1}^{n=10000} \left(V_{cond(IGBT)[n]} \cdot i_{C[n]}\right) \tag{4.15}$$

$$P_{cond(D)} = \sum_{n=1}^{n=10000} \left(V_{cond(D)[n]} \cdot i_{F[n]}\right) \tag{4.16}$$

The resulting power losses P_d are calculated from:

$$P_{d(IGBT)} = P_{ON(IGBT)} + P_{OFF(IGBT)} + P_{cond(IGBT)} \tag{4.17}$$

$$P_{d(D)} = P_{REC(D)} + P_{cond(D)} \tag{4.18}$$

Temperature variations differ according to the selected device not only due to their different thermal characteristics, but also because of the cooling method. Press-pack IGBTs allow double-side cooling, which is utilized with 2 cooling plates for each device, whereas power modules can only be cooled from the collector side. Simplified static thermal models of each device are presented in Figure 4.6. Thermal resistance values of each element are listed in Table 4.4. Technical specifications for the cooling plates are obtained from [62].

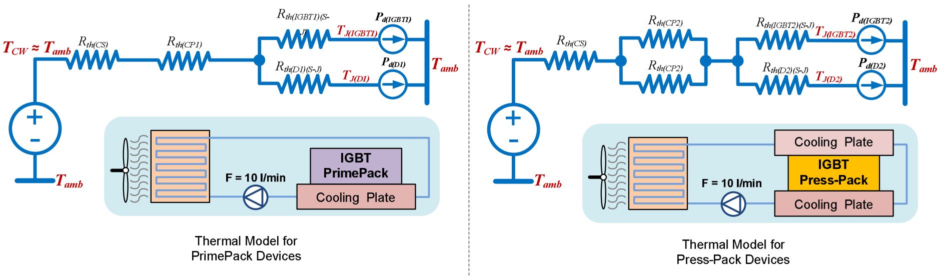

Fig. 4.6. Static thermal models for power modules (left) and press-packs (right).

Temperature estimation is realized under steady state operation of the power converter, which allows its approximate solution assuming repetitive pulse cycling mode. Figure 4.7 demonstrates assumed pulse cycling mode along with the expected temperature fluctuations. Pulse time t_p and cycling time T are calculated from:

$$t_p = \frac{t_{sample}}{N_{SW(ON)}} \sum_{n=1}^{n=10000} S_{gate[n]} \tag{4.19}$$

$$T = \frac{T_S}{N_{SW(ON)}} \tag{4.20}$$

Table. 4.4. Thermal characteristics of the applied static thermal models.

Parameter	Value
Cooling system thermal resistance $R_{th(CS)}$ [K/W]	0.008
Cooling water, flow rate F [l/min]	10
Water cooler for power module [62], thermal resistance $R_{th(CP1)}$ [K/W]	0.0065
Water cooler for press-pack [63], thermal resistance $R_{th(CP2)}$ [K/W]	0.0033
Power module thermal resistance junction to sink, IGBT, $R_{th(IGBT1)(S-J)}$ [K/W]	0.068
Power module thermal resistance junction to sink, Diode, $R_{th(D1)(S-J)}$ [K/W]	0.127
Press-pack thermal resistance junction to sink, IGBT (per die), $R_{th(IGBT2)(S-J)}$ [K/W]	0.0061
Press-pack thermal resistance junction to sink, Diode (per die), $R_{th(D2)(S-J)}$ [K/W]	0.0192

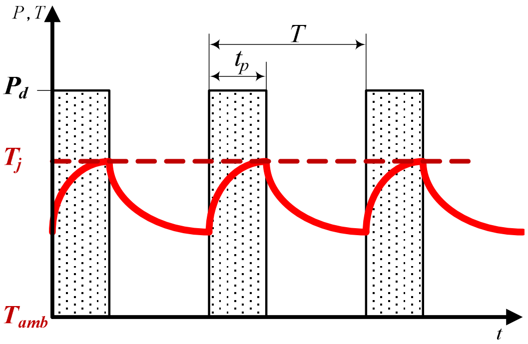

Fig. 4.7. Junction temperature variations under steady-state loading conditions.

In order to calculate maximum junction temperature for each device, approximate linear steady-state solution is derived for the repetitive power pulse response:

$$T_j = P_d \cdot \left[\delta \cdot R_{th(CS-J)} + (1-\delta)\cdot Z_{th(S-J)}(T+t_p) - Z_{th(S-J)}(T) + Z_{th(S-J)}(t_p)\right] + T_{CW} \tag{4.21}$$

where:

$$\delta = \frac{t_p}{T}\ , \tag{4.22}$$

$$R_{th(CS-J)} = R_{th(CS)} + R_{th(CP1)} + \begin{cases} R_{th(S-J)(IGBT)(1)} & \rightarrow IGBT \\ R_{th(S-J)(D)(1)} & \rightarrow Diode \end{cases} \quad \text{- power modules} \tag{4.23}$$

$$R_{th(CS-J)} = R_{th(CS)} + \frac{R_{th(CP2)}}{2} + \begin{cases} R_{th(S-J)(IGBT)(2)} & \rightarrow IGBT \\ R_{th(S-J)(D)(2)} & \rightarrow Diode \end{cases} \quad \text{- press-packs} \tag{4.24}$$

4.2.6 Distributed Cells in the Generator-Side MMC Topology

The introduced method for loss estimation requires input current signals, which flow directly through each individual semiconductor switch. As a result, hardware representation of the machine-side MMC model for system A with controlled arm voltage sources is improved by adding distributed current-controlled cells, in which measured and added capacitor cell voltages are used as the resulting arm voltage source input signal [64]. A schematic representation of the distributed cells for each arm is shown in Figure 4.8.

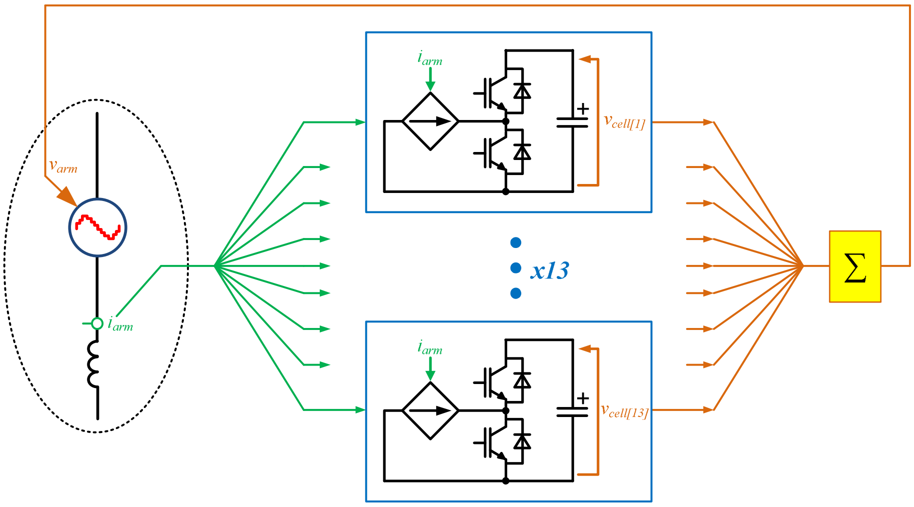

Fig. 4.8. Power loss estimation in the generator-side MMC system

The measured cell capacitor voltages are also used as input signals for the cell voltage balancing controller [82], which is responsible for keeping their values at the preferred level (more information provided in Appendix A).

4.3 Wind Turbines - Power Generation under Different Loading Conditions

4.3.1 Generator-Side

Switching and conduction power losses have been calculated for the proposed generator-side converter systems. In the transformer-less concepts, all IGBTs switch at medium voltage above 2 kV, which results in the usage of press-pack IGBTs. Low voltage wind turbine equipped with transformer utilizes power module devices interconnected in parallel. Calculated switching power losses for each system are shown in Figure 4.9.

Due to low switching frequency in system A (MMC converter), the resulting switching losses are substantially lower and kept on a similar level to high frequency switching operation of the conventional low voltage wind turbine. Under partial loading conditions, switching losses are lowest since major loss contribution coming from the RMS arm circulating currents is lowered while multilevel MMC performance with quasi-sinusoidal arm voltages practically eliminates any significant current peaks across the IGBT devices.

On the other hand, relatively high current peaks in medium voltage 2-level converter units utilized in systems B and C, combined with high switching frequency become a major loss cause for these systems.

In case of system B, proposed 2-level generator-side AC/DC converter generates approximately 90% of the total switching losses, whereas soft switching operation of the proposed DC/DC boost converter practically eliminates switching power losses coming from the DC/DC boost operation.

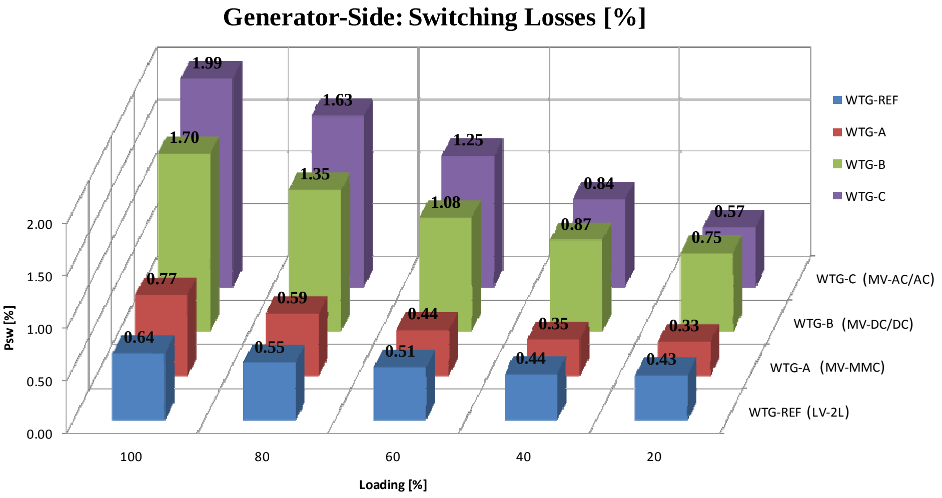

Fig. 4.9. Calculated switching power losses for different loading conditions.

In a similar manner to system A, the low switching frequency for AC/AC boost converter concept in system C makes it highly efficient with total switching loss contribution below 20%. 2-level converter unit used to re-charge cell DC capacitors contribute in total to more than 80% of the generated losses.

In terms of conduction losses, the reference low voltage system with high switching frequency provides shortest conductive periods for IGBTs, which results in lowest conduction losses. Nevertheless, results show that system A with MMC circuitry also provides lowest conduction losses among the proposed transformer-less concepts.

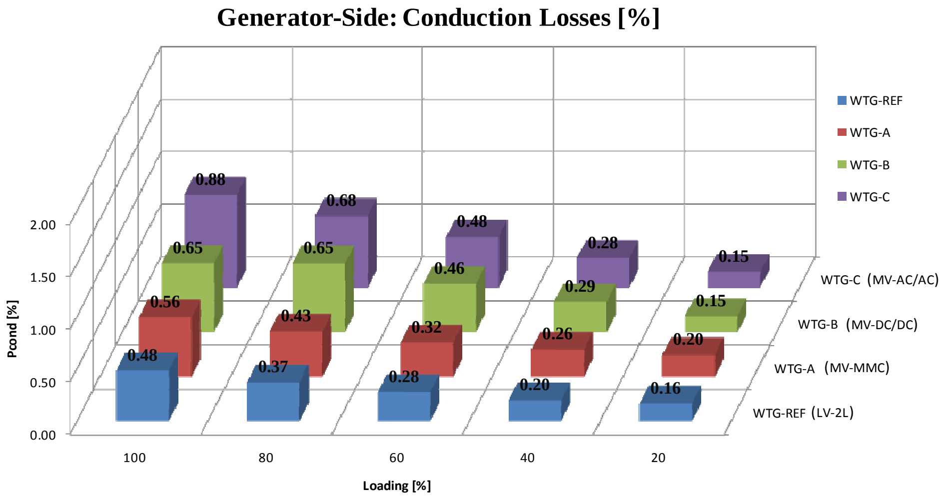

Fig. 4.10. Calculated conduction power losses for different loading conditions.

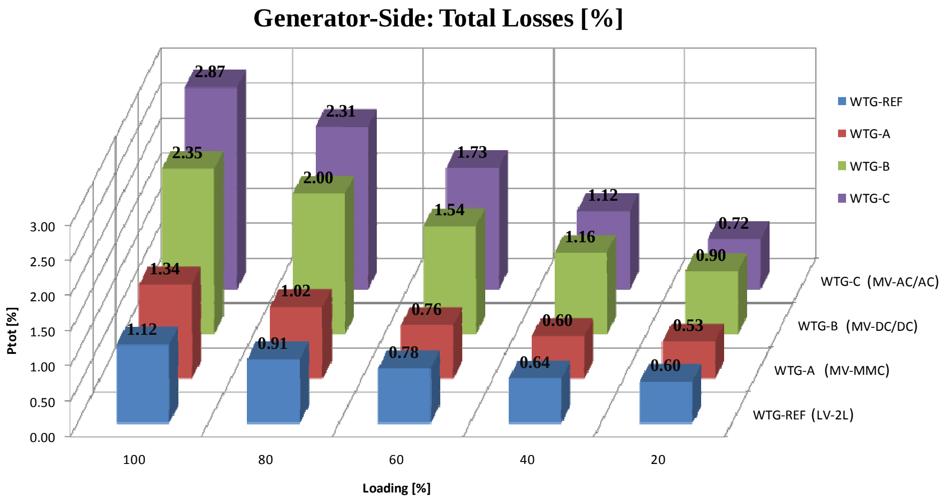

Fig. 4.11. Calculated total power losses for different loading conditions.

In system B, 40% of the conduction losses come from an IGBT branch in DC/DC boost converter. In system C, 40% of the conduction losses are coming solely from the series-connected diodes in the bridge rectifier.

Combined switching and conduction power losses are presented in Figure 4.11. It occurred that conventional 2-level low voltage converter provides most efficient operation under high loads, whereas MMC converter in system A generates lowest losses during low loads. Generator-side concepts proposed for systems B and C become not competitive to system A in terms of efficiency over the examined loading conditions.

Similar results between systems A and REF show that the applied specific power profile at a certain location will be crucial in order to determine whether system A or REF has the highest overall efficiency.

4.3.2 Grid-Side

Grid-side units proposed for the transformer-less system consist of press-pack IGBTs with the identical number of dies (6 for IGBTs; 3 for diodes). In system C, registered power losses include switching operation of the clamping bridge, which is necessary to balance adjacent DC link capacitors of the NPC-5L topology.

Switching losses of the grid-side candidates are shown in Figure 4.12. Both proposed NPC topologies generate more than 2 times the switching losses in comparison to the MMC and low voltage system.

In a similar manner to the generator-side, conventional low voltage system has lower overall switching losses at high loads, whereas MMC becomes much more efficient during partial loads.

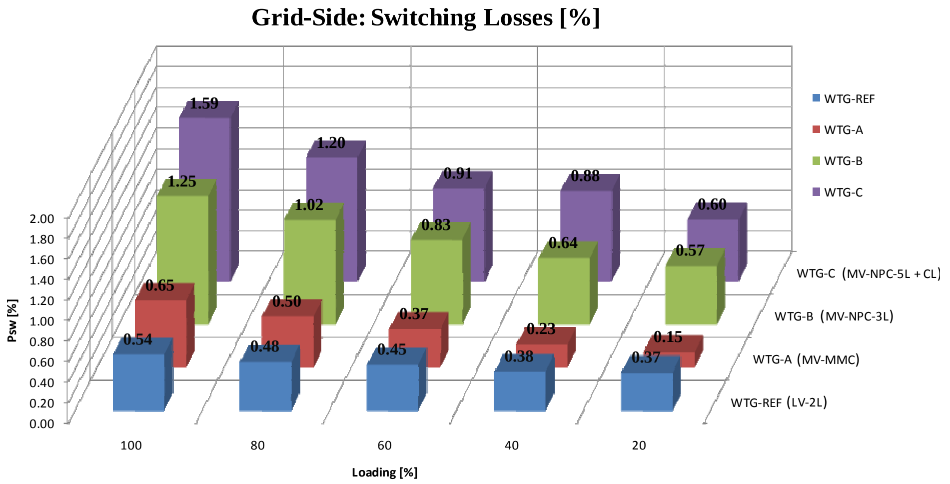

Fig. 4.12. Calculated switching power losses for different loading conditions

On the contrary to switching losses, generated conduction losses in each circuitry are maintained on a similar level. Figure 4.13 presents conduction loss distribution among the converter candidates. Good thermal properties of the press-pack devices allow loss reduction by app. 0.1% in the medium voltage converters.

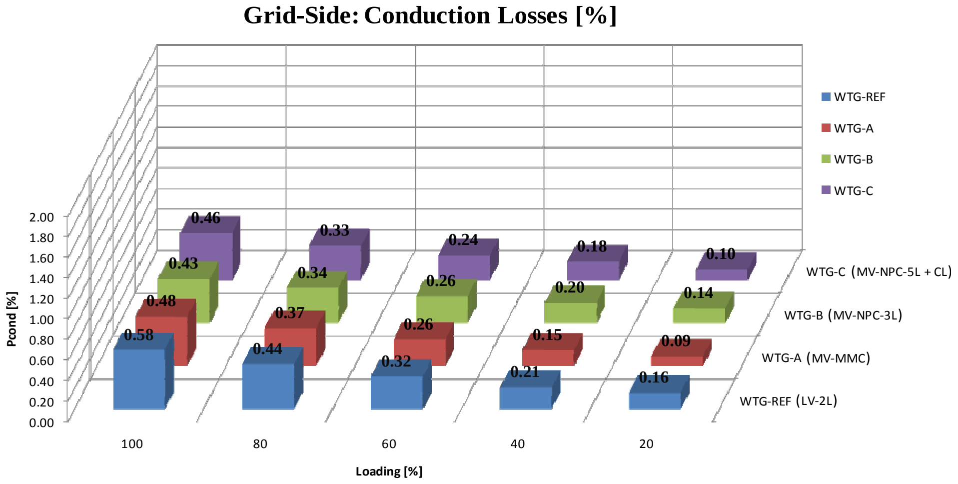

Fig. 4.13. Calculated conduction power losses for different loading conditions.

According to Figure 4.14, calculated total power losses of the grid-side converters show that MMC topology becomes most efficient candidate over the entire loading range. The performance of the MMC circuitry on the grid operating with a nominal terminal voltage results in further loss reduction by 0.2% when comparing it to the generator-side MMC unit.

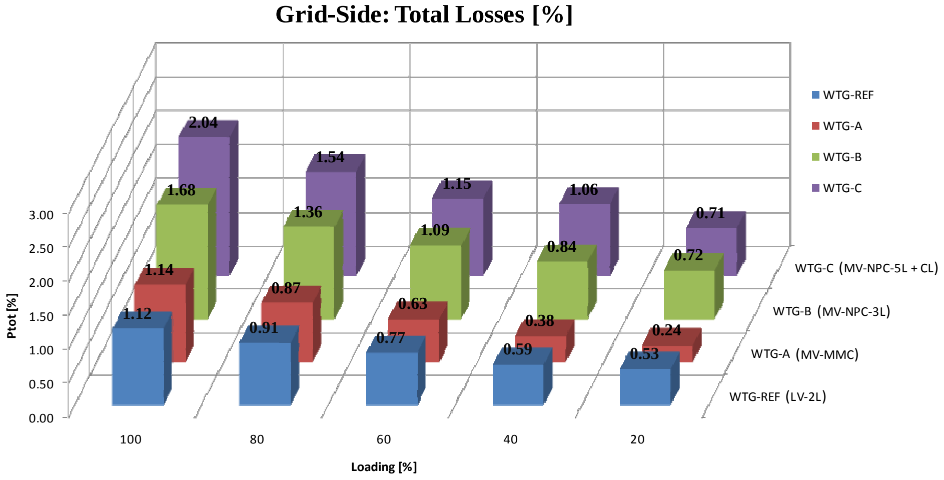

Fig. 4.14. Calculated total power losses for different loading conditions.

In summary, power generation of system A (back-to-back MMC) with press-pack devices becomes the most competitive solution among other proposed candidates for future transformer-less 10 MW wind turbines operating at 20 kV. Loss distribution is on the same level as for the conventional (REF) low voltage 2-level converter.

In order to determine whether the MMC circuit allows increased energy production, an evaluation has to be applied over the specified power generation profile, which includes power generation distribution contracted by the particular utility operator.

4.4 Qualitative Evaluation Assessment - Power Generation Distribution for Low Wind Site

4.4.1 Input Data

In order to compare wind turbine circuitries under different operating modes, a typical power-probability relation for a single turbine is introduced in Table 4.5. It includes many partial load hours, giving relatively low number of full load hours, which is the result of climate conditions and system operator demands.

Highest probability of 30% occurs under full load, while lowest 6% is during no load conditions, when turbine is either out of service, or requested not to inject more than 1% of its rated power.

Table. 4.5. Power generation distribution profile for low wind site*.

Power [%]	Probability [%]
0	6.6
1	5.9
5	7.3
10	8.3
17	8.8
28	8.9
42	8.7
60	8.1
82	7.3
100	30.1

*Source: Vestas Wind Systems A/S

4.4.2 Data Conversion

Measured wind turbine power generation at nominal loading is matched with the power generation distribution for low wind site by interpolated algebraic functions, which have been derived for power loss generation vs. loading states $P_{loss[\%]} = f(k_{[\%]})$. Table 4.6 lists developed curves associated with the algebraic formulas.

Table. 4.6. Interpolated loss functions with regard to load conditions $P_{loss[\%]} = f(k_{[\%]})$.

System	Generator-Side	Grid-Side
WTG-REF $P_{loss[\%]}$	$5.46\cdot10^{-5}\cdot\mathbf{k}^2 + 1.29\cdot10^{-5}\cdot\mathbf{k} + 5.68\cdot10^{-1}$ 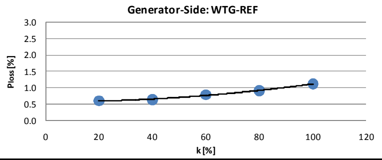	$4.75\cdot10^{-5}\cdot\mathbf{k}^2 + 1.81\cdot10^{-3}\cdot\mathbf{k} + 4.67\cdot10^{-1}$ 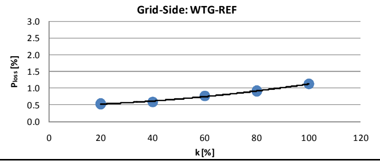
WTG-A $P_{loss[\%]}$	$1.04\cdot10^{-4}\cdot\mathbf{k}^2 + 2.30\cdot10^{-3}\cdot\mathbf{k} + 5.33\cdot10^{-1}$ 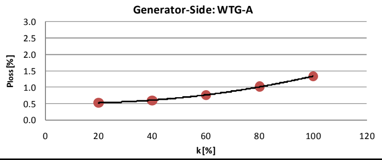	$4.54\cdot10^{-5}\cdot\mathbf{k}^2 + 5.90\cdot10^{-3}\cdot\mathbf{k} + 9.80\cdot10^{-2}$ 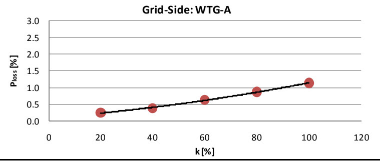
WTG-B $P_{loss[\%]}$	$4.58\cdot10^{-5}\cdot\mathbf{k}^2 + 1.33\cdot10^{-2}\cdot\mathbf{k} + 7.42\cdot10^{-1}$ 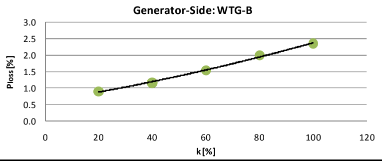	$7.47\cdot10^{-5}\cdot\mathbf{k}^2 + 3.24\cdot10^{-3}\cdot\mathbf{k} + 7.14\cdot10^{-1}$ 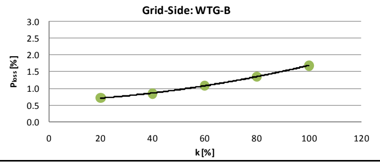
WTG-C $P_{loss[\%]}$	$5.25\cdot10^{-5}\cdot\mathbf{k}^2 + 2.12\cdot10^{-2}\cdot\mathbf{k} + 3.99\cdot10^{-1}$ 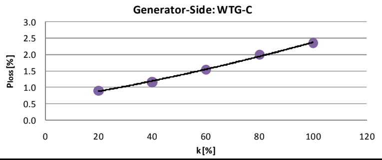	$1.10\cdot10^{-4}\cdot\mathbf{k}^2 + 2.61\cdot10^{-3}\cdot\mathbf{k} + 7.38\cdot10^{-1}$ 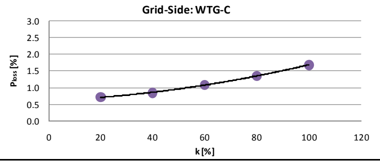

4.4.3 Comparison Results

According to the interpolated formulas provided in Table 4.6, expected wind turbine efficiencies are calculated from (4.25) for power levels provided in Table 4.5. Table 4.7 presents the calculated efficiency results $\eta_{N\%}$ for the analyzed wind distribution. Finally, the resulting weighted efficiency η_{TOT} is calculated from (4.26), which allows qualitative evaluation of the each proposed system.

$$\eta_{N\%} = \frac{P_{N\%}}{P_{N\%} + P_{loss[N\%]}} \tag{4.25}$$

$$\begin{aligned}\eta_{TOT} &= 0.059\cdot\eta_{1\%} + 0.073\cdot\eta_{5\%} + 0.083\cdot\eta_{10\%} + 0.088\cdot\eta_{17\%} + 0.089\cdot\eta_{28\%} + 0.087\cdot\eta_{42\%} \\ &+ 0.081\cdot\eta_{60\%} + 0.073\cdot\eta_{82\%} + 0.301\cdot\eta_{100\%}\end{aligned} \tag{4.26}$$

Table. 4.7. Calculated efficiencies for the given power generation distribution profile.

System	$\eta_{100\%}$	$\eta_{82\%}$	$\eta_{60\%}$	$\eta_{42\%}$	$\eta_{28\%}$	$\eta_{17\%}$	$\eta_{10\%}$	$\eta_{5\%}$	$\eta_{1\%}$	η_{TOT}	Side
REF	98.90%	98.87%	98.74%	98.44%	97.86%	96.68%	94.58%	89.78%	63.77%	**88.93%**	GEN
REF	98.89%	98.87%	98.77%	98.53%	98.06%	97.08%	95.33%	91.29%	68.08%	**89.42%**	GRID
A	98.67%	98.74%	98.73%	98.55%	98.07%	97.01%	95.05%	90.51%	65.33%	**89.10%**	GEN
A	98.87%	98.93%	98.98%	99.00%	98.94%	98.77%	98.41%	97.49%	90.58%	**91.74%**	GRID
B	97.53%	97.46%	97.24%	96.82%	96.05%	94.54%	91.92%	86.06%	56.97%	**86.91%**	GEN
B	98.25%	98.22%	98.08%	97.72%	97.01%	95.56%	92.99%	87.23%	58.23%	**87.75%**	GRID
C	97.05%	97.05%	96.99%	96.81%	96.44%	95.64%	94.20%	90.80%	70.41%	**88.18%**	GEN
C	97.94%	97.98%	97.89%	97.58%	96.89%	95.43%	92.81%	86.90%	57.45%	**87.51%**	GRID

Results in Table 4.7 show, that both resulting efficiencies η_{TOT} for the generator- and grid-side units in system A (marked red) are higher than for the conventional 2-level back-to-back converter (marked blue). **This means that for the analyzed power distribution profile, back-to-back MMC transformer-less concept provides higher annual energy production than the presently utilized system equipped with the step-up transformer.**

4.5 Quantitive Evaluation Assessment - Required Amount of Silicon in Wind Turbine Power Converters

Amount of the required silicon material partly reflects cost of the component materials. In the transformer-less systems with press-pack devices, all utilized IGBT and diode capsules consist of parallel-connected dies [65, 66], each with an identical amount of silicon. Number of dies depends on the current rating and is listed in Table 4.8. For system with power module devices, it is assumed that the enclosed power modules consist of parallel-connected IGBT and diode chips, as shown in Figure 4.15.

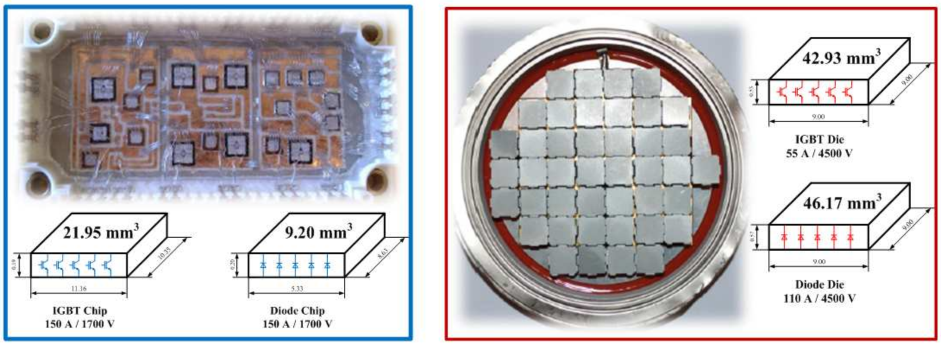

Fig. 4.15. Die / chip dimensions in power module (left) and press-pack (right) devices.

Approximate amount of silicon for 4500 V press-pack dies and 1700 V power module IGBTs is provided according to the chip dimensions given in datasheets [65-68].

Table. 4.8. Total number of the required dies / chips for each converter circuitry.

System	**Number of IGBT dies / chips**	**Number of diode dies / chips**
REF, Generator-Side	360	360
REF, Grid-Side	360	360
A, Generator-Side	936	468
A, Grid-Side	936	468
B, Generator-Side	576	384
B, Grid-Side	504	378
C, Generator-Side	900	762
C, Grid-Side	720	800

The total amount of silicon for diode and IGBT devices is presented in Figures 4.16 and 4.17. The results show, that among the transformer-less concepts, system B requires the minimum amount of silicon for IGBT and diode elements (3 times more than for LV system REF). System A with back-to-back MMC requires approximately 5 times more silicon than the conventional system with identical power ratings.

The excessive number of diodes in system C is the result of the series-connected diode bridge rectifier on the generator-side, along with exponentially increased number of clamping diodes for the NPC-5L on the grid-side.

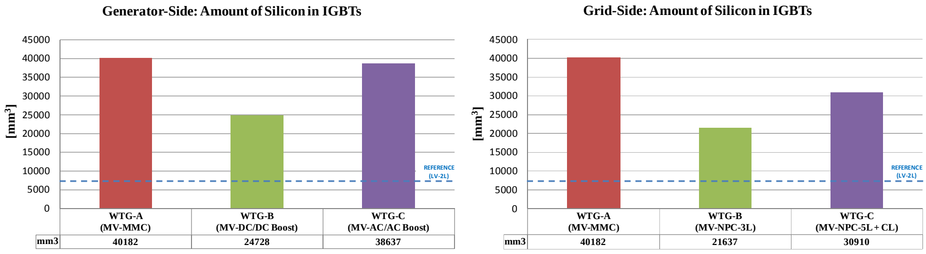

Fig. 4.16. Required amount of silicon in IGBT devices.

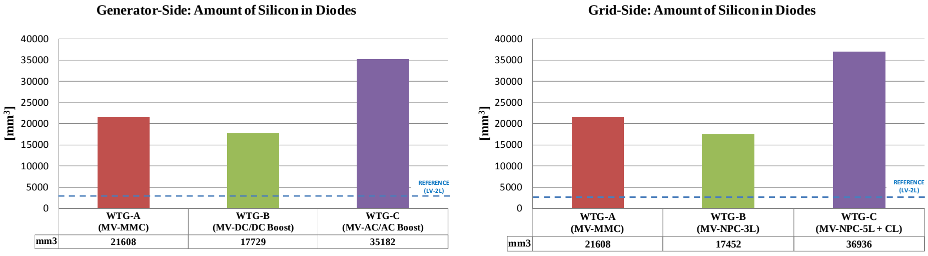

Fig. 4.17. Required amount of silicon for the diode devices.

Chapter 5

Short Circuit Analysis

5.1 Introduction

Maximum short circuit currents are calculated for the system presented in Figure 5.1. It includes a conceptual wind power plant consisting of 5 feeders interconnected in parallel. Each feeder is modelled according to the specification listed in Tables 3.5 - 3.8.

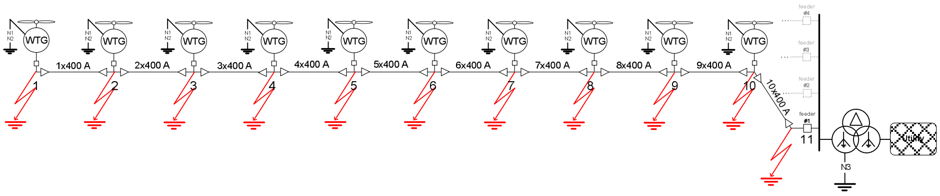

Fig. 5.1. Analyzed collector feeder system with marked ground fault locations.

In total, 7 different grounding configurations are analyzed with regard to the maximum ground short circuit currents. In order to evaluate each grounding scheme, the thermal loading of the ground conductors is compared when internal ground faults are applied at each terminal 1-11 with different grounding configuration. The obtained results may determine which grounding requires the lowest cross-section areas for the ground conductor wires in order to properly withstand short circuit current. In this manner, the least expensive (lowest amount of copper material) grounding method can be utilized for a high number of interconnected wind turbines.

The sizing of the circuit breakers located at each wind turbine and collector feeder terminals is made in a similar manner, according to the measured maximum short circuit currents that flow through the devices.

Short circuit calculations are performed according to IEC standards [69, 70] for the given system ratings and short-time withstand currents I''_k obtained from computer simulations. Due to lack of aggregated short-circuit models of the transformer-less wind turbine in the literature, detailed time-domain simulations of a single turbine are performed with respect to the applied grounding scheme.

The final part presents concept for the short-circuit protection scheme, which particularly includes fault detection over the entire feeder cable network. In order to provide selective operation, current differential relays are proposed for the primary protection. Back-up and secondary protection can be realized by means of the over-current directional elements, which are installed at each wind turbine and corresponding feeder terminals.

5.2 Solution Methodology

5.2.1 Time-Domain Modelling

The general workflow diagram for the short-circuit analysis is shown in Figures 5.2 and 5.3. It is divided into 2 functional parts. The first part includes time-domain modelling of a detailed single wind turbine model, which is interconnected to the substation transformer with a single cable Π section (Figure 5.2).

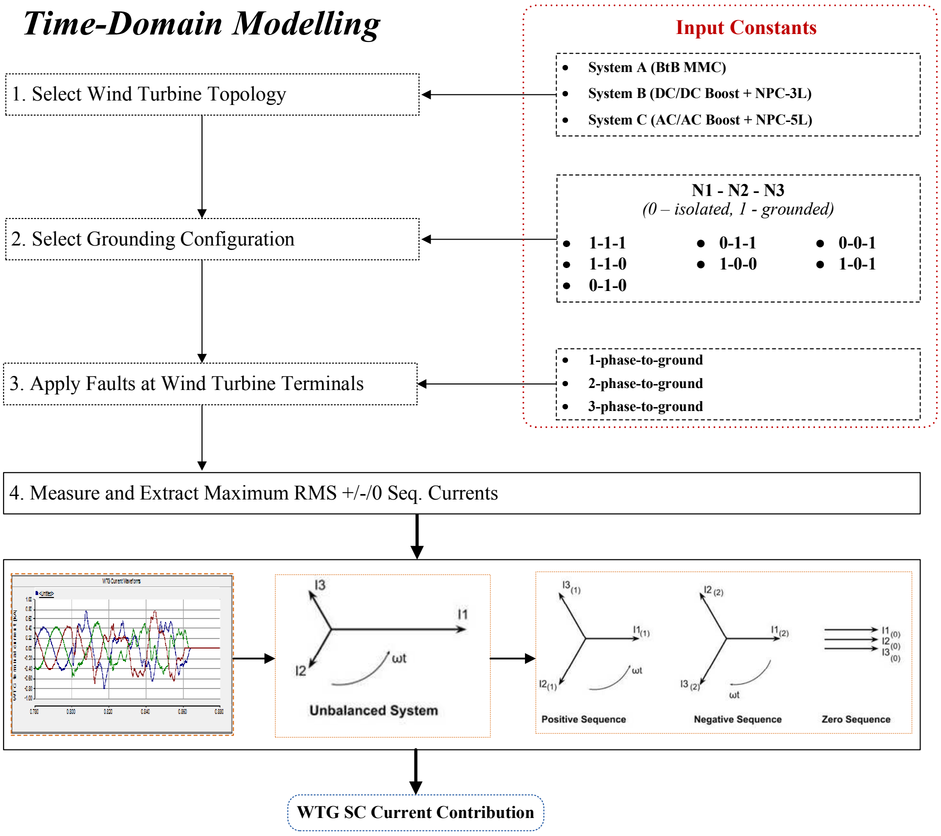

Fig. 5.2. General workflow diagram for time-domain SC analysis.

According to the selected wind turbine topology, grounding configuration, operating conditions and fault handling strategy, different types of faults are applied at the wind turbine terminals. During the fault operation period, the instantaneous currents flowing through the wind turbine terminals are measured, and their maximum RMS values are transformed into the symmetrical sequence components via Fast Fourier Transform (FFT). In this manner, maximum short circuit current contribution coming from a single wind turbine is obtained.

5.2.2 Phasor-Domain Modelling

With values obtained from the detailed time-domain simulations, wind turbine short circuit contribution can be represented with an aggregated model. The aggregated wind turbine models are used to construct complete feeder network model, which consists of the 10 wind turbines connected according to figure 5.1. General workflow diagram for the phasor-domain analysis is presented in Figure 5.3.

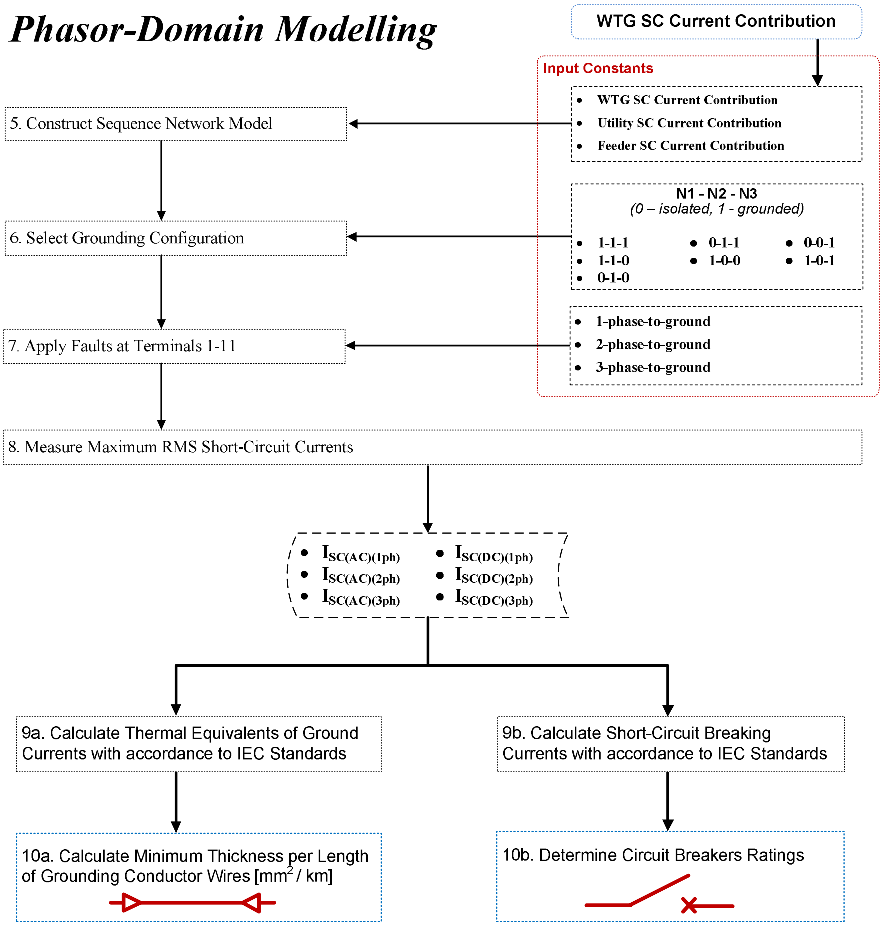

Fig. 5.3. General workflow diagram for phasor-domain SC analysis.

The phasor-domain analysis is performed over the positive, negative and zero sequence network models. Maximum resulting symmetrical RMS short circuit currents, which flow through the ground conductor wire and which flow through circuit breaker poles are measured and used to calculate thermal equivalents and breaking currents in order to determine the required ratings for the circuit breakers and the required cross-section areas of the ground wires.

5.3 Design Constraints

5.3.1 Grounding Conductor Wires

According to Table 3.10, all 3-core cable sections have been sized for nominal current loading by selecting the cross section thickness of the core. In case of copper screens, fixed thickness of 16 mm^2 is provided by the manufacturer. It is also assumed that all screens of each cable section are solid bonded on both sides in order to minimize common-mode voltage and to comply with safety requirements [32]. As semi-conductive screens are not sized to carry load currents, the shield is typically a fraction of the size of the phase conductor. During cable ground fault, the damage to the shield is more likely than the damage to the phase conductor.

In order not to over-dimension whole cable installations just for short-circuit current withstand capability, an extra bare conductive wire is routed in a trench along with cables in Figure 5.4. This wire provides an “effective” ground for cable neutral conductor bonding, so that it takes over a desired amount of fault current. Furthermore, flexible sizing of the bare conductor allows controlling ground impedance resistive value, thus making it more independent from the terrain and soil quality, especially at low frequencies.

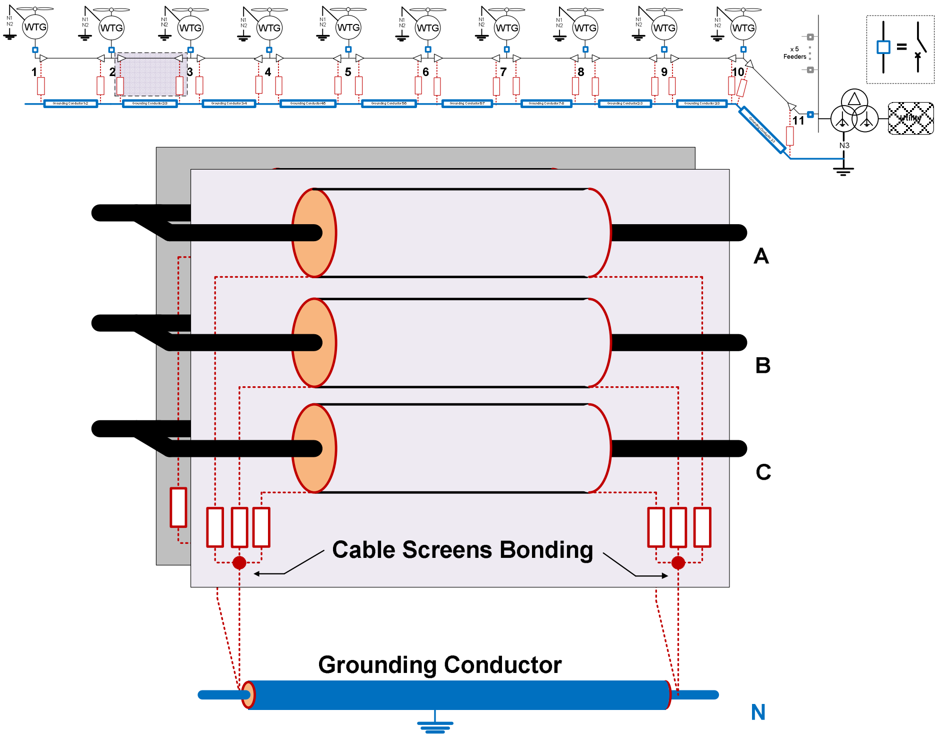

Fig. 5.4. Collector feeder grounding system with cable screens bonding method.

Cable screens are grounded (bonded) on both sides with an impedance. Its main role is to limit fault currents to the level, which screens in adjacent cable sections are able to withstand. According to the grounding configuration, connection between system neutral points: N1, N2, N3 and ground conductor wire sections N forms a short circuit current path for the analyzed system.

As a starting point for the short-circuit analysis, it is assumed that each feeder consists of N = 10 sections with separate grounding conductor wires - each with an initial cross-section area of 16 mm^2.

According to cable manufacturers, each single 16 mm^2 copper wire can carry maximum 1 s ground current of $I_{TH(1s)}$ = 2.45 kA, which results in maximum allowable temperature τ_2 = 250 ^{0}C. 1 s maximum current $I_{TH(1s)}$ is converted to its thermal equivalent for fault period T_k according to:

$$I_{TH(T_k)} = \frac{I_{TH(1s)}}{\sqrt{T_k}} \tag{5.1}$$

Based on formula (5.1), cable thermal constraints can be calculated when:

- $T_{k(21ms)}$ - both wind turbines and the utility contribute to the short circuit current. Wind turbines inject nominal active and reactive currents: $I_{TH(21ms)}$.
- $T_{k(80ms)}$ - only utility contributes to the short circuit current, with all wind turbines operating in block mode: $I_{TH(80ms)}$.

Parameters $I_{TH(21ms)}$ and $I_{TH(80ms)}$ are calculated from:

$$I_{TH(21ms)} = \frac{I_{TH(1s)}}{\sqrt{T_{k(21ms)}}} \tag{5.2}$$

$$\tau_1 = T_{k(21ms)} \cdot \left(\frac{I_{TH(21ms)}}{s} \right)^2 \cdot \frac{1}{\gamma_0 \cdot c} + \tau_0 \tag{5.3}$$

$$\tau_{AV} = \frac{\tau_1 + \tau_2}{2} \tag{5.4}$$

$$\gamma_{AV} = \frac{\gamma_0}{1 + \alpha \cdot (\tau_{AV} - \tau_0)} \tag{5.5}$$

$$I_{TH(80ms)} = s \cdot \sqrt{\gamma_{AV} \cdot c \cdot \frac{\tau_2 - \tau_1}{T_{k(80ms)} - T_{k(21ms)}}} \tag{5.6}$$

where:

τ_0	= 50 ^{0}C	ground conductor wire initial temperature (nominal loading conditions).
τ_2	= 250 ^{0}C	ground conductor wire maximum allowed temperature from datasheet [58].
s	= 16 mm^2	ground conductor wire thickness.

c	$= 2.50\ \mathrm{J/(cm^3 \cdot K)}$	copper specific heat.
α	$= 3.9 \cdot 10^{-3}\ \mathrm{K^{-1}}$	copper temperature coefficient.
γ_0	$= 47\ (\mu\Omega \cdot \mathrm{m})^{-1}$	copper conductivity at τ_0.
τ_1		ground conductor wire temp. after $T_{k(21ms)} = 21$ ms.
τ_{AV}		ground conductor wire mean temp. during utility SC contribution [58].
γ_{AV}		copper conductivity at τ_{AV}.

Figure 5.5 marks red area, in which calculated thermal equivalent coordinates for an initial 16 mm^2 grounding conductor wire, where the SC current contributions must be fitted in order to withstand fault conditions.

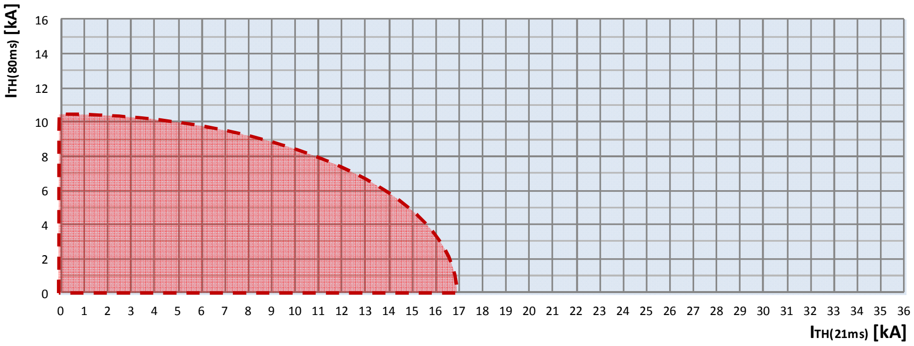

Fig. 5.5. Maximum allowed thermal capability of 16 mm^2 ground conductor.

5.3.2 Circuit Breakers

According to figure 5.6, 24 kV circuit breakers in isolated systems are sized against 3-phase faults and since tripping is made after block mode, breakers must handle only fault currents coming from the utility.

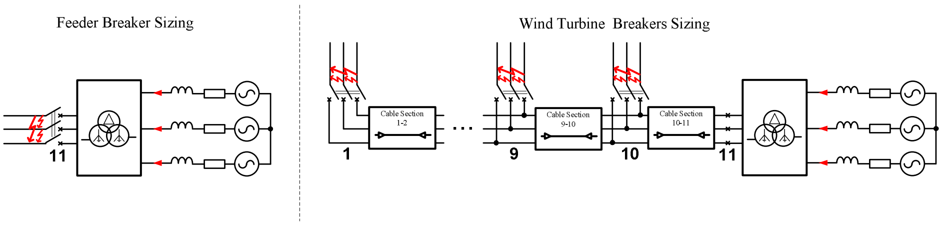

Fig. 5.6. Marked SC current locations for feeder (left) and WTGs (right) circuit breakers sizing.

Rated short circuit breaking current $I_{BRK(80ms)}$ is used as a standard parameter to dimension circuit breakers located at wind turbine and collection feeder terminals. It is composed of the AC component $I_{BRK(AC)}$ and DC component $I_{BRK(DC)}$ at a time of breaker tripping instant. According to IEC standard [70], calculated breaking current $I_{BRK(80ms)}$ is referred to its equivalent consisting of 30% of the DC component for a peak value of the maximum short circuit current equal to $2.5 \cdot I_{SC}$, where $I_{SC} \approx I_{BRK(AC)}$ is rated short time withstand current after $T_{k(80ms)}$ period.

Equation (5.7) is used in order to convert calculated DC component from (5.8) into referred 30% value for its equivalent short circuit breaking current:

$$I_{BRK(80ms)} = I_{BRK(AC)} \cdot \frac{\sqrt{1+2\cdot\left(\frac{I_{BRK(DC)}}{100}\right)^2}}{\sqrt{1+2\cdot\left(\frac{30}{100}\right)^2}} = I_{BRK(AC)} \cdot \frac{\sqrt{1+2\cdot\left(\frac{I_{BRK(DC)}}{100}\right)^2}}{1.086} \qquad (5.7)$$

Percentage ratio of the DC component $I_{BRK(DC)}$ is calculated from:

$$I_{BRK(DC)} = 100 \cdot e^{-\frac{(T_{BRK}+T_R)}{\tau_f}} \qquad (5.8)$$

where:

T_{BRK}	= 60 ms	breaker operating time.
T_R	= 20 ms	relaying time
τ_f		system time constant in form of L/R ratio for fault loop impedance.

Values for rated breaking current [kA] under the maximum short circuit [70]:

6.3	***8***	***10***	***12.5***	***16***	***20***	***25***	***31.5***	***40***	***50***	***63***

5.4 Short-Circuit Analysis of a Single Wind Turbine

As shown in Figure 5.7, the analyzed system includes single wind turbine, single cable PI section, substation transformer and grid. Faults are applied directly at the wind turbine terminals. Fault operating sequence is shown in Table 5.1.

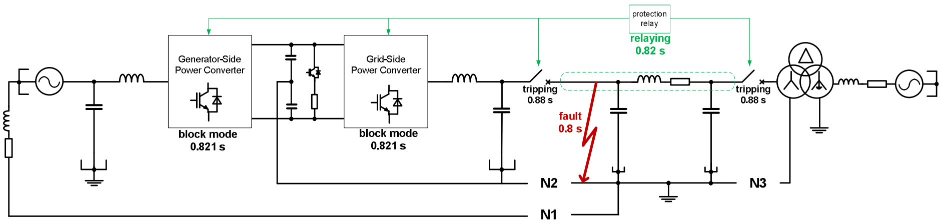

Fig. 5.7. EMTDC/PSCAD time-domain simulations for WTG SC contribution.

Prior to the fault mode, wind turbine extracts the maximum rated power from the wind, which corresponds to the worst-case scenario. During the first cycle of fault occurrence, both wind turbine and the utility contribute to the resulting fault current. During this period, wind turbine operates with full reactive current injection according to the grid code requirements provided by E.ON Netz Grid Code [71].

Table. 5.1. Fault timing sequence and system behaviour for internal feeder faults.

Event	Time [ms]
Internal ground fault within collector feeder network	00.00
Fault detection algorithm detects internal fault within cable system and sends message to all wind turbine units.	20.00
Signals for fault occurrence are received by all operating wind turbines. Block operation of the power converter is initiated	20.00
Wind turbine power converter is in block mode. Wind turbines do not contribute to short circuit current.	21.00
Feeder and wind turbine circuit breakers trip. Utility does not contribute to short-circuit current.	80.00

After the 1st cycle, fault detection mechanism detects an internal fault within the collector feeder network. As a result, block signal is sent to wind turbine converter, which blocks the wind turbine operation by switching off all IGBTs in the converter branches. The block action takes places after 100 µs from the 1st cycle. From this point, only utility supplies fault, and is disconnected by means of the wind turbine and feeder circuit breakers. According to datasheet [72], 24 kV circuit breaker requires 3 cycles to break the short-circuit current, so that fault is cleared after 80 ms from fault occurrence (60 ms interrupting time + 20 ms relaying time).

According to the described fault operating sequence, time domain simulations have been performed with regard to the wind turbine converter design, grounding method and the type of fault. Figures 5.8-5.10 demonstrate measured wind turbine instantaneous currents with an effective grounded configuration 1-1-1. Currents are registered separately at the grid-side converter terminals and at C filter terminals. Both currents are summated in order to obtain the resulting RMS sequence short circuit currents. All current waveforms obtained for each system and grounding mode are available in the Appendix F.

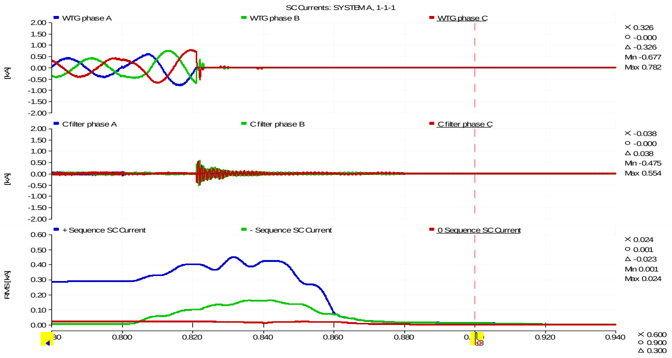

Fig. 5.8. 1-phase to ground fault for system A, grounding mode: 1-1-1

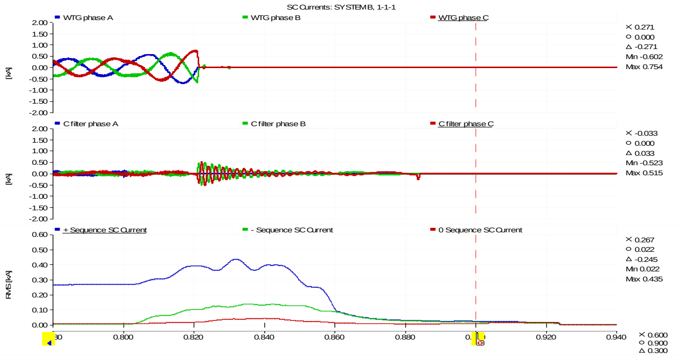

Fig. 5.9. 1-phase to ground fault for system B, grounding mode: 1-1-1

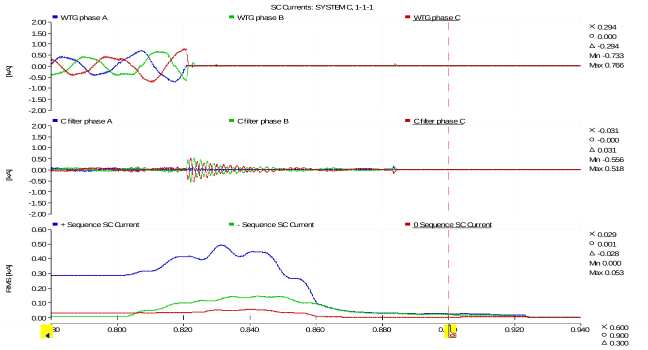

Fig. 5.10. 1-phase to ground fault for system C, grounding mode: 1-1-1

According to the simulation results for grounding 1-1-1, it is observed that systems A, B and C provide similar resulting short circuit current contributions. Pre-fault conditions for all systems remain identical, where nominal currents flow through each wind turbine terminals. Right after the fault occurrence, fault-ride through strategy is initiated. With the compliance to E.ON Netz grid code - apart from pre-fault active current flow, a nominal reactive current is injected, which results in an increased overall current feeding the fault. In other words, both active and reactive currents in 1 pu are injected during the first cycle. In this period, all systems contribute equally to the applied short circuit current.

After the 1st cycle of fault ride through operation, block mode is initiated by switching off all the existing IGBTs within the converter circuitry. Converters in systems A, B and C instantly break phase currents, which results in solid short circuit of the parallel C filter branches. As a result, C filter capacitors discharge and release its energy into the fault. Due to lack of series resistance in fault commutation path, discharging current takes form of a damped oscillations with a resonant frequency f_{res}, which is driven by the series connection of the LC elements. In case of system A with

MMC topology, lower oscillations occur due to smaller C filter that is necessary to suppress dv/dt effect.

During block mode - which lasts for 3 cycles, total energy dissipates from the C filter. Finally, WTG breaker trips and disconnects the wind turbine under no loading conditions.

RMS symmetrical sequence current components are obtained by FFT transform of the instantaneous values I_{abc}_WTG. The obtained phase current harmonics are transformed into the sequence component harmonics with a symmetrical transformation matrix (FFT block). The transformed sequence component harmonics are converted into an instantaneous sinusoidal values with an inverse FFT block and summated, as shown in Figure 5.11.

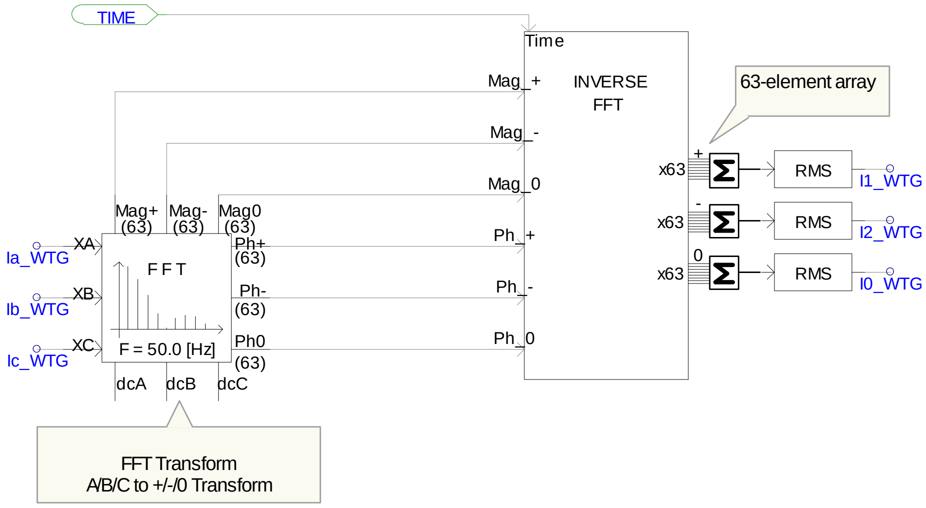

Fig. 5.11. Implemented EMTDC/PSCAD tool for the extraction and RMS computation of the symmetrical sequence component currents.

Finally, the RMS values are calculated for the instantaneous sequence currents I_{120}_WTG. Obtained maximum RMS sequence current values over the entire short circuit period are the representation of wind turbine short circuit current contribution. With this method, calculated final RMS values observed in Figure 5.10 are delayed by 2 cycles (40 ms) to the referred time frame.

According to the described methodology, derived maximum RMS sequence currents for each grounding configuration and for each wind turbine topology are presented in form of radar graphs in Figure 5.12. Among different converter circuitries, it is visible that system A (MMC) provides the minimum short circuit current contribution for any type of fault and for most grounding configurations. On the other hand, system B (NPC-3L) injects the highest short circuit currents for most grounding configurations. This can be explained by means of the DC link capacitance required for the system B, which significantly lowers the resulting wind turbine zero sequence impedance.

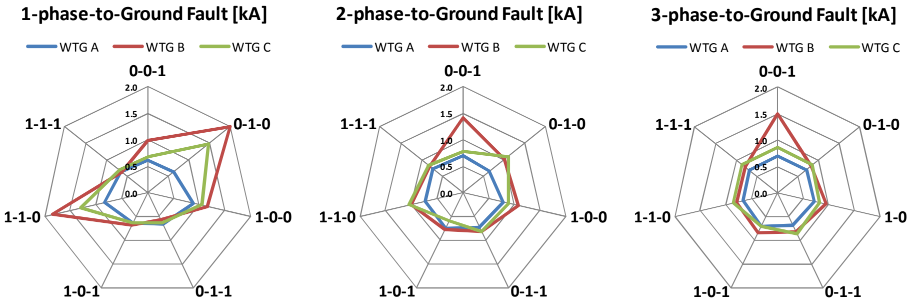

Fig. 5.12. Resulting WTG SC current contributions for different grounding modes.

Figure 5.13 presents an example of the SC current commutation path in healthy phase through common DC link capacitance for each system. It is observed that by blocking MMC cells, SC current by-passes all cell capacitances and flows only through cell diodes and small harmonic common DC link capacitor $C_{DC(MMC)}$. According to the results from 5.12, MMC feature of having the cascaded DC link instead of the common one leads to the lowest resulting SC loop impedance among the other grid-side converter topologies.

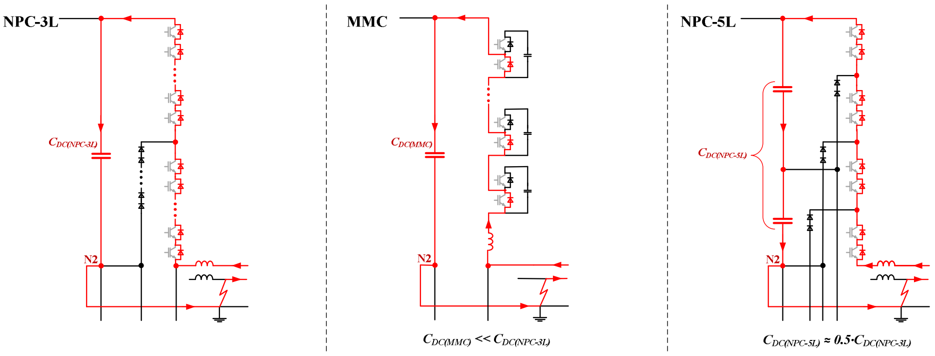

Fig. 5.13. SC current commutation path for 0-1-0 grounding mode in a 1-phase fault.

Due to its lowest short circuit current contribution, system A is selected for further investigation of optimal grounding scheme over the entire feeder network.

For phasor-domain modelling, measured maximum RMS short circuit current contribution used as an input parameter is shown in form of current symmetrical sequence components in Figure 5.14. Due to the negligible zero sequence component for a symmetrical 3-phase fault, thermal loading of ground conductor wires is analyzed only with regard to the 1-phase and 2-phase fault types.

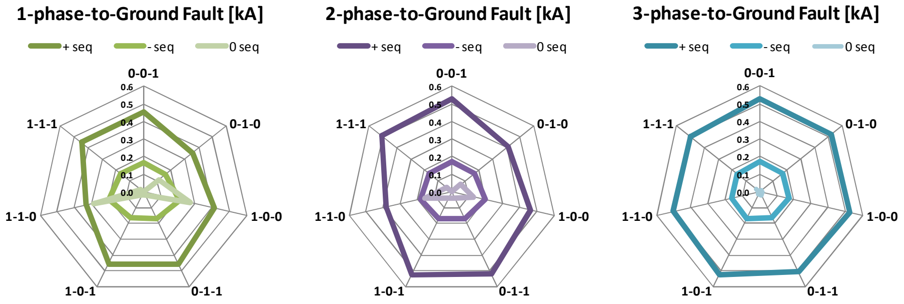

Fig. 5.14. System A, WTG SC current contributions for different grounding modes.

5.5 Short-Circuit Analysis of a Single Collector Feeder

Figure 5.15 presents a collector feeder model, which is used for the short circuit analysis in the phasor domain. Collector feeder system is modelled with a parameter values according to Tables 3.10-3.12. Wind turbines are represented either as controlled current sources with values obtained from Figure 5.14 (wind turbine short circuit contribution), or with sequence impedances (utility short circuit contribution).

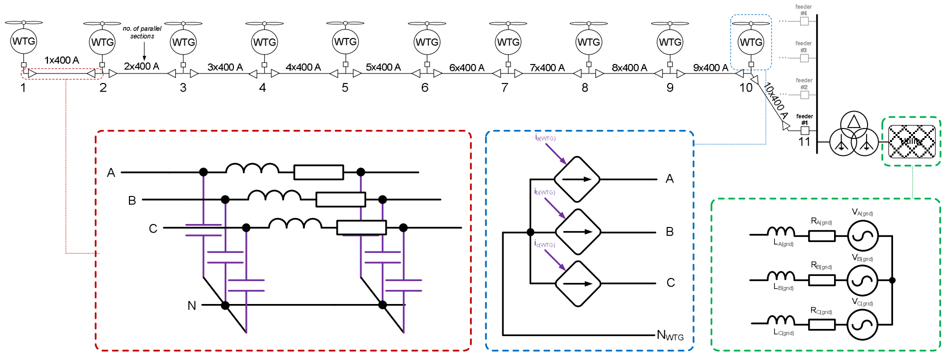

Fig. 5.15. Collector feeder system representation for the frequency-domain analysis.

In order to simplify short circuit calculations, each contribution is analyzed separately. Final short circuit current distribution across grounding wires is obtained with superposition of the short circuit current coming from the utility, adjacent feeders, and wind turbines located on the faulted feeder.

5.5.1 Utility Short Circuit Current Contribution

Schematic representation of the analyzed circuit is presented in Figure 5.16. Wind turbine and substation transformer neutrals are grounded according to the examined grounding configuration.

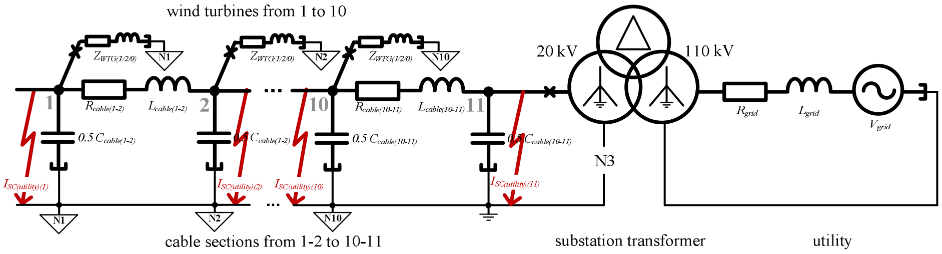

Fig. 5.16. Impedance network model for the utility short circuit current contribution.

According to figures 5.15-5.16, following statements are derived:

- Maximum ground fault currents will flow during asymmetrical ground faults: 1-phase-to-ground or 2-phase-to-ground faults, where positive and negative sequence currents contribute to the ground current.
- For systems with opened utility ground path, maximum phase short circuit currents will flow during 3-phase faults. Therefore, circuit breakers will be sized for 3-phase SC currents when N3 point is isolated (grounding configurations 1-1-0; 1-0-0; 0-1-0; 0-0-0).

According to the statements above, sequence circuit diagrams are derived for: 1-phase-to-ground (Fig. 5.17a), 2-phase-to-ground (Fig. 5.17b) and 3-phase-to-ground (Fig 5.17c). The diagrams include resulting impedances consisting of cable PI sections Z_{cable}, wind turbines impedances Z_{WTG}, transformer impedance Z_{trafo}, transformed grid impedance Z_{grid} and grid voltage V_{grid}.

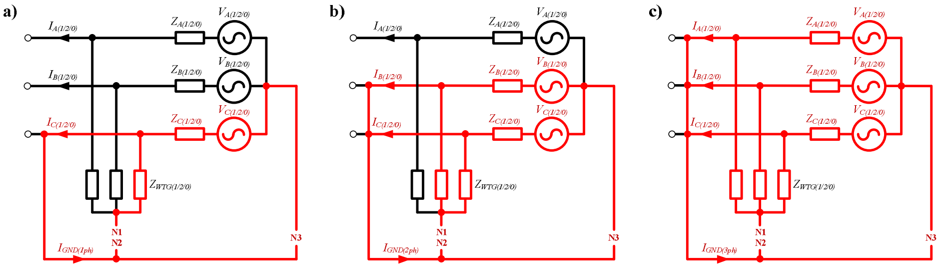

Fig. 5.17. Resulting impedance network models for different ground fault types.

Due to embedded tertiary delta winding of the substation transformer, it is assumed that the zero sequence grid impedance $Z_{grid(0)}$ does not influence analyzed system. Resulting sequence impedances are calculated from:

$$Z_1 = \left[\left(Z_{ABC(1)}\right)^{-1} + \left(Z_{WTG(1)}\right)^{-1}\right]^{-1} = \left[\left(Z_{cable(1)} + Z_{trafo(1)} + Z_{grid(1)}\right)^{-1} + \left(Z_{WTG(1)}\right)^{-1}\right]^{-1} \tag{5.9}$$

$$Z_2 = \left[\left(Z_{cable(2)} + Z_{trafo(2)} + Z_{grid(2)}\right)^{-1} + \left(Z_{WTG(2)}\right)^{-1}\right]^{-1} \tag{5.10}$$

$$Z_0 = \left[\left(Z_{cable(0)} + Z_{trafo(0)}\right)^{-1} + \left(Z_{WTG(0)}\right)^{-1}\right]^{-1} \tag{5.11}$$

In order to provide accurate values for sequence impedances of a mutually coupled substation transformer and wind turbine model, an impedance scan is made through detailed EMTDC/PSCAD time-domain simulations under its normal operation. It is therefore expected that the transformer core is dimensioned to avoid saturation effect during the short circuit period and wind turbine converters are in block mode. Resulting parameter values for all sequence impedances used for short circuit modelling are provided in Table 5.2.

Table. 5.2. Sequence impedance values for symmetrical component analysis

Component	Positive Sequence	Negative Sequence	Zero Sequence
single cable section*	$Z_{cable(1)} = 29.454\ m\Omega$	$Z_{cable(2)} = 29.454\ m\Omega$	$Z_{cable(0)} = 9.818\ m\Omega$
wind turbine (WTG)**	$Z_{WTG(1)} = 0.5 \cdot 10^{-6} + j2$	$Z_{WTG(2)} = 0.5 \cdot 10^{-6} + j2$	$Z_{WTG(0)(1\text{-}1)} = 0.125 \cdot 10^{-4} - j7.09$ $Z_{WTG(0)(1\text{-}0)} = 0.118 \cdot 10^{-1} + j6.93$ $Z_{WTG(0)(0\text{-}1)} = 0.272 \cdot 10^{-4} - j128.14$ $Z_{WTG(0)(0\text{-}0)} = \infty$
transformer ($\underline{M} = j0.675\ \Omega$)	$Z_{trafo(1)} = 80.399\ m\Omega$	$Z_{trafo(2)} = 80.399\ m\Omega$	$Z_{trafo(0)(1)} = 79.418\ m\Omega$ $Z_{trafo(0)(0)} = \infty$
transformed grid (20 kV level)	$Z_{grid(1)} = 2\ \Omega$	$Z_{grid(2)} = 2\ \Omega$	-

* all cable sections in feeder have identical design, and are connected in parallel in order to maintain required current ratings.

** values for wind turbine impedances are provided only as a part of complete methodology description. In this work, the worst-case scenario is examined, which assumes that all wind turbines are disconnected, i.e. $Z_{WTG} = \infty$.

AC components of ground RMS short circuit currents $I_{GND(AC)}$ constitute triple zero sequence currents, and are calculated according to the equations (5.12-5.13) derived from Figure 5.18a, b ($c_{max} = 1.1$). Maximum RMS value for 3-phase short circuit $I_{SC(AC)}$ is calculated from (5.14) according to Figure 5.18c.

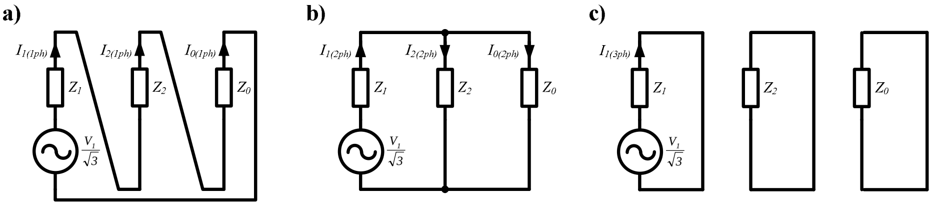

single phase to ground fault

two phase to ground fault

three phase to ground fault

Fig. 5.18. Symmetrical sequence component method for the SC analysis.

$$I_{SC(3ph)(AC)} = I_{1(3ph)} = \frac{c_{max} \cdot V_1}{\sqrt{3} \cdot Z_1} \tag{5.12}$$

$$I_{GND(1ph)(AC)} = 3 \cdot I_{0(1ph)} = 3 \cdot \frac{c_{max} \cdot V_1}{\sqrt{3} \cdot \left(Z_1 + Z_2 + Z_0\right)} \tag{5.13}$$

$$I_{GND(2ph)(AC)} = 3 \cdot I_{0(2ph)} = 3 \cdot \frac{c_{max} \cdot V_1 \cdot Z_2}{\sqrt{3} \cdot \left(Z_1 \cdot Z_2 + Z_1 \cdot Z_0 + Z_2 \cdot Z_0\right)} \tag{5.14}$$

Figure 5.19 shows AC component distribution of the maximum SC currents for the circuit breaker dimensioning**. In this analysis, it is further assumed, that worst case scenario applies, where all wind turbines remain disconnected from the feeder before fault occurrence ($Z_{WTG(1)} = Z_{WTG(2)} = Z_{WTG(0)} \rightarrow \infty$).**

In case of a ground short circuit current $I_{GND(utility)(AC)}$ used for ground conductors sizing, results include systems with both grounded and isolated utility neutral, as shown in Figure 5.20.

According to the results, circuit breakers located at each terminal shall be sized against asymmetrical ground faults for the utility grounded systems, and against 3-phase symmetrical faults for the utility isolated systems.

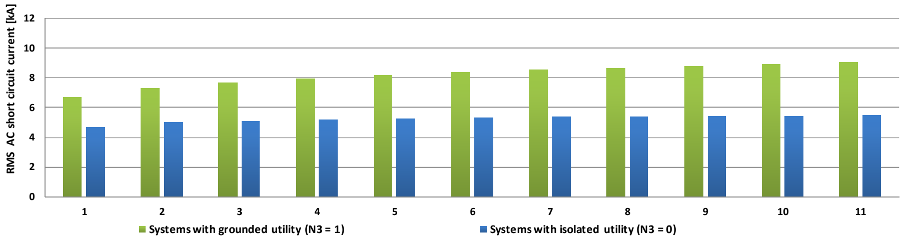

Fig. 5.19. AC component of the SC current measured at each circuit breaker poles.

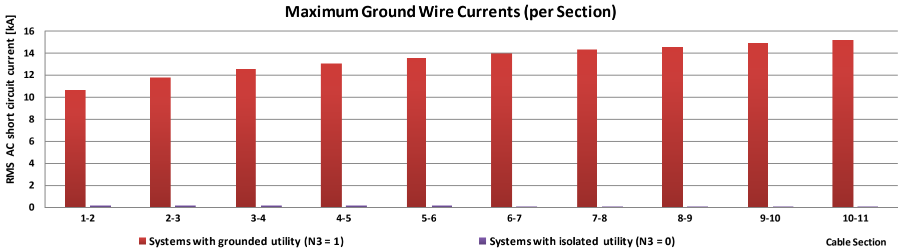

Fig. 5.20. Measured AC component of the SC ground current flowing through grounding conductor in each section.

5.5.2 Wind Turbine Short Circuit Current Contribution

Each wind turbine current contribution is represented as a sequence current source with values from Figure 5.14, obtained from time-domain simulations of a detailed wind turbine model. Input values differ according to the examined grounding configuration and type of fault.

As wind turbines do not contribute to the short circuit after switched to block mode, the wind turbine short circuit contribution is analyzed only with regard to the grounding wire dimensioning. In this manner, only the most critical 1-phase and 2-phase ground fault currents are analyzed. Ground current contribution coming from 3 phase to ground faults is negligible (below 2%) of the nominal line currents due to its symmetrical characteristics.

Schematic representation of the analyzed circuit is presented in Figure 5.21. Wind turbine and substation transformer neutrals are grounded according to the examined grounding configuration.

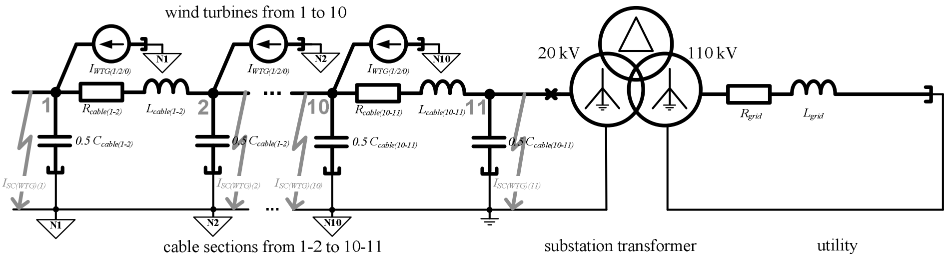

Fig. 5.21. Impedance network model for the wind turbines SC current contribution.

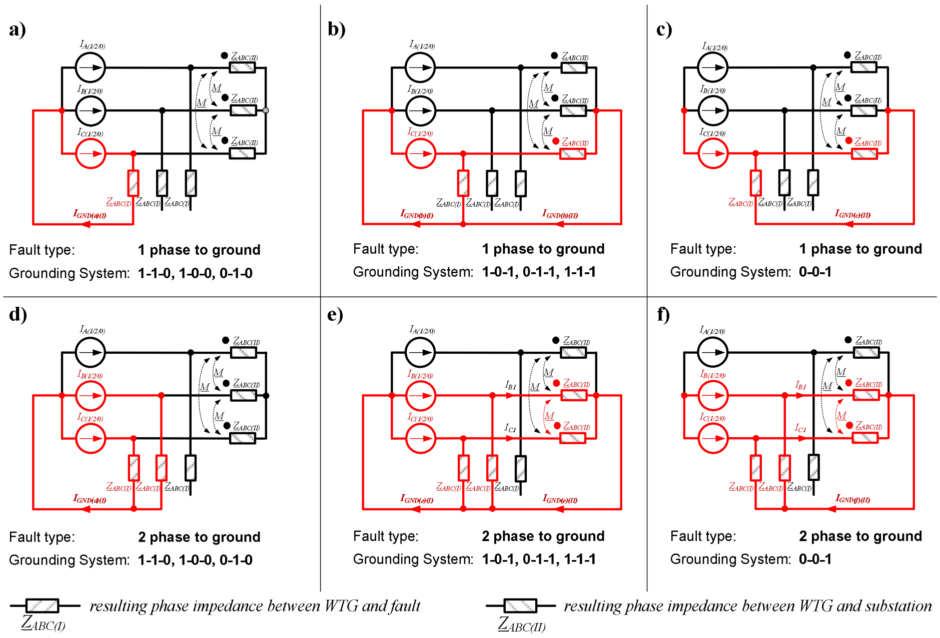

a) Fault type: **1 phase to ground**; Grounding System: **1-1-0, 1-0-0, 0-1-0**

b) Fault type: **1 phase to ground**; Grounding System: **1-0-1, 0-1-1, 1-1-1**

c) Fault type: **1 phase to ground**; Grounding System: **0-0-1**

d) Fault type: **2 phase to ground**; Grounding System: **1-1-0, 1-0-0, 0-1-0**

e) Fault type: **2 phase to ground**; Grounding System: **1-0-1, 0-1-1, 1-1-1**

f) Fault type: **2 phase to ground**; Grounding System: **0-0-1**

Fig. 5.22. Resulting impedance network models for different ground fault types.

Due to the mutual coupling of the substation transformer, standard circuit laws are applied to calculate the maximum ground short circuit current contributions coming from each wind turbine. Figure 5.22 shows 6 derived circuitries, where fault loop differs with regard to the applied grounding scheme and fault type. Table 5.3 lists derived formulas for maximum ground current contribution $I_{GND(WTG)(AC)}$.

Table. 5.3. Ground current contribution formulas for the SC analysis.

Drawing on Fig. 5.22	**Mathematical Formulas for Calculating Ground Current I_{GND}**	
a)	$\underline{I}_{GND(a)(I)} = \underline{I}_{A(1\|2\|0)} + \underline{I}_{B(1\|2\|0)} + \underline{I}_{C(1\|2\|0)}$	(5.15)
b)	$\underline{I}_{GND(b)(I)} = \underline{I}_{A(1\|2\|0)} + \underline{I}_{B(1\|2\|0)} + \underline{I}_{C(1\|2\|0)}$	(5.16)
	$\underline{I}_{GND(b)(II)} = \underline{I}_{A(1\|2\|0)} - \frac{1}{\underline{Z}_{ABC\ (II)}+\underline{Z}_{ABC\ (I)}} \cdot \left(\underline{I}_{A(1\|2\|0)} \cdot \frac{\underline{Z}_{ABC\ (II)}}{\underline{Z}_{ABC\ (I)}} + \underline{I}_{B(1\|2\|0)} \cdot \frac{\underline{M}}{\underline{Z}_{ABC\ (I)}} + \underline{I}_{C(1\|2\|0)} \cdot \frac{\underline{M}}{\underline{Z}_{ABC\ (I)}}\right) + \underline{I}_{B(1\|2\|0)} + \underline{I}_{C(1\|2\|0)}$	(5.17)
c)	$\underline{I}_{GND(c)(II)} = -\left(\underline{I}_{A(1\|2\|0)} \cdot \underline{Z}_{ABC(II)} + \underline{I}_{B(1\|2\|0)} \cdot \underline{M} + \underline{I}_{C(1\|2\|0)} \cdot \underline{M}\right) \cdot \frac{1}{\underline{Z}_{ABC\ (II)}+\underline{Z}_{ABC\ (I)}}$	(5.18)
d)	$\underline{I}_{GND(d)(I)} = \underline{I}_{A(1\|2\|0)} + \underline{I}_{B(1\|2\|0)} + \underline{I}_{C(1\|2\|0)}$	(5.19)
e)	$\underline{I}_{B1} = \left[\underline{I}_{A(1\|2\|0)} \cdot \underline{M} - \frac{\left(\underline{I}_{A(1\|2\|0)} \cdot \underline{Z}_{ABC\ (II)} + \underline{I}_{B(1\|2\|0)} \cdot \underline{M} + \underline{I}_{C(1\|2\|0)} \cdot \underline{M}\right) \cdot \underline{M}}{\underline{Z}_{ABC\ (II)}+\underline{Z}_{ABC\ (I)}} + \underline{I}_{B(1\|2\|0)} \cdot \underline{Z}_{ABC(II)} + \underline{I}_{C(1\|2\|0)} \cdot \underline{M}\right] \cdot \left[\underline{Z}_{ABC(I)} + \underline{Z}_{ABC(II)} - \frac{\underline{M}^2}{\underline{Z}_{ABC\ (I)}+\underline{Z}_{ABC\ (II)}}\right]^{-1}$	(5.20)
	$\underline{I}_{GND(e)(II)} = \underline{I}_{A(1\|2\|0)} + \underline{I}_{B(1\|2\|0)} + \underline{I}_{C(1\|2\|0)} - \underline{I}_{C1} - \underline{I}_{B1}$	(5.21)
	$\underline{I}_{GND(e)(II)} = \underline{I}_{A(1\|2\|0)} + \underline{I}_{B(1\|2\|0)} + \underline{I}_{C(1\|2\|0)} - \underline{I}_{C1} - \underline{I}_{B1}$	(5.22)
	$\underline{I}_{GND(e)(I)} = \underline{I}_{A(1\|2\|0)} + \underline{I}_{B(1\|2\|0)} + \underline{I}_{C(1\|2\|0)}$	(5.23)
f)	$\underline{I}_{B1} = \left[\underline{I}_{A(1\|2\|0)} \cdot \underline{M} + \underline{I}_{B(1\|2\|0)} \cdot \underline{Z}_{ABC(II)} + \underline{I}_{C(1\|2\|0)} \cdot \underline{M} - \left(\underline{I}_{A(1\|2\|0)} \cdot \underline{Z}_{ABC(II)} + \underline{I}_{B(1\|2\|0)} \cdot \underline{M} + \underline{I}_{C(1\|2\|0)} \cdot \underline{M}\right)\right] \cdot \left[\underline{Z}_{ABC(I)} + \underline{Z}_{ABC(II)} - \frac{\underline{M}^2}{\underline{Z}_{ABC\ (I)}+\underline{Z}_{ABC\ (II)}}\right]^{-1}$	(5.24)
	$\underline{I}_{C1} = \left(\underline{I}_{A(1\|2\|0)} \cdot \underline{Z}_{ABC(II)} + \underline{I}_{B(1\|2\|0)} \cdot \underline{M} + \underline{I}_{C(1\|2\|0)} \cdot \underline{M} - \underline{I}_{B1(1\|2\|0)} \cdot \underline{M}\right) \cdot \frac{1}{\underline{Z}_{ABC\ (II)}+\underline{Z}_{ABC\ (I)}}$	(5.25)
	$\underline{I}_{GND(f)(II)} = -\left(\underline{I}_{C1} + \underline{I}_{B1}\right)$	(5.26)

Distribution of the obtained ground short circuit currents $I_{GND(WTG)(AC)}$ flowing through ground conductors in each section is presented in Figures 5.23, 5.24. The lowest ground currents are obtained for grounding configuration 0-1-0 both in case of 1-phase-to-ground and 2-phase-to-ground faults.

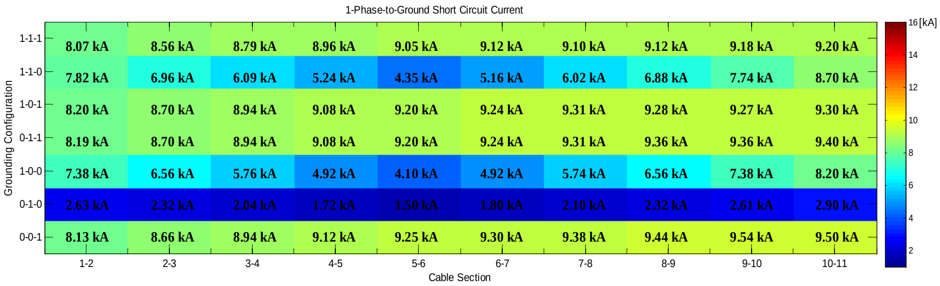

	1-2	2-3	3-4	4-5	5-6	6-7	7-8	8-9	9-10	10-11
1-1-1	8.07 kA	8.56 kA	8.79 kA	8.96 kA	9.05 kA	9.12 kA	9.10 kA	9.12 kA	9.18 kA	9.20 kA
1-1-0	7.82 kA	6.96 kA	6.09 kA	5.24 kA	4.35 kA	5.16 kA	6.02 kA	6.88 kA	7.74 kA	8.70 kA
1-0-1	8.20 kA	8.70 kA	8.94 kA	9.08 kA	9.20 kA	9.24 kA	9.31 kA	9.28 kA	9.27 kA	9.30 kA
0-1-1	8.19 kA	8.70 kA	8.94 kA	9.08 kA	9.20 kA	9.24 kA	9.31 kA	9.36 kA	9.36 kA	9.40 kA
1-0-0	7.38 kA	6.56 kA	5.76 kA	4.92 kA	4.10 kA	4.92 kA	5.74 kA	6.56 kA	7.38 kA	8.20 kA
0-1-0	2.63 kA	2.32 kA	2.04 kA	1.72 kA	1.50 kA	1.80 kA	2.10 kA	2.32 kA	2.61 kA	2.90 kA
0-0-1	8.13 kA	8.66 kA	8.94 kA	9.12 kA	9.25 kA	9.30 kA	9.38 kA	9.44 kA	9.54 kA	9.50 kA

Fig. 5.23. Distribution of grounding wire currents under 1-phase ground faults.

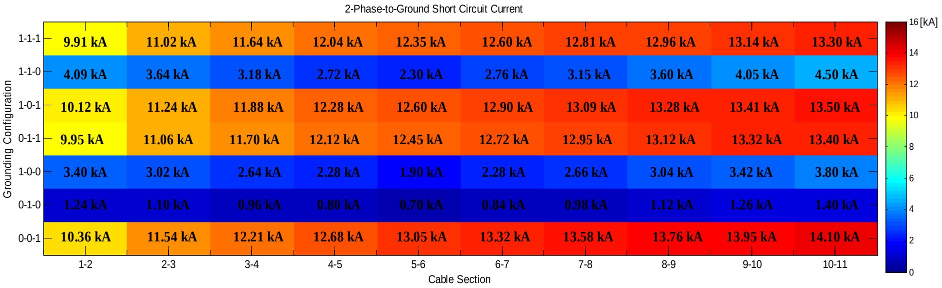

	1-2	2-3	3-4	4-5	5-6	6-7	7-8	8-9	9-10	10-11
1-1-1	9.91 kA	11.02 kA	11.64 kA	12.04 kA	12.35 kA	12.60 kA	12.81 kA	12.96 kA	13.14 kA	13.30 kA
1-1-0	4.09 kA	3.64 kA	3.18 kA	2.72 kA	2.30 kA	2.76 kA	3.15 kA	3.60 kA	4.05 kA	4.50 kA
1-0-1	10.12 kA	11.24 kA	11.88 kA	12.28 kA	12.60 kA	12.90 kA	13.09 kA	13.28 kA	13.41 kA	13.50 kA
0-1-1	9.95 kA	11.06 kA	11.70 kA	12.12 kA	12.45 kA	12.72 kA	12.95 kA	13.12 kA	13.32 kA	13.40 kA
1-0-0	3.40 kA	3.02 kA	2.64 kA	2.28 kA	1.90 kA	2.28 kA	2.66 kA	3.04 kA	3.42 kA	3.80 kA
0-1-0	1.24 kA	1.10 kA	0.96 kA	0.80 kA	0.70 kA	0.84 kA	0.98 kA	1.12 kA	1.26 kA	1.40 kA
0-0-1	10.36 kA	11.54 kA	12.21 kA	12.68 kA	13.05 kA	13.32 kA	13.58 kA	13.76 kA	13.95 kA	14.10 kA

Fig. 5.24. Distribution of grounding wire currents under 2-phase ground faults.

After calculating the short circuit current contributions coming from the utility and from the wind turbines, all analyzed grounding configurations can be compared by means of:

- required mean thickness of the grounding conductor wire per length,
- required ratings of circuit breakers for wind turbine and feeder protection.

5.6 Comparison of Grounding Systems

5.6.1 Minimum Ratings of Circuit Breakers

Maximum breaking currents are calculated according to (5.7) supported by the results from Figure 5.19. Table 5.4 provides data for all selected circuit breakers in each terminal 1-11. Systems with isolated neutral of the substation transformer require the lowest specified ratings of a 6.3 kA circuit breakers in each terminal.

Table. 5.4. Circuit breaker ratings for terminals 1-11.

	$I_{BRK(80ms)}$ for N3 = 1										
Terminal	**1**	**2**	**3**	**4**	**5**	**6**	**7**	**8**	**9**	**10**	**11**
$I_{BRK(80ms)}$ [kA]	7.41	7.73	7.89	8.02	8.12	8.21	8.29	8.37	8.44	8.51	8.58
$I_{BRK(NOM)}$ [kA]	**8**	**8**	**8**	**10**	**10**	**10**	**10**	**10**	**10**	**10**	**10**
	$I_{BRK(80ms)}$ for N3 = 0										
Terminal	**1**	**2**	**3**	**4**	**5**	**6**	**7**	**8**	**9**	**10**	**11**
$I_{BRK(80ms)}$ [kA]	5.25	5.31	5.23	5.22	5.21	5.21	5.20	5.20	5.20	5.20	5.21
$I_{BRK(NOM)}$ [kA]	**6.3**	**6.3**	**6.3**	**6.3**	**6.3**	**6.3**	**6.3**	**6.3**	**6.3**	**6.3**	**6.3**

5.6.2 Minimum Grounding Wire Thickness per Length

Grounding conductor wires in each section must withstand maximum fault currents, which are represented as thermal equivalents I_{TH} according to equation:

$$I_{TH} = \sqrt{\frac{\int_{0}^{T_k} (i_{AC} + i_{DC})^2 \, dt}{T_k}} \quad \leftarrow Joule's\ Integral \tag{5.27}$$

The resulting thermal equivalents I_{TH}, which come from the utility and the interconnected wind turbine short circuit current contributions, are calculated from [69]:

$$I_{TH(21ms)} = \sqrt{\left(I_{GND(WTG)(AC)} + I_{GND(utility)(AC)}\right)^2 + \left(\sqrt{m_{(0|21ms)}} \cdot I_{GND(utility)(AC)}\right)^2} \tag{5.28}$$

$$I_{TH(80ms)} = \sqrt{1+m_{(21ms|80ms)}} \cdot I_{GND(utility)(AC)} \tag{5.29}$$

Heat effect factor $m_{(Tk1|Tk2)}$ reflects the share between AC and DC components over the resulting thermal equivalent $I_{TH(Tk2)}$. It is related to fault loop impedance Z_f modelled with time constant τ_f. Heat effect factor m is calculated from:

$$m_{(Tk1|Tk2)} = \int_{T_{k1}}^{T_{k2}} \left(\frac{i_{GND(utility)(DC)}}{i_{GND(utility)(AC)}} \right)^2 dt = \frac{\tau_f}{T_{k2}-T_{k1}} \cdot \left[exp\left(-\frac{2 \cdot T_{k1}}{\tau_f} \right) - exp\left(-\frac{2 \cdot T_{k2}}{\tau_f} \right) \right] \tag{5.30}$$

$$\tau_{f(1ph)} = \frac{X_{f(1ph)}}{\omega \cdot R_{f(1ph)}} = \frac{Img\{Z_1+Z_2+Z_0\}}{\omega \cdot Real\{Z_1+Z_2+Z_0\}} \tag{5.31}$$

$$\tau_{f(2ph)} = \frac{X_{f(2ph)}}{\omega \cdot R_{f(2ph)}} = \frac{Img\left\{ \frac{Z_1 \cdot Z_2 + Z_1 \cdot Z_0 + Z_2 \cdot Z_0}{Z_2} \right\}}{\omega \cdot Real\left\{ \frac{Z_1 \cdot Z_2 + Z_1 \cdot Z_0 + Z_2 \cdot Z_0}{Z_2} \right\}} \tag{5.32}$$

The resulting thermal equivalents are calculated separately for periods when both wind turbines and the utility operate, and when only utility remains operational. According to detailed time domain simulations, zero sequence alternating current controller of the wind turbine converter practically eliminates the DC component from the overall short circuit current provided by the turbine. As a consequence, DC component is only included as a part of the short circuit current coming from the utility.

Results of the calculated thermal equivalents for different ground faults in systems with a single feeder are presented in Figures 5.25 and 5.26. The maximum allowable operating area (marked red) for initial 16 mm^2 wire thickness is imposed from figure 5.5. Graphs show, that systems with grounded N3 neutral require increased thickness of 16 mm^2 ground wires to withstand fault conditions.

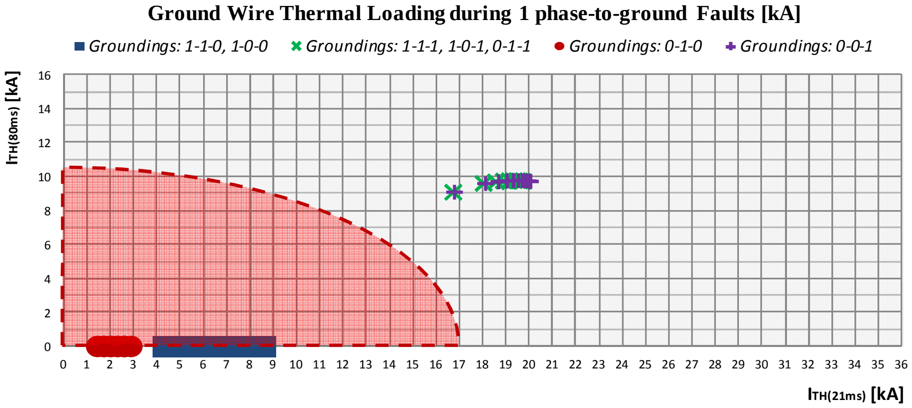

Fig. 5.25. Calculated resulting thermal equivalents of ground wires for 1-phase faults.

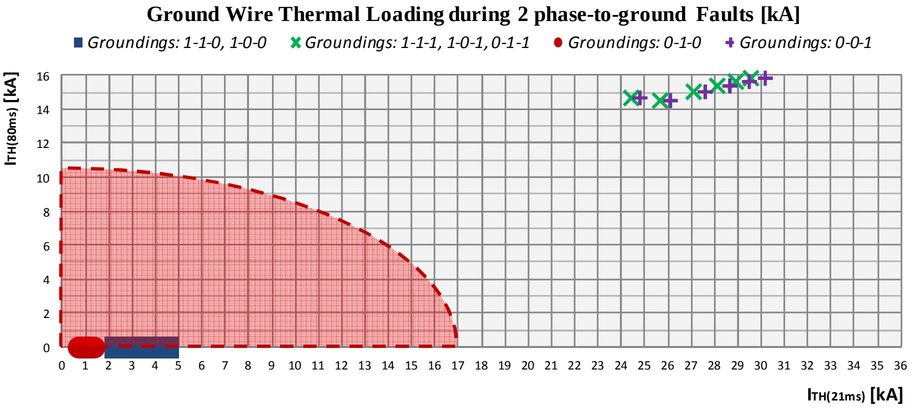

Fig. 5.26. Calculated resulting thermal equivalents of ground wires for 2-phase faults.

Finally, Table 5.5 provides the required mean thickness per length of a grounding conductor wire for each single feeder with regard to the number of interconnected feeders and grounding configurations. Grounding 0-1-0 requires minimum amount of copper, and allows interconnecting 5 non-isolated feeders while equipped only with a 16 mm^2 grounding wire for each section.

A conventional system REF with galvanically isolated turbines is added as a reference, which is grounded solely by the substation transformer. In system REF equipped with feeder zig-zag transformers, only utility contributes to the ground fault.

Table. 5.5. Required mean thickness of copper for each applied grounding mode.

Grounding	**1-1-1**	**1-0-1**	**0-1-1**	**0-0-1**	**1-1-0**	**1-0-0**	**0-1-0**	**REF**
	Mean thickness per length [mm^2 / km]							
Nominal thickness	16							
1 Feeder	40	40	40	40	16	16	16	26
2 Feeders	48	48	48	50	18	18	16	26
3 Feeders	58	58	58	62	26	26	16	26
4 Feeders	70	70	70	74	34	34	16	26
5 Feeders	82	82	82	86	42	42	16	26

According to the results obtained from the short circuit analysis, selected system for final evaluation is wind turbine A (Back-to-Back MMC) with grounding configuration 0-1-0. Final evaluation includes analysis of the fault detection operating algorithm over the collector feeder network with a single connected wind turbine. Detailed time domain simulations are performed in EMTDC/PSCAD software, which include complex wind turbine and protection relay models. Simulations are necessary to provide information whether the selected grounding will provide sufficient sensitivity and selectivity of the proposed fault detection mechanism.

5.7 Line Differential Current Fault Detection Scheme

Proposed primary protection of the collector feeder network is line differential scheme, which provides absolute selectivity over the specified protection zone established between terminals 1 and 11, as shown in Figure 5.27. Proposed differential relay measures and summates instantaneous input phase current signals from each terminal 1-10, and compares its resulting value with the output current leaving terminal 11. If the difference between measured signals i_{diff} is above the established differential threshold, then tripping logic signal is sent to power converter and circuit breakers.

In order to simplify analysis of the proposed fault detection scheme, saturation effect of current transformers during short circuit is neglected in a similar manner as for the substation transformer.

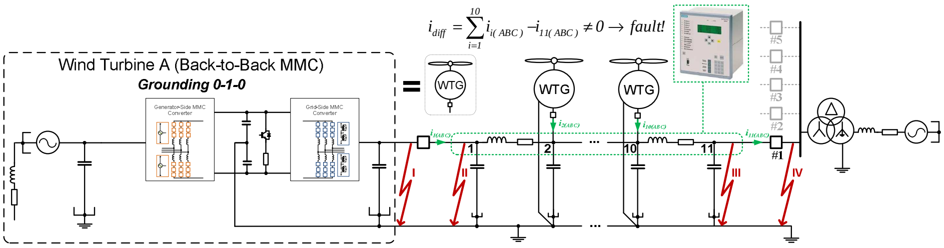

Fig. 5.27. System schematic representation for the validation of the differential fault detection scheme.

The proposed relay model is based on Siemens SIPROTEC 4 [73], and EMTDC/PSCAD time domain modelling approach is derived directly from experimentally validated model in [74]. Input parameters for the relay settings are provided in Table 5.6 according to the methodology presented in [75]. Validation of the proposed concept includes selectivity check by applying faults at locations I-IV. Relay should trip only during internal faults II and III.

Operating speed of the applied detection methods is registered, which should be below T_R = 20 ms. Sensitivity is examined by applying high resistive internal faults, which relay can still detect. In order to minimize risk for false tripping during external faults in real conditions, simulations include wind turbine operating with active and reactive current injection schemes according to the fault ride through requirements.

Table. 5.6. Relay input settings for differential short circuit protection [73].

Parameter	Value	Parameter	Value
Relay $P1$ setting	1.10	Pick-up value for phasor $I_{diff>ON}$	0.2
Relay $P2$ setting	0.03	Pick-up value for charge $I_{diff>>ON}$	0.05
Relay $P3$ setting	0.10	Seal-in time T_d	100 ms
Minimum differential current $I_{diff>}$	0.0118	Inrush restraint ratio γ_{inrush}	15 %
Minimum differential charge $I_{diff>>}$	0.05	Maximum inrush peak $I_{inrush(MAX)}$	16.13 A

On the basis of [74], 2 independent fault detection algorithms are implemented: phasor comparison I_{DIFF} and charge comparison Q_{DIFF}. Relay detects fault state between 0.8-0.9 s with the differential thresholds represented by restraint values: I_{res_phasor} and I_{res_charge} , which should be below measured differential values: accordingly I_{op_phasor} and I_{op_charge}. Figures 6.27-6.30 show registered parameter values for 1-phase, 2-phase and 3-phase faults at each I-IV terminal.

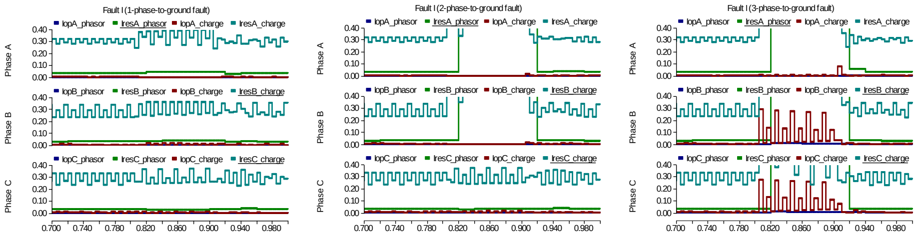
Fault I (1-phase-to-ground fault)
Fault I (2-phase-to-ground fault)
Fault I (3-phase-to-ground fault)

Fig. 5.28. Operational I_{op} and restraint I_{res} parameter values for fault at terminal I.

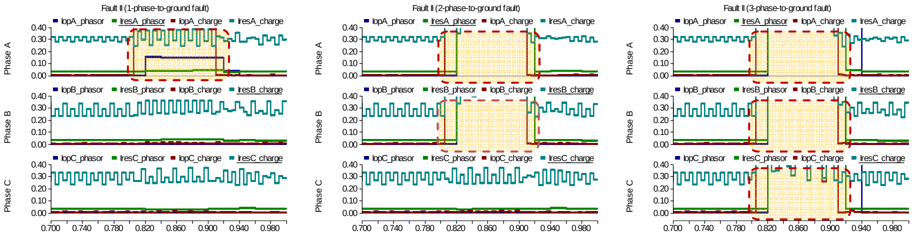
Fault II (1-phase-to-ground fault)
Fault II (2-phase-to-ground fault)
Fault II (3-phase-to-ground fault)

Fig. 5.29. Operational I_{op} and restraint I_{res} parameter values for fault at terminal II.

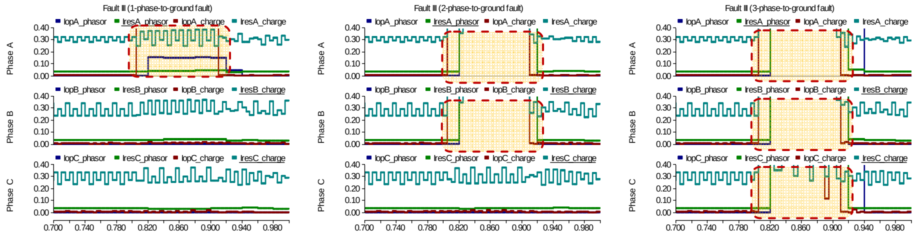
Fault III (1-phase-to-ground fault)
Fault III (2-phase-to-ground fault)
Fault III (3-phase-to-ground fault)

Fig. 5.30. Operational I_{op} and restraint I_{res} parameter values for fault at terminal III.

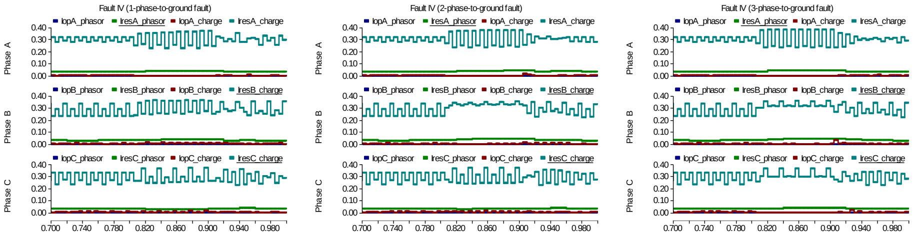
Fault IV (1-phase-to-ground fault)
Fault IV (2-phase-to-ground fault)
Fault IV (3-phase-to-ground fault)

Fig. 5.31. Operational I_{op} and restraint I_{res} parameter values for fault at terminal IV.

It is clearly seen that the differential values I_{op} are exceeding the restraint ones I_{res} for each type of fault only when the fault is applied at II or III terminal (Fig. 5.29, 5.30). On the contrary, the restraint values I_{res} are above their differential equivalents I_{op} for any fault type, only when the fault is applied at I or IV terminal (Fig. 5.28, 5.31).

Table 5.7 shows calculated values of the operating speed for internal faults along with the maximum fault resistances, at which relay can still detect fault. Measured values show that feeder cable network for the proposed wind turbine converter design and selected grounding configuration can be reliably protected even against highly resistive faults, which practically eliminates soil resistivity concerns.

Table. 5.7. Measured selectivity and sensitivity of the applied short circuit protection scheme.

Fault Terminal	**II**			**III**		
Fault Type	**1ph-G**	**2ph-G**	**3ph-G**	**1ph-G**	**2ph-G**	**3ph-G**
Operating speed *(fault detection instant)*	5 ms	5 ms	5 ms	5 ms	5 ms	5 ms
Maximum detectable fault resistance	375 Ω	455 Ω	430 Ω	365 Ω	425 Ω	430 Ω

Chapter 6

Conclusions and Future Work

6.1 Conclusions

Increasing power ratings of the multi-MW wind turbines already provide problems related to the space arrangements of their electrical systems. Developed multi-parallel converter units, along with filter modules, cables and a step-up transformer need to be placed close to each other in the nacelle to minimize losses caused by the excessive currents. In order to reduce such currents in the nacelle and provide the possibility for flexible space arrangements not only within the nacelle, but also on the base platform inside the tower, a transformer-less turbine concept has been proposed, where turbine components operate at the medium voltage level.

Medium voltage power converters differ from their low voltage equivalents. Due to the limited voltage capability provided by the available semiconductor switches, multilevel topologies are favoured, which result in lower filtering requirements along with lower switching losses. In this project, 3 medium voltage converter systems are analyzed: A, B and C. System A is a back-to-back MMC converter, which is commonly used in HVDC application. System B consists of the generator-side 2-level converter, DC/DC boost unit and a grid-side NPC-3L converter. System C is made of a series-connected full-bridge cells on the generator-side, and a grid-side NPC-5L converter. The conclusions supported by the results derived from this work are as follows:

- Among the analyzed 3 converter candidates for the medium voltage transformer-less wind turbine, it has occurred that under steady-state operation, the back-to-back MMC converter (system A) generates lower power losses for the applied power generation distribution profile, thus surpassing the other candidates: systems B and C by 6% and 5% respectively. This can be explained by means of the low switching frequency for the MMC topology.
- Calculated losses of the conventional low voltage 2-level converter in the comparison with back-to-back MMC consisting of 4500 V / 340 A press-pack IGBTs have shown that system A has higher weighed efficiency by 2% for the applied power generation distribution profile. The low voltage 2-level converter with 1700 V / 450 A has higher efficiency during peak loads, whereas MMC becomes more efficient during low loads.
- The total volume of the required silicon in IGBT press-pack devices used for the medium voltage converters is the highest in system A (100%). Systems B and C require 58% and 87% respectively. In case of silicon for the press-pack diodes,

system C requires highest amount: 167%, whereas system B needs 81% of the total amount in system A.

- The results obtained from the time domain simulations during short circuit analysis have shown, that the back-to-back MMC circuitry provides lowest maximum short circuit current contribution for all kind of ground faults located at the grid-side wind turbine terminals. By blocking IGBTs in all cells, large cell capacitors are diode blocked, which results in the lowest contribution. In systems B and C with common DC link, equivalent capacitors cannot be diode blocked. As a result, common DC link leads to a higher short circuit current contribution of each single turbine.
- Due to galvanic coupling between the transformer-less wind turbine and a collector distribution network, 3 neutral points have been defined: N1, N2 and N3, which ground potentials constitute entire grounding scheme N1-N2-N3. In this work, N1 point is a wind turbine generator neutral; N2 is a DC link midpoint with grid-side C filter formed by the wind turbine back-to-back VSC power converter; N3 is a substation transformer neutral. Each point can be either solid grounded (1), or isolated (0). In such arrangement, each feeder cable section is impedance grounded via screens on both sides to a external grounding wire (two points bonding).
- For all analyzed grounding schemes, well-known problems found in the conventional transformer-equipped turbines - related to the excessive inrush currents coming from the energization of the step-up transformer - are eliminated. No additional grounding equipment (e.g. zig-zag transformers, grounding switches, etc.) is necessary in case of the collector feeder islanded operation, since ground fault can be instantly detected with the proposed scheme due to coupled zero sequence networks between the wind turbines and cables.
- Among N1-N2-N3 grounding configurations, lowest temporary ratings of the feeder breakers and grounding wires during cable short circuit period is obtained with back-to-back MMC system for 0-1-0 grounding scheme, when only its DC link midpoint and C filter capacitors are grounded. In such configuration, amount of the additional copper required for the wind power plant consisting of 50 wind turbines is 0 mm^2 / km. It occurred that schemes 1-1-0 and 1-0-0 require 26 mm^2 / km of extra copper, whereas systems grounded through N3 point require it more than 60 mm^2 / km.
- The line current differential protection scheme has been modelled and tested in time domain EMTDC/PSCAD simulations, which role is to detect ground faults within the feeder cable network, and differentiate them from faults located at the wind turbine terminals. Differential protection consists of the current sensors located at each wind turbine terminal, and current sensors at the feeder terminals. Differential relay operates by summating all measured instantaneous currents within the established protection zone, where sum should be ideally zero.

- The proposed current differential protection scheme for fast and selective cable ground fault detection in a feeder consisting of the transformer-less wind turbines with back-to-back MMC converter has properly reacted on ground faults located only within its protection zone. It can be therefore considered as a primary fault detection mechanism for feeder distribution network. In comparison to the presently utilized over-current directional relays for low voltage systems, no intentional time delay is required in case of ground faults for coordinated protection between feeder and a turbine.

6.2 Novelty and Contributions

At present, no comprehensive research related to medium voltage transformer-less wind turbines has been provided. Some fundamental aspects, which have been covered in this work, form a list of following contributions:

- ***Defined technical challenges and potential issues related to future development of the transformer-less wind turbines.*** Obtained results define a list of topics for the next generation research projects related to the successful implementation of the transformer-less wind turbines.
- ***Proposal of three different power conversion philosophies A, B and C for the medium voltage transformer-less wind turbines*, *along with the specific converter circuitries***. System A consists of a 2-stage conversion AC/DC - DC/AC, while systems B and C consist of 3-stage conversions: AC/DC - DC/DC - DC/AC and AC/AC - AC/DC - DC/AC respectively. Main focus is put on a modular design strategy and operation within the imposed insulation limits. In this manner, proposed systems can be optimized for stacking arrangements and scaling according to the desired collector grid voltage and power levels.
- ***Proposed method for the modelling of modular multilevel converter (MMC) with derived three abstraction levels varying with regard to the complexity and functionality.*** In order to develop EMTDC/PSCAD simulation model and accurate loss model for system A, 3 theoretical models have been created, which allow implementation and verification of the selected control and modulation algorithms under the specified voltage and power ratings. 1st model is used to design and optimize high level control, and consists of MMC arms represented by ideal voltage sources. 2nd model is used to design and optimize modulation scheme, and consists of MMC arms represented by the levelized voltage sources. 3rd model is used to design and optimize low level control, and consists of MMC arms represented by the distributed cell capacitors.
- ***Developed Excel sizing tool for the MMC.*** Sizing tool has been made in order to properly size hardware circuit components for the generic HVDC application, but can be adapted for system A. It includes LC filter sizing procedure against arm

circulating currents, possible resonances and DC link faults. Certain modifications adapt its algorithms into the transformer-less wind turbine application (lack of the 2nd harmonic arm C filter, transformer, etc.).

- ***Proposed and experimentally validated 4.5 kV / 340 A IGBT-PP hybrid power loss estimation method, suitable for systems in the medium voltage area.*** Utilized sample-based method for power loss estimation has been verified through the set of switching tests conducted under the real device. It calculates generated in time-domain simulation conduction and switching losses in the IGBT based on the instantaneous gate and current signals, along with an interpolated switching energy curves. The method has been applied to estimate losses for the medium voltage transformer-less wind turbine solutions: A, B and C.
- ***Method of the grounding system design with regard to the ground wire and circuit breaker sizing under the cable ground faults in the transformer-less collector feeder systems.*** Short circuit analysis is divided into time domain and phasor domain. Time domain analysis is used to define aggregated transformer-less wind turbine models, which can be conveniently used in phasor-domain sequence network analysis as independent short circuit current contributions. In this manner, wind turbine short circuit behaviour is decoupled from the feeder network configuration, and depends only on the grounding method of the feeder neutral (N3 point).
- ***Proposed ground fault detection method for the collector cable systems consisting of the future transformer-less wind turbines.*** Removal of the transformer results in problems related to the coordinated protection between wind turbines and a feeder against the ground faults. Analyzed current differential protection operates only within the marked protection zone, which covers only feeder cable network. In this manner, cable ground faults are detected instantly and distinguished from the wind turbine internal faults.

6.3 Future Work

6.3.1 Economical Aspects

The results from losses analysis of the different medium voltage power converter candidates provide insights over the power losses of systems A, B and C when they operate at the specified power generation distribution profile. For the given 10 MVA wind turbine mission profile, annual energy production (AEP) can be calculated when improved with calculated losses coming from the LC filter and the generator.

Wind power plant availability and the maintenance annual periods can be calculated by known lifetime of the utilized components. Lifetime of the power converter topologies should be further examined based on possible redundant modes during failures of the semiconductor switches. Obtained availability and maintenance periods can be translated into operating expenditures (OPEX).

Calculated required amount of silicon, amount of copper for the ground wire, LC filters size and breaker ratings can be altogether translated into the bill of materials, which summated form capital expenditures (CAPEX).

AEP, OPEX and CAPEX parameters can be eventually used to provide the economical comparison of the entire wind power plant consisting of the transformer-less wind turbines by calculating the levelized cost of energy (LCOE).

6.3.2 Collector Feeder Network Configurations

In this work, only radial feeder network configuration has been examined with chain-connected wind turbines. This type of configuration is the most common, as it requires lowest number of cables interconnecting wind turbines. However, such configuration for multiple 10 MVA turbines provides new problems related to the limited current capabilities of the available cable break elbows (600 A) [22], which may result in longer maintenance periods and less safer handling of the each turbine. Hence, different network configurations should be investigated with regard to the short circuit analysis: ring feeder, looped feeder, bifurcated feeder and more [79].

Proposed short circuit analysis method with the assumed identical cable sections can be conveniently adapted to the various network configurations with the accordingly modified sequence networks in the phasor domain analysis.

6.3.3 66 kV Feeder Network

Due to the limited current ratings of the presently available medium voltage components (i.e. IGBTs, circuit breakers), analysis of the transformer-less wind turbines has been performed for the 20 kV voltage level at the grid-side. Further voltage increase up to 66 kV or even higher level is possible with the proposed topologies, yet applied hardware components will have to be significantly overrated, thus not utilizing their full potential and increasing overall cost of the system.

Nevertheless, future large offshore wind turbines are likely to operate at 66 kV, which is aimed at minimizing the conductive losses in the feeder cable network and the substation transformer. In order not to install overrated devices at a higher cost, a future analysis can be considered with a voltage partly reduced by the autotransformer installed at the wind turbine terminals.

6.3.4 Wind Turbine Primary and Feeder Back-up Protection

Apart from the analyzed primary differential short circuit protection for the feeder cable network, a search for both feeder back-up and wind turbine primary protection is required. For the systems where wind turbine is solid grounded with at least one point, a further analysis of the over-current directional relay is suggested [80]. More sophisticated methods are required for systems with isolated neutral, which include sineφ measurement and transient ground fault relay [81].

Bibliography

[1]- *Global Wind Report* [Online], Annual Market Update 2012, GWEC. Available: http://www.gwec.net/wp-content/uploads/2012/06/Annual_report_2012_LowRes.pdf

[2]- *Technology Roadmap - Wind Energy 2009* [Online], International Energy Agency IEA. Available: http://www.iea.org/publications/freepublications/publication/Wind_Roadmap.pdf

[3]- *Offshore Wind Toward 2020 - On the Pathway to Cost Competitiveness* [Online], Roland Berger Strategy Consultants GmbH, April 2013. Available: http://www.rolandberger.com/media/pdf/Roland_Berger_Offshore_Wind_Study_20130506.pdf

[4]- Dr. Sherif El-Henaoui; *Individual Pitch Control and Its Impact* [Online], Wind Systems, July 2012. Available: http://windsystemsmag.com/article/detail/394/individual-pitch-control-and-its-impact

[5]- P. Gipe; *100% renewable and higher: The new trend in energy targets* [Online], RenewEconomy, April 2013. Available: http://reneweconomy.com.au/2013/

[6]- E.H. Camm; M.R. Behnke; O. Bolado; *et al.*; "Characteristics of wind turbine generators for wind power plants," *Power & Energy Society General Meeting, 2009*, vol., no., pp. 1, 5, 26-30 July 2009.

[7]- R. Mittal; K.S. Sandhu; D.K. Jain; "Fault ride- through capability of grid connected variable speed permanent magnet synchronous generator for wind energy conversion system," *Electrical Power & Energy Conference (EPEC), 2009 IEEE* , vol., no., pp.1,6, 22-23 Oct. 2009.

[8]- M. Bash; S. Pekarek; S. Sudhoff; J. Whitmore; M. Frantzen; "A comparison of permanent magnet and wound rotor synchronous machines for portable power generation," *Power and Energy Conference at Illinois (PECI), 2010* , vol., no., pp.1,6, 12-13 Feb. 2010.

[9]- T. Burton; N. Jenkins; D. Sharpe; E. Bossanyi; *Wind Energy Handbook*, John Wiley & Sons, 2011, ISBN: 9781119993926

[10]- M. Liserre; R. Cardenas; M. Molinas; J. Rodriguez; "Overview of Multi-MW Wind Turbines and Wind Parks," *Trans. Industrial Electronics, IEEE*, vol.58, no.4, pp.1081,1095, April 2011.

[11]- *PCS 6000 for large wind turbines - Medium voltage, full power converters up to 9 MVA*, ABB brochure, 2013.

[12]- *How A Wind Turbine Comes Together* [Online], www.renewable-energy-sources.com, 2013. Available: http://www.restrends.com/2012/11/01/how-a-wind-turbine-comes-together/

[13]- R. Marquardt, “Current rectification circuit for voltage source inverters with separate energy stores replaces phase blocks with energy storing capacitors,” DE Patent 1 010 303 1A1, July 25 2002.

[14]- *Siemens drives innovative use of regenerative energy sources*, Siemens AG Drive Technology Media Newsletter, 2013.

[15]- M. Rahimo; A. Kopta; R. Schnell; U. Schlapbach; R. Zehringer; S.Linder; “2.5kV-6.5kV Industry Standard IGBT Modules Setting a New Benchmark in SOA Capability”, *Proc. of the 10th European Power Quality Conference (PCIM’04)*, Germany, 25-27 May.

[16]- Iversen, T.M. (2012). “Multilevel Converters for a 10 MW, 100 kV Transformer-less Offshore Wind Generator System,” Ph.D. Dissertation, Norwegian Univ. of Science and Technology (NTNU), Norway.

[17]- S. Katoh; S. Ueda; H. Sakai; T. Ishida; Y. Eguichi; "Active-gate-control for snubberless IGBTs connected in series," *in Proc. Annual Power Electronics Specialists Conf., PESC’02. 2002*, vol. 2, no., pp. 609, 613 vol. 2, 2002.

[18]- Y. Uchida; Y. Seki; Y. Takahashi; M. Ichijoh, "Development of high power press-pack IGBT and its applications," *in Proc. 22nd Int. Conf. on Microelectronics*, vol. 1, no., pp.125, 129 vol. 1, 2000.

[19]- G. Stone, E.A. Boulter, I. Culbert, H. Dhirani, *Electrical Insulation for Rotating Machines: Design, Evaluation, Aging, Testing, and Repair.* Ontario, CA: John Wiley & Sons, 2004.

[21]- IEC 60034-18-41, *Evaluation and Qualification of Electrical Insulation Systems Used in Rotating Electrical Machines When Fed from Voltage Converters*, draft version, 30 November 2004.

[22]- E.H. Camm, M.R Behnke, O. Bolado, et al., "Wind power plant collector system design considerations: IEEE PES wind plant collector system design working group," *Power & Energy Society General Meeting, 2009. PES '09. IEEE* , vol., no., pp.1,7, 26-30 July 2009.

[23]- J. Adabi; F. Zare; G. Ledwich; *et al.*, "Leakage current and common mode voltage issues in modern AC drive systems," *Power Engineering Conference, 2007. AUPEC 2007*. Australasian Universities , vol., no., pp.1,6, 9-12 Dec. 2007.

[24]- J. Wang; R. Lascu, "Zero sequence circuit of three-legged core type transformers," *Protective Relay Engineers, 62nd Annual Conf.*, vol., no., pp.188,213, March 30 2009-April 2 2009.

[25]- D. Boian; C. Biris; R. Teodorescu; et al., "Development of modulation strategies for NPC converter addressing DC link voltage balancing and CMV reduction," *Power Electronics for Distributed Generation Systems (PEDG), 2012 3rd IEEE International Symposium*, vol., no., pp. 828 - 835, 25-28 June 2012.

[26]- R.C Clinker, "Harmonic Voltages and Currents in Y- and Delta-Connected Transformers," *American Institute of Electrical Engineers Trans.*, vol. XXXIII, no.1, pp. 723,733, Jan. 1914.

[27]- W.L.A. Neves; H.W. Dommel, "Saturation curves of delta-connected transformers from measurements," *Power Delivery, IEEE Trans.*, vol.10, no.3, pp.1432,1437, Jul 1995.

[28]- Colonel Wm. T. McLyman, *Transformer and Inductor Design Handbook, Third Edition*, CRC Press, 2004.

[29]- K. Boyce, *Safety Standards for Wind Turbines* [Online]. Dewi Magazin No. 41, August 2012. Available: http://www.dewi.de/dewi/fileadmin/pdf/publications/Magazin_41/02.pdf

[30]- *Managing humidity in offshore wind turbines,* Cotes A/S brochure, 2013.

[31]- M. Bradt; M.R. Behnke; W.G. Bloethe; *et al.* "Power transformer application for wind plant substations," *Transmission and Distribution Conf. and Exposition, 2010 IEEE PES*, vol., no., pp.1,6, 19-22 April 2010.

[32]- NESC Interpretation IR532, Section 9: *Grounding Methods;* Rule 96C: *Ground Resistance Requirements* [Online]; 2003. Available: http://standards.ieee.org/about/nesc/ir532.pdf

[33]- M. Leijon; K. Johannesson; S. Milton; *et al.*, “Conductor for high-voltage windings and a rotating electric machine comprising a winding including the conductor,” U.S. Patent 6 376 775 B1, April 23, 2002.

[34]- *Dura-Bilt5i MV - Medium Voltage AC Drive Topology Comparisons & Feature-Benefits* [Online], TME GE Automation Systems, 2005. Available:
http://tmeic-ge.com

[35]- S. Martin Paul, “Impregnated film capacitors,” U.S. Patent 3 584 272 A, June 8, 1971.

[36]- H. Takeoka; H. Kubota; H. Fujii; *et al.*, “Metalized film capacitor,” U.S. Patent 8 451 579 B2, May 28, 2013.

[37]- *Self-healing Process in Metallized Capacitors* [Online], WIMA brochure, Available: http://www.wima.com/EN/selfhealing.htm

[38]- A. Bjorklund; E. Persson; L.G. Virsberg, “Sheet-wound transformer or reactor,” U.S. Patent 4 295 113 A, October 13, 1981.

[39]- G. Broszat, “Disc coil winding with interleaved singular or double coils,” U.S. Patent 0 088 934 A1, September 21, 1983.

[40]- U. Reggiani; G. Grandi; G. Sancineto; *et al.*, "Comparison between air-core and laminated iron-core inductors in filtering applications for switching converters,*" Power Electronics Congress, 2000. CIEP 2000. VII IEEE International*, vol., no., pp.9,14, 2000.

[41]- G. Leonhardt; M. Marchi; G. Rivetti, SF6 or *Vacuum? Choosing the right MV circuit-breaker* [Online], ABB Review 4/2000. Available:
http://www.abb.com.

[42]- L.T. Falkingham; G.F. Montillet, "A history of fifty years of vacuum interrupter development - (the English connection)," *Power Engineering Society General Meeting, 2004. IEEE* , vol., no., pp. 706, 711 Vol.1, 6-10 June 2004.

[43]- J.J Emmet, “High power vacuum circuit breaker contacts and arc-extinguishing means therefor,” U.S. Patent 3 196 236 A, July 20, 1965.

[44]- D. Koch, *SF_6 properties, and use in MV and HV switchgear* [Online], Cahier Technique Schneider Electric no. 188 / p.2. Available:
http://www.schneider-electric.com.

[45]- A. Iturregi; E. Torres; I. Zamorra; et al., “High Voltage Circuit Breakers: SF6 vs. Vacuum,” in *Int. Conf. on Renewable Energies and Power Quality (ICREPQ’09), 2009,* European Association for the Development of Renewable Energies Environment and Power Quality.

[46]- O.S. Senturk (2011). “High Power Density Power Electronics Converter for Large Wind Turbines,” Ph.D. Dissertation, Aalborg Univ. (AAU), Denmark.

[47]- S. Thielemans, (2012). “Balancing and Control of Power Electronic Flying Capacitor Multilevel Converters**,”** Ph.D. Dissertation, Ghent Univ. (GU), Belgium.

[48]- A. Lesnicar; R. Marquardt, "An innovative modular multilevel converter topology suitable for a wide power range," *Power Tech Conference Proceedings, 2003 IEEE Bologna* , vol.3, no., pp.6 pp. Vol.3,, 23-26 June 2003.

[49]- R. H. Baker; L. H. Bannister, "Electric Power Converter," U.S. Patent 3 867 643 A, February 18, 1975.

[50]- B. Jacobson; P. Karlsson; G. Asplund; *et al.* “VSC-HVDC transmission with cascaded two-level converters,” *in Proc. CIGRE, 2010, paper B4-110*.

[51]- L. Vereb; P. Osmokrovic; M. Vujisic; *et al.*, "Prospects of constructing 20 kV asynchronous motors," *IEEE Trans. Dielectrics and Electrical Insulation*, vol.16, no.1, pp.251,256, February 2009.

[52]- D. Saez; J. Iglesias; *et al.*, “Evaluation of 72 kV collection grid on offshore wind farms,” [Online] *EWEA Annual Event*, April 2012. Available: http://proceedings.ewea.org/annual2012/allfiles2/1407_EWEA2012presentation.pdf

[53]- J. Dawidziuk, "Review and comparison of high efficiency high power boost DC/DC converters for photovoltaic applications" *Bulletin of the Polish Academy of Sciences: Technical Sciences*, 59.4 (2012): 499-506. Retrieved 14 Oct. 2013.

[54]- W. Chen, W; A.Q. Huang; *et al.*, "Analysis and Comparison of Medium Voltage High Power DC/DC Converters for Offshore Wind Energy Systems," *IEEE Trans. Power Electronics*, vol.28, no.4, pp.2014,2023, April 2013.

[55]- C. Oates, "A methodology for developing ‘Chainlink’ converters," *Power Electronics and Applications, 2009. EPE '09. 13th European Conf.*, vol., no., pp.1,10, 8-10 Sept. 2009.

[56]- L. Maharjan, S. Inoue, *et al.*, "A transformerless battery energy storage system based on a multilevel cascade PWM converter," *Power Electronics Specialists Conf., 2008. PESC 2008. IEEE* , pp. 4798,4804, 15-19 June 2008.

[57]- R. Chibani; E.M. Berkouk; M.S. Boucherit, „Five Level NPC-VSI Capacitor Voltage Balance Using a Recent Capacitive Clamping Bridge,” Journal ACTA ELECTROTEHNIKA, vol.53, no.4, Mediamira Science Publisher, 2012.

[58]- *XLPE Submarine Cable Systems Attachment to XLPE Land Cable Systems - User´s Guide* [Online], ABB brochure, 2010. Available: http://www.abb.com

[59]- *Insulated Gate Bi-Polar Transistor, Type T0340VB45G* [Online], Westcode Semiconductors Ltd, IGBT Datasheet, 2012. Available: http://www.westcode.com

[60]- *PrimePACK™2 module and NTC, Type FF450R17IE4* [Online], Infineon, IGBT Datasheet, 2013. Available: http://www.infineon.com/

[61]- M. Sztykiel, R. Teodorescu, S. Munk-Nielsen, C. Busca, “Losses Analysis of Different Grounding Schemes for Transformer-less Wind Turbine with Full-Scale Power Converter”, *12th Int. Wind Integration Workshop*, 22-24 October 2013, London, United Kingdom.

[62]- *Heat sinks and water coolers, aluminum extrusion profiles and friction stir weld water coolers - Type VK-165-150-25-A* [Online], AB WEBRA INDUSTRI & AMS Technologies AG, Water Cooler Datasheet, 2012. Available: http://www.amstechnologies.com/

[63]- *Heat sinks and water coolers, aluminum extrusion profiles and friction stir weld water coolers - Type VK-370-300-22* [Online], AB WEBRA INDUSTRI & AMS Technologies AG, Water Cooler Datasheet, 2012. Available: http://www.amstechnologies.com/

[64]- J. Xu, C. Zhao, W. Liu, *et al.*, "Accelerated Model of Modular Multilevel Converters in PSCAD/EMTDC," *IEEE Trans. Power Delivery*, vol. 28, no. 1, pp. 129-136, January 2013.

[65]- *IGBT-Die, Type 5SMY 12N4501* [Online], ABB, IGBT Die Datasheet for the press-pack packaging, 2011. Available: http://www.abb.com

[66]- *Fast-Diode Die, Type 5SLY 12N4500* [Online], ABB, Diode Die Datasheet for the press-pack packaging , 2011. Available: http://www.abb.com

[67]- *IGBT3 Power Chip, Type IGC168T170S8RM* [Online], Infineon, IGBT Chip Datasheet for the wire bonded packaging, 2010. Available: http://www.infineon.com/

[68]- *Emitter Controlled Diode3 Chip, Type SIDC78D170H* [Online], Infineon, Diode Chip Datasheet for the wire bonded packaging , 2011. Available: http://www.infineon.com/

[69]- IEC 60502 Std.: Power cables with extruded insulation and their accessories for rated voltage from 1 kV ($U_m = 1.2$ kV) up to 30 kV ($U_m = 36$ kV).

[70]- IEC 60909 Std.: The Calculation of Short-Circuit Currents in Three-Phase AC Systems, 2001.

[71]- Grid Code Std.: Grid Code for High and Extra High Voltage, E.ON Netz GmbH, Bayreuth, April 1, 2006.

[72]- *ADVAC/AMVAC vacuum circuit breakers Accessories, style, & pricing guide - Selection Guide* [Online], ABB brochure, 2010. Available: http://www.abb.com

[73]- *SIPROTEC 4 Differential Protection 7SD52 V4.1 Manual*, Siemens AG, Nuremberg, Germany, 2002.

[74]- M. Sztykiel, C. Leth Bak, *et al.* “Line Differential Protection Scheme Modeling for Underground 420 kV Cable System”. *IEEE MEPS’10 International Symposium - Modern Electric Power Systems* 2010, 20-22 September 2010, Wroclaw, Poland.

[75]- M. Sztykiel, “Protection philosophies for HVAC transmission network,” M.S. thesis, IET, Aalborg Univ., Aalborg, Denmark, 2009.

[76]- B. Wu, *High-Power Converters and AC Drives*, IEEE Press, ISBN: 10 0-471-73171-4, 2006, p. 6.

[77]- *1.2 kV to 46 kV Class Dry-Type Medium Voltage Distribution (Power) Transformers 500 kVA To 34 MVA* [Online], Hammond Power Solutions Inc. brochure, 2010. Available: http://www.hammondpowersolutions.com

[78]- *High Power Capacitors For Power Electronics* [Online], AVX brochure, 2009. Available: http://www.avx.com

[79]- M.L. Reichard; D. Finney; J.T. Garrity, "Windfarm System Protection Using Peer-to-Peer Communications," *Protective Relay Engineers, 2007. 60th Annual Conference for* , vol., no., pp.511,521, 27-29 March 2007

[80]- *Directional Overcurrent Protection Relay GRD140 Instruction Manual*, Toshiba Corporation, Japan, 2009.

[81]- *Earth-Fault Protection in Systems with Isolated Star Point - Applications for SIPROTEC Protection Relays* [Online], Siemens AG, Germany, 2005.
Available: http://www.energy.siemens.com

[82]- M. Hagiwara and H. Akagi, “Control and experiment of pulsewidth-modulation modular multilevel converters,” *IEEE Trans. on Power Electronics*, vol. 24, no. 7, pp. 1737-1746, July 2009.

[83]- Krismer, F. (2010). “Modeling and Optimization of Bidirectional Dual Active Bridge DC–DC Converter Topologies,” Ph.D. Dissertation, ETH Zurich, Switzerland.

A. System A: Back-to-Back MMC

A.1 Introduction

Figure A.1 presents a schematic diagram of the proposed concept. As MMC has an independent AC/DC conversion feature and maintains high number of voltage levels, an idea is that the generator-side can be kept at lower AC voltage, limited by the generator insulation system.

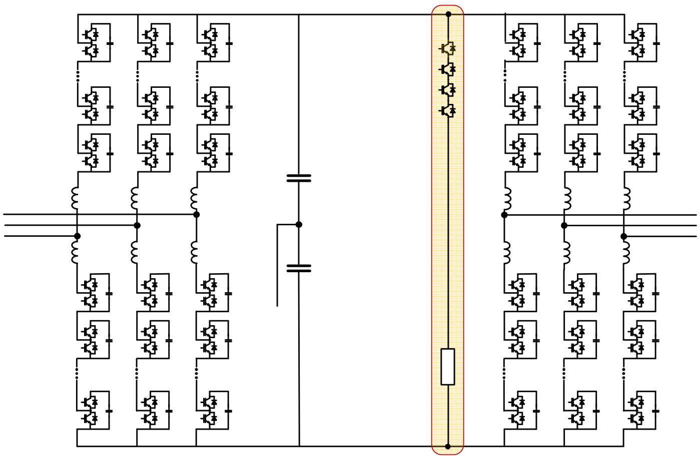

Fig. A.1 The schematic representation of system A.

This system is proposed for the relatively low difference between generator AC and grid AC voltages. Unwanted voltage surplus is clamped by the unused generator-side MMC cells. On the other hand, grid-side MMC can perform normal operation at requested grid voltage level.

In practice, generator voltage should be kept at high level (e.g. 15 kV) due to cell balancing problems and low cell switching frequency connected with decreasing number of operating voltage levels.

A.2 MMC Operating Principles - Abstraction Levels

Following circuit candidates are referred as:

- **A:** system with controllable voltage sources per arm/leg (simplest).
- **B:** system with distributed DC voltage sources per arm/leg.
- **C:** system with distributed capacitors per arm/leg (most complex).

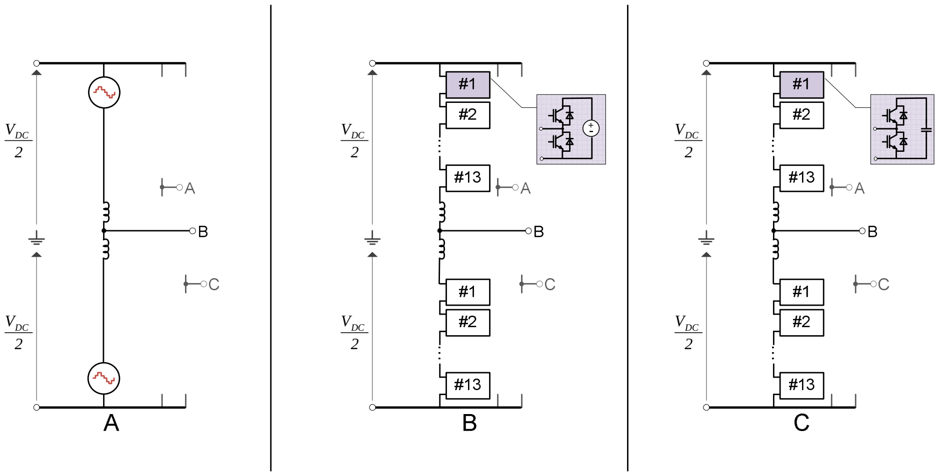

Fig. A.2 Grid-side circuit candidates with varying aggregation level of complexity.

A.3 MMC - General Control Architecture

a. Introduction

Following chapter contains description of MMC control algorithm, which includes high-level AC current control, zero-sequence control, DC voltage control, arm energies balancing control, low-level cell voltage balancing controller and PWM modulator.

Control algorithm is made in a generic form, so that it can be easily adapted to different topologies and different ratings.

b. Electrical Sensors - Location

Figure A.3 shows displacement of the required current and voltage sensors in order to properly operate MMC system.

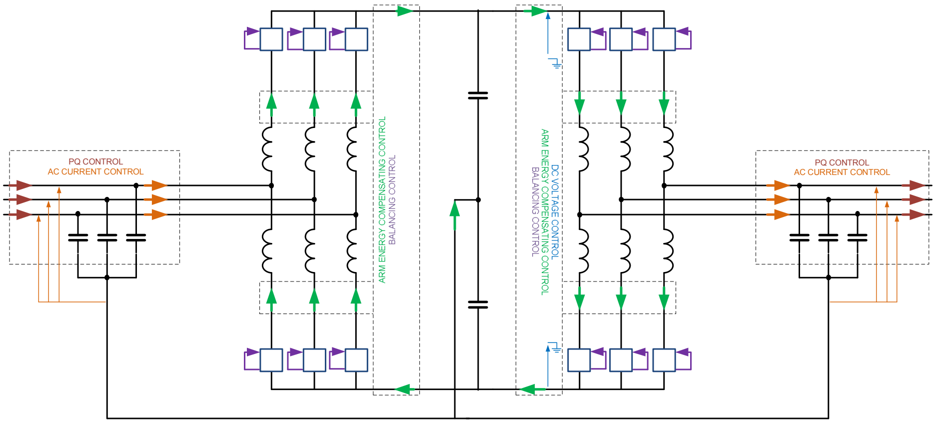

Fig. A.3 Sensor locations for all required measured electrical signals.

Following controllers are involved for each side:

- **PQ power controller (only grid-side unit):**
  - *x3 phase AC current sensors placed after C filter branches [$i_{AC(A)}$ | $i_{AC(B)}$ | $i_{AC(C)}$].*
  - *x3 phase AC voltage sensors placed after C filter branches [$v_{AC(A)}$ | $v_{AC(B)}$ | $v_{AC(C)}$].*
- **DC voltage controller (only grid-side unit):**
  - *x2 DC voltage sensors placed between each DC pole and common-mode point [$v_{DC(U)}$ | $v_{DC(L)}$].*
- **AC current controller:**
  - *x3 phase AC current sensors placed between converter legs and C filter branches [$i_{AC(A)}$ | $i_{AC(B)}$ | $i_{AC(C)}$].*
  - *x3 phase AC voltage sensors placed after C filter branches [$v_{AC(A)}$ | $v_{AC(B)}$ | $v_{AC(C)}$].*
- **DC voltage balancing (zero-sequence) controller:**
  - *x2 DC voltage sensors placed between each DC pole and common-mode point [$v_{DC(U)}$ | $v_{DC(L)}$].*
- **Arm energy compensating controller:**
  - *x6 arm DC current sensors placed between cells and arm reactors [$i_{arm(AU)}$ | $i_{arm(BU)}$ | $i_{arm(CU)}$ | $i_{arm(AL)}$ | $i_{arm(BL)}$ | $i_{arm(CL)}$].*
  - *x6 arm DC voltage sensors placed between pole and arm reactors [$v_{arm(AU)}$ | $v_{arm(BU)}$ | $v_{arm(CU)}$ | $v_{arm(AL)}$ | $v_{arm(BL)}$ | $v_{arm(CL)}$].*
  - *x2 DC current sensors placed on each pole [$i_{DC(U)}$ | $i_{DC(L)}$].*
  - *x2 DC voltage sensors placed between each DC pole and common-mode point [$v_{DC(U)}$ | $v_{DC(L)}$].*
- **Cell voltage balancing controller (only abstraction level C):**
  - *Nx6 DC voltage sensors placed across each cell capacitor (where N = number of cells per arm).*

A.4 Abstraction Level A - Control Architecture

a. Introduction

Generalized control diagram is shown in Figure A.4. As a result, complete control system is divided into 4 units according to the controlled merit. Output arm voltage references are obtained by summating output signals from the decoupled DC circuit and AC circuit controllers.

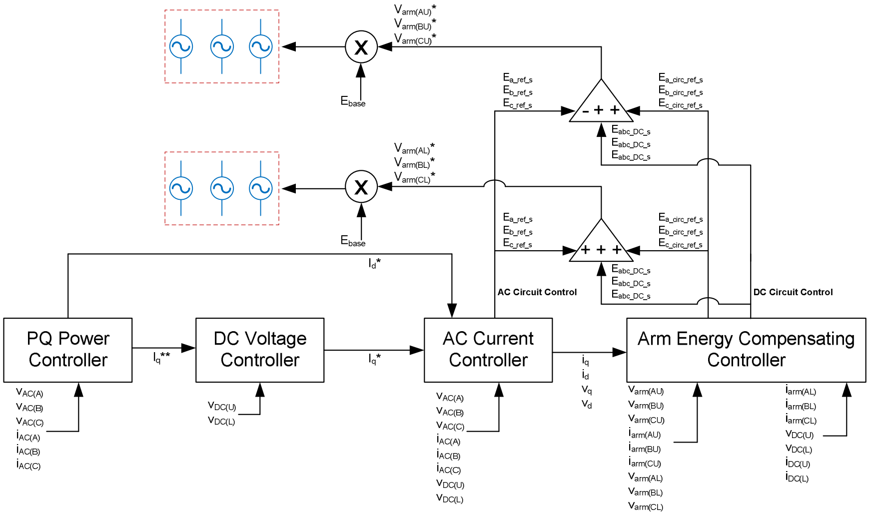

Fig. A.4 Abstraction Level A - Schematic Control Structure.

b. PQ Power Controller (Only Grid-Side Unit)

PQ controller is implemented by calculating active P_g and reactive Q_g power at the WTG output terminals. For this reason, PI controllers are implemented along with a feedback loop. I_{q_ref} and I_{d_ref} are user-input values, which specify desired active and reactive powers accordingly (in [pu]). Global I_{q_ref} and I_{d_ref} output values further enter into AC current controller.

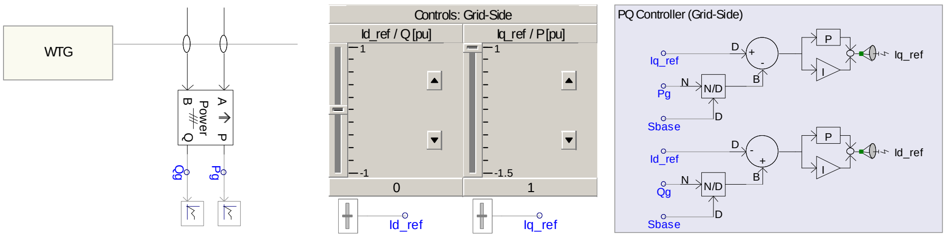

Fig. A.5 PQ Power Controller - EMTDC/PSCAD implementation.

Fault Ride Through Strategy (only Grid-Side Q Power Controller)

During external fault operation (low grid voltage), specific control strategy is applied for the grid-side PQ controller. According to grid voltage measured at PCC V_{pcc}, its value is compared to the nominal one, and then per-unitized.

Obtained voltage difference is then sent to X-Y table function, which output reactive current value is set according to specific grid code standard ($I_{reactive}[\Delta V_{pcc}]$ function). This value is then added/subtracted from user-set reference value I_{d_ref}, and the resulting value is used to properly compensate output reactive power according to the requirements.

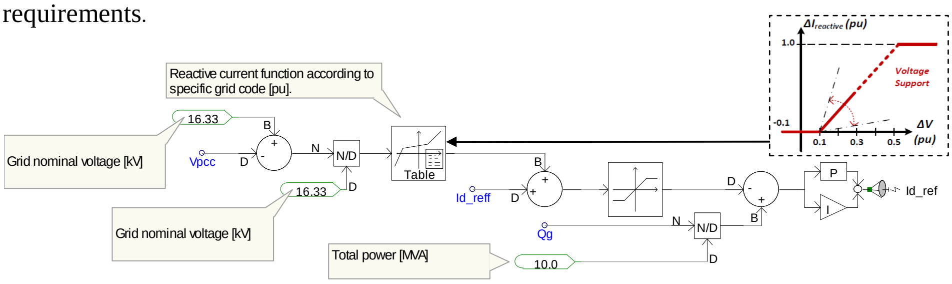

Fig. A.6 FRT Strategy according to German Grid Code [71] - EMTDC/PSCAD implementation.

c. DC Voltage Controller (Only Grid-Side Unit)

DC voltage controller consists of a feed-back loop and a PI controller. Input user-set reference signal E_{dc_ref} is set in [pu] mode. Measured input DC pole-to-CM point voltages E_{dc1} (upper) and E_{dc2} (lower) are firstly per-unitized (E_{dc1_pu} & E_{dc2_pu}) and later sampled (E_{dc1_s} & E_{dc2_s}) with specified sampling frequency. Base voltage E_{base} for all latter conversions is set to be half of the DC-link voltage.

Final output values E_{dc_x} and E_{dc_y} correspond to upper and lower DC voltage references, and are further sent to AC current controller as input references.

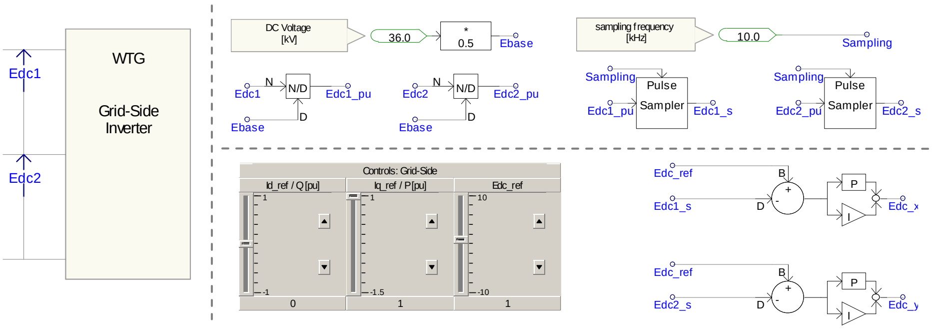

Fig. A.7 DC Voltage Controller - EMTDC/PSCAD implementation.

d. AC Current Controller + DC Link Balancing Controller

Input reference parameters for AC current controller are I_{q_ref} and I_{d_ref} from PQ power controller and E_{dc_x}, E_{dc_y}, E_{dc1_s}, E_{dc2_s} from DC voltage controller for the grid-side unit. Input measured parameters are phase currents I_a, I_b, I_c phase voltages V_a, V_b, V_c.

Measured merits are firstly per-unitized (I_{a_pu}, I_{b_pu}, I_{c_pu}, E_{a_pu}, E_{b_pu}, E_{c_pu}) and later pre-sampled (I_{a_s}, I_{b_s}, I_{c_s}, E_{a_s}, E_{b_s}, E_{c_s}) with the specified sampling frequency *Sampling*.

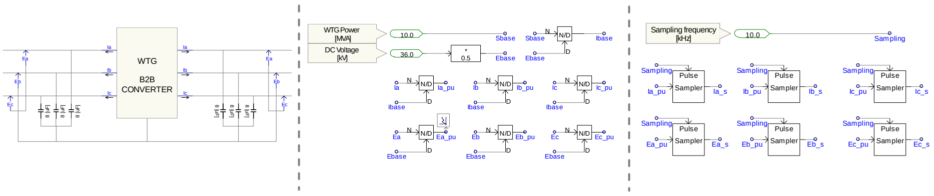

Fig. A.8 AC Current Controller, Signal Measurement/Sampling/PU.

Base voltage E_{base} for all latter conversions is set to be half of the DC-link voltage. Base current I_{base} for all latter conversions is calculated from: $I_{base} = E_{base} / S_{base}$, where S_{base} is base power equal to nominal WTG power [MVA].

Next step is to transform pre-sampled voltages and currents from ABC to dq0 frame. In dq frame used for AC current control, converted pre-sampled phase currents are I_{d_s} and I_{q_s}, while converted phase voltages are V_{d_s} and V_{q_s}. In 0 frame used for DC link balancing control, converted pre-sampled phase current is I_{0_s}.

For ABC/dq0 conversion, *Theta* parameter representing a rotating angle is set manually with a signal generator. Assuming symmetrical grid and generator conditions under normal operation along with constant frequency mode, *Theta* can be ideally modelled by saw-tooth periodic carrier. Frequency f_{base} of such carrier is equal to the grid/generator frequency. Initial phase of such signal will correspond to the initial phase value set to the grid/generator Thevenin source.

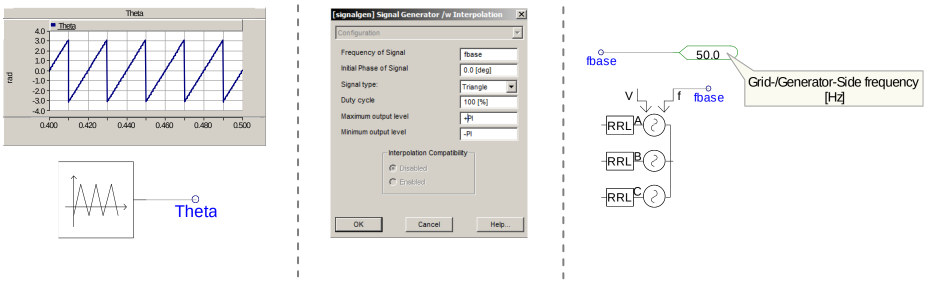

Frequency of Signal: fbase
Initial Phase of Signal: 0.0 [deg]
Signal type: Triangle
Duty cycle: 100 [%]
Maximum output level: +PI
Minimum output level: -PI
Interpolation Compatibility: ● Disabled ○ Enabled

Fig. A.9 AC Current Controller, Theta measurement/generation - EMTDC/PSCAD implementation.

DC link balancing control is implemented by creating control loop between differential DC voltage E_{dc1_s}, E_{dc2_s} and transformed zero-sequence AC current $I0\_s$. Obtained signal difference after PI controller E_{0_ref} is used as a 0-frame component in dq0/ABC transformation for final output AC reference voltages. In this manner DC link voltage imbalance between upper pole-to-CM point and CM point-to-lower-pole is compensated.

Next step is to compensate arm reactor transfer function within AC current controller. For this reason, user-specified arm inductance L_{arm} is included and per-unitized. Firstly, arm inductance is converted into reactance $X_{arm} = 2\pi \cdot f_{base} \cdot L_{arm}$. Secondly, Z_{base} is defined as: $Z_{base} = E_{base} / I_{base}$. Thirdly, per-unitized value $\mathrm{X}_{\mathrm{arm\_pu}}$ is obtained: $X_{arm\_pu} = X_{arm} / Z_{base}$. Finally, additional parameter must be entered by the user, which is line-to-line RMS nominal AC voltage E_{ac} [kV].

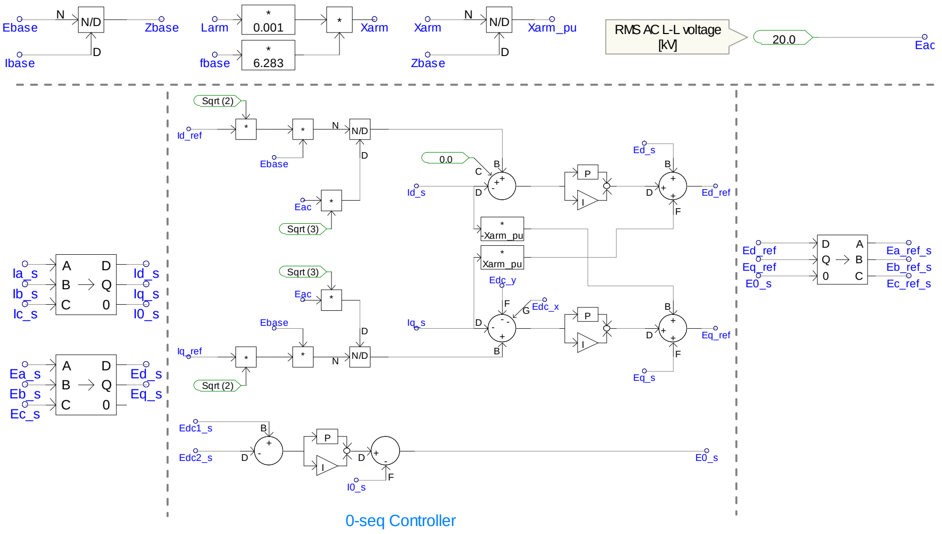

Fig. A.10 AC Current Controller, ABC/dq0 transformation + feedback control loop.

After AC current control loop shown in Fig. A.10, output dq0 voltage references E_{d_ref}, E_{q_ref} are transformed back into ABC frame through dq0/ABC transform. In order to avoid DC link voltage imbalance, 0-sequence component E_{0_ref} is also included. In this manner, no rising DC-offset shall appear. Final output values [pu] from AC circuit control are $E_{a\_ref\_s}$, $E_{b\_ref\_s}$, $E_{c\_ref\_s}$.

e. Arm Energy Compensating Controller

This controller is explicit only for MMC circuitry. Its role is to control DC circuit through compensating resulting arm energies and keep them balanced under any grid abnormal condition. Input measured parameters are:

- measured arm (cell) voltages: E_{arm_1}, E_{arm_2}, E_{arm_3}, E_{arm_4}, E_{arm_5}, E_{arm_6}.
- measured arm currents: I_{arm_1}, I_{arm_2}, I_{arm_3}, I_{arm_4}, I_{arm_5}, I_{arm_6}.
- measured pole DC currents: I_{dc1}, I_{dc2}.
- measured common-mode (ground) current: I_{gnd}

Per unitized parameters (from previously defined E_{base} and I_{base}) are:

- per-unitized arm currents: $I_{arm\_1\_pu}$, $I_{arm\_2\_pu}$, $I_{arm\_3\_pu}$, $I_{arm\_4\_pu}$, $I_{arm\_5\_pu}$, $I_{arm\_6\_pu}$.
- per-unitized pole DC currents: I_{dc1_pu}, I_{dc2_pu}.
- per-unitized common-mode (ground) current: I_{gnd_pu}.

Pre-sampled parameters (from defined new sampling rate *Sampling_E*) are:

- pre-sampled arm currents: $I_{arm\_1\_s}$, $I_{arm\_2\_s}$, $I_{arm\_3\_s}$, $I_{arm\_4\_s}$, $I_{arm\_5\_s}$, $I_{arm\_6\_s}$.
- pre-sampled pole DC currents: I_{dc1_s}, I_{dc2_s}.
- pre-sampled common-mode (ground) current: I_{gnd_s}.

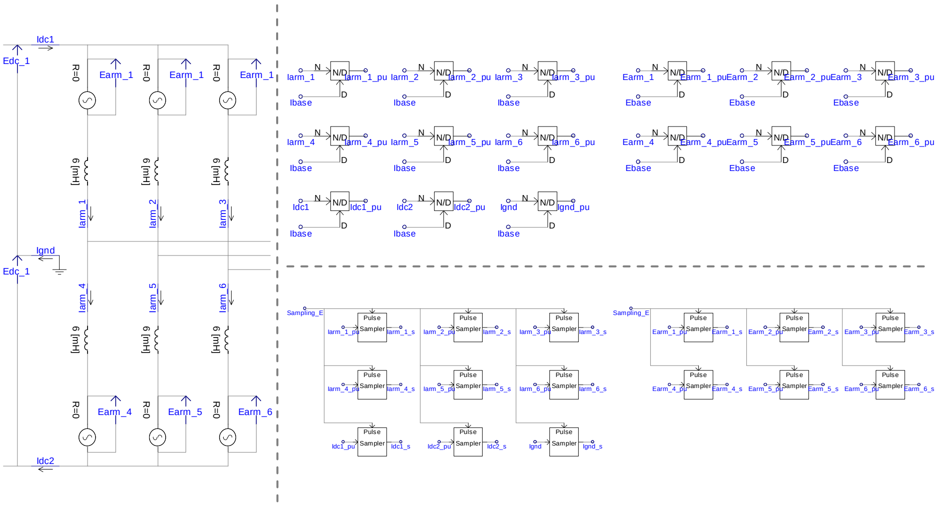

Fig. A.11 Arm Energy Compensating Controller, Signal Measuring / Sampling / PU.

Next step is to calculate arm energies, which is realized by multiplying and integrating measured arm voltages E_{arm_s} [kV] with corresponding arm currents I_{arm_s} [kA]. In order to eliminate possible parasitic ground current influence I_{gnd} on the controller, ⅙ of its measured and sampled value I_{gnd_s} is subtracted from upper arm currents $I_{arm\_123\_s}$, and summated to the lower arm currents $I_{arm\_456\_s}$. It is therefore assumed that I_{gnd} is distributed equally among each arm. Such assumption is correct to high degree, as upper and lower arms share identical AC voltage references along with arm reactor inductance/resistance values.

Obtained parameters are: *Energy_Au*, *Energy_Bu*, *Energy_Cu*, *Energy_Al*, *Energy_Bl*, *Energy_Cl* [MJ]. Mode parameter specifies whether converter generates AC power (+1), or consumes (-1). At the same time, circulating DC current is averaged in order to further minimize ground component I_{gnd} influence.

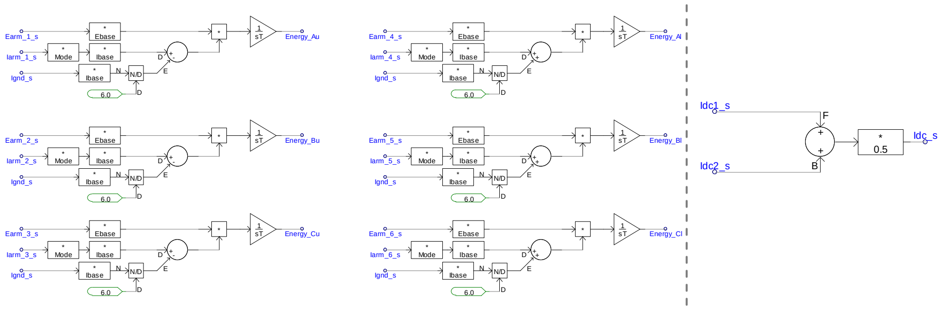

Fig. A.12 Arm Energy Compensating Controller, Arm Energy Calculation.

Theoretical Analysis

Theoretical analysis is based on MMC fundamentals described by its inventor R. Marquardt. The analyzed converter model with marked characteristic parameters is shown below:

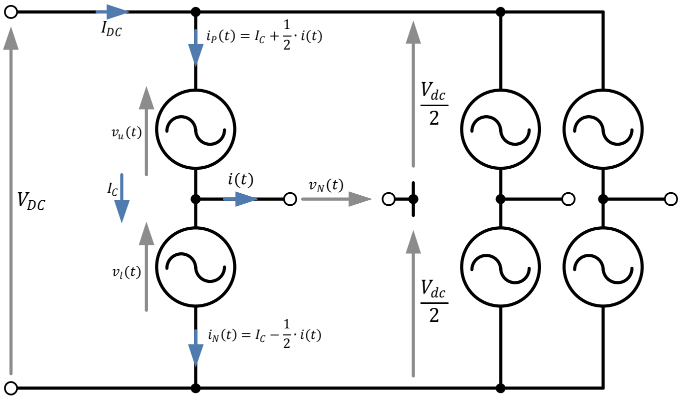

Fig. A.13 MMC Fundamentals - current and voltage distribution across MMC arms and phase legs.

Each arm is represented as a controlled voltage source with a sinusoidal voltage output. The arm currents consist of two parts, *i(t)* which flows to the output of the converter and I_C that circulates in the leg, thus loading and unloading it with energy.

The output current is equally divided between the upper and lower arms. This leads to the equation of the upper arm current:

$$i_P(t) = I_C + \frac{1}{2} i_m \sin(\omega_N t + \varphi) \tag{A.1}$$

where:

i_m - peak output current.
ω_N - output angular pulsation.
ϕ - phase shift between voltage and current.

If the 3-phase system is symmetrical, the circulating current in each phase I_C is equal to 1/3 of the total DC link current I_{DC}:

$$I_C = \frac{1}{3} I_{DC} \tag{A.2}$$

The current modulation index m is given by:

$$m = \frac{i_m}{2 \cdot I_C} \tag{A.3}$$

Substituting equations (A.1) and (A.2) into (A.3) leads to:

$$i_P(t) = \frac{1}{3} I_{DC} \cdot \left(1 + m \cdot \sin(\omega_N t + \varphi)\right) \tag{A.4}$$

The upper arm voltage $v_p(t)$ and voltage modulation index k can be expressed as following:

$$v_p(t) = \frac{V_{DC}}{2} - v_N(t) = \frac{V_{DC}}{2} - v_m \cdot \sin(\omega_N t) \tag{A.5}$$

$$k = \frac{2 \cdot v_m}{V_{DC}} \tag{A.6}$$

where:

v_m - peak line/neutral AC output voltage.
V_{DC} - pole/pole DC link voltage.

Substituting (A.4) with (A.5) and (A.6) leads to:

$$v_p(t) = \frac{V_{DC}}{2} \cdot \left(1 - k \cdot \sin(\omega_N t)\right) \tag{A.7}$$

The active power P_{AC} supplied by the converter to the grid can be represented as:

$$P_{AC} = \frac{2 \cdot v_m \cdot i_m}{\sqrt{3} \cdot \sqrt{2}} \cdot \cos\varphi = \frac{3 \cdot V_{DC} \cdot I_C}{2} \cdot k \cdot m \cdot \cos\varphi = \frac{P_{DC}}{2} \cdot k \cdot m \cdot \cos\varphi \tag{A.8}$$

where:

P_{DC} - transferred DC power.

Ignoring the converter losses ($P_{DC} = P_{AC}$), the current modulation index m from equation (A.3) can be expressed through voltage modulation index k:

$$m = \frac{2}{k \cdot \cos\varphi} \tag{A.9}$$

According to equations (A.8) and (A.9), signals of interests are obtained from:

$$i_m = \sqrt{i_d^2 + i_q^2} \qquad v_m = \sqrt{v_d^2 + v_q^2} \qquad \cos\varphi = \frac{i_q}{i_m} \qquad k = \frac{2 \cdot v_m}{V_{DC}}$$

where:

i_d - d-axis current (reactive power).

i_q - q-axis current (active power).

v_d - d-axis voltage.

v_q - q-axis voltage.

Parameters i_d, i_q, v_d, v_q are obtained from previously described AC current controller accordingly as: I_{q_s}, I_{d_s}, E_{q_s}, E_{d_s}. Mathematical implementation in EMTDC/PSCAD environment is shown in Fig. A.14. *cosφ* is modelled as *cos_fi*.

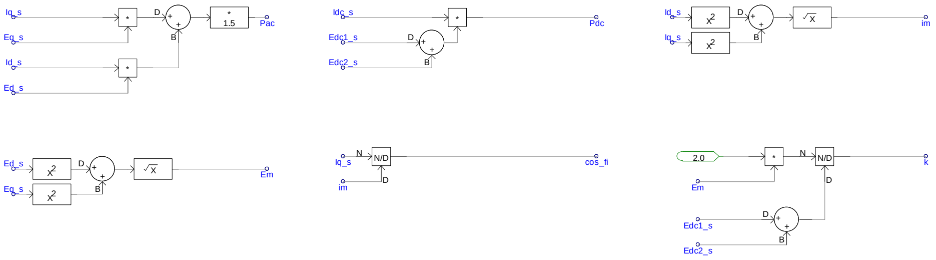

Fig. A.14 Arm Energy Compensating Controller, Operating Principle.

After defining signals of interest, next part is to establish an arm energy balancing mechanism. In order to do so, first thing is to define possible directions for arm energy fluctuations of each single arm and leg. As shown in Fig. A.15, each phase leg may exchange energies with corresponding legs in horizontal direction (between phases), and internally within its upper and lower arm in vertical direction (between arms).

In order to reflect this phenomenon on a mathematical ground, so-called differential-mode energies *En_ABC_DIFF* and common-mode energies *En_ABC_SUM* are introduced, which values under ideal conditions should remain constant in time and equal either to 0 (differential-mode), or to the reference DC component *En_ref_SUM* (common-mode).

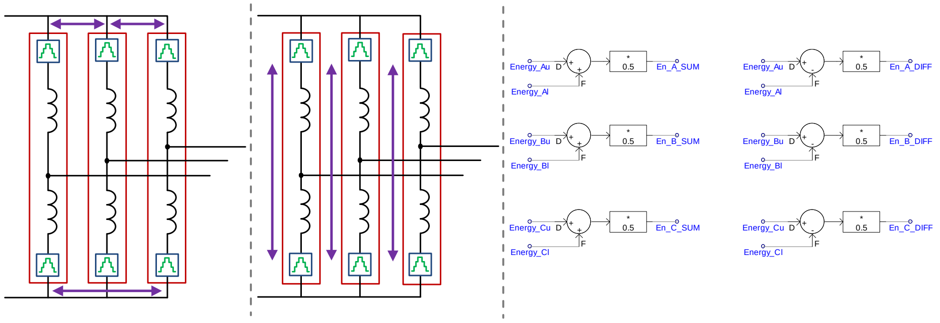

Fig. A.15 Arm Energy Compensating Controller, Differential-Mode and Common-Mode Energies.

Following differential-mode and common-mode energies are defined as:

- for phase leg A:

$$En\_A\_DIFF = \frac{Energy\_Au - Energy\_Al}{2} \qquad En\_A\_SUM = \frac{Energy\_Au + Energy\_Al}{2}$$

- for phase leg B:

$$En\_B\_DIFF = \frac{Energy\_Bu - Energy\_Bl}{2} \qquad En\_B\_SUM = \frac{Energy\_Bu + Energy\_Bl}{2}$$

- for phase leg C:

$$En\_C\_DIFF = \frac{Energy\_Cu - Energy\_Cl}{2} \qquad En\_C\_SUM = \frac{Energy\_Cu + Energy\_Cl}{2}$$

Horizontal Balancing

After defining common-mode energies *En_ABC_SUM*, desired circulating current references *Icirc_ABC_H* for each arm can be individually set. Horizontal balancing can be successfully realized with DC component control of the circulating current. Firstly, assuming ideal symmetrical operation, in order to fulfil condition (A.10), calculated circulating current I_{C_ref} should be:

$$I_{C\_ref} = \frac{i_m \cdot k \cdot cos\,\varphi}{4} \tag{A.10}$$

Under real conditions, value calculated from (A.10) should be however improved by including calculated common-mode energies. Therefore, a P regulator is added with hard limiter, which controls circulating current so that corresponding common-mode energy value is equal to arm energy reference *En_arm_ref*. If it is below, circulating current DC component reference increases above the value from (A.10) until it charges the corresponding leg.

On the other hand, when calculated common-mode energy value is below *En_arm_ref*, then circulating current decreases below the value from (A.10) in order to discharge corresponding leg to the desired level.

Upper and lower threshold limits should be adjusted individually to maintain optimal compromise between dynamic performance (high thresholds - fast response) and component ratings (low thresholds - low arm ripple currents and voltages).

Reference value *En_arm_ref* = E_{arm_ref} is calculated according to user-set parameters, and it represents measured nominal amount of the DC energy stored within a single arm. Its value can be derived from specified number of cells per arm *N* and cell capacitance C_{cell}.

Assuming that at any time, *N* cells will be always inserted within each phase leg, nominal arm energy is obtained according to formula:

$$E_{arm\_ref} = \frac{1}{2} \cdot E_{leg\_ref} = \frac{1}{2} \cdot N \cdot \left[\frac{1}{2} \cdot C_{cell} \cdot \left(\frac{V_{DC}}{N} \right)^2 \right] \tag{A.11}$$

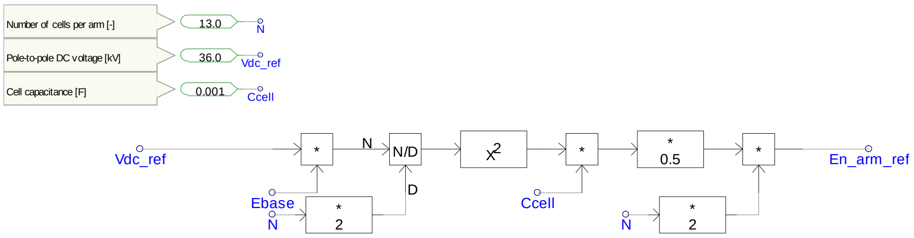

Fig. A.16 Calculation of Arm Energy Reference Signal.

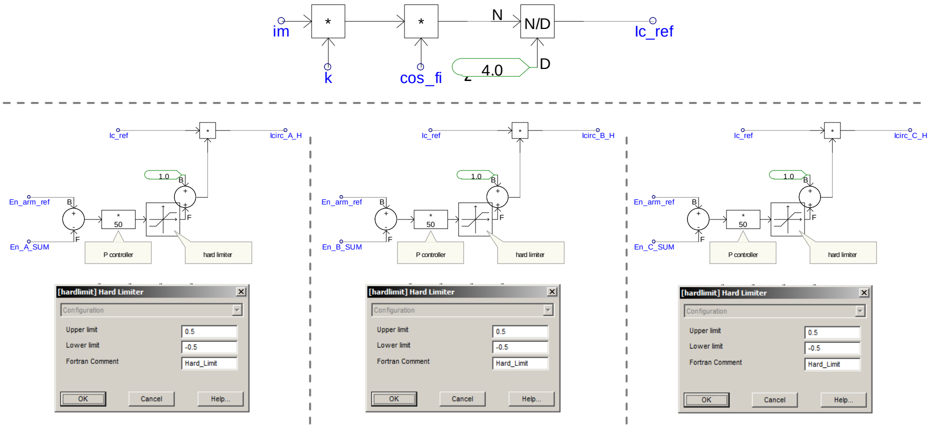

Upper limit 0.5
Lower limit -0.5
Fortran Comment Hard_Limit

Upper limit 0.5
Lower limit -0.5
Fortran Comment Hard_Limit

Upper limit 0.5
Lower limit -0.5
Fortran Comment Hard_Limit

Fig. A.17 Arm Energy Compensating Controller, Nominal (Reference) Arm DC.

Circulating current DC component references *Icirc_A_H*, *Icirc_B_H*, *Icirc_C_H* are compared with the measured ones. Measured DC components of circulating currents are obtained by summating measured arm currents flowing across each arm. In this manner, only uni-directional current values appear. Therefore, their values for each phase are calculated from:

$$I_{circ(A)} = \frac{I_{arm\_1\_s} + I_{arm\_4\_s}}{2} \tag{A.12}$$

$$I_{circ(B)} = \frac{I_{arm\_2\_s} + I_{arm\_5\_s}}{2} \tag{A.13}$$

$$I_{circ(C)} = \frac{I_{arm\_3\_s} + I_{arm\_6\_s}}{2} \tag{A.14}$$

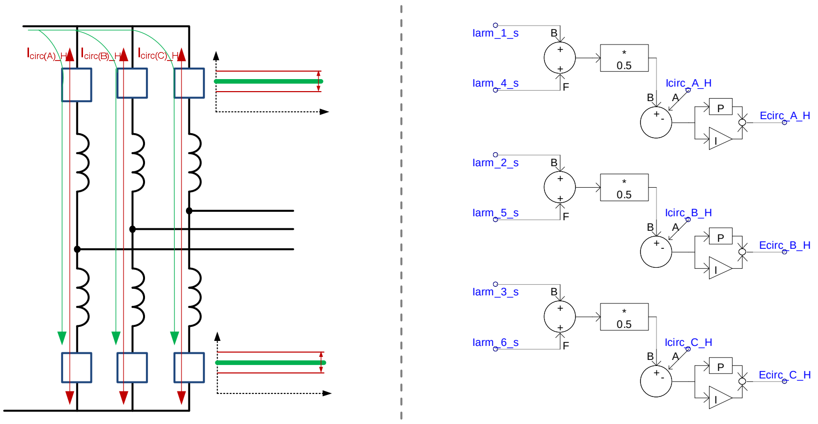

Fig. A.18 Arm Energy Compensating Controller, Horizontal Balancing.

All feedback loops are realized via PI controllers (fig. A.18). Obtained output reference voltages for horizontal balancing are: *Ecirc_A_H*, *Ecirc_B_H*, *Ecirc_C_H*.

Vertical Balancing

After defining differential-mode energies, desired circulating current references $I_{circ\_ABC\_V}$ for each arm can be individually set. Vertical balancing can be successfully realized with bi-directional AC component control of the circulating current.

Assuming that AC circuit phase voltage references are identical for upper and lower arms, it can be seen that AC currents flow in opposite direction towards the grid.

By injecting bidirectional AC component circulating current, resulting AC currents of upper and lower arm become unequal. This is because resulting AC current on the upper arms is subtracted, while on the lower arms is summated. Therefore, a voltage difference appears between upper and lower arm, which forces flow of the differential AC current.

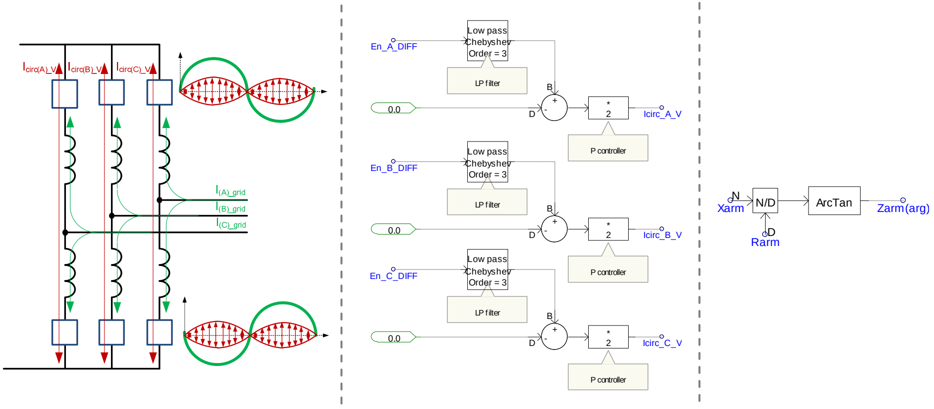

Fig. A.19 Arm Energy Compensating Controller - Vertical Balancing.

Such current is set to flow based on measured differential-mode energy. When *En_ABC_DIFF* > 0, it means that upper arm has higher energy than the lower arm. So the resulting AC current is formed to discharge upper arm and at the same time charge lower arm. Similar, when *En_ABC_DIFF* < 0, it means that lower arm has higher energy than the upper arm. So the resulting AC current is formed to discharge lower arm and at the same time charge upper arm.

In practical implementation, low pass filters are included for differential-mode energy measurements mainly to eliminate non-compensated AC 1st harmonic component (fig. A.20). P controllers are used to obtain necessary circulating current instant values $I_{circ\_ABC\_V}$.

Finally, circulating currents must be converted to reference arm voltages $E_{circ\_ABC\_V}$. Simulation cases have shown, that for most optimal performance these voltages need to be synchronized / locked in phase with measured AC grid voltages E_{abc_s}, and further phase shifted by arm impedance argument $Z_{arm(arg)}$:

$$Z_{arm(arg)} = arctan\left(\frac{X_{arm}}{R_{arm}}\right) \qquad \Big| \quad for\ R_{arm} \cong 0,\quad Z_{arm(arg)} = 90^0 \tag{A.15}$$

Phase tracking of each phase individually is realized through FFT block by extracting fundamental component phases $E_{abc\_s\_P}$ of each AC phase voltage.

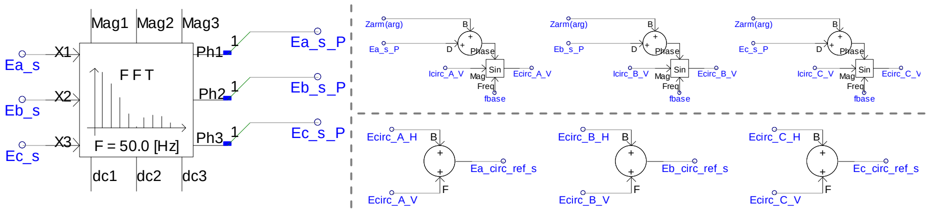

Fig. A.20 Arm Energy Compensating Controller, Phase Synchronization for Vertical Balancing.

Then, circulating currents constitute rotating magnitudes of the circulating voltage references $E_{circ\_ABC\_V}$. These references are formed as sinusoidal signals with initial phase dictated by summated $E_{abc\_ref\_P} + Z_{arm(arg)}$ values, magnitude dictated by $I_{circ\_ABC\_V}$ values and frequency set to base value f_{base}. Final voltage references for circulating current arm energy compensating control are $E_{abc\_circ\_ref\_s}$ given by:

$$E_{a\_circ\_ref\_s} = \left(E_{circ\_A\_V} + E_{circ\_A\_H}\right) \tag{A.16}$$

$$E_{b\_circ\_ref\_s} = \left(E_{circ\_B\_V} + E_{circ\_B\_H}\right) \tag{A.17}$$

$$E_{c\_circ\_ref\_s} = \left(E_{circ\_C\_V} + E_{circ\_C\_H}\right) \tag{A.18}$$

It should be noted that common-mode energies E_{n_SUM} consist ideally not only of DC component, but also of parasitic 2nd harmonic AC component. If not compensated, this harmonic component will enter into circulating current reference.

As a result, parasitic 2nd harmonic will be injected into arm currents of each phase. As each phase is controlled independently, these 2nd harmonic components may become +/-/0 sequence, adding unnecessary losses and distortions.

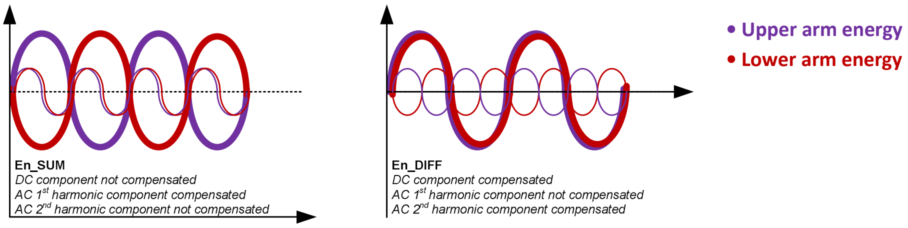

Fig. A. 21 Arm Energy Compensating Controller - Harmonic Component Compensation for Differential- and Common-mode Energies.

In order to eliminate issues related with 2nd harmonic, two solutions are possible:

- apply low-pass filters for common-mode energies E_{n_SUM}, which will allow filtering 2nd harmonic component (control option).
- apply 2nd harmonic arm capacitors across split arm reactors for harmonic trap in each phase leg (hardware option).

A.5 Abstraction Level B - Control Architecture

a. Introduction

Generalized control diagram is shown in Fig. A.22. All controllers: design and their operating principles remain identical as for abstraction level A. The only difference is that PWM Modulator block is added, which modulates AC reference voltage waveforms for each cell individually.

Output 0/1 logic signals are then summed up, summated with DC arm reference voltages, divided by user-set number of cells per arm N, and finally multiplied by E_{base}. In this manner, levelized arm voltage sources are obtained.

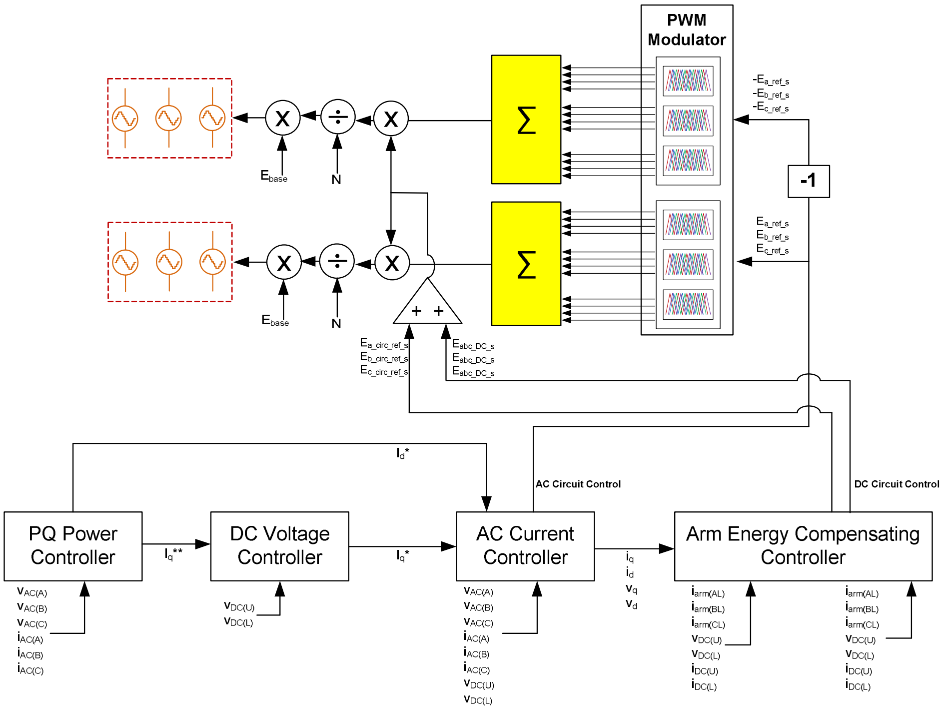

Fig. A.22 Abstraction Level B - Schematic Control Structure.

b. PQ Power Controller, DC Voltage Controller, AC Current Controller, Arm Energy Compensating Controller

All implementation procedure is identical as for abstraction level A. Considered output parameters are:

- from AC Current Controller (+ DC Link Balancing Controller):
  $E_{a\_ref\_s}$, $E_{b\_ref\_s}$, $E_{c\_ref\_s}$
- from Arm Energy Compensating Controller:
  $E_{aU\_circ\_ref\_s}$, $E_{bU\_circ\_ref\_s}$, $E_{cU\_circ\_ref\_s}$, $E_{aL\_circ\_ref\_s}$, $E_{bL\_circ\_ref\_s}$, $E_{cL\_circ\_ref\_s}$

c. PWM Modulator

Each phase PWM modulator block consists of individual N cell modulators, for which each is represented by a single carrier waveform. Modulation is made by phase-shifting carriers at a constant angle. AC voltage references $E_{a\_ref\_s}$, $E_{b\_ref\_s}$, $E_{c\_ref\_s}$ are asymmetrically re-sampled every half-carrier interval times number of cells per arm N. Re-sampled values are sent to cell comparators, which output logic signals for each cell operation.

As input variables are voltage reference signals from AC Current Controller $E_{abc\_ref\_s}$, first thing is to specify required new input constants. These are: switching (carrier/cell) frequency $f_{carrier}$ and re-sampling frequency *Resampling*. Switching frequency $f_{carrier}$ is defined as a product of nominal frequency f_{base} and a user-set pulse ratio p. Re-sampling frequency of the AC voltage references, which will be used when comparing to carrier is defined as a double product of switching frequency $f_{carrier}$ and number of cells per arm N.

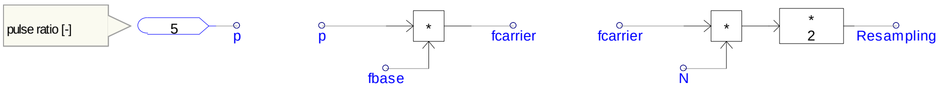

Fig. A.23 PWM Modulator, Defining Input Constants - EMTDC/PSCAD implementation.

Next thing is to determine phase shift [deg] between each carrier according to number of cells (carriers) N. This is realized by following formulas below. Ready values are implemented as global substitutions within the dialog box.

$$\begin{bmatrix} shift\_1u\_ABC \\ shift\_2u\_ABC \\ \vdots \\ shift\_Nu\_ABC \end{bmatrix} = \frac{360}{N} \cdot \begin{bmatrix} 0 \\ 1 \\ \vdots \\ N-1 \end{bmatrix} \tag{A.19}$$

$$\begin{bmatrix} shift\_1l\_ABC \\ shift\_2l\_ABC \\ \vdots \\ shift\_Nl\_ABC \end{bmatrix} = \frac{360}{N} \cdot \begin{bmatrix} 0 \\ 1 \\ \vdots \\ N-1 \end{bmatrix} + 180 \tag{A.20}$$

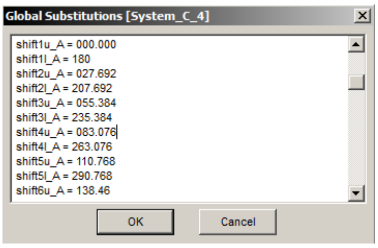

shift1u_A = 000.000
shift1l_A = 180
shift2u_A = 027.692
shift2l_A = 207.692
shift3u_A = 055.384
shift3l_A = 235.384
shift4u_A = 083.076
shift4l_A = 263.076
shift5u_A = 110.768
shift5l_A = 290.768
shift6u_A = 138.46

These parameters are necessary in order to provide accurate sample delay for input voltage references and initial phase of each carrier signal. Absolute sample delays [s] are calculated according to:

$$\begin{bmatrix} delay\_1u\_ABC \\ delay\_2u\_ABC \\ \vdots \\ delay\_Nu\_ABC \end{bmatrix} = \frac{1}{360} \cdot \frac{1}{f_{carrier}} \cdot \begin{bmatrix} shift\_1u\_ABC \\ shift\_2u\_ABC \\ \vdots \\ shift\_Nu\_ABC \end{bmatrix} \tag{A.21}$$

$$\begin{bmatrix} delay\_1l\_ABC \\ delay\_2l\_ABC \\ \vdots \\ delay\_Nl\_ABC \end{bmatrix} = \frac{1}{360} \cdot \frac{1}{f_{carrier}} \cdot \begin{bmatrix} shift\_1l\_ABC \\ shift\_2l\_ABC \\ \vdots \\ shift\_Nl\_ABC \end{bmatrix} \tag{A.22}$$

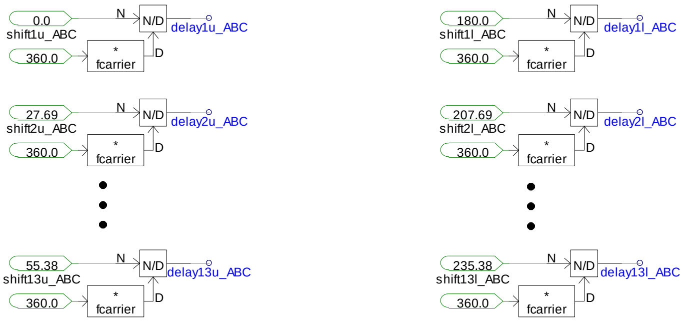

Fig. A.24 PWM Modulator, Reference Sample Shifting per Cell.

Initial phase of each carrier signal is obtained by individually delaying sampling clock for each cell over the calculated value. Binary ON delay block accompanied with AND logic gate delivers desired logic pulse train for re-sampling AC voltage reference signal.

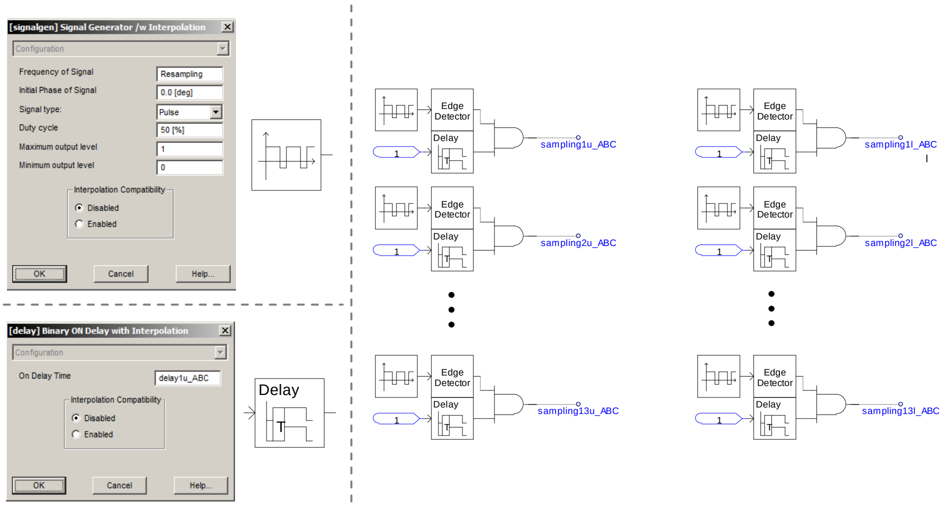

[signalgen] Signal Generator /w Interpolation

Configuration

Frequency of Signal: Resampling
Initial Phase of Signal: 0.0 [deg]
Signal type: Pulse
Duty cycle: 50 [%]
Maximum output level: 1
Minimum output level: 0

Interpolation Compatibility
● Disabled
○ Enabled

[delay] Binary ON Delay with Interpolation

Configuration

On Delay Time: delay1u_ABC

Interpolation Compatibility
● Disabled
○ Enabled

Fig. A.25 PWM Modulator, Reference Sample Shifting per Cell.

Finally, re-sampled reference values are compared with carrier waveforms, which results in output cell *2·N* switching 0/1 signals for each phase: $E_{abc(1\text{-}N)u\_d}$, $E_{abc(1\text{-}N)l\_d}$.

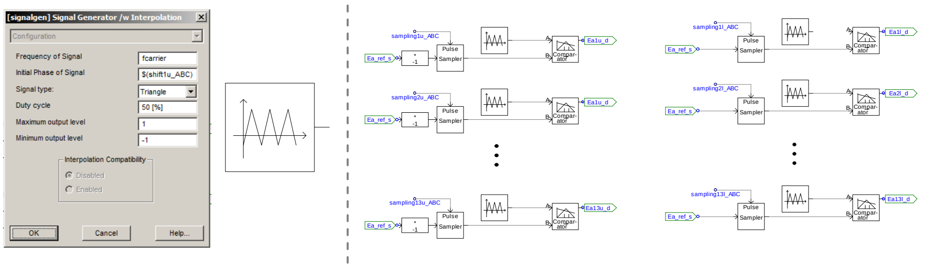

[signalgen] Signal Generator /w Interpolation

Configuration

Frequency of Signal: fcarrier
Initial Phase of Signal: $(shift1u_ABC)
Signal type: Triangle
Duty cycle: 50 [%]
Maximum output level: 1
Minimum output level: -1

Interpolation Compatibility
● Disabled
○ Enabled

Fig. A.26 PWM Modulator, Final PWM Logic Signals.

d. Firing Signals - Abstraction Level B

Final voltage signals are obtained by summating/subtracting DC circuit control signals with AC circuit control signals. DC circuit control signals include circulating current reference signals $E_{abc\_circ\_ref\_s}$ and DC voltage reference signal $E_{abc\_DC\_s}$ is calculated from [pu]:

$$E_{abc\_DC\_s} = \frac{V_{DC(ref)}}{E_{base}} = 2 \tag{A.23}$$

Final voltage signals [pu] are obtained from:

$$V_{arm(AU)} = \left(\frac{E_{circ\_ref\_s}}{N} + \frac{E_{abc\_DC\_s}}{N} \right) \cdot \sum_{i=1}^{N} E_{a(i)u\_d} \tag{A.24}$$

$$V_{arm(AU)} = \left(\frac{E_{circ\_ref\_s}}{N} + \frac{E_{abc\_DC\_s}}{N} \right) \cdot \sum_{i=1}^{N} E_{a(i)u\_d} \tag{A.25}$$

$$V_{arm(AU)} = \left(\frac{E_{circ\_ref\_s}}{N} + \frac{E_{abc\_DC\_s}}{N} \right) \cdot \sum_{i=1}^{N} E_{a(i)u\_d} \tag{A.26}$$

Signals that directly enter into arm controlled voltage sources are also pre-multiplied by E_{base} to convert from [pu] to [kV]:

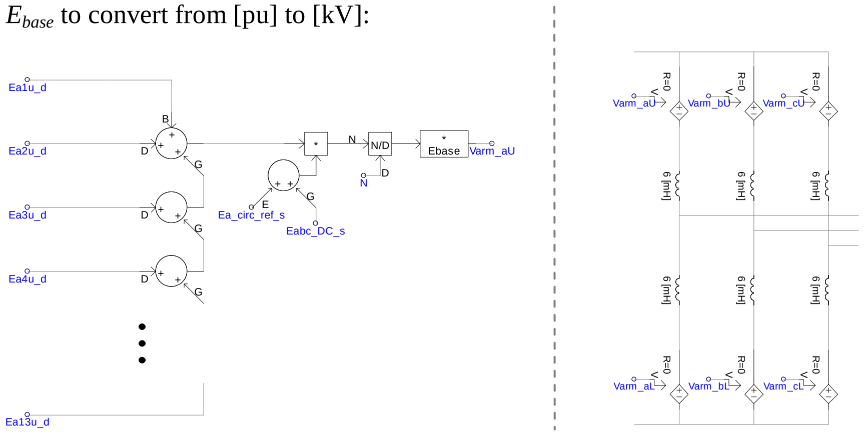

Fig. A.27 Abstraction Level B: Resulting arm voltage signals.

A.6 Abstraction Level C - Control Architecture

a. Introduction

Generalized control diagram is shown in Fig. A.28. All controllers and PWM modulator: design and their operating principles remain identical as for abstraction level B. The main difference is that signals from DC circuit control are not injected directly into arm voltage sources, but rather used as a reference cell voltage values for additional cell voltage balancing controller. Furthermore, as arm voltage sources are replaced by cell capacitors, each cell voltage must be now measured individually to control its value.

Cell voltage balancing control action takes place before PWM modulation, which allows controlling each AC reference voltage separately. As a result, DC and AC circuit control signals summate before PWM modulation and not after, as has been discussed in the abstraction level B.

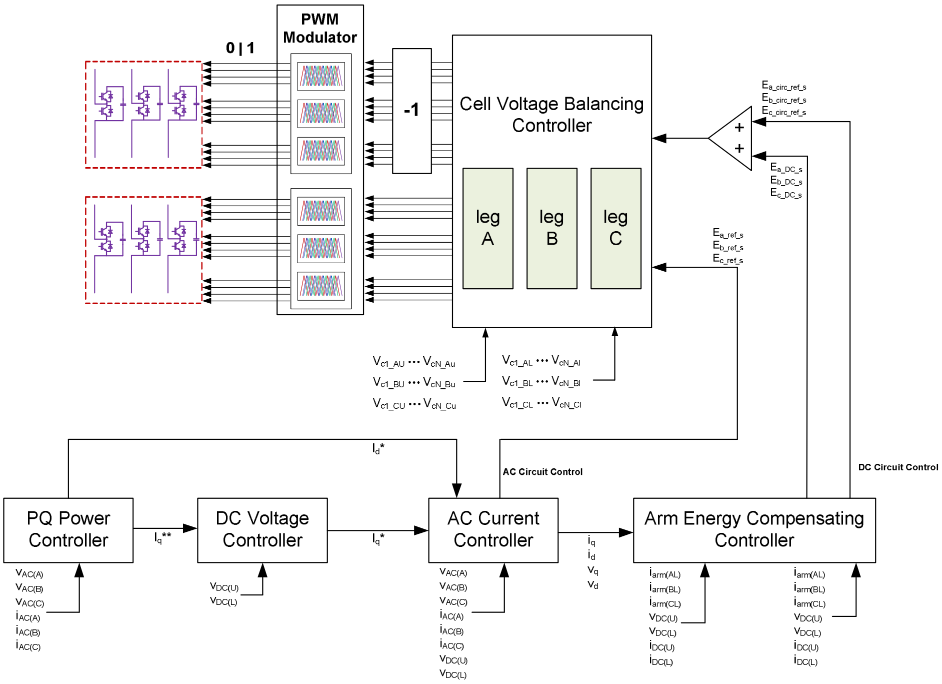

Fig. A.28 Abstraction Level C - Schematic Control Structure.

b. PQ Power Controller, DC Voltage Controller, AC Current Controller, Arm Energy Compensating Controller

All implementation procedure is identical as for abstraction level A. Considered output parameters are:

- from AC Current Controller (+ DC Link Balancing Controller):
  $E_{a\_ref\_s}$, $E_{b\_ref\_s}$, $E_{c\_ref\_s}$
- from Arm Energy Compensating Controller:
  $E_{aU\_circ\_ref\_s}$, $E_{bU\_circ\_ref\_s}$, $E_{cU\_circ\_ref\_s}$, $E_{aL\_circ\_ref\_s}$, $E_{bL\_circ\_ref\_s}$, $E_{cL\_circ\_ref\_s}$

c. Cell Voltage Balancing Controller [82]

Cell balancing controller block is based on [82] and consists of three individual phase leg controllers, where input variable signals are:

- measured upper and lower arm cell voltages: $V_{c(1\text{-}N)\_AU}$, $V_{c(1\text{-}N)\_AL}$, $V_{c(1\text{-}N)\_BU}$, $V_{c(1\text{-}N)\_BL}$, $V_{c(1\text{-}N)\_CU}$, $V_{c(1\text{-}N)\_CL}$.
- circulating current reference signals: $E_{abcU\_circ\_ref}$, $E_{abcL\_circ\_ref}$.
- DC voltage reference signal: $E_{abc\_DC\_s}$.
- AC voltage reference signals: $E_{abc\_ref\_s}$.

Input constants include user-set P controller gains / limits, sampling frequency *Sampling_B*, base voltage *Ebase* and number of cells per arm *N*. First step is to sample all entering measured cell voltages with *Sampling_B* value.

Sampled $E_{cell(1\text{-}N)\_abcU\_s}$, $E_{cell(1\text{-}N)\_abcL\_s}$ signals can be now used to properly regulate DC cell voltages within each single cell. Reference cell voltages $V_{cell\_abc\_ref\_s}$ are [kV] calculated from:

$$V_{cell\_a\_ref\_s} = \left(\frac{E_{a\_circ\_ref\_s}}{N} + \frac{E_{abc\_DC\_s}}{N} \right) \cdot E_{base} \tag{A.27}$$

$$V_{cell\_b\_ref\_s} = \left(\frac{E_{b\_circ\_ref\_s}}{N} + \frac{E_{abc\_DC\_s}}{N} \right) \cdot E_{base} \tag{A.28}$$

$$V_{cell\_c\_ref\_s} = \left(\frac{E_{c\_circ\_ref\_s}}{N} + \frac{E_{abc\_DC\_s}}{N} \right) \cdot E_{base} \tag{A.29}$$

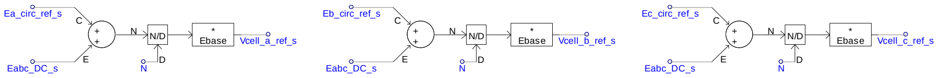

Fig. A.29 Reference cell voltages with DC Circuit & Circulating Current Control.

These voltages are compared with each measured cell voltage across upper and lower arm in the corresponding leg. P controllers are used to compensate difference between signals. Finally, desired command signals for DC circuit control are added to common AC voltage reference, which results in *2N* individual AC voltage references for each phase $E_{abc(1\text{-}N)U\_s}$, $E_{abc(1\text{-}N)L\_s}$ integrated with DC circuit command.

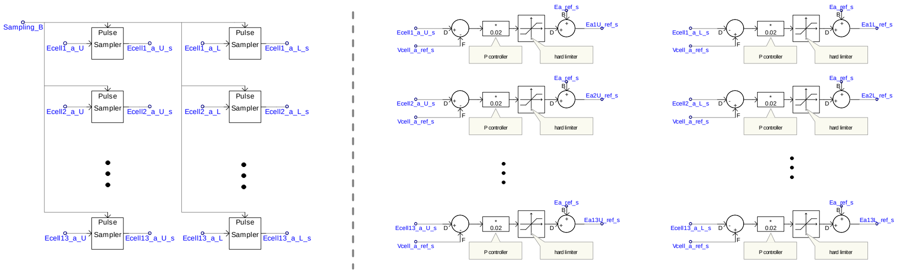

Fig. A.30 Measured cell voltage sampling and cell voltage control.

d. PWM Modulator

All implementation procedure is identical as for abstraction level B. The only difference is cell voltage reference input signal, which for abstraction level B was pure AC reference voltage $E_{abc\_ref\_s}$, identical for each cell.

Now, each cell has its own input reference $E_{abc(1\text{-}N)UL}$, re-sampled cell reference values are compared with carrier waveforms, which results in output cell *2N* switching 0/1 signals for each phase: $E_{abc(1\text{-}N)u\_d}$, $E_{abc(1\text{-}N)l\_d}$.

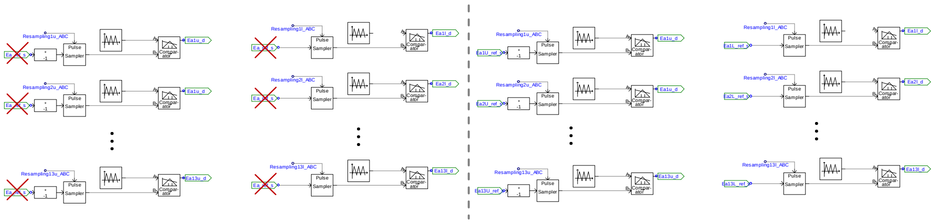

Fig. A.31 PWM modulator - individual cell voltage references instead of common one.

e. Firing Signals - Abstraction Level C

Switching 0/1 signals for each phase from PWM modulator: $E_{abc(1\text{-}N)u\_d}$, $E_{abc(1\text{-}N)l\_d}$ correspond to switching operation of each cell according to:

$$E_{abc(1-N)u\_d} = \begin{cases} 1, & cell\ \ ON \\ 0, & cell\ \ OFF \end{cases} \qquad\qquad E_{abc(1-N)l\_d} = \begin{cases} 1, & cell\ \ ON \\ 0, & cell\ \ OFF \end{cases}$$

Logic signals are then directly transferred as inputs to IGBT gate drivers, which inter-switch each cell according to their values.

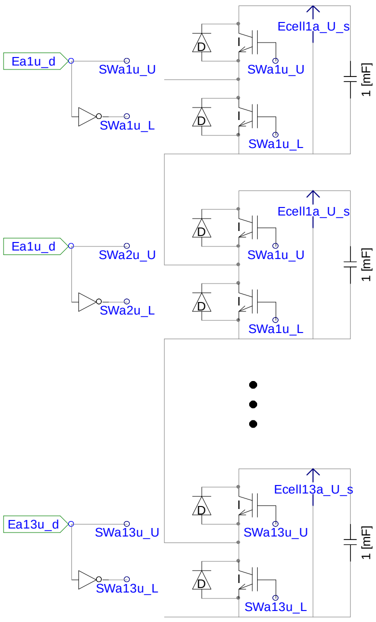

Fig. A.32 Abstraction Level C: Resulting IGBT Logic Signals.

A.7 Energization Sequence for System A

Figure A.33 shows back-to-back MMC system with marked AC contactors *BRK1-4_ABC* and DC making switches *BRK1-23_DC*. Start-up procedure is valid for abstraction level B at the generator-side and for abstraction level C at the grid-side.

Table A.1 Energization sequence for BtB MMC system (System A).

lp.	Unit	Parameter	Pre-State	Activation Time	Post-State	Parameter
1	Generator-Side PQ Controller	`Id_ref_G = 0` `Iq_ref_G = -1`	**ON**	**0.00 s**	**ON**	`Id_ref_G = 0` `Iq_ref_G = -1`
2	Generator-Side AC Current Controller		**ON**	**0.00 s**	**ON**	
3	Generator-Side Circulating Current Controller		**ON**	**0.00 s**	**ON**	
4	Grid-Side PQ Controller	`Id_ref = 0` `Iq_ref = 1`	**ON**	**0.00 s**	**ON**	`Id_ref = 0` `Iq_ref = 1`
5	Grid-Side DC Voltage Controller		**ON**	**0.00 s**	**ON**	
6	Grid-Side AC Current Controller		**ON**	**0.00 s**	**ON**	
7	Grid-Side Circulating Current Controller		**ON**	**0.00 s**	**ON**	

8	Generator-Side Insertion Resistors BRK1_ABC, BRK2_ABC	`R1_ABC = 100 OHM`
		`R2_ABC = 100 OHM`
		`BRK1_ABC = CLOSE`
		`BRK2_ABC = OPEN`
			ON	**0.20 s**	**OFF**	`BRK1_ABC = OPEN`
						`BRK2_ABC = CLOSE`

9	Grid-Side Insertion Resistors BRK3_ABC, BRK4_ABC	`R3_ABC = 100 OHM`
		`R4_ABC = 100 OHM`
		`BRK3_ABC = CLOSE`
		`BRK4_ABC = OPEN`
			ON	**0.20 s**	**OFF**	`BRK3_ABC = OPEN`
						`BRK4_ABC = CLOSE`

10	DC Bus Breakers BRK5_DC, BRK6_DC	`BRK5_DC = OPEN` `BRK6_DC = OPEN`	**OFF**	**0.16 s**	**ON**	`BRK5_DC = CLOSE` `BRK6_DC = CLOSE`
11	Auxiliary DC Voltage Breaker BRK7_DC	`V_DC = 36 kV (1 pu)` `BRK7_DC = CLOSE`	**ON**	**0.60 s**	**OFF**	`V_DC = 0 kV (0 pu)` `BRK7_DC = OPEN`

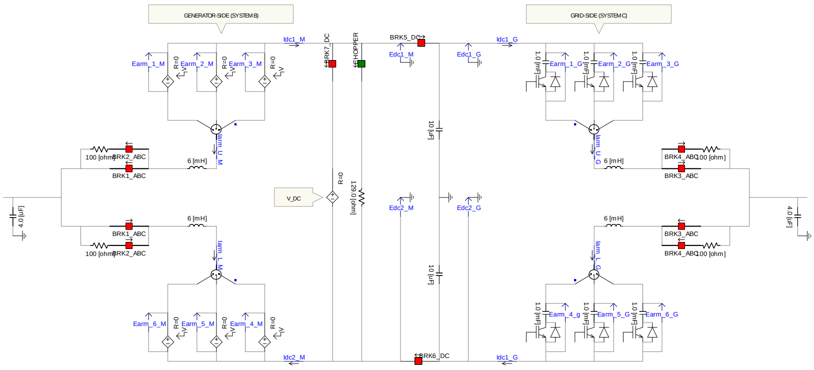

Fig. A.33 Insertion Resistors & Breaker Locations for Energization Mode.

During start-up sequence, generator-side is energized by means of virtual DC voltage source, which gets disconnected after arm energies from system B reach their nominal values. Grid-side unit is firstly galvanically isolated from the generator-side, which allows preliminary cell capacitor charging from the grid to the total maximum value of $\sqrt{2}\cdot V_{(ABC)}$ for each leg.

In order to avoid high DC currents that appear when interconnecting generator- and grid-sides due to DC voltages difference, arm insertion resistors are added. After first DC current transients, arm insertion resistors are by-passed and both sides continue charging until nominal arm energy values are reached.

Finally, when all signals become stable, virtual DC voltage source is disconnected from the DC link and reduced to 0. After few periods required for DC voltage control, MMC system is ready for service.

B. System B: DC/DC Boost Converter + NPC-3L Converter

B.1 Introduction

Figure B.1 presents schematic diagram of the proposed concept. On the contrary to the System A, generator operating voltage can be flexibly set to much lower values (i.e. 3.3 kV), and system can be easily scaled for the desired value. On the generator-side, conventional 2L converter is utilized.

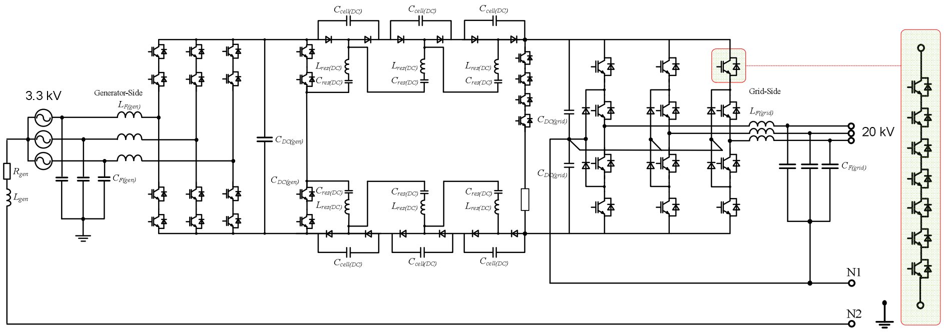

Fig. B.1 Schematic Representation of System B.

Switched resonant capacitor DC/DC boost converter is proposed [54], and can be easily scaled and/or replaced by another capacitor-ladder type. Scaling is made by adding/removing DC passive capacitor cells from the topology. One extra DC cell should be considered for possible redundant operation.

On the grid-side, NPC-3L is proposed as it has most experience on the industrial field among other multilevel converters. Extra IGBTs are added in each valve for possible redundant operation

B.2 2L + DC/DC Boost + NPC-3L - General Control Architecture

a. Introduction

Following chapter shows position of the required signal sensors for three individual operating units: VSC-2L, DC/DC Boost and NPC-3L. This includes high-level active/reactive power, current control and DC voltage controllers, low-level PWM modulator. Control algorithms are identical as for system A (back-to-back MMC).

b. Electrical Sensors - Location

Figure B.2 shows displacement of the required current and voltage sensors in order to properly operate system B.

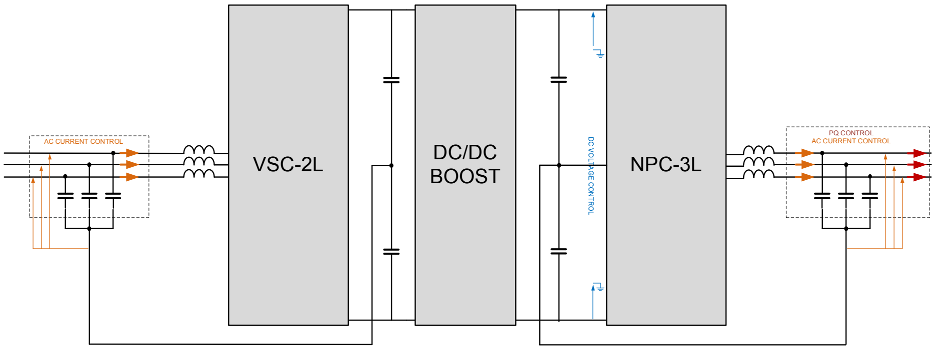

Fig. B.2 Sensor locations for all required measured electrical signals.

Following controllers are involved for each side:

- **PQ power controller (only grid-side unit):**
  - x3 phase AC current sensors placed after C filter branches [$i_{AC(A)}$ | $i_{AC(B)}$ | $i_{AC(C)}$].
  - x3 phase AC voltage sensors placed after C filter branches [$v_{AC(A)}$ | $v_{AC(B)}$ | $v_{AC(C)}$].
- **DC voltage controller (only grid-side unit):**
  - x2 DC voltage sensors placed between each DC pole and common-mode point [$v_{DC(U)}$ | $v_{DC(L)}$].
- **AC current controller:**
  - x3 phase AC current sensors placed between converter legs and C filter branches [$i_{AC(A)}$ | $i_{AC(B)}$ | $i_{AC(C)}$].
  - x3 phase AC voltage sensors placed after C filter branches [$v_{AC(A)}$ | $v_{AC(B)}$ | $v_{AC(C)}$].
- **DC voltage balancing (zero-sequence) controller:**
  - x2 DC voltage sensors placed between each DC pole and common-mode point [$v_{DC(U)}$ | $v_{DC(L)}$].

B.3 VSC-2L - Control Architecture

a. Introduction

Standard control diagram for 2-level converters is shown in Fig. B.3. As a result, complete control system is divided into 2 units: AC current control and PWM modulator.

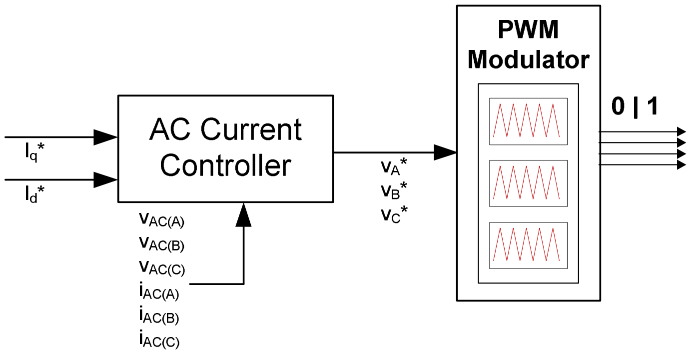

Fig. B.3 VSC-2L - Schematic Control Structure.

b. AC Current Controller

AC current controller is similar as for system A (back-to-back MMC). DC link balancing controller is deactivated by setting E_{0_ref} value to 0. Output signals are E_{a_ref}, E_{b_ref}, E_{c_ref}.

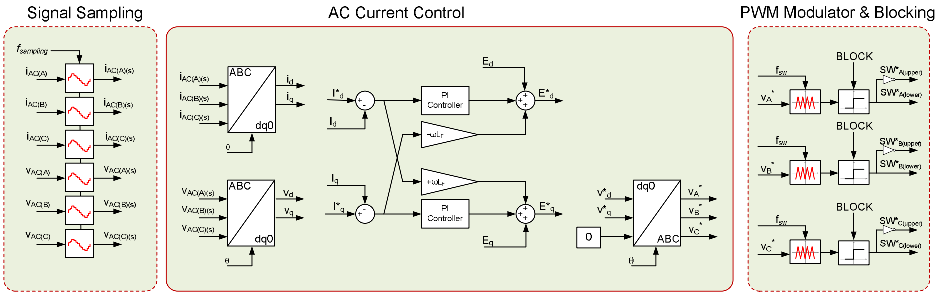

Fig. B.4 AC Current Control in the rotating dq reference frame.

Due to stationary operation, frequency can be controlled externally with no need for PLL regulator (no frequency control). PWM modulator is carrier-based bipolar with asymmetrically sampled voltage reference signals: v_a^*, v_b^*, v_c^*. User-specified switching frequency f_{sw} equals carrier frequency.

c. PWM Modulator

PWM triangular carrier-based modulator is used. In practice, its design is identical as for system A when number of cells $N = 1$.

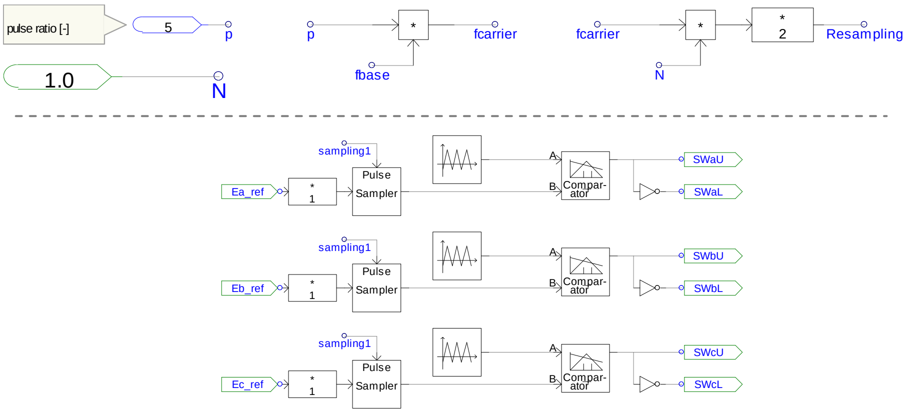

Fig. B.5 PWM Modulator for VSC-2L - EMTDC/PSCAD Implementation

d. Firing Signals

Upper and lower cells are now equivalent to upper and lower ideal valves, each represented by ideal IGBT with anti-parallel diode. Each logic signal enters to corresponding phase leg.

VSC-2L is implemented as a standard generator-side 2-level converter unit, since it provides lowest DC current ripple flowing through the generator-side circuit.

B.4 DC/DC Boost Converter - Control Architecture

a. Introduction / Cell Balancing Controller

Utilized switched capacitor resonant converter has almost no control capability. It consists only of two active IGBT valves: T1 and T2, which must be inter-switched at fixed resonant frequency f_{res} in order to balance upper and lower cell capacitors.

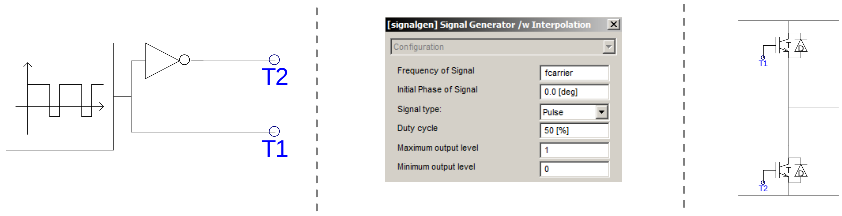

Frequency of Signal: fcarrier
Initial Phase of Signal: 0.0 [deg]
Signal type: Pulse
Duty cycle: 50 [%]
Maximum output level: 1
Minimum output level: 0

Fig. B.5 DC/DC Boost Converter Capacitor Charging Control - EMTDC/PSCAD Implementation.

Theoretical Analysis

ZCS converter includes a pair of valves with series-connected IGBTs on the generator DC-side along with cascaded passive modular cells, each containing: storage capacitor, resonant capacitor, resonant inductor and a pair of free-wheeling diodes.

Required number of cells in upper DC leg N and in lower DC leg M is proportional to the desired output voltage V_{OUT} according to formula (B.1), where V_{IN} is input DC voltage from 2-level generator-side converter:

$$V_{OUT} = \left(N + M - 1\right) \cdot V_{IN} \tag{B.1}$$

Resonant components are used to form a resonant path, so that charging and discharging currents can be passed through series resonance in order to achieve soft switching. As a result, valves T1 and T2 are controlled complementary with 50% duty cycle and switched at resonant frequency f_{res}. Operating sequence is shown in Figure B.6.

1. Operating sequence: T1 =ON, T2 = OFF

All the negative resonant capacitors (C_{n1}, C_{n2}, …, $C_{n(M)}$) are charged by input voltage source V_{IN} and negative filter capacitors (C_{no1}, C_{no2}, …, $C_{no(M)}$) through negative resonant inductors (L_{n1}, L_{n2}, …, $L_{n(M)}$) in a sinusoidal shape, and in the meanwhile, the energy stored in the positive resonant capacitors *(*C_{p1}, C_{p2}, …, $C_{p(N)}$) are released to positive filter capacitors (C_{po1}, C_{po2}, …, $C_{po(N)}$) through positive resonant inductors (L_{p1}, L_{p2}, …, $L_{p(N)}$) in a sinusoidal waveform.

At the end of half switching period, all the currents of resonant inductors decrease to zero when the switching frequency is the same as resonant frequency.

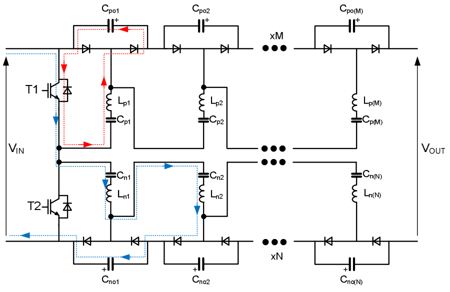

Sequence #1: **T1 = ON, T2 = OFF**

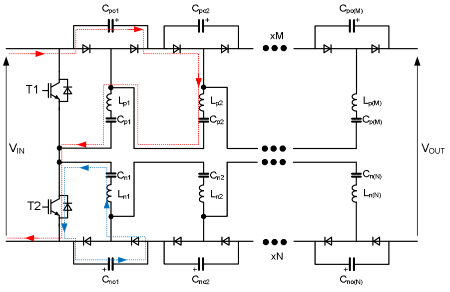

Sequence #2: **T1 = OFF, T2 = ON**

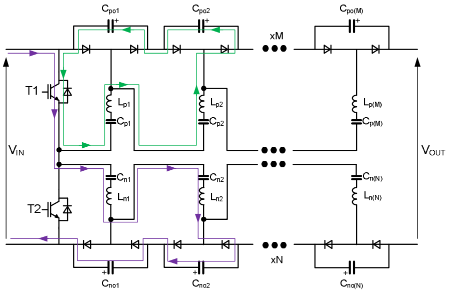

Sequence #3: **T1 = ON, T2 = OFF**

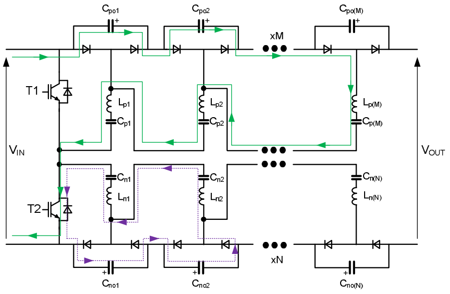

Sequence #4: **T1 = OFF, T2 = ON**

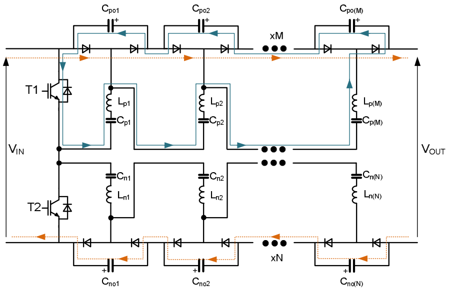

Sequence #4: **T1 = ON, T2 = OFF**

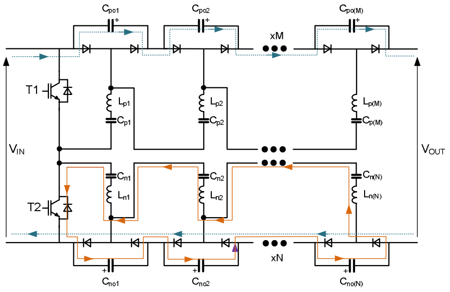

Sequence #6: **T1 = OFF, T2 = ON**

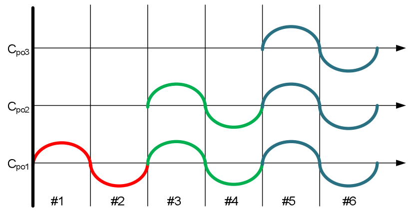

Current in upper DC leg

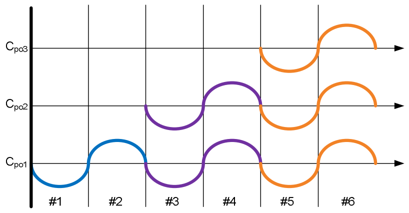

Current in lower DC leg

Fig. B.6 DC/DC Boost Converter Operating Principle - resonant soft switched capacitor charging operation.

2. Operating sequence: T1 =OFF, T2 = ON

The energy stored in the negative resonant capacitors, which are charged in the first half switching period, are released to the corresponding negative filter capacitors through the negative resonant inductors in a sinusoidal shape, and in the meanwhile, all the positive resonant capacitors (C_{p1}, C_{p2},…, $C_{p(N)}$) are charged by the input voltage source or/and positive filter capacitors through the positive resonant inductors in a sinusoidal waveform. All the filter capacitors and the input voltage source power the load.

Figure B.6 presents charging and discharging current commutation loops for transferring energy in first 6 sequences. More information on this topology is available in [54].

b. Delimitations

In order to maintain optimal performance for DC/DC boost operation according to reference [54], following design constraints appear:

- Converter is symmetrical, i.e. number of cells in upper branch M and in lower branch N is equal: $N = M$.
- Each voltage cell V_{cell} is equal to V_{in}. This gives desired output voltage with regard to number of cells/levels $N+M$ as:

$$V_{out} = V_{in} \cdot (N + M + 1) \tag{B.2}$$

- In order to minimize distortions, switching/resonant frequency is chosen to be equal of VSC-2L carrier frequency $f_{res} = f_{carrier}$. Assuming resonant filter inductance $L_p = L_n = L_{res}$, filter capacitance is calculated from:

$$C_n = C_p = \frac{1}{(2 \cdot \pi \cdot f_{res})^2 \cdot L_{res}} \tag{B.3}$$

- Upper cell capacitors are equal to lower cell capacitors $C_{no} = C_{po}$.

DC/DC Boost converter is chosen specifically due to its modular design, simple control, and low number of active switches. Required energy for boost operation is transferred in resonant frequency through cell capacitors, which minimize cost of the overall design.

B.5 NPC-3L Converter - Control Architecture

a. Introduction

Standard control diagram for 3-level converters is shown in Fig. B.7. As a result, complete control system is divided into four units: PQ control, DC voltage control, AC current control and PWM modulator.

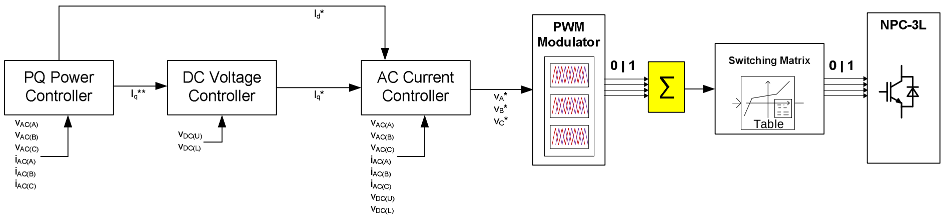

Fig. B.7 NPC-3L - Schematic Control Structure.

b. PQ Power Controller

PQ power controller is identical as for system A (back-to-back MMC). Output signals are I_{q_ref}, I_{d_ref}.

c. DC Voltage Controller

DC voltage controller is identical as for system A (back-to-back MMC). Output signals are E_{dc_x}, E_{dc_y}.

d. AC Current Controller + DC Link Balancing Controller

AC current controller is similar as for system A (back-to-back MMC). Output signals are E_{a_ref}, E_{b_ref}, E_{c_ref}.

e. PWM Modulator

PWM triangular phase-shifted carrier-based modulator is used. In practice, its design is identical as for system A when number of cells $N = 2$. In total, 12 output switching logic signals are obtained

f. Firing Signals

Switching output 0/1 signals are summated for each phase and enter into switching matrix, in which specific switching pattern for all phase switches is provided. In simulation model, this function is provided by X-Y transfer function block. *X* is input parameter from PWM modulator, while *Y* is user-set logic parameter according to NPC operating principles.

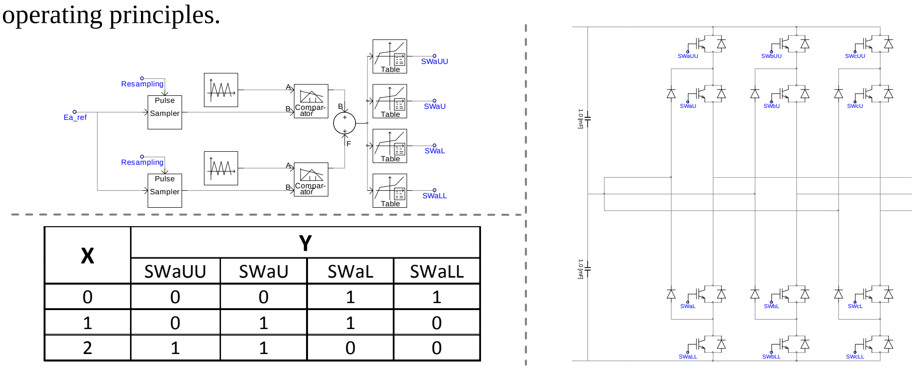

X	Y			
	SWaUU	SWaU	SWaL	SWaLL
0	0	0	1	1
1	0	1	1	0
2	1	1	0	0

Fig. B.8 NPC-3L PWM Modulator - EMTDC/PSCAD Implementation.

B.6 Energization Sequence for System B

System B provides unidirectional power flow (from generator to the grid). As a result, special considerations are required on the procedure for how to start the system. An idea to energize the generator-side converter is by connecting it to the grid. In order to do so, a voltage on the feeder network needs to be decreased for the generator-side system. This is obtained by 3 methods:

- **Method I:**
  Additional 3rd winding of the substation transformer (small feeders).
- **Method II:**
  Tap changer on substation transformer windings and an autotransformer for each feeder.
- **Method III:**
  Conventional transformer for each feeder.

Described methods I, II and III are presented in Figure B.9.

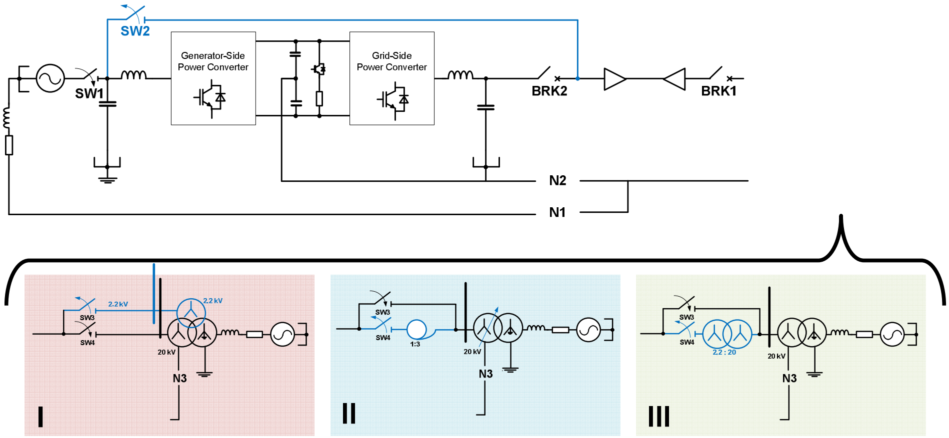

Fig. B.9 Energization sequence for generator-side systems with uni-directional power flow.

Optimal method can be determined by the specific size and feeder network configuration. The energization sequence for methods I, II and III is as follows:

Table. B.1 Switching sequence during start-up procedure for system B.

Switching Sequence	Switches / Breakers (0 = OFF, 1 = ON)					
	SW1	SW2	SW3	SW4	BRK1	BRK2
Converter units are blocked	0	1	1	0	0	0
Grid energizes power converter through its generator-side. Power surplus is burned in chopper	0	1	1	0	**1**	0
Generator is connected to the generator-side converter	**1**	**0**	1	0	1	0
Feeder voltage increase to the grid-side converter level	1	0	**0**	**1**	1	0
Feeder is connected to the grid-side converter	1	0	0	1	1	**1**

C. System C: AC/AC Boost Converter + NPC-5L Converter

C.1 Introduction

Figure C.1 presents schematic diagram of the proposed concept. Similarly for system A (Back-to-Back MMC), generator operating voltage should be kept relatively high (e.g. 12 kV) in order to minimize number of IGBT devices/amount of silicon, but it is not so related with voltage on the grid side, as chain link cells have independent DC link voltages from the common DC link voltage (seen by the grid-side unit). Therefore in practice, voltage can be also set to any desired value. It is assumed that chain link cells are equipped with pre-charged DC sources. DC sources are being constantly re-charged by an external 2-level converter.

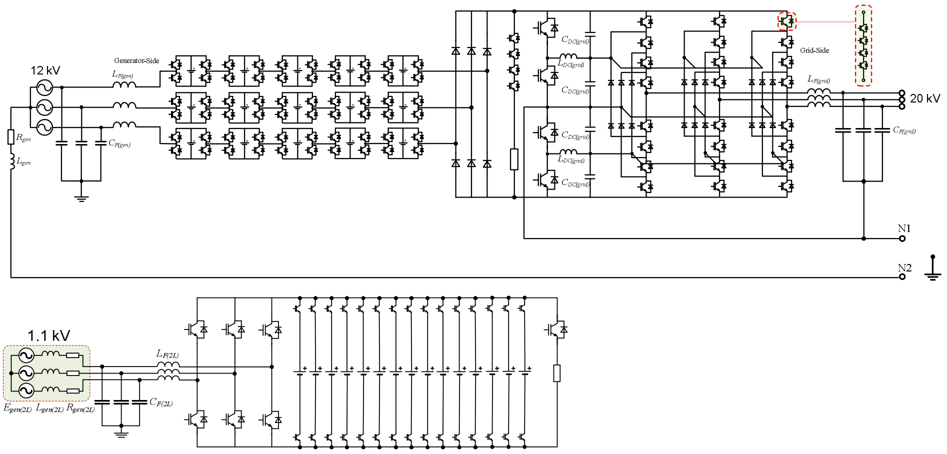

Fig. C.1 Schematic Representation of System C.

Rectification at the common DC link voltage is done by passive diode rectifier, which includes series-connected diodes in each arm. On the grid-side, NPC-5L is proposed with a balancing clamping bridge. Extra IGBTs are added in each arm for possible redundant operation.

C.2 VSC-2L + AC/AC Boost + NPC-5L - General Control Architecture

a. Introduction

Following chapter shows position of the required signal sensors for three individual operating units: chain link, clamping bridge and NPC-5L. This includes AC current control and DC voltage control, low-level DC link balancing control. High-level control algorithms for the grid-side are identical as for A and B systems.

b. Electrical Sensors - Location

Figure C.2 shows displacement of the required current and voltage sensors in order to properly operate system C.

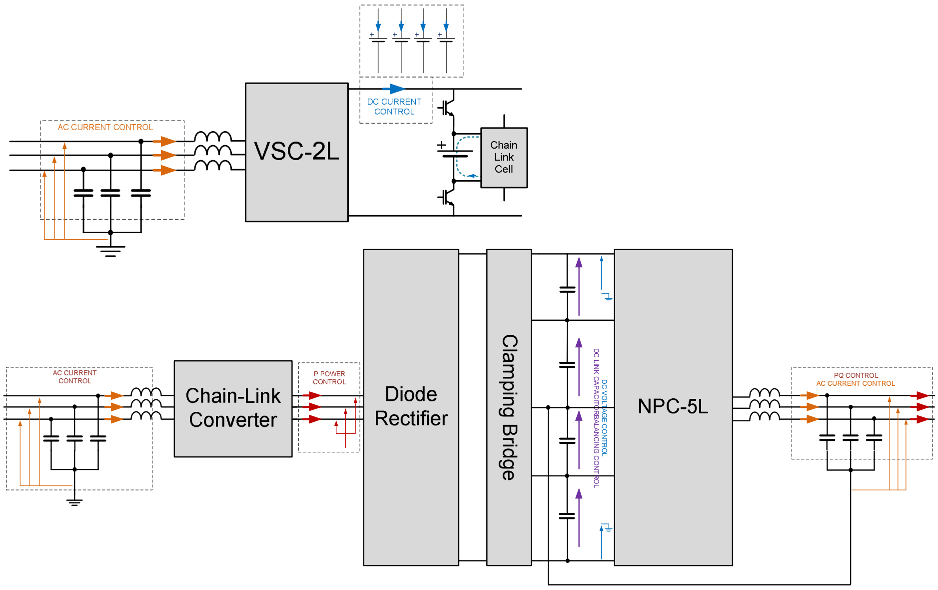

Fig. C.2 Sensor locations for all required measured electrical signals.

Following controllers are involved for each unit:

- **DC current controller (only 2-level converter):**
  - *x18 phase current sensors placed in branches with cell DC batteries [$i_{AC(A)}$ | $i_{AC(B)}$ | $i_{AC(C)}$].*
  - *x1 DC current sensor placed on the 2-level converter DC link [$v_{AC(A)}$ | $v_{AC(B)}$ | $v_{AC(C)}$].*
- **P power controller (only generator-side unit):**
  - *x3 phase AC current sensors placed at the diode rectifier terminals [$i_{AC(A)}$ | $i_{AC(B)}$ | $i_{AC(C)}$].*
  - *x3 phase AC voltage sensors placed after the diode rectifier terminals [$v_{AC(A)}$ | $v_{AC(B)}$ | $v_{AC(C)}$].*
- **PQ power controller (only grid-side unit):**
  - *x3 phase AC current sensors placed after C filter branches [$i_{AC(A)}$ | $i_{AC(B)}$ | $i_{AC(C)}$].*
  - *x3 phase AC voltage sensors placed after C filter branches [$v_{AC(A)}$ | $v_{AC(B)}$ | $v_{AC(C)}$].*
- **DC voltage controller (only grid-side unit):**
  - *x2 DC voltage sensors placed between each DC pole and common-mode point [$v_{DC(U)}$ | $v_{DC(L)}$].*
- **DC link capacitor balancing controller (grid-side clamping bridge):**
  - *x4 DC voltage sensors placed across each clamped DC link capacitor [$v_{DC(UU)}$ | $v_{DC(U)}$ | $v_{DC(L)}$ | $v_{DC(LL)}$].*
- **AC current controller:**
  - *x3 phase AC current sensors placed between converter legs and C filter branches [$i_{AC(A)}$ | $i_{AC(B)}$ | $i_{AC(C)}$].*
  - *x3 phase AC voltage sensors placed after C filter branches [$v_{AC(A)}$ | $v_{AC(B)}$ | $v_{AC(C)}$].*
- **DC voltage balancing (zero-sequence) controller:**
  - *x2 DC voltage sensors placed between each DC pole and common-mode point [$v_{DC(U)}$ | $v_{DC(L)}$].*

C.3 VSC-2L Control Architecture

a. Introduction

The need for an external 2-level converter can be explained by means of Figure C.2. It presents discharging current commutation loops of the chain link converter for positive and negative generator voltages.

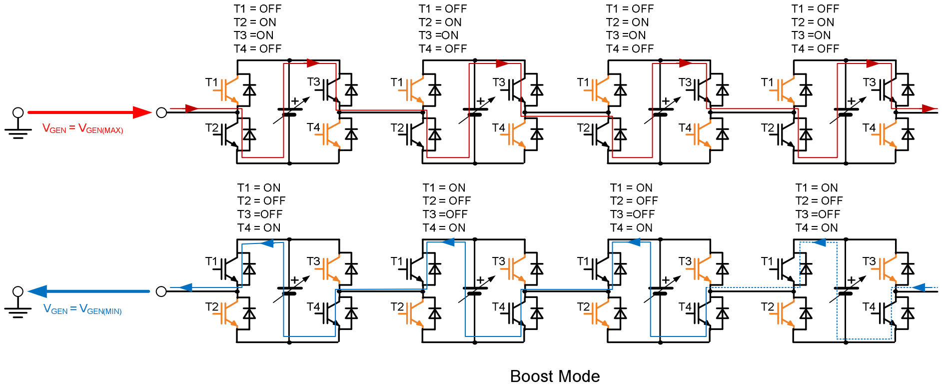

Fig. C.2 Current commutation path in the chain link converter for AC/AC boost operation.

When no external circuitry is applied, boost operation of chain link converter will result in uni-directional currents flowing through cell capacitors. If no net power balance is achieved, then eventually the capacitors will discharge providing no more boost operation.

In order to keep DC capacitors charged, an isolated 2-level converter is used. It controls RMS DC currents with values equal to the ones generated by chain link converter control, but forces currents to flow in opposite direction, as shown in Figure C.2. IGBT switches in series with DC sources are used to decouple 2-level converter from the chain link converter operation.

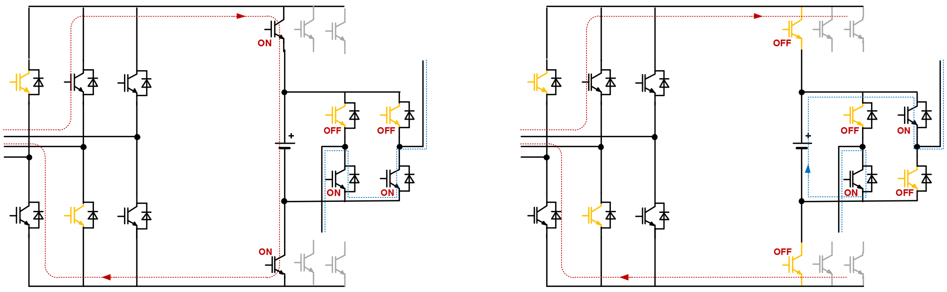

DC source charging (chain link cell OFF / by-passed)

DC source discharging (chain link cell ON)

Fig. C.2 DC source loading states: charging (left) and discharging (right).

When a specific chain link cell is bypassed, then the series connected IGBTs in the corresponding branch will be turned ON and DC source charged. On the contrary, when chain link cell is ON, then IGBTs in the corresponding branch are turned OFF to isolate chain link circuit from the 2-level external circuit. Figure C.3 demonstrates decoupling between chain link cell and a 2-level branch.

In order to simplify the external circuit control, it is assumed that all the existing DC sources are connected in parallel to the DC link of a single 2-level converter. This assumption is justified for following conditions:

- All existing cell capacitors operate at identical DC voltage values in any time $V_{DC(cell)}$.
- All existing chain link cells are switched at the identical switching frequency $f_{sw(cell)}$.
- Generator operation remains symmetrical with equal loading of each phase.

Figure C.3 shows calculation of the required resulting DC charging current for all DC batteries in the system. All RMS currents flowing through DC sources $i_{DC(cell)}$ are measured, summated and averaged. Finally, value $I_{DC(CL)}{}^*$ is obtained as a reference for the DC current controller.

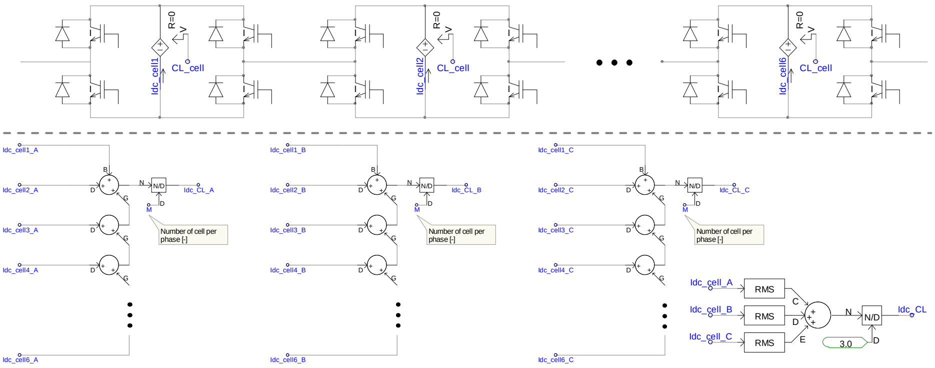

Fig. C.4 Averaging of the instantaneous current flowing through the DC battery.

Standard control diagram for the 2-level converter is shown in Fig. C.5. The complete control system is divided into 3 units: DC current control, AC current control and PWM modulator.

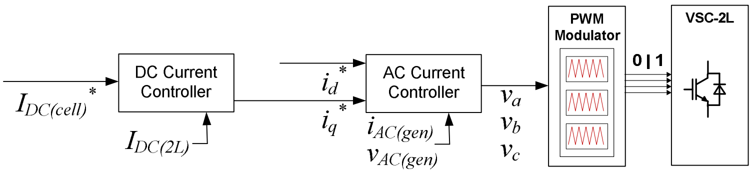

Fig. C.5 VSC-2L - Schematic Control Structure.

b. DC Current Control

DC current is controlled by measuring RMS current flowing through the DC link $i_{DC(2L)}$. PI controller is used to regulate output q-axis reference current $i_q{}^*$ so that discharging RMS current $I_{DC(CL)}{}^*$ equals DC link charging RMS current $I_{DC(2L)}$.

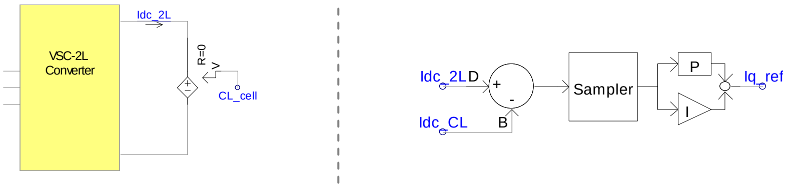

Fig. C.6 DC Current Controller - EMTDC/PSCAD implementation.

c. AC Current Control , PWM Modulator, Firing Signals

Models for AC current controller, PWM modulator and firing signals are identical as for the equivalent 2-level converter in system B.

C.4 AC/AC Boost Converter - Control Architecture

a. Introduction

Standard control diagram for the chain link converter is shown in Fig. C.7. As a result, complete control system is divided into 3 units: CL AC voltage control (magnitude), CL AC voltage control (phase) and PWM modulator.

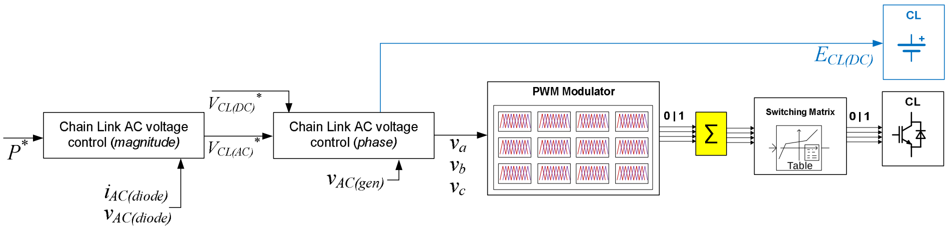

Fig. C.7 Chain Link (CL) Boost Converter - Schematic Control Structure.

b. Chain Link AC Voltage Control (Magnitude)

Chain Link AC Voltage (Magnitude) controller acts as a P controller, similar to PQ power controller in systems A and B. Chain link source voltages are synchronized in phase with generator voltages to maintain boost operation, and then only the resulting voltage magnitude is used to control active power (current) flow $P_{AC(diode)}$.

First step is to measure 3-phase active power $P_{AC(diode)} = P_d$ at the diode bridge terminals by multiplying instantaneous current and voltage values, and adding them together. P_d^* is a user-input value [pu], which regulates amount of the delivered input power. Using feedback loop with PI controller, a reference voltage magnitude V_{CL}^* [kV] is obtained for the chain link controller.

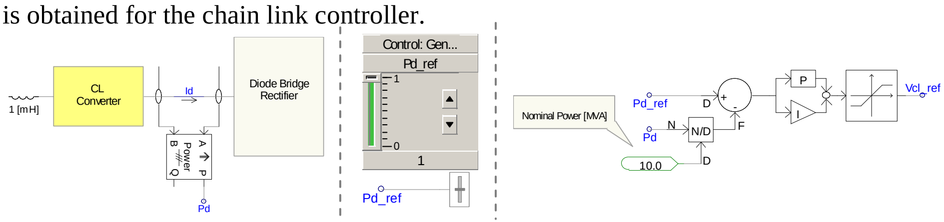

Fig. C.8 Chain Link AC Voltage (Magnitude) controller - EMTDC/PSCAD implementation.

c. Chain Link AC Voltage Control (Phase)

In order to allow chain link boost operation, modulated voltage phase references should be synchronized with the corresponding generator phase voltages. Therefore, phase voltages at the generator terminals $V_{gen(A)}$, $V_{gen(B)}$, $V_{gen(C)}$ are measured. Ideally, reference phase voltage *Theta_M* is equal to initial phase of the voltage source, which models generator rotor flux angle. In reality, rotor flux calculator should be implemented to determine flux angle. In this work, it is assumed that rotor phase angle is directly obtained from signal generator (in the same manner as for the previous systems).

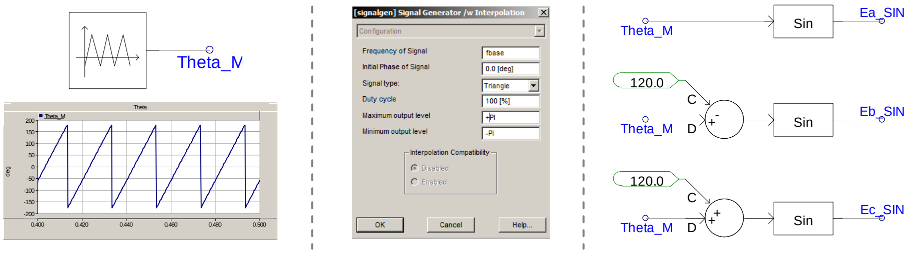

[signalgen] Signal Generator /w Interpolation

Configuration

Frequency of Signal: fbase
Initial Phase of Signal: 0.0 [deg]
Signal type: Triangle
Duty cycle: 100 [%]
Maximum output level: +PI
Minimum output level: -PI

Interpolation Compatibility
● Disabled
○ Enabled

Fig. C.9 Chain Link AC Voltage (Phase) controller, Theta measurement/generation - EMTDC/PSCAD implementation.

Finally, voltage references for chain link converter are obtained by multiplying sinusoidal interpolation of phases with previously calculated voltage magnitudes. In order to per-unitize values, they are further divided by user-specified total chain-link DC voltage value $E_{dc(CL)}$ [kV].

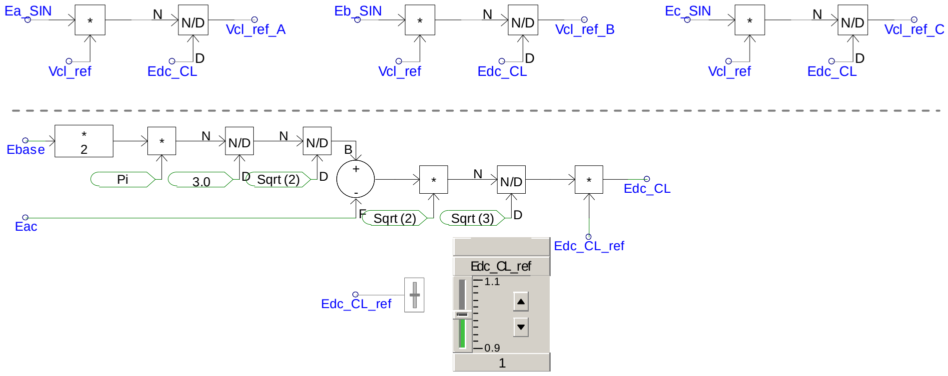

Fig. C.10 Chain Link output voltage references - EMTDC/PSCAD implementation.

In order to provide [pu] values of voltage references for any possible system ratings, the total chain-link DC voltage $E_{dc(CL)}$ [kV] is calculated according to formula:

$$E_{DC(CL)} = \left(E_{DC} \cdot \frac{\pi}{3 \cdot \sqrt{2}} - E_{AC} \right) \cdot \frac{\sqrt{2}}{\sqrt{3}} \cdot E_{DC(CL)}^{\ *} \tag{C.1}$$

where:

E_{DC}	- pole-to-pole DC base voltage [kV]
E_{AC}	- line-to-line generator AC RMS base voltage [kV]
$E_{DC(CL)}^{*}$	- user-input reference resulting chain link voltage [pu]
$E_{DC(CL)}$	- resulting chain link voltage [kV]

Formula is obtained based on the required average DC voltage for six-pulse diode rectification [76]. User may slightly adjust nominal value (e.g. from 0.9 to 1.1) as a compromise between amount of distortions on the generator-side and active power capability.

d. PWM Modulator

PWM phase-shifted triangular carrier-based modulator is used. In practice, its design is identical as for system A, where $N = 2 \cdot M$, in which M is the number of full-bridge chain link cells per phase. Each full-bridge chain link cell is modulated in the same manner as NPC-3L system, as it provides three voltage output levels. In total, $4 \cdot N$ output switching logic signals are obtained.

e. Firing Signals

Switching output 0/1 signals are summated for each cell and enter into switching matrix, in which specific switching pattern for all cell switches is provided. In simulation model, this function is provided by X-Y transfer function block. X is input parameter from PWM modulator, while Y is user-set logic parameter according to full-bridge operating principles. $CL_{(cell)}$ parameter is obtained by equal voltage sharing between cells, and is calculated from:

$$CL_{(cell)} = \frac{E_{DC(CL)}}{M} \tag{C.2}$$

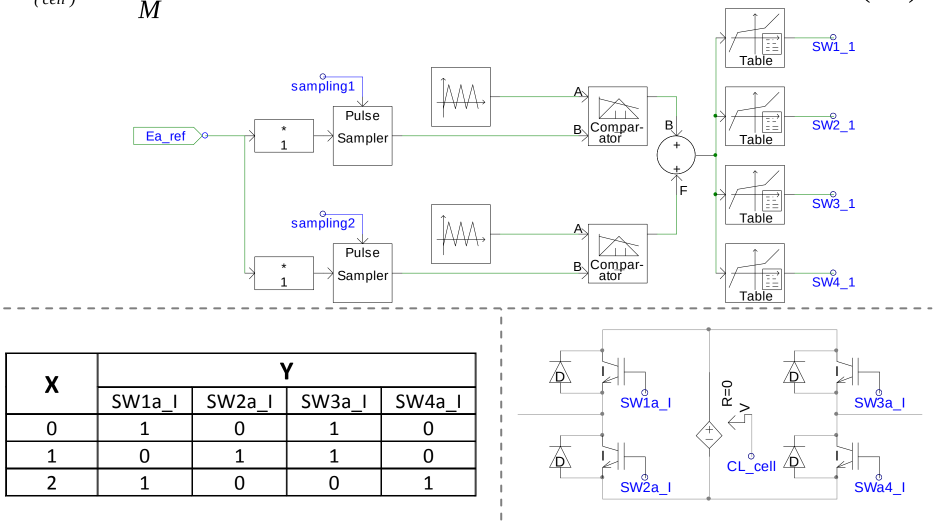

X	Y			
	SW1a_I	SW2a_I	SW3a_I	SW4a_I
0	1	0	1	0
1	0	1	1	0
2	1	0	0	1

Fig. C.11 Chain Link Cell PWM Modulator - EMTDC/PSCAD Implementation.

C.5 NPC-5L Converter - Control Architecture

a. Introduction

Standard control diagram for 5-level converters is shown in Fig. C.12. As a result, complete control system is divided into 4 units: PQ control, DC voltage control, AC current control and PWM modulator.

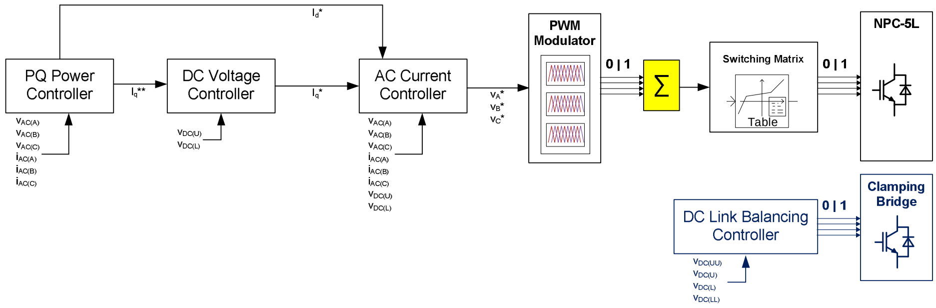

Fig. C.12 Chain Link Cell PWM Modulator - EMTDC/PSCAD Implementation.

a. PQ Power Controller

PQ power controller is identical as for system A (back-to-back MMC). Output signals are I_{q_ref}, I_{d_ref}.

b. DC Voltage Controller

DC voltage controller is identical as for system A (back-to-back MMC). Output signals are E_{dc_x}, E_{dc_y}.

c. DC Link Capacitor Balancing Controller

DC link balancing controller is necessary in order to avoid energy fluctuations between adjacent DC link capacitors. This function is realized by means of active clamping bridge, consisting of IGBT switches and inductors. Balancing is realized by measuring DC capacitor voltages, which are then pre-sampled and compared with each other (upper-top with upper-middle, and lower-top with lower-middle).

By utilizing resonant inductors, capacitors can be charged or discharged by the energy stored from the inductors. Occurring states are listed on table C.1:

Table C.1 Action sequence for DC link capacitor voltage differences within upper and lower arms.

Clamping Bridge - Switching Sequence			
E1 > E2	**E1 < E2**	**E3 > E4**	**E3 < E4**
- T1 turns ON - loop circuit *T1*/*C1*/*L1* - energy from *C1* to *L1* - T2 turns OFF - loop circuit *D2*/*C2*/*L1* - energy from *L1* to *C2*	- *T1* turns OFF - *T2* turns ON - energy from *C2* to *C1*	- *T3* turns ON - loop circuit *T3*/*C3*/*L2* - energy from *C3* to *L2* - *T4* turns OFF - loop circuit *D4*/*C4*/*L2* - energy from *L2* to *C4*	- *T3* turns OFF - *T4* turns ON - energy from *C4* to *C3*

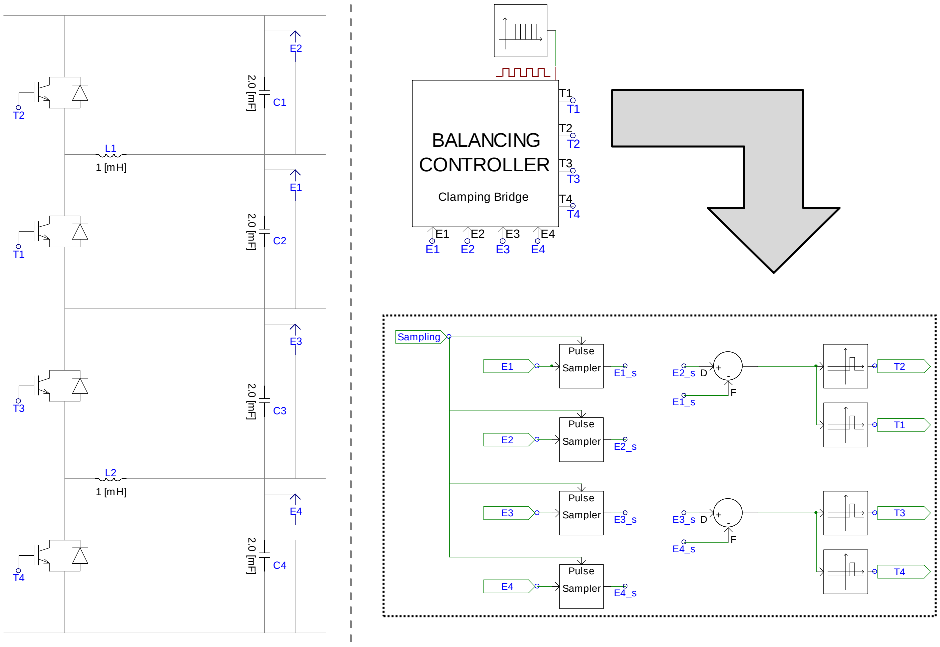

Fig. C.13 DC Link Capacitor Balancing Controller - EMTDC/PSCAD implementation.

In order to avoid multi-switching transitions, a non-sensitivity margin *dE* = 5% is set. If voltage difference lies within this margin, no switching occurs. This correspond to the blocking state, where: $T1 = 0$ and $T2 = 0$ (or $T3$ and $T4 = 0$). Non-sensitivity margin is directly set in [kV] through range comparator blocks.

d. PWM Modulator

PWM triangular phase-shifted carrier-based modulator is used. In practice, its design is identical as for system A when number of cells $N = 4$. In total, 12 output switching logic signals are obtained

e. Firing Signals

Switching output 0/1 signals are summated for each phase and enter into the switching matrix, in which specific switching pattern for all phase switches is provided. In simulation model, this function is provided by X-Y transfer function block. *X* is input parameter from PWM modulator, while *Y* is user-set logic parameter according to NPC operating principles.

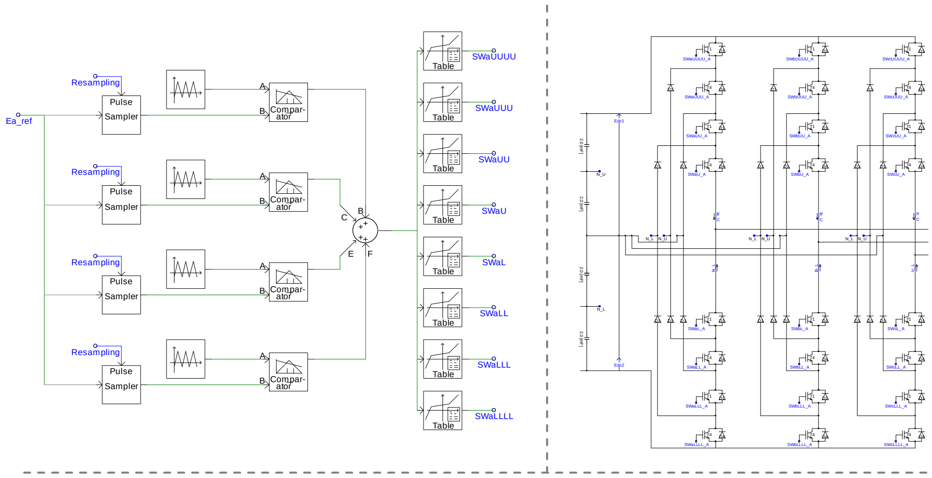

X	**Y**							
	SWa_UUUU	SWa_UUU	SWa_UU	SWa_U	SWa_L	SWa_LL	SWa_LLL	SWa_LLLL
0	0	0	0	0	1	1	1	1
1	0	0	0	0	1	1	1	0
2	0	0	1	1	1	1	0	0
3	0	1	1	1	0	0	0	0
4	1	1	1	1	0	0	0	0

Fig. C.14 NPC-5L PWM Modulator - EMTDC/PSCAD Implementation

C.6 Energization Sequence for System C

System C provides unidirectional power flow (from generator to the grid). As a result, special considerations are required on the procedure for how to start the system. An idea to energize the generator-side converter is by connecting it to the grid. In order to do so, a voltage on the feeder network needs to be decreased for the generator-side system. This is obtained by 3 methods:

- **Method I:**
  Additional 3rd winding of the substation transformer (small feeders).
- **Method II:**
  Tap changer on substation transformer windings and an autotransformer for each feeder.
- **Method III:**
  Conventional transformer for each feeder.

Described methods I, II and III are presented in Figure C.14.

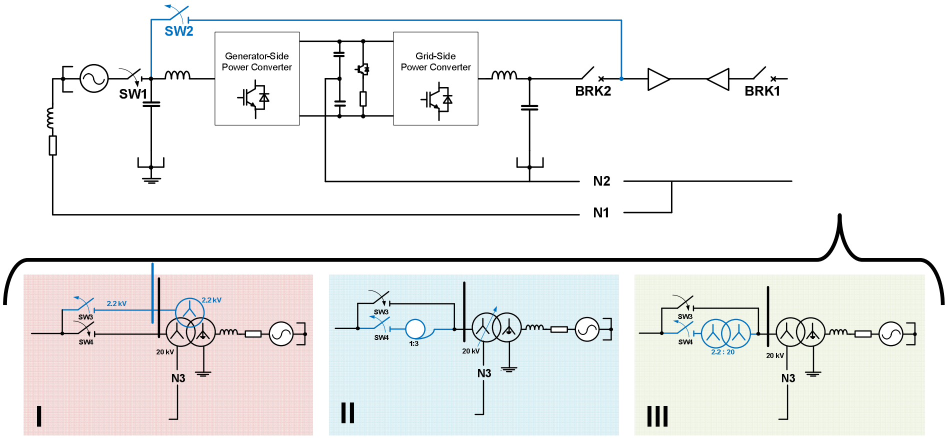

Fig. C.14 Energization sequence for generator-side systems with uni-directional power flow.

Optimal method can be determined by the specific size and feeder network configuration. The energization sequence for methods I, II and III is as follows:

Table. C.2 Switching sequence during start-up procedure for system C.

Switching Sequence	Switches / Breakers (0 = OFF, 1 = ON)					
	SW1	SW2	SW3	SW4	BRK1	BRK2
Converter units are blocked	0	1	1	0	0	0
Grid energizes power converter through its generator-side. Power surplus is burned in chopper	0	1	1	0	**1**	0
Generator is connected to the generator-side converter	**1**	**0**	1	0	1	0
Feeder voltage increase to the grid-side converter level	1	0	**0**	**1**	1	0
Feeder is connected to the grid-side converter	1	0	0	1	1	**1**

D. Excel Sizing Tool for the MMC (HVDC Application)

D.1 System Description - Loading Considerations

a. Introduction

As a starting point, it is assumed that two-terminal back-to-back system is considered. Rectifier is loaded with the power coming from the AC source (e.g. wind farm), whereas inverter supplies AC grid with the power coming from the DC link. Three main loading states can be split for each converter unit, with regard to its interaction with external system:

- **AC loading**, where MMC supplies/loads AC grid with its internal cell capacitance power (direct interaction with AC side).
- **DC loading**, where MMC circuitry is loaded only with the DC power coming from the DC link (direct interaction with DC side).
- **Internal loading**, where internal 2nd harmonic circulating currents flow within the MMC circuitry (no direct interaction).

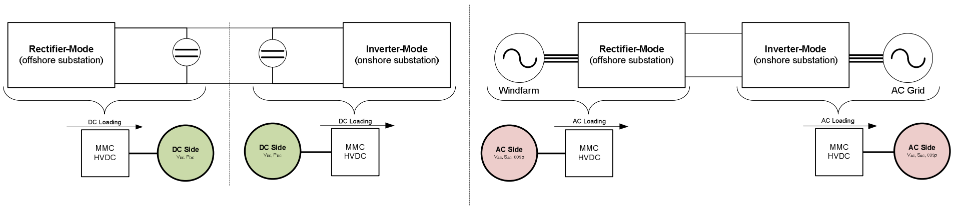

Fig. D.1 System description with possible AC (left) and DC (right) loading conditions.

Fig. D.2 System description with possible internal loading conditions.

b. DC loading - DC Load Distribution

For the DC loading case, following diagrams can be provided for each converter unit:

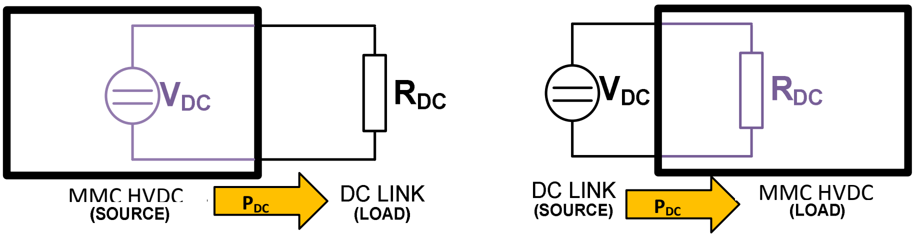

Fig. D.3 System description with possible internal loading conditions.

DC load resistance R_{DC} reflects the amount of the DC power P_{DC} transferred through the DC link:

$$R_{DC} = \frac{V_{DC}^2}{P_{DC}} \tag{D.1}$$

As each phase leg in MMC topology is controlled independently, it is possible to divide DC load resistance R_{DC} into three equivalent load leg resistances for each leg separately (fig. D.4).

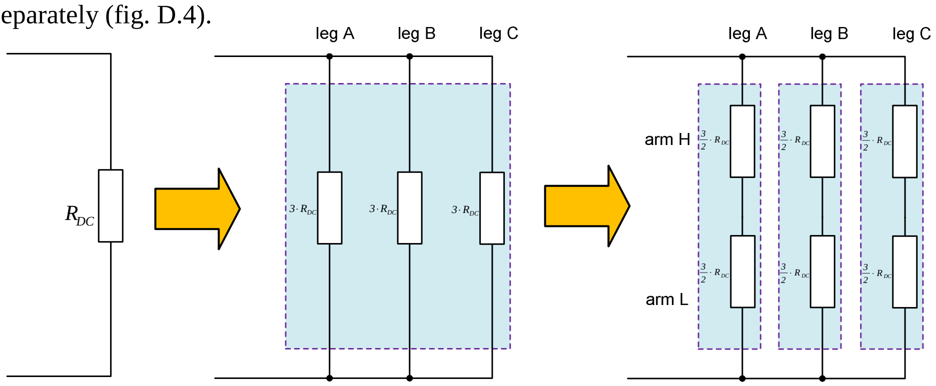

Fig. D.4 DC loads distribution among each converter leg and its corresponding arms.

By doing so, two goals are obtained:

1) 1 three-leg DC circuit can be replaced by 3 separate single-leg DC circuits, which simplifies calculations.

2) DC load circuitry of the rectifier unit will be identical with the DC load circuitry of the inverter unit.

In order to fulfill energy conservation law, in which power coming from the source must equal power coming to the load (losses are neglected), following relation must be maintained for legs connected in parallel:

$$R_{DC} = \frac{R_{leg\_A(DC)} + R_{leg\_B(DC)} + R_{leg\_C(DC)}}{3} \tag{D.2}$$

In order to simplify analysis, it will be further assumed that all three legs share the same amount of DC load. Hence, assumed load resistance per leg will be given by:

$$R_{leg(DC)} = R_{leg\_A(DC)} = R_{leg\_C(DC)} = R_{leg\_C(DC)} = 3 \cdot R_{DC} \tag{D.3}$$

Furthermore, DC load is distributed among each arm, which can be reflected by further splitting each DC load leg resistance $R_{leg(DC)}$ between corresponding arms. For each phase leg, two arms are connected in series to each other in the DC circuit:

$$R_{leg\_A(DC)} = R_{arm\_AH(DC)} + R_{arm\_AL(DC)} \tag{D.4}$$

$$R_{leg\_B(DC)} = R_{arm\_BH(DC)} + R_{arm\_BL(DC)} \tag{D.5}$$

$$R_{leg\_C(DC)} = R_{arm\_CH(DC)} + R_{arm\_CL(DC)} \tag{D.6}$$

As arms in each leg are symmetrical and operate in identical manner, it is assumed that each arm shares the same amount of DC load (no floating ground point reference), so that DC load resistances per arm are identical.

Therefore, assumed single load resistance per arm is given by:

$$\begin{aligned} R_{arm(DC)} &= R_{arm\_AH(DC)} = R_{arm\_AL(DC)} = R_{arm\_BH(DC)} = R_{arm\_BL(DC)} = R_{arm\_CH(DC)} = \\ &= R_{arm\_CL(DC)} = \frac{1}{2} \cdot R_{leg(DC)} = \frac{3}{2} \cdot R_{DC} \end{aligned} \tag{D.7}$$

c. Internal Loading - Circulating Currents Phenomenon

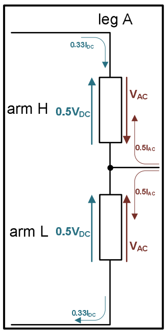

Internal loading state appears due to energy fluctuations within phase legs, when both DC-side and AC-side exchange total power. Ideally, resulting phase leg power should consist only of DC component currents and voltages (coming from DC loading):

$$I_{leg(ideal)} = \frac{I_{DC}}{3} \quad \text{(D.8)} \qquad V_{leg(ideal)} = V_{DC} \quad \text{(D.9)} \qquad P_{leg(ideal)} = \frac{I_{DC}}{3} \cdot V_{DC} \quad \text{(D.10)}$$

However, when examined each arm individually, its currents and voltages will be made from DC component and an AC component, as following:

$$I_{armH} = \frac{I_{DC}}{3} - \frac{I_{AC}}{2} \cdot \sin \omega t \quad \text{(D.11)} \qquad I_{armL} = \frac{I_{DC}}{3} + \frac{I_{AC}}{2} \cdot \sin \omega t \quad \text{(D.13)}$$

$$V_{armH} = \frac{V_{DC}}{2} - V_{AC} \cdot \sin \omega t \quad \text{(D.12)} \qquad V_{armL} = \frac{V_{DC}}{2} + V_{AC} \cdot \sin \omega t \quad \text{(D.14)}$$

As arms for a single leg are connected in series, summated power of both arms should be equal to the previously presented phase leg power consisting only of DC component:

$$P_{armH} = I_{armH} \cdot V_{armH} = \left(\frac{I_{DC}}{3} - \frac{I_{AC}}{2} \cdot \sin \omega t \right) \cdot \left(\frac{V_{DC}}{2} - V_{AC} \cdot \sin \omega t \right) \tag{D.15}$$

$$P_{armL} = I_{armH} \cdot V_{armH} = \left(\frac{I_{DC}}{3} + \frac{I_{AC}}{2} \cdot \sin \omega t \right) \cdot \left(\frac{V_{DC}}{2} + V_{AC} \cdot \sin \omega t \right) \tag{D.16}$$

$$P_{leg(real)} = P_{armH} + P_{armL} = \left(\frac{I_{DC}}{3} \cdot V_{DC} \right) + \left(V_{AC} \cdot I_{AC} \cdot \sin^2 \omega t \right) = P_{leg(ideal)} + P_{2h} \tag{D.17}$$

As the calculated value is not equal to the $P_{leg(ideal)}$, it occurs that additional power P_{2h} must be flowing internally within converter legs. In order to analyze phenomenon that is responsible for generating this power, its energy is calculated with the integral:

$$E_{2h} = \int P_{2h} dt = \int \left(V_{AC} \cdot I_{AC} \cdot sin^2 \omega t \right) dt \equiv sin 2\omega t \tag{D.18}$$

$$E_C = \frac{1}{2} \cdot C \cdot U^2 \tag{D.19}$$

From the design point of view, almost all energy in each leg comes from cell capacitors. Therefore, internal energy fluctuations can be related with the energy stored inside capacitors.

Assuming constant capacitance of cell capacitors, capacitor's energy is related with voltage (19), so that 2nd harmonic energy fluctuations correspond to 2nd harmonic voltage fluctuations (ripple). Such ripple will generate internal 2nd harmonic circulating currents, which are large enough to be taken into considerations for further MMC loading analysis.

d. AC Loading - Positive Sequence Controller

For AC loading case, following diagram can be provided, which allows bidirectional power flow, so that it can be used both for inverter and rectifier units loading analysis.

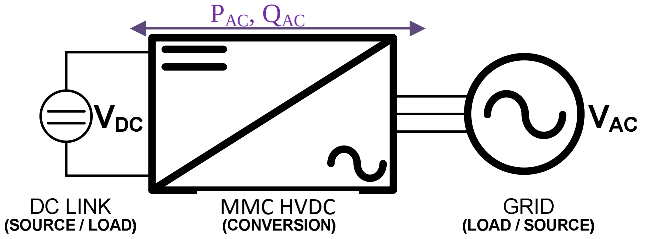

Fig. D.5 General circuit diagram for bidirectional power flow.

Due to individual operation of each phase leg, a three-phase AC electrical circuit can be represented by three single phase sequence circuits for AC loading considerations.

In this work, only plain positive-sequence power controller is designed, which allows to obtain desired values and directions of active and reactive power at PCC through phasor computations. If loading conditions are to be examined under different control modes, specific values for reference voltage magnitudes and phase shifts for each phase are required.

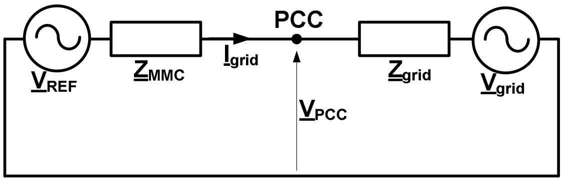

Fig. D.6 General circuit diagram for bidirectional power flow.

Manually tuned variable is reference voltage phasor $\underline{V}_{REF}$ (magnitude and phase), which value is set to obtain desired active & reactive power flow based on selected grid parameters (voltage $\underline{V}_{grid}$, short-circuit impedance $\underline{Z}_{grid}$) and calculated MMC Thevenin impedance $\underline{Z}_{MMC}$. Desired active and reactive power values are calculated directly from:

$$P_{AC} = REAL\left\{3 \cdot \underline{V}_{PCC} \cdot \underline{I}^{*}_{grid}\right\} \tag{D.20}$$

$$Q_{AC} = IMG\left\{3 \cdot \underline{V}_{PCC} \cdot \underline{I}^{*}_{grid}\right\} \tag{D.21}$$

D.2 System Description - Schematic Representation

a. General Description (Dead State)

General schematic representation of the analyzed MMC topology is shown in Fig. D.7

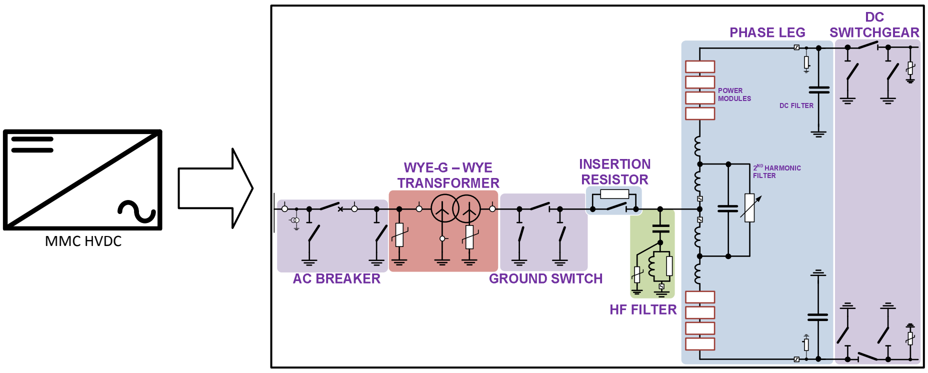

Fig. D.7 MMC HVDC Diagram - Hardware Layout.

It consists of following components:

- **AC breaker**, which is responsible for disconnecting MMC from the AC side. Associated ground switches are installed for safety precautions.
- **Wye-grounded / Wye Transformer (Power Transformer)**, responsible for assuring equal AC & DC voltage levels, providing neutral point grounding and over-voltage protection for the MMC from the AC side.
- **Ground switch**, used for safety precautions in case of transformer damage.
- **Insertion resistor**, responsible for limiting charging currents during MMC start-up.
- **High-Frequency AC Filter**, used for reactive power compensation and optimal loading distribution among components.
- **2nd Harmonic Filter (Converter Reactors + Capacitor)**, used for cancelling 2nd harmonic voltage ripple within internal arm loops.
- **Power Modules**, responsible for shaping output voltage waveforms.
- **DC Filter**, responsible for DC-side voltage ripple attenuation.
- **DC Switchgear**, used when interconnecting MMC to the DC-side. Associated ground switches are installed for safety precautions.

Described scheme is used as a “starting point” for future specific study cases.

b. Normal Operation - AC Loading State

In order to properly analyze MMC under normal operation, following components from the fig. 9 are included for further analysis: **Power Transformer, High-Frequency AC Filter, 2nd Harmonic Filter and Power Modules.** Schematic representation of the analyzed MMC is shown in Figure D.8.

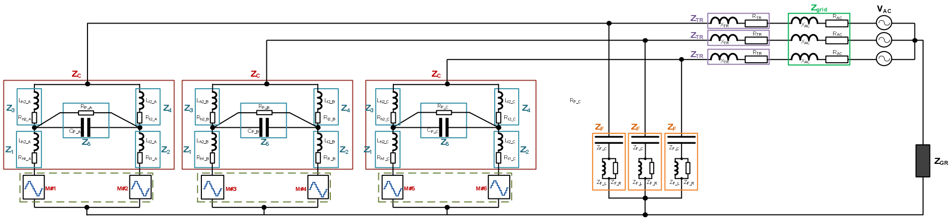

Fig. D.8 Detailed Circuit Representation for AC Loading Analysis.

c. Normal Operation - AC Loading State

In order to properly analyze MMC under normal operation, following components from the fig. 10 are included for further analysis: **2nd Harmonic Filter, Power Modules and DC Filter.** Schematic representation of the analyzed MMC is shown in Figure D.9.

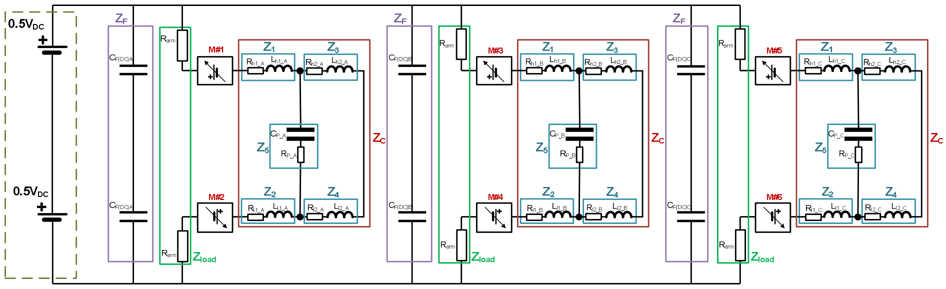

Fig. D.9 Detailed Circuit Representation for DC Loading Analysis.

d. Normal Operation - AC Loading State

In order to properly analyze MMC under normal operation, following components from the fig. 4 are included for further analysis: **2nd Harmonic Filter and Power Modules.** Schematic representation of the analyzed MMC is shown in Figure D.10.

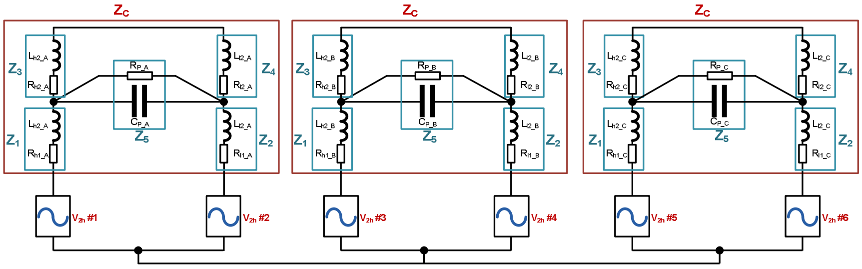

Fig. D.10 Detailed Circuit Representation for Internal Loading Analysis.

D.3 System Specification

a. Introduction

Each component is characterized by its original self-parameters, which are given accordingly for **Grid, Power Transformer, High-Frequency AC Filter, 2nd Harmonic Filter and Power Modules.**

Self-parameters are divided into input constants and input variables. Input constants are parameters specified by the user, while input variables are parameters calculated from input constants.

b. Grid

Table D.1 Grid Specification (🟠) - input constants, (🟢) - input variables.

No.	Parameter	Cell	Symbol	Unit
	AC Side			
1	Rated apparent power (BASE):	D3	$S_{ACgrid(B)}$	[MVA]
2	Rated AC line-to-line voltage (RMS):	D4	V_{ACgrid}	[kV]
3	Rated SC ratio:	D5	$SC_{(ratio)}$	[-]
4	Rated X/R ratio:	D6	X/R	[-]
5	AC grid impedance (BASE):	D7	$Z_{ACgrid(B)}$	[Ω]
6	Power factor:	D8	cosρ	[-]
7	Rated AC frequency	D9	f_{ACgrid}	[Hz]
8	AC grid impedance:	D10	Z_{ACgrid}	[Ω]
9	AC grid resistance:	D11	R_{ACgrid}	[Ω]
10	AC grid reactance:	D12	X_{ACgrid}	[Ω]
11	AC grid inductance:	D13	L_{ACgrid}	[Ω]
	DC Side			
12	Nominal DC power:	D16	P_{DC}	[pu]
13	Nominal DC voltage (pole-to-pole):	D17	V_{DC}	[H]
14	DC load resistance:	D18	R_{DC}	[pu]
15	DC arm resistance (DC loading):	D19	$R_{DC(ARM)}$	[H]

Input constants (user-defined values): **V_{ACgrid}, $SC_{(ratio)}$, X/R, cosρ, f_{AC}, P_{DC}** and **V_{DC}**.

Input variables: **$S_{ACgrid(B)}$, $Z_{ACgrid(B)}$, Z_{ACgrid}, R_{ACgrid}, X_{ACgrid}, L_{ACgrid}, R_{DC}** and **$R_{DC(arm)}$**.

Formulas:

$$S_{ACgrid(B)} = P_{DC} \qquad (D.22)$$

$$Z_{ACgrid(B)} = \frac{V_{ACgrid}^2}{S_{ACgrid}} \qquad (D.23)$$

$$Z_{ACgrid} = \frac{Z_{ACgrid(B)}}{SC_{(ratio)}} \qquad (D.24)$$

$$R_{ACgrid} = \frac{Z_{ACgrid}}{\sqrt{(X/R)^2 - 1}} \qquad (D.25)$$

$$X_{ACgrid} = R_{ACgrid} \cdot (X/R) \qquad (D.26)$$

$$L_{ACgrid} = \frac{X_{ACgrid}}{2 \cdot \pi \cdot f_{ACgrid}} \qquad (D.27)$$

$$R_{DC} = \frac{V_{DC}^2}{P_{DC}} \qquad (D.28)$$

$$R_{DC(arm)} = \frac{3}{2} \cdot R_{DC} \qquad (D.29)$$

c. Grounding Scheme

Table D.2 Grounding Scheme Specification (🟠) - input constants, (🟢) - input variables.

No.	Parameter	Cell	Symbol	Unit
1	Ground resistance:	D27	R_{GR}	[Ω]
2	Ground inductance:	D28	L_{GR}	[H]
3	Ground capacitance:	D29	C_{GR}	[F]

Input constants (user-defined values): **R_{GR}, L_{GR}**, and **C_{GR}**.

Input variables: none.

Figures:

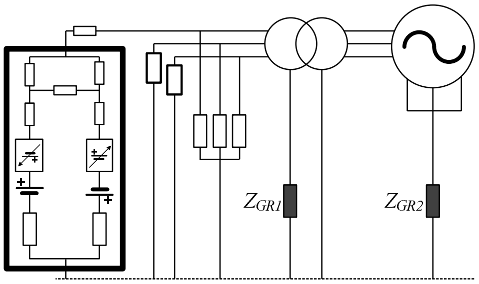

Fig. D.11 Implemented grounding system

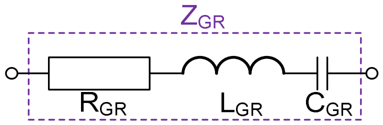

Fig. D.12 Ground impedance - simplified model.

d. Modulation Parameters - Positive Sequence Controller

Table D.3 Positive Sequence Controller Specification (●) - input constants, (●) - input variables, (●) - constant-related main variables.

No.	Parameter	Cell	Symbol	Unit
1	Modulation index:	D65	m	[-]
2	Phase reference voltage:	D66	θ_{REF}	[]
3	Voltage at Point of Common Coupling:	D78	$\underline{V}_{PCC}$	[kV]
4	Generated Active Power at PCC:	D79	P	[MW]
5	Generated Reactive Power at PCC:	D80	Q	[Mvar]
6	Pulse number:	D81	p	[-]
7	Carrier frequency	D82	$f_{carrier}$	[Hz]

Input constants (user-defined values): **m**, **θ_{REF}**, and **p**.

Input variables: **$\underline{V}_{PCC}$**, **P**, **Q**, and **$f_{carrier}$**.

Formulas:

$$P = REAL\left\{3\cdot \underline{V}_{PCC}\cdot \underline{I}^{*}_{PCC}\right\} \quad \text{(D.30)}$$

$$\underline{V}_{PCC} = \underline{V}_{AC} - \underline{V}_{7} \quad \text{(D.33)}$$

$$Q = IMG\left\{3\cdot \underline{V}_{PCC}\cdot \underline{I}^{*}_{PCC}\right\} \quad \text{(D.31)}$$

$$f_{carrier} = p\cdot f_{ACgrid} \quad \text{(D.34)}$$

$$m = \frac{2\cdot\sqrt{2}\cdot\left|\underline{V}_{REF}\right|}{V_{DC}} \quad \text{(D.32)}$$

Figures:

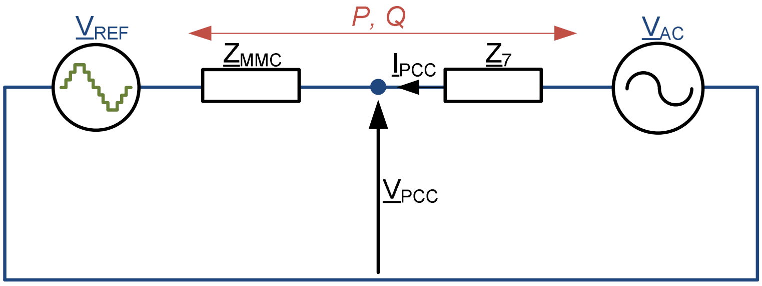

Fig. D.13 Simplified Control Diagram for calculating modulation parameters.

e. Power Transformer

Table D.4 Power Transformer Specification (●) - input constants, (●) - input variables, (●) - constant-related main variables.

No.	Parameter	Cell	Symbol	Unit
1	Rated AC power:	N3	S_{TR}	[pu]
2	AC phase voltage at the converter-side terminal:	N4	$V_{ACconverter}$	[pu]
3	Voltage ratio:	N5	η	[-]
4	Leakage inductance:	N6	L_L	[pu]
5	Fe-loss:	N7	p_{Fe}	[pu]
6	Cu-loss:	N8	p_{Cu}	[pu]
7	Knee point voltage:	N9	V_{knee}	[pu]
8	Transformed AC grid resistance:	N10	R_{AC}	[pu]
9	Transformed AC grid reactance:	N11	X_{AC}	[pu]
10	Transformer base impedance (BASE):	N12	$Z_{TR(B)}$	[pu]
11	Transformer reactance:	N13	X_{TR}	[pu]
12	Transformer resistance:	N14	R_{TR}	[pu]
13	Transformed AC grid inductance:	N15	L_{AC}	[pu]
14	Total power at the converter's terminal:	N16	S_{AC}	[pu]

Input constants (user-defined values): **V_{TR}, L_L, P_{Fe}, P_{Cu},** and **V_{knee}.**

Input variables: **S_{TR}, η, R_{AC}, X_{AC}, Z_{TR}, X_{TR}, R_{TR}, Z_{AC}** and **S_{AC}.**

Formulas:

$$S_{TR} = \sqrt{P^2 + Q^2} \tag{D.35}$$

$$\eta = \frac{V_{ACconverter}}{V_{ACgrid}} \tag{D.36}$$

$$R_{AC} = R_{ACgrid} \cdot \eta^2 \tag{D.37}$$

$$X_{AC} = X_{ACgrid} \cdot \eta^2 \tag{D.38}$$

$$Z_{TR(B)} = \frac{V^2_{ACconverter}}{S_{TR}} \tag{D.39}$$

$$X_{TR} = Z_{TR(B)} \cdot L_L \tag{D.40}$$

$$R_{TR} = Z_{TR(B)} \cdot p_{Cu} \tag{D.41}$$

$$L_{AC} = \frac{X_{AC}}{2 \cdot \pi \cdot f_{ACgrid}} \tag{D.42}$$

f. Power Modules

Table D.5 Power Modules Specification (●) - nominal constants, (●) - input constants, (●) - input variables.

No.	Parameter	Cell	Symbol	Unit
IGBT Press-Pack Chips: Ratings(1)				
1	IGBT RMS collector current	I12	$I_{C(IGBT)}$	[A]
2	Diode RMS forward current	I13	$I_{F(DIODE)}$	[A]
3	IGBT short-circuit current	I14	$I_{SC(IGBT)}$	[A]
4	Diode peak forward current	I15	$I_{FM(DIODE)}$	[A]
5	IGBT short-circuit SOA (Safe Operating Area)	I16	$t_{psc(IGBT)}$	[µs]
6	IGBT turn-OFF time delay	I17	$t_{d(OFF-IGBT)}$	[µs]
7	IGBT fall time	I18	$t_{fall(IGBT)}$	[µs]
Cell Capacitors: Ratings(3)				
14	Maximum allowable voltage per cell:	I3	$V_{MAX(CELL)}$	[pu]
15	Voltage ripple level, for which capacitors are sized:	I4	$V_{RIPPLE(CELL)}$	[%]
16	Cell capacitance (trial formula):	I5	$E_{C(CELL)}$	[kJ]
17	Required converter rating:	N21	$S_{(converter)}$	[pu]
18	AC current flowing through converter terminal:	N20	$I_{AC(converter)}$	[pu]
19	AC current flowing through converter arm:	N22	$I_{AC(ARM)}$	[kA]
20	DC current flowing through converter arm:	N23	$I_{DC(ARM)}$	[kA]

21	Number of modules per arm:	N26	N_{CELLS}	[-]
22	Nominal voltage per module:	N27	$V_{NOM(CELL)}$	[pu]
23	Single cell capacitance:	N28	$C_{(CELL)}$	[mF]
24	Maximum current rating for a single arm (RMS):	N29	$I_{MAX(CELL)}$	[kA]
26	Number of IGBT chips in parallel per device:	N31	$N_{chips(IGBT)}$	[-]
27	Number of diode chips in parallel per device:	N32	$N_{chips(DIODE)}$	[-]

Input constants (user-defined values): $\mathbf{I_{C(IGBT)}}$, $\mathbf{I_{F(DIODE)}}$, $\mathbf{I_{SC(IGBT)}}$, $\mathbf{I_{FM(DIODE)}}$, $\mathbf{t_{psc(IGBT)}}$, $\mathbf{t_{d(OFF\text{-}IGBT)}}$, $\mathbf{t_{fall(IGBT)}}$, $\mathbf{I_{StakPak\_1}}$,$\mathbf{I_{StakPak\_2}}$, $\mathbf{I_{StakPak\_3}}$, $\mathbf{N_{StakPak\_1}}$, $\mathbf{N_{StakPak\_2}}$ and $\mathbf{N_{StakPak\_3}}$.

Input variables: $\mathbf{I_{AC(converter)}}$, $\mathbf{S_{(converter)}}$, $\mathbf{I_{AC(ARM)}}$, $\mathbf{I_{DC(ARM)}}$, $\mathbf{N_{CELLS}}$, $\mathbf{V_{NOM(CELL)}}$,$\mathbf{C_{(CELL)}}$, $\mathbf{I_{MAX(CELL)}}$, $\mathbf{N_{StakPak}}$, $\mathbf{N_{chips(IGBT)}}$ and $\mathbf{N_{chips(DIODE)}}$.

Formulas:

$$S_{converter} = P_{DC} \tag{D.43}$$

$$I_{AC(converter)} = \frac{S_{converter}}{3 \cdot V_{ACconverter}} \tag{D.44}$$

$$I_{AC(ARM)} = 0.5 \cdot I_{AC(converter)} \tag{D.45}$$

$$I_{DC(ARM)} = \frac{1}{3} \cdot \frac{P_{DC}}{V_{DC}} \tag{D.46}$$

$$N_{chips(IGBT)} = \left. \frac{I_{MAX(CELL)}}{I_{C(IGBT)}} \right|_{round\ up} \tag{D.47}$$

$$N_{CELLS} = 0.01 \cdot (V_{RIPPLE(CELL)} + 1) \cdot \left. \frac{V_{DC}}{V_{MAX(CELL)}} \right|_{round\ up} \tag{D.48}$$

$$V_{NOM(CELL)} = \frac{V_{DC}}{N_{CELLS}} \tag{D.49}$$

$$C_{(CELL)} = \frac{I_{DC(ARM)} + I_{AC(ARM)(AV)} + I_{2H(ARM)(AV)}}{f_{carrier} \cdot \frac{V_{NOM(CELL)}}{\sqrt{2}} \cdot 0.01 \cdot V_{RIPPLE(CELL)}} \tag{D.50}$$

$$I_{MAX(CELL)} = I_{AC(ARM)} + I_{DC(ARM)} \tag{D.51}$$

$$N_{chips(diode)} = \left. \frac{I_{MAX(CELL)}}{I_{F(DIODE)}} \right|_{round\ up} \tag{D.52}$$

g. Power Modules

Table D.6 Current Limiting Reactors Specification (●) - input constants, (●) - input variables, (●) - constant-related main variables.

No.	Parameter	Cell	Symbol	Unit
1	Permissible Short-Circuit DC current:	N38	$I_{SC(DC)}$	[A]
2	Minimum required current rate of rise:	N39	α_{rise}	[kA/s]
3	De-rating factor:	N40	ρ	[%]
4	Minimum half-arm inductance per reactor (1):	N41	L_{h1} // L_{l1}	[mH]
5	Minimum half-arm inductance per single reactor (2):	N42	L_{h2} // L_{l2}	[mH]
6	Inner resistance per inductor (1):	N43	R_{h1} // R_{l1}	[mΩ]
7	Inner resistance per inductor (2):	N44	R_{h2} // R_{l2}	[mΩ]
8	Voltage drop across reactor arm:	N45	$\Delta V_{reactor}$	[pu]
9	Measured voltage at AC converter terminals:	N46	$V_{AC(converter)}$	[pu]

Input constants (user-defined values): $\boldsymbol{\rho}$, $\mathbf{R_{h1} = R_{l1}}$ and $\mathbf{R_{h2} = R_{l2}}$.

Input variables: $\mathbf{I_{SC(CELL)}}$, $\boldsymbol{\alpha}_{\mathbf{rise}}$, $\mathbf{L_{h1} = L_{l1}}$, $\mathbf{L_{h2} = L_{l2}}$, $\mathbf{\Delta V_{reactor}}$ and $\mathbf{V_{AC(converter)}}$.

Formulas:

$$I_{SC(DC)} = \left. \begin{cases} N_{chips(IGBT)} \cdot I_{SC(IGBT)} \\ N_{chips(Diode)} \cdot I_{FM(Diode)} \end{cases} \right|_{minimum} \tag{D.53}$$

$$\Delta V_{reactor} = I_{MAX(CELL)} \cdot \sqrt{(R_{h1} + R_{h2})^2 + 4 \cdot \pi^2 \cdot f_{ACgrid}^2 \cdot (L_{h1} + L_{h2})^2} \tag{D.54}$$

$$\alpha_{rise} = \frac{I_{SC(DC)}}{t_{psc(IGBT)} + t_{d(OFF-IGBT)} + t_{fall(IGBT)}} \qquad \text{(D.55)}$$

$$V_{AC(converter)} = V_{TR} - \Delta V_{reactor} \qquad \text{(D.57)}$$

$$L_{h1} = L_{l1} = L_{h2} = L_{l2} = \frac{V_{DC}}{\alpha_{rise}} \qquad \text{(D.56)}$$

Figures:

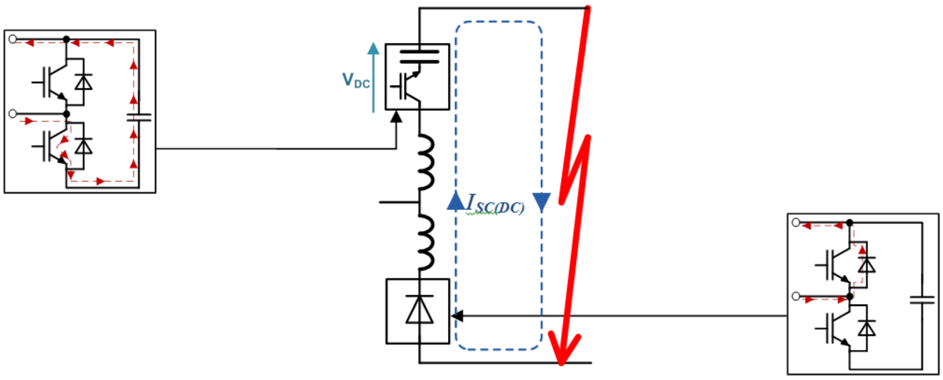

Fig. D.14 Minimum inductance of the converter arm reactors sized for IGBT press-pack capability to suppress energy from cells under the DC fault.

h. 2nd Harmonic Filter (Capacitor)

Table D.7 2nd Harmonic Filter Specification (●) - input variables.

No.	Parameter	Cell	Symbol	Unit
1	Capacitance:	N60	C_P	[µF]
2	EPR for given capacitance:	N61	R_P	[mΩ]

Input constants (user-defined values): **R_P.**

Input variables: **C_P.**

Formulas:

$$C_P = \frac{1}{8 \cdot (2 \cdot \pi \cdot f_{ACgrid})^2 \cdot L_{h1}} \qquad \text{(D.58)}$$

Admittance in s-domain for the circulating current:

$$Y_C(s) = \frac{(F \cdot A + B \cdot D) + \left(F + \frac{A \cdot E}{H}\right) \cdot s + \left(\frac{A+E}{H}\right) \cdot s^2 + \left(\frac{1}{H}\right) \cdot s^3}{(F \cdot C + B \cdot G) + \left(\frac{C \cdot E}{H}\right) \cdot s + \left(\frac{C}{H}\right) \cdot s^2} \qquad \text{(D.59)}$$

$A = \frac{R_{l1}}{L_{l1}}$	(D.60)	$B = \frac{1}{2 \cdot L_{l1}}$	(D.63)	$C = \frac{1}{L_{l1}}$	(D.66)
$D = \frac{R_{h1} + R_{l1}}{2} \cdot \left(\frac{1}{L_{l1}} - \frac{1}{L_{h1}}\right)$	(D.61)	$E = \frac{R_{h1}}{L_{h1}}$	(D.64)	$F = 0.5 \cdot \left(\frac{1}{L_{l1}} + \frac{1}{L_{h1}}\right)$	(D.67)
$G = \frac{1}{L_{h1}}$	(D.62)	$H = \frac{1}{C_P}$	(D.65)		

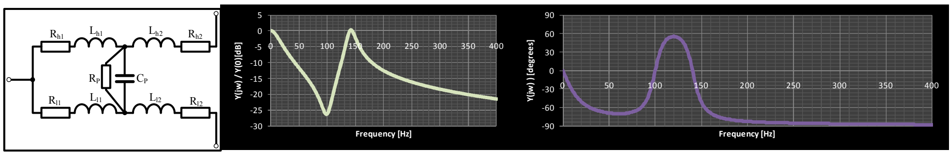

Fig. D.15 Frequency spectrum of admittance for the circulating current (400 samples: 0.1 Hz - 400 Hz).

i. High Frequency (HF) Capacitor Filter

Table D.8 HF Filter Specification (●) - input variables, (●) - constant-related main variables.

No.	Parameter	Cell	Symbol	Unit
1	Phase Reactive power variations:	N74	$Q_{ACreactor}$	[Mvar]
2	Resonant frequency:	N75	f_{RES}	[Hz]
3	Quality factor:	N76	q	[-]
4	Filter capacitance:	N77	C_{filter}	[μF]
5	Filter inductance:	N78	L_{filter}	[mH]
6	Filter resistance:	N79	R_{filter}	[mΩ]

Input constants (user-defined values): **$Q_{ACreactor}$, f_{RES}** and **q**.

Input variables: **C_{filter}, L_{filter}** and **R_{filter}.**

Formulas:

$$C_{filter} = \frac{Q_{ACreactor}}{3 \cdot V_{ACgrid}^2 \cdot (2 \cdot \pi \cdot f_{ACgrid})} \tag{D.68}$$

$$L_{filter} = \frac{1}{(2 \cdot \pi \cdot f_{RES})^2 \cdot C_{filter}} \tag{D.70}$$

$$R_{filter} = 2 \cdot \pi \cdot f_{RES} \cdot L_{filter} \cdot q \tag{D.69}$$

Discrete sequence transfer function for optimal filter harmonics tuning (f_{RES} and q parameters):

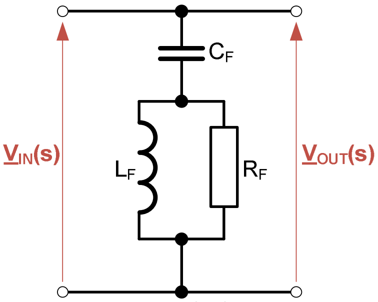

$$Y_F(s) = \frac{V_{OUT}(s)}{V_{IN}(s)} \equiv \left\{ \begin{array}{l} \frac{\underline{V}_{OUT}(s_1)}{\underline{V}_{IN}(s_1)} \\ \\ \frac{\underline{V}_{OUT}(s_2)}{\underline{V}_{IN}(s_2)} \\ \\ \ddots \\ \\ \frac{\underline{V}_{OUT}(s_n)}{\underline{V}_{IN}(s_n)} \end{array} \right. \tag{D.71}$$

Fig. D.16 Filter's transfer function analysis.

Discrete sequence voltage phasors $\underline{V}_{IN}$ and $\underline{V}_{OUT}$ are calculated for up to 511th harmonic order (n = 51100π).

Fig. D.17 Frequency spectrum of the discrete transfer function - example.

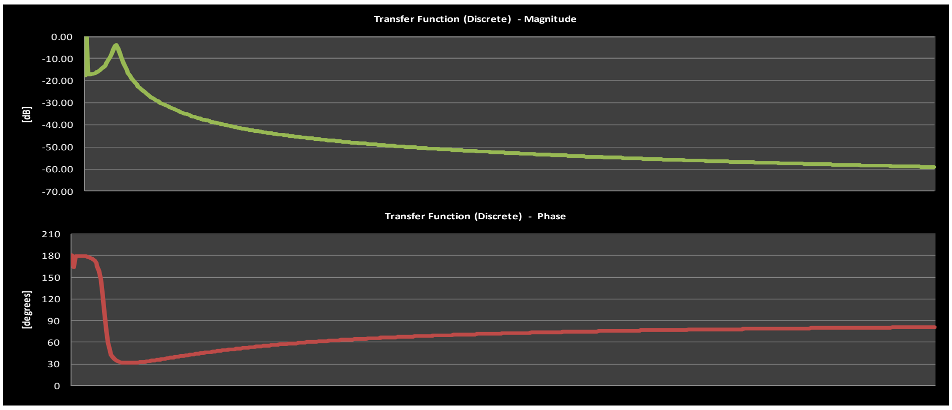

Fig. D.18 Frequency spectrum of the discrete transfer function - example.

j. DC Filter

Table IX. DC Filter Specification (●) - input constants, (●) - input variables.

No.	Parameter	Cell	Symbol	Unit
1	Capacitance:	N119	$C_{FILTER(DC)}$	[µF]
2	ESR resistance:	N120	$R_{FILTER(DC)}$	[-]
3	Non-filtered DC voltage ripple (MAX):	N121	ΔV_{DCNF}	[kV]
4	Filtered DC voltage ripple (MAX):	N122	ΔV_{DCF}	[kV]

Input constants (user-defined values):	$\mathbf{C_{FILTER(DC)}}$ and $\mathbf{R_{FILTER(DC)}}$.
Input variables:	$\Delta V_{\mathbf{DCNF}}$ and $\Delta V_{\mathbf{DCF}}$.

Formulas:

$$\Delta V_{DCNF} = max(V_{DCripple(A)}, V_{DCripple(B)}, V_{DCripple(C)}) \tag{D.72}$$

$$\Delta V_{DCF} = \frac{\Delta Q}{C_{FILTER(DC)}} \tag{D.73}$$

D.3 Theoretical Analysis - AC Loading

a. Introduction

Theoretical circuit analysis is performed in order to analyze accurate input values for negative sequence controller $\underline{V}_{REF}$, components loading, harmonic distortions (THD) and HF filter's transfer function. Thevenin approach is utilized. Following general circuit diagram is presented in Fig. D.19.

Furthermore, it is assumed that all corresponding phase impedances are equal:

$$\underline{Z}_{1A} = \underline{Z}_{1B} = \underline{Z}_{1C} \tag{D.74}$$

$$\underline{Z}_{2A} = \underline{Z}_{2B} = \underline{Z}_{2C} \tag{D.75}$$

$$\underline{Z}_{3A} = \underline{Z}_{3B} = \underline{Z}_{3C} \tag{D.76}$$

$$\underline{Z}_{4A} = \underline{Z}_{4B} = \underline{Z}_{4C} \tag{D.77}$$

$$\underline{Z}_{5A} = \underline{Z}_{5B} = \underline{Z}_{5C} \tag{D.78}$$

$$\underline{Z}_{6A} = \underline{Z}_{6B} = \underline{Z}_{6C} \tag{D.79}$$

$$\underline{Z}_{7A} = \underline{Z}_{7B} = \underline{Z}_{7C} \tag{D.80}$$

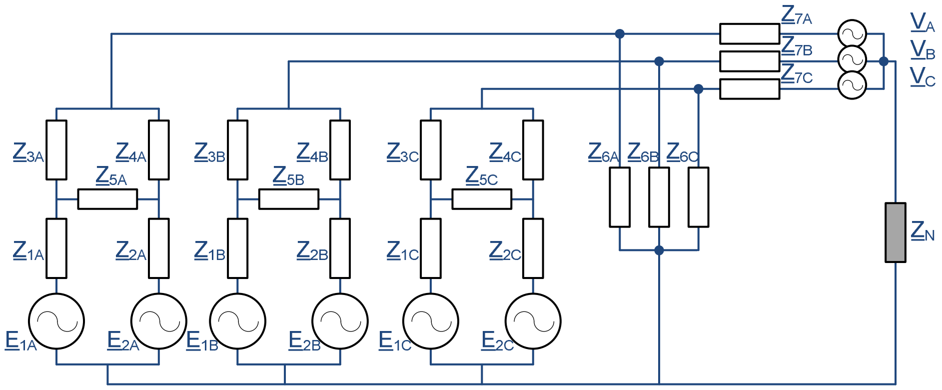

Fig. 19 General schematic circuit representation for circuit AC loading analysis.

b. Zero-, Positive- and Negative-Sequence Transformation

Assumption for identical corresponding phase impedances will allow to replace a 3-phase circuit diagram with 3 single-phase zero- positive- and negative-sequence circuits:

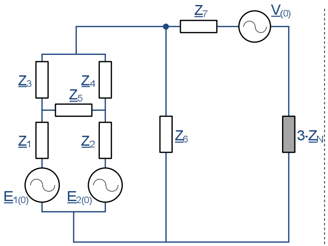

Fig. D.20 Zero-seq. 1-phase circuit.

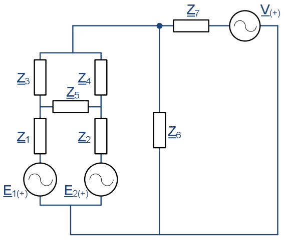

Fig. D.21 Pos-seq. 1-phase circuit.

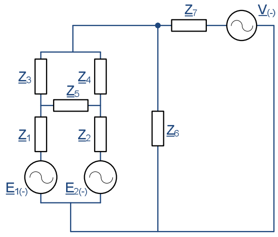

Fig. D.22 Neg-seq. 1-phase circuit.

Next step is to introduce transformation of phase voltage sources into sequence components with the usage of symmetrical component matrix:

$$\left[\underline{E}_{1(0)} \quad \underline{E}_{1(-)} \quad \underline{E}_{1(+)}\right] = \frac{1}{3} \cdot \begin{bmatrix} 1 & 1 & 1 \\ 1 & \underline{a} & \underline{a}^2 \\ 1 & \underline{a}^2 & \underline{a} \end{bmatrix} \cdot \begin{bmatrix} \underline{E}_{1A} \\ \underline{E}_{1B} \\ \underline{E}_{1C} \end{bmatrix} \quad \text{(D.81)}$$

$$\left[\underline{V}_{(0)} \quad \underline{V}_{(-)} \quad \underline{V}_{(+)}\right] = \frac{1}{3} \cdot \begin{bmatrix} 1 & 1 & 1 \\ 1 & \underline{a} & \underline{a}^2 \\ 1 & \underline{a}^2 & \underline{a} \end{bmatrix} \cdot \begin{bmatrix} \underline{V}_{A} \\ \underline{V}_{B} \\ \underline{V}_{C} \end{bmatrix} \quad \text{(D.83)}$$

$$\left[\underline{E}_{2(0)} \quad \underline{E}_{2(-)} \quad \underline{E}_{2(+)}\right] = \frac{1}{3} \cdot \begin{bmatrix} 1 & 1 & 1 \\ 1 & \underline{a} & \underline{a}^2 \\ 1 & \underline{a}^2 & \underline{a} \end{bmatrix} \cdot \begin{bmatrix} \underline{E}_{2A} \\ \underline{E}_{2B} \\ \underline{E}_{2C} \end{bmatrix} \quad \text{(D.82)}$$

$$\underline{a} = 1 \cdot e^{j120^0} \quad \text{(D.84)}$$

c. Circuit Analysis

Impedance components from fig. 21-23 are defined as:

$$\underline{Z}_1 = R_{h1} + j\omega L_{h1} + \frac{2}{3} \cdot R_{DC} \quad \text{(D.85)}$$

$$\underline{Z}_3 = R_{h2} + j\omega L_{h2} \quad \text{(D.86)}$$

$$\underline{Z}_5 = \frac{1}{R_P} - j\frac{1}{\omega C_P} \quad \text{(D.87)}$$

$$\underline{Z}_4 = R_{l2} + j\omega L_{l2} \quad \text{(D.88)}$$

$$\underline{Z}_N = \underline{Z}_{GR1} \quad \text{(D.89)}$$

$$\underline{Z}_6 = \left(\frac{1}{R_F} + \frac{1}{j\omega L_F}\right)^{-1} + \frac{1}{j\omega C_F} \quad \text{(D.90)}$$

$$\underline{Z}_7 = \left(R_{TR} + R_{AC} \cdot \eta^2\right) + j\omega\left(L_{TR} + L_{AC} \cdot \eta^2\right) \qquad \text{(D.91)}$$

First task is to make an impedance delta-wye transformation ($\underline{Z}_3$, $\underline{Z}_4$ and $\underline{Z}_5$):

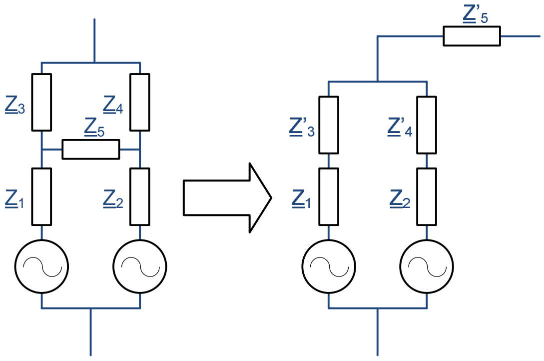

$$\underline{Z}'_3 = \frac{\underline{Z}_3 \cdot \underline{Z}_5}{\underline{Z}_3 + \underline{Z}_4 + \underline{Z}_5} \qquad \text{(D.92)}$$

$$\underline{Z}'_4 = \frac{\underline{Z}_4 \cdot \underline{Z}_5}{\underline{Z}_3 + \underline{Z}_4 + \underline{Z}_5} \qquad \text{(D.93)}$$

$$\underline{Z}'_5 = \frac{\underline{Z}_3 \cdot \underline{Z}_4}{\underline{Z}_3 + \underline{Z}_4 + \underline{Z}_5} \qquad \text{(D.94)}$$

Fig. D.23 Impedance delta-wye transformation - diagram.

Desired impedance values are numerically calculated for each frequency harmonic. Next task is to obtain Thevenin converter voltage source $\underline{E}_T$ and Thevenin converter impedance $\underline{Z}_T$:

$$\underline{E}_T = \frac{\underline{Y}_{1+3'} \cdot \underline{E}_1 + \underline{Y}_{2+4'} \cdot \underline{E}_2}{\underline{Y}_{1+3'} + \underline{Y}_{2+4'}} \qquad \text{(D.95)} \qquad \underline{Z}_T = \left(\underline{Y}_{1+3'} + \underline{Y}_{2+4'}\right)^{-1} + \underline{Z}_{5'} + \underline{Z}_{TR} \qquad \text{(D.96)}$$

Finally, resulting Thevenin voltage and impedance are obtained from:

$$\underline{E}_{thevenin} = \begin{cases} \dfrac{\underline{E}_T \cdot \underline{Y}_T + \underline{V} \cdot \underline{Y}_{7+3N}}{\underline{Y}_{T+7+3N}} & (0seq) \\ \dfrac{\underline{E}_T \cdot \underline{Y}_T + \underline{V} \cdot \underline{Y}_7}{\underline{Y}_{T+7}} & (-/+\,seq) \end{cases} \qquad \text{(D.97)} \qquad \underline{Z}_{thevenin} = \begin{cases} \underline{Z}_{T+7+3N} & (0seq) \\ \underline{Z}_{T+7} & (-/+\,seq) \end{cases} \qquad \text{(D.98)}$$

Sequence current and voltage loadings are obtained from equations below:

$$\underline{I}_6 = \frac{\underline{E}_{thevenin}}{\underline{Z}_{thevenin} + \underline{Z}_6} \qquad \text{(D.99)} \qquad \underline{V}_6 = \underline{I}_6 \cdot \underline{Z}_6 \qquad \text{(D.102)} \qquad \underline{V}_2 = \underline{I}_2 \cdot \underline{Z}_2 \qquad \text{(D.105)}$$

$$\underline{I}_{5'} = \underline{I}_{TR} = \frac{\underline{E}_T - \underline{V}_6}{\underline{Z}_T} \qquad \text{(D.100)} \qquad \underline{V}_7 = \underline{I}_7 \cdot \underline{Z}_7 \qquad \text{(D.103)} \qquad \underline{V}_1 = \underline{I}_1 \cdot \underline{Z}_1 \qquad \text{(D.106)}$$

$$\underline{V}_{3'} = \underline{I}_{3'} \cdot \underline{Z}_{3'} \qquad \text{(D.101)} \qquad \underline{V}_{4'} = \underline{I}_{4'} \cdot \underline{Z}_{4'} \qquad \text{(D.104)} \qquad \underline{V}_{5'} = \underline{I}_{5'} \cdot \underline{Z}_{5'} \qquad \text{(D.107)}$$

$$\underline{I}_7 = \begin{cases} \dfrac{\underline{V} - \underline{V}_6}{\underline{Z}_{7+3N}} & (0seq) \\ \dfrac{\underline{V} - \underline{V}_6}{\underline{Z}_7} & (+/-\,seq) \end{cases} \qquad \text{(D.108)}$$

Wye voltage drops are transformed into delta voltage drops:

$$\underline{V}_3 = \underline{V}_{4'} + \underline{V}_{5'} \qquad \text{(D.109)} \qquad \underline{V}_4 = \underline{V}_{3'} + \underline{V}_{5'} \qquad \text{(D.110)} \qquad \underline{V}_5 = \underline{V}_{3'} - \underline{V}_{4'} \qquad \text{(D.111)}$$

And eventually, delta currents are obtained from:

$$\underline{I}_3 = \frac{\underline{V}_3}{\underline{Z}_3} \quad \text{(D.112)} \qquad \underline{I}_4 = \frac{\underline{V}_4}{\underline{Z}_4} \quad \text{(D.113)} \qquad \underline{I}_5 = \frac{\underline{V}_5}{\underline{Z}_5} \quad \text{(D.114)}$$

d. Components Loading Analysis

Based on derived equations, loading of each individual component with sequence current/voltage harmonics is obtained, and can be shown on a frequency spectrum (up to 511th order harmonic). An example for $\underline{Z}_4$ impedance loading (half-arm current limiting reactor) is shown below:

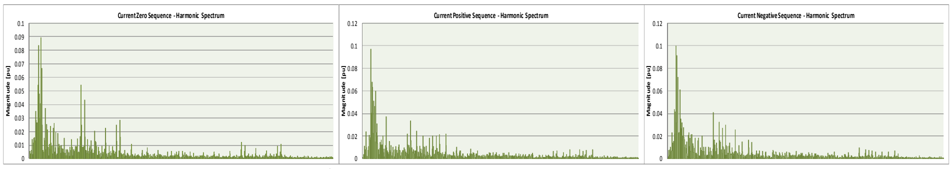

Fig. D.24 Sequence current loading - frequency spectrum.

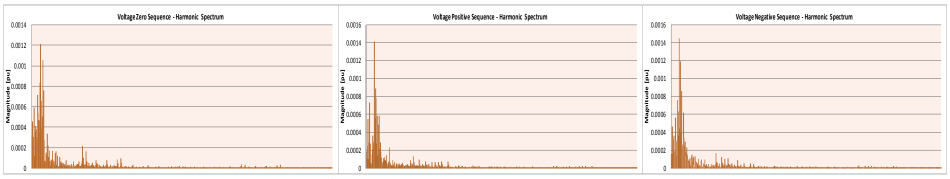

Fig. D.25 Sequence voltage loading - frequency spectrum.

THD factors for voltage and current distortions are derived, allowing to assess the performance of the component with applied self-parameter values. THD factors are calculated numerically according to equations:

$$THD_i = \sqrt{\frac{\sum_{h=2}^{511} I_h^2}{I_1}} \quad \text{(D.115)} \qquad THD_v = \frac{\sqrt{\sum_{h=2}^{511} U_h^2}}{U_1} \quad \text{(D.116)}$$

e. Components Loading Analysis

From a given harmonic spectrum, discrete transfer function can be formed for HF filter tuning with the equations obtained from circuit analysis:

$$Y_F(s) = \frac{V_{OUT}(s)}{V_{IN}(s)} \equiv \begin{cases} \dfrac{\underline{V}_{OUT}(f_1)}{\underline{V}_{IN}(f_1)} \\ \dfrac{\underline{V}_{OUT}(f_2)}{\underline{V}_{IN}(f_2)} \\ \because \\ \dfrac{\underline{V}_{OUT}(f_{511})}{\underline{V}_{IN}(f_{511})} \end{cases} \quad \text{(D.117)}$$

$$\underline{V}_{OUT}(f) = \begin{cases} \underline{V}(f) - \underline{I}_7(f) \cdot (\underline{Z}_7(f) + 3\underline{Z}_N(f)) & 0seq \\ \underline{V}(f) - \underline{V}_7(f) & -/+seq \end{cases} \quad \text{(D.118)}$$

$$\underline{V}_{IN}(f) = \underline{E}_T(f) - \underline{I}_{5'}(f) \cdot \left(\underline{Z}_T(f) + \underline{Z}_{5'}(f)\right) \quad \text{(D.119)}$$

Interpolated magnitudes and phases discrete function values are superimposed on the Bode plot, so that resonant harmonic peaks are clearly visible along with filter's quality characteristics (under-, over-, critically-damped). In this manner, tuning can be applied manually from observing plot characteristics.

D.4 Theoretical Analysis - DC Loading

a. Introduction

Theoretical circuit analysis is performed in order to analyze components loading. Thevenin approach is utilized. Following general circuit diagram is presented below:

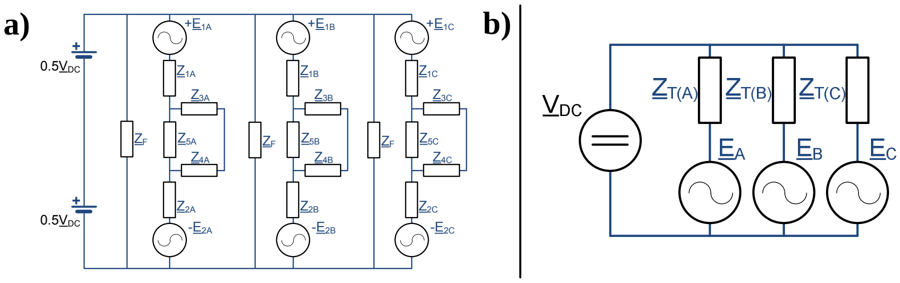

Fig. D.26 General schematic circuit representation for DC circuit analysis: a) detailed, b) simplified.

It is assumed that all corresponding phase impedances are equal:

$$\underline{Z}_{1A} = \underline{Z}_{1B} = \underline{Z}_{1C} \tag{D.120}$$

$$\underline{Z}_{4A} = \underline{Z}_{4B} = \underline{Z}_{4C} \tag{D.121}$$

$$\underline{Z}_{7A} = \underline{Z}_{7B} = \underline{Z}_{7C} \tag{D.122}$$

$$\underline{Z}_{2A} = \underline{Z}_{2B} = \underline{Z}_{2C} \tag{D.123}$$

$$\underline{Z}_{5A} = \underline{Z}_{5B} = \underline{Z}_{5C} \tag{D.124}$$

$$\underline{Z}_{3A} = \underline{Z}_{3B} = \underline{Z}_{3C} \tag{D.125}$$

$$\underline{Z}_{6A} = \underline{Z}_{6B} = \underline{Z}_{6C} \tag{D.126}$$

b. Circuit Analysis

Impedance components from fig. D.26 are defined as:

$$\underline{Z}_1 = R_{h1} + j\omega L_{h1} + \frac{1}{6} \cdot R_{DC} \tag{D.127}$$

$$\underline{Z}_5 = -j\frac{1}{\omega C_P} \tag{D.128}$$

$$\underline{Z}_2 = R_{l1} + j\omega L_{l1} + \frac{1}{6} \cdot R_{DC} \tag{D.129}$$

$$\underline{Z}_3 = R_{h2} + j\omega L_{h2} \tag{D.130}$$

$$\underline{Z}_4 = R_{l2} + j\omega L_{l2} \tag{D.131}$$

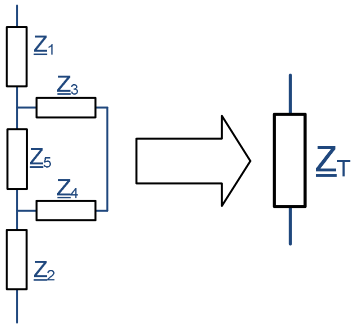

$$\underline{Z}_{T(A)} = \underline{Z}_{1A} + \underline{Z}_{2A} + \left(\underline{Y}_{5A} + \left(\underline{Z}_{3A+4A}\right)^{-1}\right)^{-} \quad \text{(D.132)} \qquad (133)$$

$$\underline{Z}_{T(B)} = \underline{Z}_{1B} + \underline{Z}_{2B} + \left(\underline{Y}_{5B} + \left(\underline{Z}_{3B+4B}\right)^{-1}\right)^{-1} \quad \text{(D.133)} \qquad (134)$$

$$\underline{Z}_{T(C)} = \underline{Z}_{1C} + \underline{Z}_{2C} + \left(\underline{Y}_{5C} + \left(\underline{Z}_{3C+4C}\right)^{-1}\right)^{-1} \quad \text{(D.134)} \qquad (135)$$

Fig. D.27 Resulting phase leg impedance - calculations.

Currents flowing through arms are given below:

$$\underline{I}_A = \frac{V_{DC} - \left(\underline{E}_{1A} + \underline{E}_{2A}\right)}{\underline{Z}_{T(A)}} \quad \text{(D.135)} \qquad \underline{I}_B = \frac{\left(\underline{E}_{1B} + \underline{E}_{2B}\right)}{\underline{Z}_T} \quad \text{(D.136)} \qquad \underline{I}_C = \frac{\left(\underline{E}_{1C} + \underline{E}_{2C}\right)}{\underline{Z}_T} \quad \text{(D.137)}$$

Finally, all flowing currents are given by equations:

$$\underline{I}_{1A} = \underline{I}_{2A} = \underline{I}_A \quad \text{(D.138)} \qquad \underline{I}_{3A} = \underline{I}_{4A} = \underline{I}_A \cdot \frac{\underline{Z}_{5A}}{\underline{Z}_{5A} + \underline{Z}_{3A} + \underline{Z}_{4A}} \quad \text{(D.141)} \qquad \underline{I}_{5A} = \underline{I}_A \cdot \frac{\underline{Z}_{3A} + \underline{Z}_{4A}}{\underline{Z}_{5A} + \underline{Z}_{3A} + \underline{Z}_{4A}} \quad \text{(D.144)}$$

$$\underline{I}_{1B} = \underline{I}_{2B} = \underline{I}_B \quad \text{(D.139)} \qquad \underline{I}_{3B} = \underline{I}_{4B} = \underline{I}_B \cdot \frac{\underline{Z}_{5B}}{\underline{Z}_{5B} + \underline{Z}_{3B} + \underline{Z}_{4B}} \quad \text{(D.142)} \qquad \underline{I}_{5B} = \underline{I}_B \cdot \frac{\underline{Z}_{3B} + \underline{Z}_{4B}}{\underline{Z}_{5B} + \underline{Z}_{3B} + \underline{Z}_{4B}} \quad \text{(D.145)}$$

$$\underline{I}_{1C} = \underline{I}_{2C} = \underline{I}_C \quad \text{(D.140)} \qquad \underline{I}_{3C} = \underline{I}_{4C} = \underline{I}_C \cdot \frac{\underline{Z}_{5C}}{\underline{Z}_{5C} + \underline{Z}_{3C} + \underline{Z}_{4C}} \quad \text{(D.143)} \qquad \underline{I}_{5C} = \underline{I}_C \cdot \frac{\underline{Z}_{3C} + \underline{Z}_{4C}}{\underline{Z}_{5C} + \underline{Z}_{3C} + \underline{Z}_{4C}} \quad \text{(D.146)}$$

Associated voltage drops on each component are obtained from:

$$\underline{V}_{1A} = \underline{I}_{1A} \cdot \left(R_{h1} + j\omega L_{h1}\right) \quad \text{(D.147)} \qquad \underline{V}_{3A} = \underline{I}_{3A} \cdot \underline{Z}_{3A} \quad \text{(D.153)} \qquad \underline{V}_{4C} = \underline{I}_{4C} \cdot \underline{Z}_{4C} \quad \text{(D.158)}$$

$$\underline{V}_{1B} = \underline{I}_{1B} \cdot \left(R_{h1} + j\omega L_{h1}\right) \quad \text{(D.148)} \qquad \underline{V}_{3B} = \underline{I}_{3B} \cdot \underline{Z}_{3B} \quad \text{(D.154)} \qquad \underline{V}_{5A} = \underline{I}_{5A} \cdot \underline{Z}_{5A} \quad \text{(D.159)}$$

$$\underline{V}_{1C} = \underline{I}_{1C} \cdot \left(R_{h1} + j\omega L_{h1}\right) \quad \text{(D.149)} \qquad \underline{V}_{3C} = \underline{I}_{3C} \cdot \underline{Z}_{3C} \quad \text{(D.155)} \qquad \underline{V}_{5B} = \underline{I}_{5B} \cdot \underline{Z}_{5B} \quad \text{(D.160)}$$

$$\underline{V}_{2A} = \underline{I}_{2A} \cdot \left(R_{l1} + j\omega L_{l1}\right) \quad \text{(D.150)} \qquad \underline{V}_{4A} = \underline{I}_{4A} \cdot \underline{Z}_{4A} \quad \text{(D.156)} \qquad \underline{V}_{5C} = \underline{I}_{5C} \cdot \underline{Z}_{5C} \quad \text{(D.161)}$$

$$\underline{V}_{2B} = \underline{I}_{2B} \cdot \left(R_{l1} + j\omega L_{l1}\right) \quad \text{(D.151)} \qquad \underline{V}_{4B} = \underline{I}_{4B} \cdot \underline{Z}_{4B} \quad \text{(D.157)}$$

$$\underline{V}_{2C} = \underline{I}_{2C} \cdot \left(R_{l1} + j\omega L_{l1}\right) \quad \text{(D.152)}$$

c. DC Filter - Voltage Ripple Analysis

In order to assess necessity for DC filter, maximum non-filtered ripple voltage ΔV_{DCNF} is obtained by tracking time waveforms of modulated converter voltages: $\underline{E}_A$, $\underline{E}_B$ and $\underline{E}_C$, from which highest ripple value is obtained (fig. D.28).

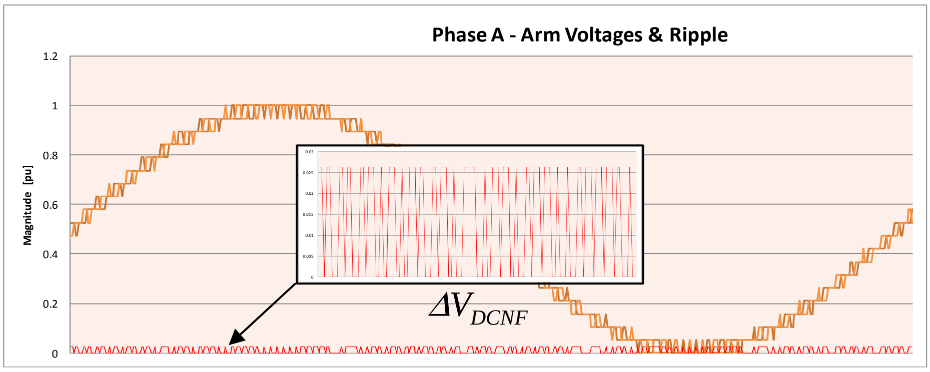

Fig. D.28 DC Voltage ripple appearance for non-filtered DC link (phase leg A).

It is assumed that 6 filter units are installed, each connected to individual converter's arm (fig. D.29).

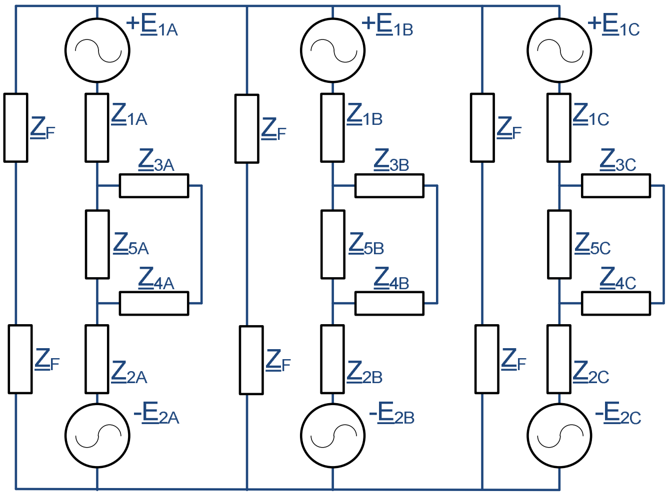

Fig. D.29 Circuit Analysis for DC filter current loading.

In order obtain minimum DC voltage ripple value based on entered capacitance value, following formula is provided: (163)

$$\Delta V_{DCF} = \frac{\Delta Q}{C_{FILTER(DC)}} \qquad \text{(D.162)}$$

$$\Delta Q = \int i \cdot dt \cong \sum i \cdot \Delta t \qquad \text{(D.164)}$$

$$\underline{Z}_F = R_{FILTER(DC)} - j\frac{1}{\omega \cdot C_{FILTER(DC)}} \qquad \text{(D.163)}$$

It is therefore required to calculate how charge changes within the filter's capacitor. As charge can be reflected by (165), it is obtained numerically in following steps:

1) Calculate AC harmonic currents flowing through filter capacitor based on circuit analysis from fig. provided with equations:

$$\underline{E}=\frac{\underline{Y}_{T(A)}\cdot\left(\underline{E}_{1A}+\underline{E}_{2A}\right)+\underline{Y}_{T(B)}\cdot\left(\underline{E}_{1B}+\underline{E}_{2B}\right)+\underline{Y}_{T(C)}\cdot\left(\underline{E}_{1C}+\underline{E}_{2C}\right)}{\underline{Y}_{T(A)}+\underline{Y}_{T(B)}+\underline{Y}_{T(C)}} \quad (D.165)$$

$$\underline{I}_F=\frac{\underline{E}}{\left(\underline{Y}_{T(A)}+\underline{Y}_{T(B)}+\underline{Y}_{T(C)}\right)^{-1}+\frac{2}{3}\cdot\underline{Z}_F} \quad (D.166)$$

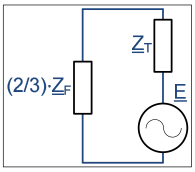

2) Based on obtained magnitude and phase angle of calculated currents, provide sinusoidal time distribution of each harmonic for a given number of cycles:

$$\begin{aligned}\underline{I}_1&=\left|\underline{I}_1\right|\cdot sin(\omega_1\cdot t+\varphi_1)=i_1\\ \underline{I}_2&=\left|\underline{I}_2\right|\cdot sin(\omega_2\cdot t+\varphi_2)=i_2\\ &\ldots\\ \underline{I}_n&=\left|\underline{I}_n\right|\cdot sin(\omega_n\cdot t+\varphi_n)=i_n\end{aligned} \quad (D.167)$$

3) Summate all absolute harmonic current instantaneous values for each cycle time interval to obtain average time waveform of the resulting current flowing through the filter:

$$i_{sum}(t)=0.5\cdot\sum_{i=1}^{n}\left|i_i(t)\right| \quad (D.168)$$

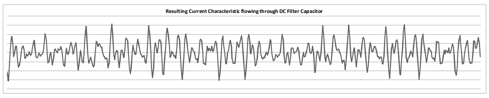

4) Calculate average charge per cycle by dividing summated current waveforms with number of cycles, and multiplying by a single cycle time interval:

$$\Delta Q=\left(\sum_{i=1}^{n_{samples}}i_{sum}(t_i)\right)\cdot\frac{t_{sample}}{n_{samples}} \quad (D.169)$$

Value obtained in (D.169) is used to enter proper DC filter capacitance in (D.162).

D.5 Theoretical Analysis - Internal Loading

a. Introduction

Theoretical circuit analysis is performed in order to analyze components internal loading states. From chapter D1c: “Internal Loading - Circulating Currents Phenomenon”, it is assumed that voltage ripple is composed predominantly from 2nd harmonic component. Thevenin approach is utilized. Following general circuit diagram is presented in Fig. D.30. It is assumed that all corresponding phase impedances are equal:

$\underline{Z}_{1A}=\underline{Z}_{1B}=\underline{Z}_{1C}$ (D.170) $\underline{Z}_{2A}=\underline{Z}_{2B}=\underline{Z}_{2C}$ (D.173) $\underline{Z}_{4A}=\underline{Z}_{4B}=\underline{Z}_{4C}$ (D.176)

$\underline{Z}_{5A}=\underline{Z}_{5B}=\underline{Z}_{5C}$ (D.171) $\underline{Z}_{6A}=\underline{Z}_{6B}=\underline{Z}_{6C}$ (D.174)

$\underline{Z}_{7A}=\underline{Z}_{7B}=\underline{Z}_{7C}$ (D.172) $\underline{Z}_{3A}=\underline{Z}_{3B}=\underline{Z}_{3C}$ (D.175)

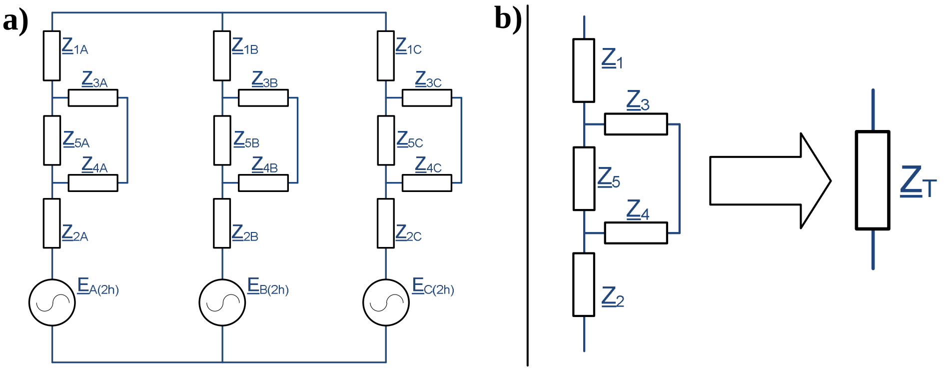

Fig. D.30 a) General schematic circuit representation for circuit analysis; b) Phase leg impedance derivation.

b. Circuit Analysis

First task is to obtain resulting leg impedances and common-mode sum cell voltage ripples modeled via leg voltage sources:

$$\underline{Z}_{T(A)} = \underline{Z}_{1A} + \underline{Z}_{2A} + \left(\underline{Y}_{5A} + \left(\underline{Z}_{3A+4A}\right)^{-1}\right)^{-1} \quad \text{(D.177)} \qquad \underline{E}_{A(2h)} = \left|\underline{E}_{A(2h)}\right| \cdot e^{j0} \quad \text{(D.180)}$$

$$\underline{Z}_{T(B)} = \underline{Z}_{1B} + \underline{Z}_{2B} + \left(\underline{Y}_{5B} + \left(\underline{Z}_{3B+4B}\right)^{-1}\right)^{-1} \quad \text{(D.178)} \qquad \underline{E}_{B(2h)} = \left|\underline{E}_{B(2h)}\right| \cdot e^{-j120} \quad \text{(D.181)}$$

$$\underline{Z}_{T(C)} = \underline{Z}_{1C} + \underline{Z}_{2C} + \left(\underline{Y}_{5C} + \left(\underline{Z}_{3C+4C}\right)^{-1}\right)^{-1} \quad \text{(D.179)} \qquad \underline{E}_{C(2h)} = \left|\underline{E}_{C(2h)}\right| \cdot e^{j120} \quad \text{(D.182)}$$

$$\left|\underline{E}_{A(2h)}\right| = \left|\underline{E}_{B(2h)}\right| = \left|\underline{E}_{B(2h)}\right| = N_{CELLS} \cdot V_{RIPPLE(CELL)} \cdot V_{NOM(CELL)} \quad \text{(D.183)}$$

Common-mode sum cell voltage ripple is obtained in (D.183) by multiplying number of cells per arm N_{CELLS} by single cell voltage ripple $V_{RIPPLE(CELL)}$. Circulating 2nd harmonic current flowing within each arm is obtained from:

$$\underline{I}_{A(2h)} = \frac{\underline{E}_{A(2h)}}{\underline{Z}_{T(A)}} \quad \text{(D.184)} \qquad \underline{I}_{B(2h)} = \frac{\underline{E}_{B(2h)}}{\underline{Z}_{T(B)}} \quad \text{(D.185)} \qquad \underline{I}_{C(2h)} = \frac{\underline{E}_{C(2h)}}{\underline{Z}_{T(C)}} \quad \text{(D.186)}$$

By manually tuning current limiting reactors and parallel resistance, it is possible to limit circulating current flow to the desired level.

D.6 Numerical Analysis

a. Introduction

Numerical analysis is used in order to obtain specific shapes of the corresponding converter voltage waveforms for each single arm, mostly based on given system specification ratings. As a result, Fourier analysis can be further included, which allows usage of Fast Fourier Transform FFT technique to determine harmonics from the generated waveforms.

b. Converter Phase Voltages

Each phase leg is operated independently according to its modulation pattern. Based on specification, carrier-based phase-shift modulation is implemented. This includes individual carrier waveform per single cell and a possibility to adjust modulation pulse number *p* for optimal performance. Implementation is made with the usage of Triangular wave ***Tri_Wave*** function available through Visual Basic (VBA) code. Its content is shown below:

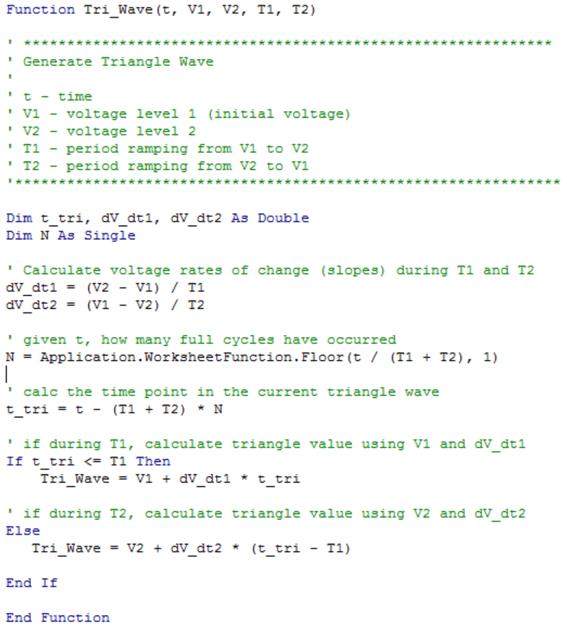

```
Function Tri_Wave(t, V1, V2, T1, T2)

' *************************************************************
' Generate Triangle Wave
'
' t - time
' V1 - voltage level 1 (initial voltage)
' V2 - voltage level 2
' T1 - period ramping from V1 to V2
' T2 - period ramping from V2 to V1
'**************************************************************

Dim t_tri, dV_dt1, dV_dt2 As Double
Dim N As Single

' Calculate voltage rates of change (slopes) during T1 and T2
dV_dt1 = (V2 - V1) / T1
dV_dt2 = (V1 - V2) / T2

' given t, how many full cycles have occurred
N = Application.WorksheetFunction.Floor(t / (T1 + T2), 1)

' calc the time point in the current triangle wave
t_tri = t - (T1 + T2) * N

' if during T1, calculate triangle value using V1 and dV_dt1
If t_tri <= T1 Then
    Tri_Wave = V1 + dV_dt1 * t_tri

' if during T2, calculate triangle value using V2 and dV_dt2
Else
   Tri_Wave = V2 + dV_dt2 * (t_tri - T1)

End If

End Function
```

Fig. D.31 Visual Basic (VBA) code for ***Tri_Wave*** function.

Triangular waveforms are generated in cell matrix. Implemented conditional formulas in matrix cell act as a comparator, which compares triangular signal in each sample time with the established reference sinusoidal signal. Comparator output signals (0 or 1) are given in cell matrix.

Finally, compared signals can be summated for each individual arm forming in total six voltage waveforms for the given number of time samples. Samples are distributed equally for each phase among single full cycle period. Typical voltage waveforms for 36 cells per leg are shown below:

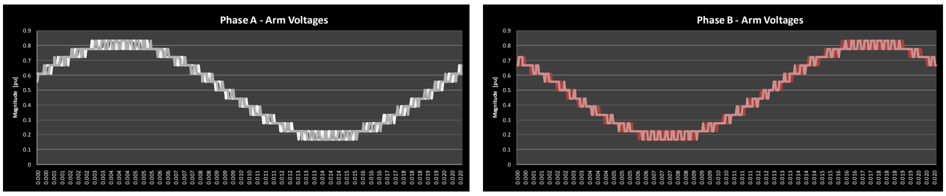

Fig. D.32 Generated converter output voltage waveforms for 36 cells per phase leg.

c. Circuit Analysis

FFT is realized in Excel with the usage of pre-defined complex arrays and matrices. Calculations for Fourier coefficients for n-th harmonic **H_n** is made based on equation (182):

$$H_n = \sum_{k=0}^{N-1} h_k \cdot e^{j \cdot k \cdot \frac{2 \cdot \pi \cdot n}{N}} \qquad \text{(D.187)}$$

Where:

h_k	- k-th sample function value.
n	- harmonic order.
N	- number of samples.

N generated samples of each arm voltage waveform are being instantly transformed into sinusoidal harmonic coefficients, which include magnitude and phase values for different frequencies.

Finally, circuit analysis becomes possible with the usage of conventional and standard AC circuit laws.

E. IGBT & Diode Power Loss Formulas - Experimental Testing

In order to validate experimentally described power loss estimator; a lab test set-up has been prepared, shown in Fig E.1. It consists of a single-phase 2-level converter leg with 4500 V / 340 A IGBTs [5] interconnected to the inductive load. 2 pulse signals are injected to the IGBT, which command ON and OFF switching operation. IGBT switches at $V_{C-E(DC)} = 1000$ V.

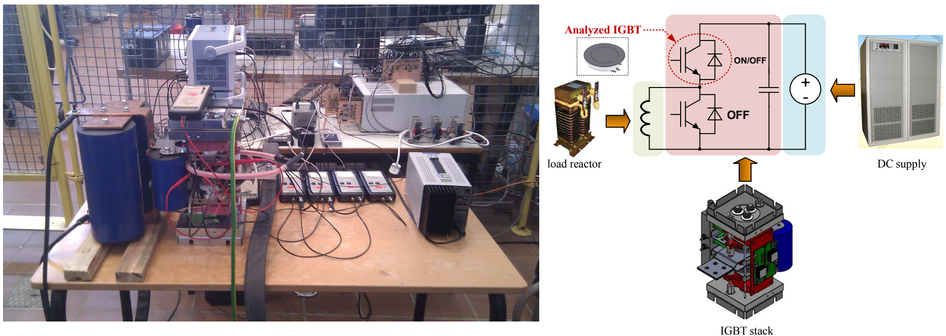

Fig. E.1 Experimental test set-up for power loss modelling estimation.

Length of pulse signals is set to switch IGBT at specific I_c values shown in table E.1. Measured instantaneous I_c and V_{CE} from Fig. E.2 are then integrated at switching time intervals to provide $E_{ON(m)}$ and $E_{OFF(m)}$ parameters for single switching. In total, 10 switching iterations have been made for the identical set of I_c currents, where integrated switching energy iterations have been averaged for the resulting value in table E.1.

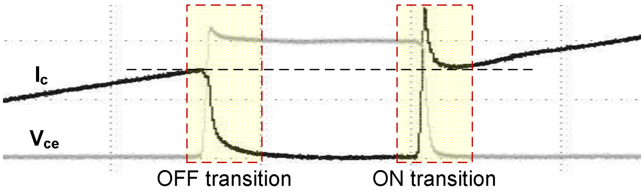

Fig. E.2 Measured iteration of a single turn-ON and turn-OFF switching transitions.

Calculated energy values are then compared to the ones obtained theoretically: $E_{ON(t)}$ and $E_{OFF(t)}$. Complete list of the used formulas is given in table E.2. Results show approximately 10% error between measured and calculated value.

Table E.1 Measured and calculated E_{ON}, E_{OFF} switching energies - comparison results (1000 V)

I_c [A]	$E_{ON(m)}$ [mJ]	$E_{ON(t)}$ [mJ]	δ_{error} [%]	$E_{OFF(m)}$ [mJ]	$E_{OFF(t)}$ [mJ]	δ_{error} [%]
50	61	51	16	83	55	34
100	115	102	11	134	127	5
150	195	171	12	212	196	8

Table E.2 Interpolated loss formulas for the IGBT & Diode press-packs.

IGBT/Diode Press-Pack [59] **(per die)**		
$E_{ON(IGBT)} = f(v, i_C, T_j) = [a_{ON} \cdot i_C^3 + b_{ON} \cdot i_C^2 + c_{ON} \cdot i_C] \cdot [d_{ON} \cdot T_j + e_{ON}]$		Turn-ON Energy (IGBT)
$a_{ON} = 1.54 \cdot 10^{-14} \cdot v^2 - 5.03 \cdot 10^{-11} \cdot v + 3.98 \cdot 10^{-8}$	$d_{ON} = 2.25 \cdot 10^{-3}$	
$b_{ON} = -7.36 \cdot 10^{-12} \cdot v^2 + 2.91 \cdot 10^{-8} \cdot v - 1.87 \cdot 10^{-5}$	$e_{ON} = 7.19 \cdot 10^{-1}$	
$c_{ON} = 9.03 \cdot 10^{-10} \cdot v^2 - 1.71 \cdot 10^{-6} \cdot v + 1.81 \cdot 10^{-3}$		
$E_{OFF(IGBT)} = f(v, i_C, T_j) = \begin{cases} [a_{OFF} \cdot i_C^3 + b_{OFF} \cdot i_C^2 + c_{OFF} \cdot i_C] \cdot [f_{OFF} \cdot T_j + g_{OFF}] & \rightarrow i_C < 55\,A \\ [d_{OFF} \cdot i_C + e_{OFF}] \cdot [f_{OFF} \cdot T_j + g_{OFF}] & \rightarrow i_C \geq 55\,A \end{cases}$		Turn-OFF Energy (IGBT)
$a_{OFF} = -4.94 \cdot 10^{-15} \cdot v^2 - 6.54 \cdot 10^{-12} \cdot v - 1.66 \cdot 10^{-9}$	$e_{OFF} = 3.07 \cdot 10^{-8} \cdot v^2 - 1.37 \cdot 10^{-5} \cdot v + 1.81 \cdot 10^{-1}$	
$b_{OFF} = 2.46 \cdot 10^{-12} \cdot v^2 - 3.09 \cdot 10^{-9} \cdot v - 1.31 \cdot 10^{-6}$	$f_{OFF} = 2.69 \cdot 10^{-3}$	
$c_{OFF} = -5.19 \cdot 10^{-10} \cdot v^2 + 2.61 \cdot 10^{-6} \cdot v + 2.40 \cdot 10^{-4}$	$g_{OFF} = 6.64 \cdot 10^{-1}$	
$d_{OFF} = -3.37 \cdot 10^{-10} \cdot v^2 + 2.35 \cdot 10^{-6} \cdot v - 9.24 \cdot 10^{-4}$		
$E_{REC(D)} = f(v = 2800\,V, i_F, T_j) = a_{REC} \cdot i_F \cdot [b_{REC} \cdot T_j + c_{REC}]$		Reverse Recovery Energy (Diode)
$a_{REC} = 1.20 \cdot 10^{-3}$	$c_{REC} = 4.94 \cdot 10^{-1}$	
$b_{REC} = 4.05 \cdot 10^{-3}$		
$V_{CE(sat)(IGBT)} = f(i_C, T_j) = a_{cond(IGBT)} \cdot i_C^{b_{cond(IGBT)}} \cdot [c_{cond(IGBT)} \cdot T_j + d_{cond(IGBT)}]$		ON-state Voltage, IGBT
$a_{cond(IGBT)} = 0.2554$	$c_{cond(IGBT)} = 2.69 \cdot 10^{-3}$	
$b_{cond(IGBT)} = 0.4501$	$d_{cond(IGBT)} = 6.76 \cdot 10^{-1}$	
$V_{F(D)} = f(i_F, T_j) = a_{cond(D)} \cdot i_C^{b_{cond(D)}} \cdot [c_{cond(D)} \cdot T_j + d_{cond(D)}]$		ON-state Voltage, Diode
$a_{cond(D)} = 0.373$	$c_{cond(D)} = 8.70 \cdot 10^{-4}$	
$b_{cond(D)} = 0.383$	$d_{cond(D)} = 8.91 \cdot 10^{-1}$	

Table E.3 Interpolated loss formulas for the IGBT & Diode power modules.

IGBT/Diode Power Module [60] **(per device)**		
$E_{ON(IGBT)} = f(v = 900V, i_C, T_j) = [a_{ON} \cdot i_C^3 + b_{ON} \cdot i_C^2 + c_{ON} \cdot i_C + d_{ON}] \cdot [e_{ON} \cdot T_j + f_{ON}]$		Turn-ON Energy (IGBT)
$a_{ON} = 6.94 \cdot 10^{-10}$	$d_{ON} = 6.96 \cdot 10^{-3}$	
$b_{ON} = -3.39 \cdot 10^{-7}$	$e_{ON} = 2.50 \cdot 10^{-3}$	
$c_{ON} = 4.45 \cdot 10^{-4}$	$f_{ON} = 6.88 \cdot 10^{-1}$	
$E_{OFF(IGBT)} = f(v = 900V, i_C, T_j) = [a_{OFF} \cdot i_C^3 + b_{OFF} \cdot i_C^2 + c_{OFF} \cdot i_C + d_{OFF}] \cdot [e_{OFF} \cdot T_j + f_{OFF}]$		Turn-OFF Energy (IGBT)
$a_{OFF} = -7.10 \cdot 10^{-12}$	$d_{OFF} = 8.48 \cdot 10^{-3}$	
$b_{OFF} = 9.77 \cdot 10^{-9}$	$e_{OFF} = 3.43 \cdot 10^{-3}$	
$c_{OFF} = 2.91 \cdot 10^{-4}$	$f_{OFF} = 5.71 \cdot 10^{-1}$	
$E_{REC(D)} = f(v = 900V, i_F, T_j) = [a_{REC} \cdot i_F^3 + b_{REC} \cdot i_F^2 + c_{REC} \cdot i_F + d_{REC}] \cdot [e_{REC} \cdot T_j + f_{REC}]$		Reverse Recovery Energy (Diode)
$a_{REC} = 1.09 \cdot 10^{-10}$	$d_{REC} = 2.04 \cdot 10^{-2}$	
$b_{REC} = -3.00 \cdot 10^{-7}$	$e_{REC} = 4.67 \cdot 10^{-3}$	
$c_{REC} = 3.01 \cdot 10^{-4}$	$f_{REC} = 4.17 \cdot 10^{-1}$	
$V_{CE(sat)(IGBT)} = f(i_C, T_j) = a_{cond(IGBT)} \cdot i_C^{b_{cond(IGBT)}} \cdot [c_{cond(IGBT)} \cdot T_j + d_{cond(IGBT)}]$		ON-state Voltage, IGBT
$a_{cond(IGBT)} = 18.96 \cdot 10^{-2}$	$c_{cond(IGBT)} = 2.22 \cdot 10^{-3}$	
$b_{cond(IGBT)} = 41.92 \cdot 10^{-2}$	$d_{cond(IGBT)} = 7.22 \cdot 10^{-1}$	
$V_{F(D)} = f(i_F, T_j) = a_{cond(D)} \cdot i_C^{b_{cond(D)}} \cdot [c_{cond(D)} \cdot T_j + d_{cond(D)}]$		ON-state Voltage, Diode
$a_{cond(D)} = 19.9 \cdot 10^{-2}$	$c_{cond(D)} = 1.11 \cdot 10^{-3}$	
$b_{cond(D)} = 37.6 \cdot 10^{-2}$	$c_{cond(D)} = 8.61 \cdot 10^{-1}$	

F. EMTDC/PSCAD: WTG Short Circuit Contributions

Table F.1 1-phase fault current waveforms in the transformer-less WTGs

Grounding	System A	System B	System C
1-1-1	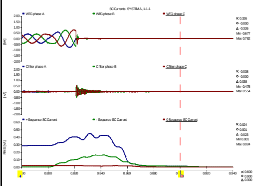	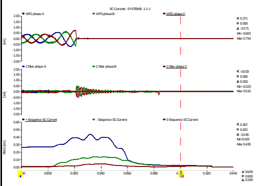	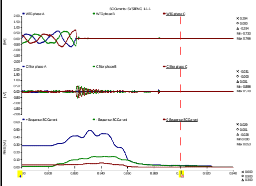
1-1-0	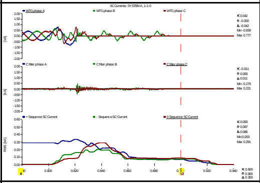	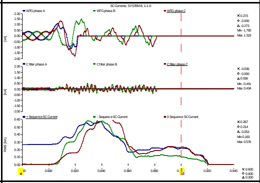	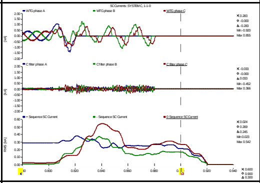
1-0-1	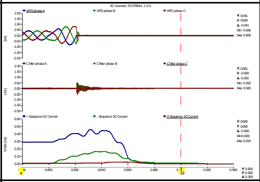	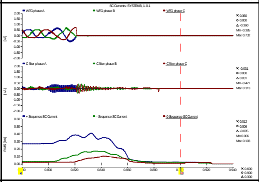	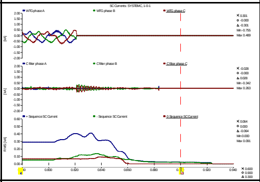
0-1-1	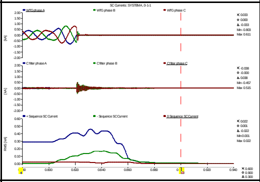	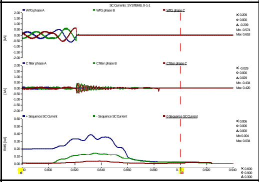	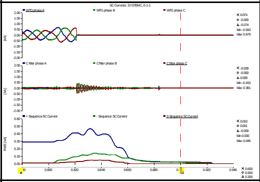
1-0-0	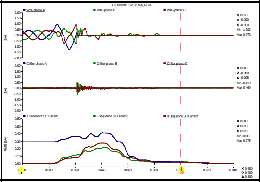	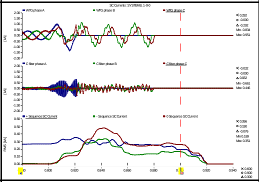	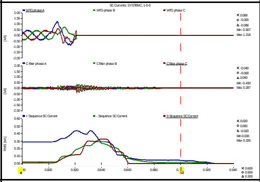
0-1-0	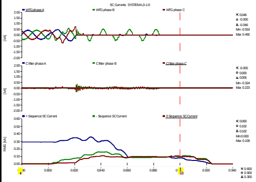	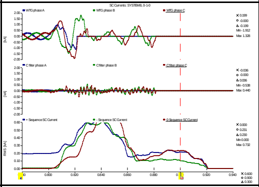	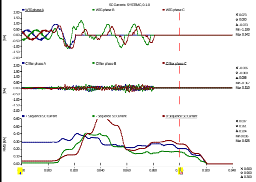
0-0-1	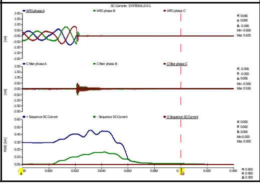	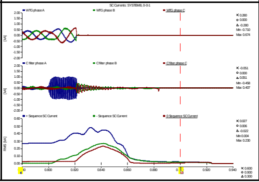	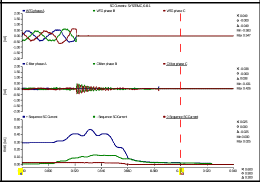

Table F.2 2-phase fault current waveforms in the transformer-less WTGs

Grounding	System A	System B	System C
1-1-1	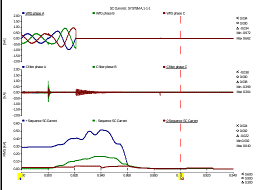	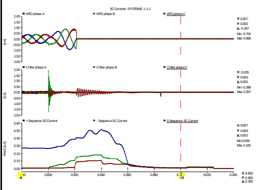	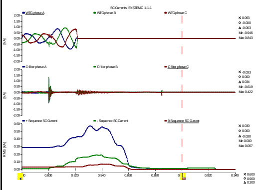
1-1-0	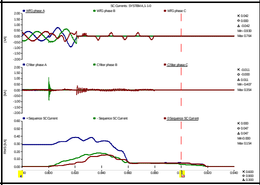	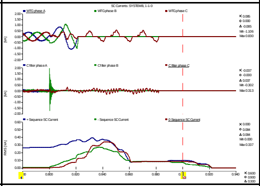	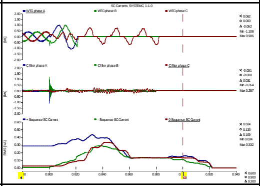
1-0-1	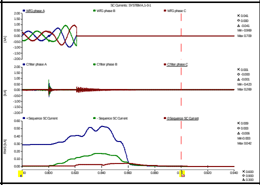	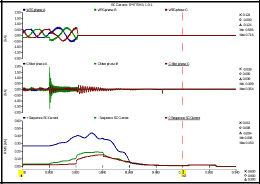	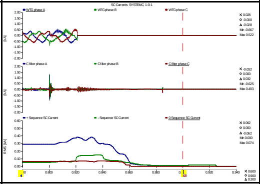
0-1-1	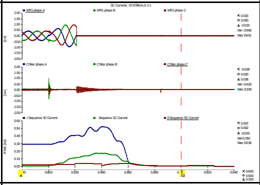	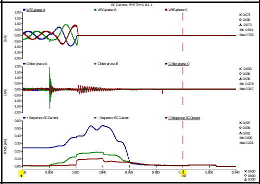	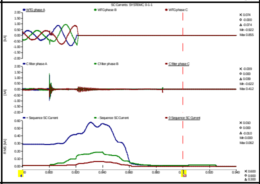
1-0-0	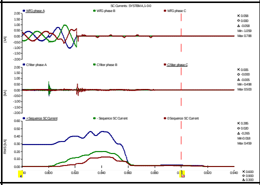	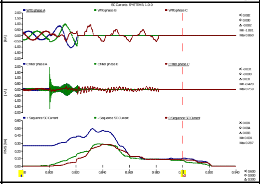	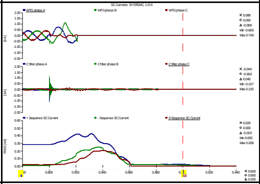
0-1-0	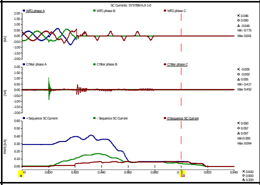	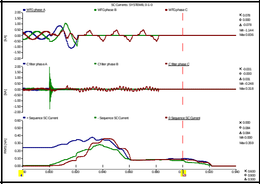	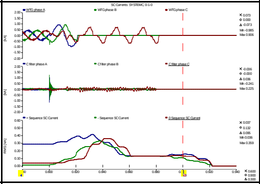
0-0-1	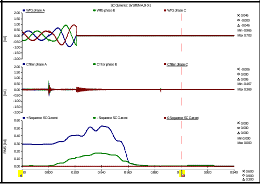	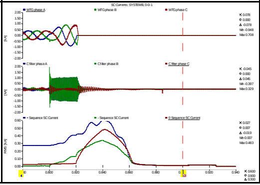	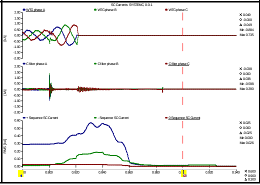

Table F.3 3-phase fault current waveforms in the transformer-less WTGs

Grounding	System A	System B	System C
1-1-1	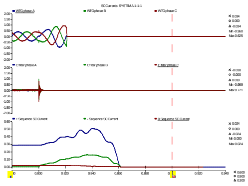	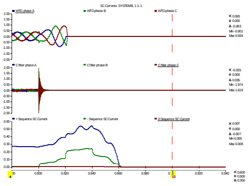	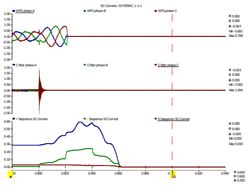
1-1-0	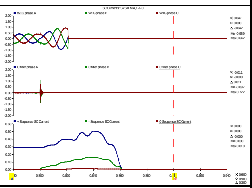	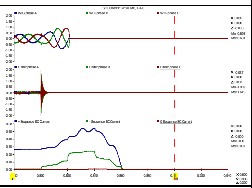	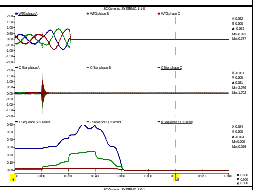
1-0-1	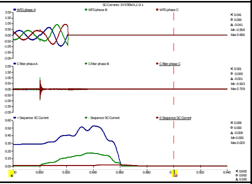	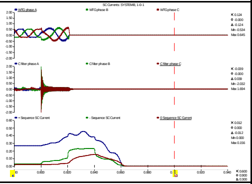	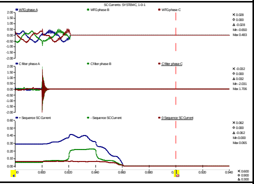
0-1-1	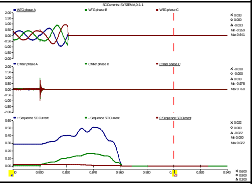	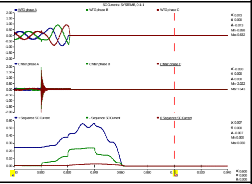	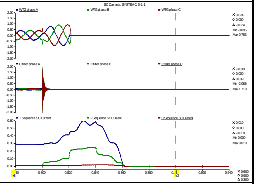
1-0-0	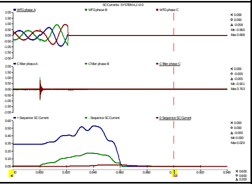	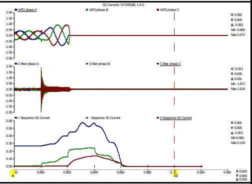	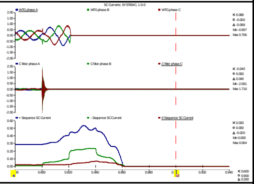
0-1-0	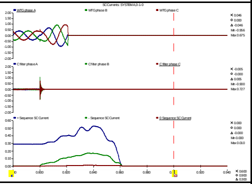	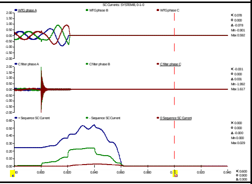	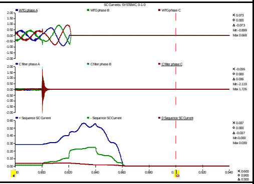
0-0-1	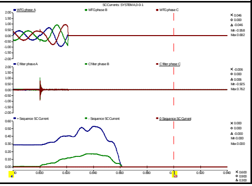	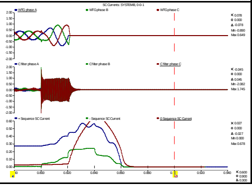	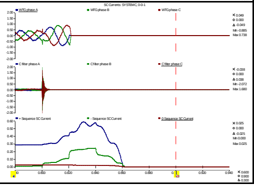

G. PI Controllers in PQ Closed Loop Control

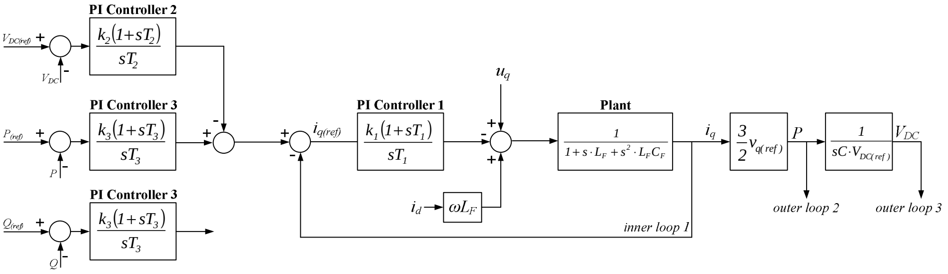

Fig. G.1 AC circuit PI controllers for tuning: PQ power, DC voltage and AC current.

Closed loop s-transfer functions used as an input data for PI controller tuning in SISO tool:

- **Inner loop 1:** $$G_1(s)=\frac{k_1(1+sT_1)}{sT_1}\cdot\frac{1}{1+s\cdot L_F+s^2\cdot L_F C_F}$$
- **Outer loop 2:** $$G_2(s)=\frac{k_2(1+sT_2)}{sT_2}\cdot\frac{3}{2}v_{q(ref)}\cdot\frac{1}{sC\cdot V_{DC(ref)}}$$
- **Outer loop 3:** $$G_3(s)=\frac{k_3(1+sT_3)}{sT_3}\cdot\frac{3}{2}v_{q(ref)}$$

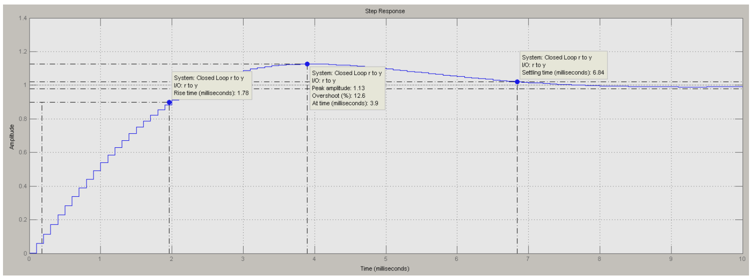

Fig. G.2 Quantized step response in SISO tool - example.

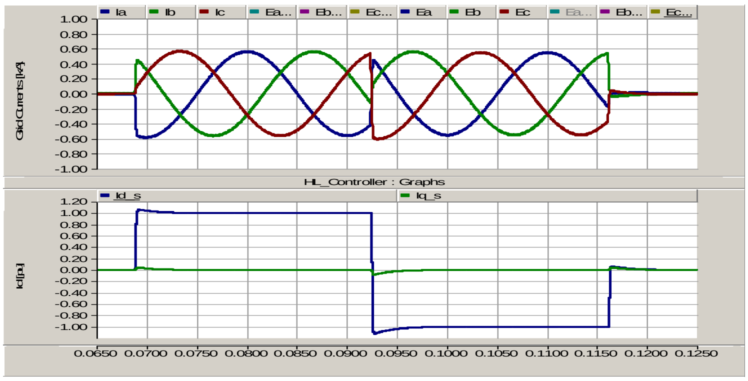

Fig. G.3 d-axis current controller step response (bottom); AC grid currents (top) - example.

H. EMTDC/PSCAD Relay - Experimental Testing

Experimental analysis of the EMTDC/PSCAD differential relay has been explained in details in [75]. Figure H.1 provides lab test set-up used to test sensitivity and operating speed of the relay model. Results obtained both from the experimental testing and time-domain simulations are compared in tables H.1 and H.2. Both real relay and the EMTC/PSCAD relay model have identical input settings.

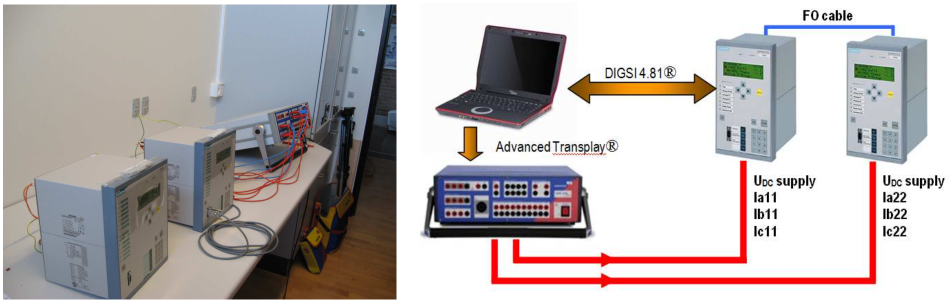

Fig. H.1 Experimental test set-up for the validation of relay selectivity and the operating speed.

Results show, that the relaying time differs by maximum 6 ms for a single faults; 1 ms for a 2-phase faults and 3 ms for a 3-phase faults, whereas the sensitivity differences are negligible.

Table H.1 Measured and calculated relaying times of the real relay and the EMTDC/PSCAD relay model.

Fault Type	**Time interval (ms)**	
	Experimental Results	***PSCAD Simulation Results***
Single-phase to ground internal fault	8	14
Two-phase to ground internal fault	14 │ 14	15 │ 15
Three-phase to ground internal fault	18 │ 12 │ 18	15 │ 10 │ 15

Table H.2 Measured and calculated sensitivity margins of the real relay and the EMTDC/PSCAD relay model.

Internal fault resistance [Ω]	**Differential phasor $I_{diff>}$ threshold for tripping**		**Differential phasor $I_{diff>}$ threshold for non-tripping**	
	Experimental Results	***PSCAD Simulation Results***	***Experimental Results***	***PSCAD Simulation Results***
55	4,02	4,05	4,03	4,06
70	3,23	3,25	3,24	3,26
145	1,72	1,73	1,73	1,74
210	1,31	1,32	1,32	1,33